



**SOLID-STATE NMR OF HYDROGEN-BONDED  
MATERIALS**

SOLID-STATE NMR ANALYSES OF  
MOLECULAR STRUCTURE AND DYNAMICS IN  
HYDROGEN-BONDED MATERIALS

BY

GABRIELLE FORAN, M. Sc.

A Thesis Submitted to the School of Graduate Studies in Partial  
Fulfillment of the Requirements for the Degree

DOCTOR OF PHILOSOPHY

McMaster University

© Copyright by Gabrielle Foran, August 2019

Ph. D. Thesis – G. Foran; McMaster University - Chemistry

McMaster University, Hamilton, Ontario

DOCTOR OF PHILOSOPHY (2019) Chemistry and Chemical Biology

TITLE: Solid-State NMR Analyses of Molecular Structure and Dynamics in Hydrogen-Bonded Materials

AUTHOR: Gabrielle Foran, B. Sc., M. Sc. (University of Guelph)

SUPERVISOR: Professor Gillian R. Goward

NUMBER OF PAGES: xxiv, 245

## **Lay Abstract**

Hydrogen bonds are intermolecular interactions that are significant in many structural (low crystal density in ice) and dynamic (enzymatic processes occurring under biological conditions) processes that are necessary to maintain life. In this thesis, solid-state nuclear magnetic resonance (NMR) spectroscopy is used to explore proton dynamics of hydrogen-bonded networks in various materials. Advanced NMR experiments that probe homo- and heteronuclear dipolar coupling interactions revealed possible pathways for proton transport in phosphate-based proton conducting materials. This study provided a better understanding of ion conducting mechanisms that can be used in intermediate-temperature fuel cell applications. Additionally, solid-state NMR was used in the identification of hydrogen bonding and other coordination modes in silicone boronate acids (SiBA), a class of elastomers with potential applications as contact lens. Boron coordination in SiBA elastomers was dependent on both boronic acid loading and boronic acid packing density.

## **Abstract**

This thesis presents analyses of hydrogen-bonded materials using solid-state nuclear magnetic resonance (NMR) spectroscopy. Proton dynamics were investigated in two classes of phosphate-based proton conductors: phosphate solid acids and tin pyrophosphates. These materials have the potential to be used as solid-state proton conductors in fuel cells. Proton dynamics in phosphate solid acids were probed based on the attenuation of homonuclear dipolar coupling with increasing temperature. These studies showed that homonuclear dipolar recoupling NMR techniques can be employed in complex multi-spin systems. Additionally, two pathways for proton hopping in monoclinic  $\text{RbH}_2\text{PO}_4$ , a sample with two proton environments, were identified and quantified for the first time using a combination of dipolar recoupling and proton exchange NMR methods. Tin pyrophosphates, another class of solid-state proton conductor with analogous phosphate tetrahedral structure, were studied. Proton dynamics had to be analyzed via exchange-based NMR techniques as a result of low proton concentration in these materials. Proton mobility in tin pyrophosphate was found to increase with increased protonation. Furthermore, hydrogen bonding was investigated as a coordination mode in silicone boronic acid (SiBA) elastomers, potential materials for contact lens manufacture. As in the phosphate-based proton conductors, hydrogen bonding played an important role in the structure of the SiBA elastomers as one of the mechanisms through which these materials crosslink. In addition to

hydrogen bonding, covalent bonding between boronic acids was found to occur at three- and four-coordinate boron centers. The purpose of this study was to determine the influence of boronic acid loading and packing density on crosslinking in SiBA elastomers. Boron coordination environments were investigated by  $^{11}\text{B}$  quadrupolar lineshape analysis. The incidence of four-coordinate dative bonding, a predictor of the stress-strain response in these materials, increased with boronic acid loading but was most heavily influenced by boronic acid packing density.

## **Acknowledgements**

I would like to thank my supervisor, Dr. Gillian Goward, for initially accepting me as a PhD student and for continuing to support me for the duration of my studies at McMaster University. Gillian was instrumental in creating a supportive environment in which I could develop as a scientist by undertaking research in a field in which I had minimal prior experience. Gillian also encouraged me in many of my extra-curricular pursuits by supporting my decisions to take part in campus activities including varsity athletics, volunteering with Let's Talk Science, enrolling in additional chemistry and education courses and working as a Coordinator in the Course Design/Delivery Consultants Program. In addition, I am also grateful for the continued support of my committee members: Dr. Darren Brouwer and Dr. Yuriy Mozharivskyj who have both helped me immensely in developing my critical thinking skills. I am particularly thankful to Darren for helping me get started with NMR data collection for my phosphate solid acids project and for offering helpful insight through his participation in Goward group meetings during the summer months. I am thankful to Yuriy for allowing me to have access to his X-ray diffractometer which has been very useful in the characterization of materials for the phosphate solid acid and tin pyrophosphate projects.

In addition to my advisory committee, there are several other members of the McMaster University chemistry department whose contributions and time have

been essential to my accomplishments as a graduate student. In terms of instrumentation, am grateful to the NMR facility management team for providing training and assistance as well as the expertise necessary for keeping the spectrometers operational. In terms of knowledge, I am appreciative of Dr. Giuseppe Melacini and his NMR course for teaching me how pulse sequences actually work. I would also like to thank all the Goward group members, past and present, who I have had the privilege of working with for the time that we have spent together in settings both scientific and non. I am happy that I have had the opportunity to meet and learn from a group of people with diverse skill sets.

In addition, I would like to thank all my non-scientific supporters including my parents and other family members, my running coach, my co-workers at the MacPherson Institute, my training partners and my relationship partner. You have all made my time at McMaster University and in the Hamilton community better by being supportive of my goals, helping me face challenges and celebrating my achievements.

## Table of Contents

Contents	
<b>Lay Abstract</b> .....	<b>iii</b>
<b>Abstract</b> .....	<b>iv</b>
<b>Acknowledgements</b> .....	<b>vi</b>
<b>Table of Contents</b> .....	<b>viii</b>
<b>List of Figures</b> .....	<b>xii</b>
<b>List of Tables</b> .....	<b>xix</b>
<b>List of Abbreviations and Symbols</b> .....	<b>xx</b>
<b>Declaration of Academic Achievement</b> .....	<b>xxiv</b>
<b>Chapter 1: Introduction</b> .....	<b>1</b>
<b>1.1 Scope of the Thesis</b> .....	<b>1</b>
<b>1.2 Hydrogen Bonding</b> .....	<b>3</b>
<b>1.2.1 Defining Hydrogen Bonding</b> .....	<b>3</b>
<b>1.2.2 Structure and Energetics of Hydrogen Bonds</b> .....	<b>4</b>
<b>1.3 Hydrogen Bonding in Hard Solids</b> .....	<b>7</b>
<b>1.3.1 Fuel Cell Electrolytes: An Application of Connectivity in         Hydrogen-Bonded Networks</b> .....	<b>8</b>
<b>1.3.2 Phosphate-based Proton Conductors as Fuel Cell Electrolytes</b> .....	<b>11</b>
<b>1.4 Hydrogen Bonding in Soft Solids</b> .....	<b>18</b>
<b>1.4.1 Boronic Acid Functionalized Polydimethylsiloxane</b> .....	<b>19</b>
<b>1.5 Analyses of Hydrogen-Bonded Materials</b> .....	<b>24</b>
<b>1.6 References</b> .....	<b>24</b>
<b>Chapter 2: Methodology</b> .....	<b>29</b>
<b>2.1 Solid State NMR</b> .....	<b>30</b>
<b>2.1.1 Interactions Between Nuclei and An External Magnetic Field</b> .....	<b>30</b>
<b>2.1.2 Applied Radiofrequency Pulses</b> .....	<b>34</b>
<b>2.1.3 Mechanisms of Relaxation</b> .....	<b>36</b>
<b>2.1.4 Chemical Shift</b> .....	<b>38</b>
<b>2.1.5 Solid-State NMR and Magic Angle Spinning</b> .....	<b>39</b>

<b>2.2 Solid-State NMR of Dipolar Nuclei .....</b>	<b>41</b>
<b>2.2.1 Homonuclear Dipolar Coupling Interactions in spin ½ Nuclei .....</b>	<b>41</b>
<b>2.2.2 Symmetry-Based Dipolar Recoupling in Homonuclear Systems ...</b>	<b>42</b>
<b>2.2.3 Heteronuclear Dipolar Coupling Interactions in spin ½ Nuclei.....</b>	<b>47</b>
<b>2.2.4 Approximating Heteronuclear Dipolar Coupling with Cross-Polarization .....</b>	<b>47</b>
<b>2.3 Chemical Exchange .....</b>	<b>51</b>
<b>2.3.1 Introduction to Chemical Exchange .....</b>	<b>51</b>
<b>2.3.2 Exchange Spectroscopy .....</b>	<b>54</b>
<b>2.3.3 Selective Inversion .....</b>	<b>57</b>
<b>2.4 Solid-State NMR of Quadrupolar Nuclei.....</b>	<b>63</b>
<b>2.4.1 Interactions and Energetics of Quadrupolar Nuclei .....</b>	<b>63</b>
<b>2.4.2 Challenges in the Elucidation of Coordination Environments in Quadrupolar Systems.....</b>	<b>66</b>
<b>2.4.3 Experimental Techniques for the Resolution Non-Equivalent Sites .....</b>	<b>67</b>
<b>2.4.4 Multiple Quantum Magic Angle Spinning .....</b>	<b>69</b>
<b>2.5 Additional Experimental Techniques.....</b>	<b>72</b>
<b>2.5.1 Electrochemical Impedance Spectroscopy .....</b>	<b>72</b>
<b>2.5.2 Powder X-ray Diffraction .....</b>	<b>76</b>
<b>2.5.3 Thermogravimetric Analysis.....</b>	<b>79</b>
<b>2.6 References .....</b>	<b>80</b>
<b>Chapter 3: Quantifying Site-Specific Proton Dynamics in Phosphate Solid Acids by <sup>1</sup>H Double Quantum NMR Spectroscopy .....</b>	<b>85</b>
<b>3.1 Introduction .....</b>	<b>85</b>
<b>3.2 Experimental.....</b>	<b>89</b>
<b>3.2.1 Sample Preparation.....</b>	<b>89</b>
<b>3.2.2 Impedance Spectroscopy.....</b>	<b>90</b>
<b>3.2.3 Powder X-ray Diffraction .....</b>	<b>91</b>
<b>3.2.4 NMR Measurements.....</b>	<b>91</b>
<b>3.3 Results and Discussion.....</b>	<b>92</b>

3.3.1 Proton Conductivity in Systems Containing Phosphate Tetrahedra .....	92
3.3.2 Overview of Site-Specific Proton Motion .....	93
3.3.3 Calcium Hydroxyapatite: A non-conductive reference .....	96
3.3.4 $\text{KH}_2\text{PO}_4$ : A Single Proton Site with Dynamics .....	96
3.3.4 $\text{RbH}_2\text{PO}_4$ : Two Proton Sites with Dynamics.....	100
3.3.5 Proton Hopping Pathways in $\text{RbH}_2\text{PO}_4$ .....	105
3.4 Conclusion.....	109
3.5 References .....	110
<b>Chapter 4: An Alternate Pathway for Proton Hopping in Monoclinic <math>\text{RbH}_2\text{PO}_4</math> .....</b>	<b>113</b>
4.1 Introduction .....	114
4.2 Experimental.....	117
4.2.1 Sample Preparation .....	117
4.2.2 Electrical Impedance Spectroscopy .....	118
4.2.3 Solid State NMR .....	118
4.3 Results .....	119
4.3.1 Proton EXSY in Monoclinic $\text{RbH}_2\text{PO}_4$ .....	119
4.3.2 Proton Selective Inversion in Monoclinic $\text{RbH}_2\text{PO}_4$ .....	123
4.3.3 Proton Conductivity in Monoclinic RDP.....	128
4.4 Discussion.....	129
4.5 Conclusions .....	133
4.6 References .....	133
<b>Chapter 5: Proton Dynamics in Tin Pyrophosphates.....</b>	<b>137</b>
5.1 Introduction .....	138
5.2 Experimental.....	145
5.2.1 Tin Pyrophosphate Synthesis .....	145
5.2.2 Powder X-ray Diffraction .....	146
5.2.3 Electrochemical Impedance Spectroscopy .....	146
5.2.4 Solid-State NMR.....	147
5.3 Results and Discussion .....	147

5.3.1 Tin Pyrophosphate Synthesis .....	147
5.3.2 Tin Pyrophosphate Structure .....	152
5.3.3 Proton Dynamics in Tin Pyrophosphates .....	163
5.4 Conclusion.....	175
5.5 References .....	176
<b>Chapter 6: Solid-State NMR Study of Boron Coordination Environments in Boron-Containing Polymers .....</b>	<b>179</b>
6.1 Introduction .....	180
6.2 Experimental.....	187
6.2.1 Synthesis of SiBAs .....	187
6.2.2 Thermal gravimetric analysis .....	188
6.2.3 Solid-State NMR.....	188
6.3 Results and Discussion .....	189
6.3.1 <sup>11</sup> B MQMAS NMR.....	189
6.3.2 Boron Coordination Environments in SiBA Elastomers .....	193
6.3.3 Boron Coordination Environments in Commercial Silly Putty ...	208
6.4 Conclusion.....	214
6.5 References .....	215
<b>Chapter 7: Summary and Future Work.....</b>	<b>219</b>
7.1 Summary .....	219
7.2 Future Work .....	224
7.2.1 Phosphate Solid Acids .....	224
7.2.2 Tin Pyrophosphates.....	225
7.2.3 Boronic Acid-Containing Elastomers .....	228
7.3 References .....	229
<b>Appendix.....</b>	<b>233</b>
<b>A.1 Quadrupolar Lineshape Fitting in SiBA Elastomers .....</b>	<b>233</b>
<b>A.2 Direct Analyses of <sup>1</sup>H Coordination in SiBA Elastomers .....</b>	<b>240</b>
<b>A.3 Coordination Environments in Silly Putty.....</b>	<b>242</b>
<b>A.4 References .....</b>	<b>244</b>

## List of Figures

<b>Figure 1. 1.</b> Energy diagram showing potential wells for various oxygen-oxygen distances in O-H···O systems. These diagrams are adapted from computational work presented by Huggins <sup>6</sup> on H-O···H bonds in solid and liquid water. 2.75 Å is a typical oxygen-oxygen distance in this system. <sup>6</sup> The energy barrier in the potential well disappears when the oxygen-oxygen distance decreases to 2.55 Å. <sup>6</sup> .....	<b>5</b>
<b>Figure 1. 2.</b> Packing density of water molecules in the solid and liquid states. The cage-like structure is conserved upon freezing resulting in a low-density solid. ...	<b>7</b>
<b>Figure 1. 3.</b> Schematic of a generic fuel cell.....	<b>9</b>
<b>Figure 1. 4.</b> Superprotonic transition from monoclinic CDP to cubic CDP results in significant disordering of the hydrogen-bonded network facilitating proton hopping. ....	<b>13</b>
<b>Figure 1. 5.</b> Ionic phase transition from tetragonal to monoclinic RDP. The phase change occurs over a temperature range as opposed to one specific temperature.	<b>14</b>
<b>Figure 1. 6.</b> Cubic tin pyrophosphate is comprised of phosphate tetrahedra and tin octahedra. The material is unprotonated in its native state. ....	<b>16</b>
<b>Figure 1. 7.</b> PDMS monomer unit.....	<b>20</b>
<b>Figure 2. 1.</b> Diagram showing Zeeman splitting of a spin ½ nucleus in a strong magnetic field ( $B_0$ ). ....	<b>31</b>
<b>Figure 2. 2.</b> Larmor precession in a strong magnetic field ( $B_0$ ). The presence of a second weak field ( $B_1$ ) perpendicular to $B_0$ results in torque ( $T$ ) that increases the angle between $\mu$ and $B_0$ . ....	<b>34</b>
<b>Figure 2. 3.</b> Effects of a rf pulse ( $\omega_{rf}$ ) in the x-direction on the magnetization vector ( $M$ ). ....	<b>35</b>
<b>Figure 2. 4.</b> Powder sample packed in a rotor rotating at an angle $\theta$ relative to the external magnetic field ( $B_0$ ). Broadening due to chemical shift anisotropy and dipolar coupling interactions is significantly reduced when $\theta$ is equal to 54.7°...	<b>40</b>
<b>Figure 2. 5.</b> Normalization of DQ intensity from the analysis of calcium hydroxyapatite with the R264 <sup>11</sup> pulse sequence on a 7.0 T spectrometer with 13.7 kHz MAS: a) signal intensities of the DQ, reference and MQ spectra, b) Fresnel function fit to the first three points of the normalized DQ build up curve. ....	<b>45</b>
<b>Figure 2. 6.</b> Cross polarization pulse sequence for the transfer of magnetization between an abundant (I) spin and a dilute (S) spin. ....	<b>48</b>

<b>Figure 2. 7.</b> Schematic demonstrating magnetization transfer during a CP experiment. Magnetization is transferred between I and S spins until it is lost to the lattice due to $T_{1\rho}$ decay. ....	<b>50</b>
<b>Figure 2. 8.</b> EXSY pulse sequence.....	<b>54</b>
<b>Figure 2. 9.</b> Sample $^1\text{H}$ EXSY spectrum showing crosspeaks which are indicative of exchange. The $\text{RbH}_2\text{PO}_4$ spectrum was acquired at $95\text{ }^\circ\text{C}$ with a mixing time of $0.009\text{ s}$ with $15\text{ kHz MAS}$ at $7.0\text{ T}$ . ....	<b>56</b>
<b>Figure 2. 10.</b> Intensity build up curve for $\text{RbH}_2\text{PO}_4$ $^1\text{H}$ EXSY experiment collected at $95\text{ }^\circ\text{C}$ . Spectra were collected at $7.0\text{ T}$ with $15\text{ kHz MAS}$ . ....	<b>57</b>
<b>Figure 2. 11.</b> Selective inversion pulse sequence.....	<b>58</b>
<b>Figure 2. 12.</b> Selective inversion spectra of $\text{RbH}_2\text{PO}_4$ acquired at $7.0\text{ T}$ with $15\text{ kHz MAS}$ . The $11.5\text{ ppm}$ site was inverted using a $1400\text{ ms}$ selective pulse. Each spectrum is labeled with the $\nu_d$ time at which it was collected. ....	<b>59</b>
<b>Figure 2. 13.</b> Plot of signal intensity as a function of mixing time following an inversion recovery experiment. The sample analyzed was monoclinic $\text{RbH}_2\text{PO}_4$ at room temperature with $7.0\text{ T}$ and $15\text{ kHz MAS}$ . ....	<b>60</b>
<b>Figure 2. 14.</b> Plot showing normalized intensity of the non-inverted site from a series of selective inversion spectra as a function of $\nu_d$ (black squares) with the corresponding CIFIT-derived fit (red dashed line). The selective inversion experiment was performed on monoclinic $\text{RbH}_2\text{PO}_4$ at $44\text{ }^\circ\text{C}$ using a $7.0\text{ T}$ spectrometer with $15\text{ kHz MAS}$ . ....	<b>62</b>
<b>Figure 2. 15.</b> Energy level diagram of a $I = 3/2$ system subjected to Zeeman splitting and then first and second order quadrupole splitting.....	<b>64</b>
<b>Figure 2. 16.</b> Three-pulse MQMAS sequence. ....	<b>70</b>
<b>Figure 2. 17.</b> Sample Nyquist plot for a capacitor and a resistor that are connected in series. ....	<b>74</b>
<b>Figure 2. 18.</b> Sample Bode plots, phase angle as a function of $\log \omega$ (A) and $\log Z$ as a function of $\log \omega$ (B) for a capacitor and a resistor that are connected in series. ....	<b>75</b>
<b>Figure 2. 19.</b> Relationship between the incident ( $k_i$ ) and scattered ( $k_f$ ) waves following interaction with a scatter site in a non-homogenous medium. ....	<b>78</b>
<b>Figure 3. 1.</b> Monoclinic RDP with b- and c-axes labelled. ....	<b>88</b>
<b>Figure 3. 2.</b> PXRD pattern (step size = $0.017^\circ$ ) and proton NMR spectra ( $7.0\text{ T}$ , $13.7\text{ kHz MAS}$ ) showing the phase transition from the tetragonal (blue) to the monoclinic (red) phase in RDP following overnight heating to $130\text{ }^\circ\text{C}$ . ....	<b>90</b>
<b>Figure 3. 3.</b> Proton conductivity of KDP, RDP and CaHA measured via EIS between $50$ and $170\text{ }^\circ\text{C}$ . ....	<b>93</b>
<b>Figure 3. 4.</b> 1D $^1\text{H}$ NMR of CaHA, KDP and RDP acquired at room temperature at $7.0\text{ T}$ with $13.7\text{ kHz MAS}$ . ....	<b>94</b>

<b>Figure 3. 5.</b> Calculated $D_{\text{app}}^0$ in tetragonal KDP and RDP as a function of coordination sphere size.....	<b>95</b>
<b>Figure 3. 6.</b> The rate of buildup of DQ intensity as a function of recoupling time in KDP.....	<b>97</b>
<b>Figure 3. 7.</b> $D_{\text{app}}^T$ in KDP measured between -7 and 107 °C at 7.0 T with 13.7 kHz MAS compared to $D_{\text{app}}^0$ .....	<b>100</b>
<b>Figure 3. 8.</b> $^1\text{H}$ NMR spectra of RDP acquired between -7 and 130 °C at 7.0 T with 13.7 kHz MAS demonstrating the transition between the tetragonal and monoclinic phases.....	<b>101</b>
<b>Figure 3. 9.</b> Top: $^1\text{H}$ NMR spectrum of monoclinic RDP at 7.0 T and 13.7 kHz MAS demonstrating deconvoluted individual peaks. Bottom: DQ build-up curves with fitting at both sites: A at 14.2 ppm and B at 11.7 ppm.....	<b>102</b>
<b>Figure 3. 10.</b> $D_{\text{app}}^T$ in tetragonal (T) and monoclinic (M) RDP calculated from DQ build-up curves resulting from experiments performed at 7.0 T and 13.7 kHz MAS. ....	<b>104</b>
<b>Figure 3. 11.</b> Site A protons (blue and white) hop between disordered hydrogen-bonded sites along the b-axis in phase II monoclinic RDP. The atoms partially occupy two sites and form disordered hydrogen bonds. The adjacent phosphorous tetrahedra exist in two possible orientations creating a disordered network of oxygen (red and white) which the protons are hydrogen bonded to. Proton hopping occurs at the A site and follows the pathway indicated by the blue arrows. This process is facilitated by the disorder of the hydrogen bonded network and the proton-proton internuclear distance. It is noted that the site B protons (white) are bonded to oxygen which exist in one possible orientation resulting in ordered hydrogen bonds along the c-axis. Proton motion was observed at a lesser extent at the B site. ....	<b>109</b>
<b>Figure 4. 1.</b> $^1\text{H}$ NMR of monoclinic RDP acquired at 7.0 T with 13.7 kHz MAS. ....	<b>116</b>
<b>Figure 4. 2.</b> Crystal structure of monoclinic RDP illustrating the b- and c-axis.....	<b>119</b>
<b>Figure 4. 3.</b> $^1\text{H}$ EXSY of monoclinic RDP acquired at 7.0 T with 15 kHz MAS. The EXSY mixing time was 0.01 s. Sample temperature was 95 °C. ....	<b>120</b>
<b>Figure 4. 4.</b> Normalized integrated crosspeak intensity for a monoclinic RDP sample analyzed at 95 °C and plotted as a function of mixing time. The EXSY build-up curve was fit using a first-order exponential decay function. $^1\text{H}$ spectra were acquired at 7.0 T with 15 kHz MAS. ....	<b>121</b>
<b>Figure 4. 5.</b> Rate of proton exchange between site A and site B in monoclinic RDP determined via $^1\text{H}$ EXSY from 80 to 95 °C plotted as a function of sample temperature. $^1\text{H}$ EXSY spectra were acquired at 7.0 T with 15 kHz MAS. ....	<b>122</b>

<b>Figure 4. 6.</b> Eyring plot of the rate of A-B proton exchange in monoclinic RDP between 80 and 95 °C. Rates of proton exchange were determined from <sup>1</sup> H EXSY spectra acquired at 7.0 T with 15 kHz MAS.....	<b>123</b>
<b>Figure 4. 7.</b> Three conditions of site-selective inversion in monoclinic RDP performed at 7.0 T with 15 kHz MAS.....	<b>124</b>
<b>Figure 4. 8.</b> Normalized intensity of the non-inverted peak (experimental) and the CIFIT model (fit) as a function of mixing time for three different inversion methods: invert site A (A, B), invert site B (C, D), partially invert site B (E). All selective inversion experiments were performed at 91 °C at 7.0 T with 15 kHz MAS.....	<b>126</b>
<b>Figure 4. 9.</b> Eyring plot for the determination of activation energy for proton exchange between A and B sites in monoclinic RDP. All spectra were collected by inverting site B at 7.0 T with 15 kHz MAS.....	<b>128</b>
<b>Figure 4. 10.</b> Arrhenius plot for the determination of activation energy of proton transport in monoclinic RDP constructed based on EIS proton conductivity measurements.....	<b>129</b>
<b>Figure 5. 1.</b> Partial cubic tin pyrophosphate unit cell with interstitial protons added at the Sn-O-P and P-O-P bridge sites.....	<b>141</b>
<b>Figure 5. 2.</b> <sup>1</sup> H- <sup>31</sup> P CP and <sup>31</sup> P spectra of SnP <sub>2</sub> O <sub>7</sub> adapted from Nishida et al. <sup>10</sup> with protonated phosphorous environments colour-coded: polyphosphoric acid (red), protonated pyrophosphate (blue) and unprotonated pyrophosphate (purple). Spectra were acquired at 9.4 T with 9 kHz MAS.....	<b>144</b>
<b>Figure 5. 3.</b> PXRD patterns of tin pyrophosphate samples with 0 to 30 % indium doping. The powder patterns were acquired at room temperature using a 0.134 nm Cu source with a 0.017 2θ step size at a rate of 0.35°/min.....	<b>149</b>
<b>Figure 5. 4.</b> <sup>1</sup> H NMR spectrum of undoped tin pyrophosphate with and without additional heating and glovebox storage at 7.0 T and 15 kHz MAS.....	<b>152</b>
<b>Figure 5. 5.</b> <sup>31</sup> P spectra of tin pyrophosphates with 0 to 20 % indium loading acquired at 20.0 T with 30 kHz MAS.....	<b>153</b>
<b>Figure 5. 6.</b> Molecular structures for bulk and protonated pyrophosphates. Pyrophosphate protonation occurs via hydrogen bonding to the M-O-P or the P-O-P bridge. In this schematic, M represents both tin and indium centers.....	<b>154</b>
<b>Figure 5. 7.</b> <sup>1</sup> H- <sup>31</sup> P HMQC spectrum of undoped tin pyrophosphate acquired at 20.0 T with 30 kHz MAS.....	<b>156</b>
<b>Figure 5. 8.</b> <sup>1</sup> H spectra of tin pyrophosphate with 0 to 20 % indium loading acquired at 7.0 T with 15 kHz MAS.....	<b>158</b>
<b>Figure 5. 9.</b> <sup>1</sup> H spectra of 0 % and 10 % indium-doped tin pyrophosphates acquired at 7.0 T with 15 kHz MAS. Each spectrum was fit with three proton sites at 9.0, 5.5	

- and 1.0 ppm. The acquired spectrum is represented by a solid line. The fit is represented by a dashed line. .... 160
- Figure 5. 10.** FWHM as a function of temperature for indium-doped tin pyrophosphate samples. Spectra were acquired at 7.0 T with 15 kHz MAS..... 161
- Figure 5. 11.** Proton  $T_1$  values for 5.5 and 9.0 ppm sites in indium-doped tin pyrophosphate measured at room temperature with 15 kHz MAS at 7.0 T. .... 162
- Figure 5. 12.** Proton conductivity of tin pyrophosphate samples doped with 0 to 20 % indium measured via EIS between 50 and 150 °C. The lines represent linear fits which were used to calculate activation energies for proton conduction in these materials..... 164
- Figure 5. 13.** Activation energy for proton conduction in tin pyrophosphate as a function of indium loading. Activation energies were calculated based on proton conductivity data acquired between 50 and 150 °C..... 165
- Figure 5. 14.**  $^1\text{H}$  EXSY spectra of tin pyrophosphates with 0 to 20 % (A to E) indium loading. All spectra were acquired at 7.0 T with 15 kHz MAS. Sample temperature was 90 °C and mixing time was 0.05 s. .... 168
- Figure 5. 15.** 1D projections taken from EXSY spectra of tin pyrophosphates acquired with a mixing time of 0.1 s compared with 1D spectra. All spectra were collected at 7.0 T with 15 kHz MAS. Sample temperature was 67 °C. Lineshape fitting at the M-O-P and P-O-P sites is displayed..... 170
- Figure 5. 16.** Normalized crosspeak intensity build up curves for tin pyrophosphate samples with 5 and 10 % indium loading (A, B) and the respective Eyring plots (C, D). .... 172
- Figure 6. 1.** The two-step synthesis of SiBA: (A) protection with dimethyl-L-tartrate followed by (B) hydrosilylation of the protected VPBA to yield telechelic (B-i) and pendant (B-ii) protected Tar-SiBA. (C) The addition of moisture results in hydrolysis of the protecting group to yield SiBA elastomers. Possible crosslink bonding modes are illustrated in Figure 6.3..... 182
- Figure 6. 2.** Elastomers can be formed via the condensation of boric acid with PDMS. Crosslinking via three- (A) and four- (B, C) coordinate centers is shown. Gel formation via the condensation of borate with guar polysaccharide. Single (D) and double (E) condensation reactions are possible with  $k_2$  being twice as large as  $k_1$ . .... 184
- Figure 6. 3.** Possible boronic acid binding motifs. Three-Coordinate: A dative bonding between boronic acids, B free boronic acid, C hydrogen-bonded boronic acids. Four-Coordinate: D dative bonding between a boronic acids, E dative bonding between a boronic acid and oxygen on the PDMS backbone..... 185

<b>Figure 6. 4.</b> $^{11}\text{B}$ spectra of boric acid (A) and datolite (B). A was acquired experimentally at 7.0 T with 15 kHz spinning. B is a simulated spectrum that was created based on data obtained by Hansen et al. <sup>22</sup> .....	<b>191</b>
<b>Figure 6. 5.</b> Thermogravimetric decomposition profiles of VPBA and SiBA materials acquired between 30 and 800 °C with a 10 °C/min heating rate under an argon atmosphere. <b>T-5</b> was not analyzed via TGA due to low viscosity. ....	<b>194</b>
<b>Figure 6. 6.</b> Background suppressed $^{11}\text{B}$ spectra of each elastomer collected at a magnetic field of 7.0 T with 15 kHz MAS (A), 11.7 T with 30 kHz MAS (B) and 20.0 T with 30 kHz MAS (C). The spectra of the <b>T-5</b> sample were collected without spinning at 7.0 and 20.0 T (A, C). .....	<b>196</b>
<b>Figure 6. 7.</b> Sheared MQMAS $^{11}\text{B}$ spectrum of <b>P-49</b> collected at 20.0 T with 30 kHz MAS. The differences in chemical shift between the direct and indirect dimensions were used to calculate $C_Q$ and $\eta$ for each site. Isotropic projections for each site are shown on the right. ....	<b>198</b>
<b>Figure 6. 8.</b> Lineshape fits for <b>P-49</b> spectra at 7.0 (A), 11.7 (B) and 20.0 (C) T based on quadrupolar parameters derived from the MQMAS experiment. Sites are colour-coded based on structural motif as seen in Figure 6.9.....	<b>199</b>
<b>Figure 6. 9.</b> 1D spectrum of <b>P-49</b> acquired at 20 T with 30 kHz MAS. The lineshape is fit using the quadrupole parameters that were obtained from MQMAS NMR with the dashed line showing the sum of the fits. Each site is labelled with the corresponding boron coordination environment from Figure 6.3 with the symbol R being used to denote the VPBA group and the PDMS chain. ....	<b>202</b>
<b>Figure 6. 10.</b> A) Relative proportion of four-coordinate boron, and B) Young's modulus as a function of boronic acid loading. ....	<b>206</b>
<b>Figure 6. 11.</b> Sheared $^{11}\text{B}$ MQMAS spectrum of Silly Putty collected at 20.0 T with 30 kHz MAS. The 1D spectra on the right are projections of the F1 dimension. ....	<b>209</b>
<b>Figure 6. 12.</b> 1D Silly Putty $^{11}\text{B}$ spectrum acquired at 20 T with 30 kHz MAS. The lineshape was fit with the quadrupole parameters that were obtained from the MQMAS experiments with the dashed line showing the sum of the fits. Each site is labeled with the corresponding coordination environment (A-D). The symbol R denotes the PDMS backbone. ....	<b>211</b>
<b>Figure A. 1.</b> $^{11}\text{B}$ spectra of <b>P-37</b> at A) 7.0 T and 15 MAS, B) 11.7 T and 30 MAS and C) 20.0 T and 30 MAS with lineshape fitting.....	<b>233</b>
<b>Figure A. 2.</b> $^{11}\text{B}$ spectra of <b>P-13</b> at A) 7.0 T and 15 MAS, B) 11.7 T and 30 MAS and C) 20.0 T and 30 MAS with lineshape fitting.....	<b>235</b>
<b>Figure A. 3.</b> $^{11}\text{B}$ spectra of <b>T-21</b> at A) 7.0 T and 15 MAS, B) 11.7 T and 30 MAS and C) 20.0 T and 30 MAS with lineshape fitting.....	<b>237</b>

<b>Figure A. 4.</b> $^{11}\text{B}$ spectra of <b>T-5</b> at A) 7.0 T (static), B) 11.7 T and 30 MAS and C) 20.0 T (static) with lineshape fitting. ....	<b>239</b>
<b>Figure A. 5.</b> Infrared spectrum of <b>T-23</b> elastomer (pink) and the tartrate-protected oil precursor (gray). The peak at $3300\text{ cm}^{-1}$ that is present in the elastomer spectrum but not the oil spectrum is indicative of hydrogen bonding.....	<b>241</b>
<b>Figure A. 6.</b> $^1\text{H}$ NMR spectra of <b>T-23</b> and <b>P-13</b> acquired at 20.0 T with 5 kHz MAS. These spectra contain do not contain a signal at 8.1 ppm suggesting that boroxines are not present in the SiBA elastomers. ....	<b>242</b>
<b>Figure A. 7.</b> $^1\text{H}$ NMR spectrum of Silly Putty acquired at 20.0 T with 30 kHz MAS. Site labels correspond to the structures in polydimethyl siloxane and castor oil that are responsible for the observed signals. ....	<b>243</b>
<b>Figure A. 8.</b> $^{11}\text{B}$ spectrum of boric acid acquired at 20.0 T with 30 kHz MAS. The lineshape was fit with quadrupole parameters yielding a $C_Q$ of 2.55 MHz and an $\eta$ of 0.05. ....	<b>244</b>

## List of Tables

**Table 3. 1.** Site-Specific Apparent Proton Dipolar Coupling Calculated Based on the Crystal Structure of Monoclinic RDP ..... **106**

**Table 4. 1.** Rates of Proton Exchange and Activation Energy Obtained via Variations on the Selective Inversion Experiment..... **127**

**Table 4. 2.** Activation Energy for Proton Exchange in Monoclinic RDP ..... **130**

**Table 6. 1.** Lineshape Fitting Parameters for **P-49** Calculated based on an MQMAS Spectrum ..... **200**

**Table 6. 2.** Lineshape Fitting Parameters for Silly Putty Calculated based on an MQMAS Spectrum ..... **210**

**Table A. 1.** Lineshape Fitting Parameters for **P-37** Calculated based on an MQMAS Spectrum ..... **234**

**Table A. 2.** Lineshape Fitting Parameters for **P-13** Derived from Lineshape Fitting at Three Magnetic Fields..... **236**

**Table A. 3.** Lineshape Fitting Parameters for **T-21** Derived from Lineshape Fitting at Three Magnetic Fields..... **238**

**Table A. 4.** Lineshape Fitting Parameters for **T-5** Derived from Lineshape Fitting at Three Magnetic Fields ..... **239**

## List of Abbreviations and Symbols

1D	One dimensional
2D	Two dimensional
A	Area (Chapter 2)
A, B	<sup>1</sup> H labels in monoclinic RbH <sub>2</sub> PO <sub>4</sub> (Chapters 3 and 4)
a, b, c	Crystallographic axis in monoclinic RbH <sub>2</sub> PO <sub>4</sub> (Chapters 3 and 4)
a <sub>x</sub>	Translational vector
B <sub>1</sub>	Applied magnetic field
BaBa	Back to back
B <sub>o</sub>	External magnetic field
B-O-B	Boron-oxygen-boron bond
B-O-Si	Boron-oxygen-silicone bond
b <sub>x</sub>	Reciprocal vector
c	Charge carrier concentration
CaHA	Calcium hydroxyapatite
CDP	Cesium dihydrogen phosphate
CIFIT	Program in C for selective inversion fitting
CODEX	Center-band only detection of exchange
CP	Cross polarization
C <sub>Q</sub>	Quadrupolar coupling constant
d	Diameter
d	Spacing between crystallographic planes (Chapter 2.5.2)
D <sup>0</sup> <sub>app</sub>	Apparent dipolar coupling constant without motion
d <sup>2</sup>	Second order Legendre polynomial
d <sup>4</sup>	Fourth order Legendre polynomial
D <sub>app</sub>	Apparent dipolar coupling constant
DAS	Dynamic angle spinning
D <sub>jk</sub>	Dipolar coupling constant
dl	Change in crystallographic dimension length
DOR	Double rotation
DQ	Double quantum
D <sup>T</sup> <sub>app</sub>	Apparent dipolar coupling constant at temperature T
E	Eigenvalue
EFG	Electric field gradient
EIS	Electrochemical impedance spectroscopy
E <sub>o</sub>	Potential at t = 0
eQ	Electronic quadrupolar moment
E <sub>t</sub>	Alternating potential
EXSY	Exchange spectroscopy
F <sub>c</sub>	Cos Fresnel integral
F <sub>s</sub>	Sin Fresnel integral

FWHM	Full-width half-maximum
H	Hamiltonian
$\hbar$	Planck's constant / $2\pi$
$h^*$	Electron hole
$\hat{H}_D$	Hamiltonian operator for homonuclear dipolar coupling
$H_i^*$	Interstitial proton
HMQC	Heteronuclear multi-quantum coherence
$H_Q$	Quadrupolar Hamiltonian
$H_z$	Zeeman Hamiltonian
I	Nuclear spin
$\hat{I}$	Spin operator
$I_o$	Initial magnetization on spin I
$I_o$	Current at $t = 0$ (Chapter 2.5.1)
IR	Infra-red
$I_t$	Alternating current
K	Equilibrium constant
KDP	Potassium dihydrogen phosphate
$k_I$	Rate of polarization transfer from I spin to lattice
$k_i$	Incident wave vector
$k_{IS}$	Rate of polarization transfer between I and S spins
$k_S$	Rate of polarization transfer from S spin to lattice
$k_s$	Scattered wave vector
$L_o$	Crystallographic dimension length
M	Magnetization vector
MAS	Magic angle spinning
MEA	Membrane electrode assembly
M-O-P	Metal-oxygen-phosphorous bond
MQ	Multi-quantum
MQMAS	Multiple quantum magic angle spinning
$M_z$	Magnetization along the z-direction
nDQ	Normalized double quantum intensity
NMR	Nuclear magnetic resonance
NOESY	Nuclear Overhauser effect spectroscopy
$oH_o^*$	Interstitial proton
$O^x_o$	Lattice with oxygen removed
P	Spin angular momentum
PDMS	Polydimethylsiloxane
PEM	Proton exchange membrane
$p_j$	Site occupancy
P-O-P	Phosphorous-oxygen-phosphorous bond
ppm	Parts per million
$P_Q$	Quadrupolar product
$p_{ir}^{eq}$	Equilibrium population of a spin energy level
P-x	Pendant elastomer

PXRD	Powder X-ray diffraction
q	Charge
r	Radius
r	Space (Chapter 2.5.2)
RDP	Rubidium dihydrogen phosphate
REF	Reference spectrum
rf	Radio frequency
$r_{jk}$	Spin internuclear distance
$r_s$	Scatter site
S(t)	Magnetization on spin S at time t
SiBA	Silicone boronate acid
Sn-O-P	Tin-oxygen-phosphorous bond
STMAS	Satellite transition magic angle spinning
T	Torque force (Chapter 2.1)
T	Temperature
t	Time
$T_1$	Longitudinal relaxation
$T_{1\rho}$	Spin-lattice relaxation
$T_2$	Transverse relaxation
$t_c$	Correlation time
TGA	Thermogravimetric analysis
$t_{null}$	Null time
T-x	Telechelic elastomer
u	Charge carrier mobility
V	EFG tensor
$v_d$	Variable delay
$V\ddot{o}$	Oxygen vacancy
VPBA	Vinylphenyl boronic acid
Y	Plane wave diffraction
$Y_o$	Plane wave amplitude
$Z'$	Resistance
$Z''$	Reactance
$\gamma$	Gyromagnetic ratio
$\delta_{iso}$	Chemical shift in the indirect dimension
$\delta_{MQ}$	Chemical shift in the direct dimension
$\Delta U$	Energy difference between nuclear spin states
$\eta$	Asymmetry parameter
$\theta$	Angle relative to external magnetic field (Chapter 2.1)
$\theta$	Diffraction angle (Chapter 2.5.2)
$\kappa$	Scaling factor for dipolar coupling
$\mu$	Magnetic moment
$\mu_o$	Magnetic constant
$\sigma$	Conductivity
$\phi$	Time-independent eigenfunction

$\psi$	Wavefunction
$\omega$	Angular frequency
$\omega_0$	Larmor frequency
$\omega_q$	Quadrupolar frequency

## **Declaration of Academic Achievement**

Professor Darren H. Brouwer assisted in the initial experimental set up and data interpretation in the determination of apparent dipolar coupling constants in phosphate solid acids that was presented in Chapter 3 of this thesis. The SiBA materials that are analyzed in Chapter 6 of this thesis were prepared by Benjamin Macphail who also acquired the infra-red spectrum and Young's modulus data. Dr Kristopher J. Harris assisted in the initial experimental set up and data interpretation of the  $^{11}\text{B}$  multiple quantum magic angle spinning data sets that are also presented in Chapter 6. All other sample preparation, data acquisition and interpretation were performed by Gabrielle Foran.

## **Chapter 1: Introduction**

### **1.1 Scope of the Thesis**

Work presented in this thesis demonstrates the use of solid-state nuclear magnetic resonance (NMR) spectroscopy, among other experimental techniques, to characterize local structure and proton dynamics in both hard (crystalline) and soft (elastomeric) hydrogen-bonded materials. Dipolar coupling and exchange mediated  $^1\text{H}$  NMR experiments are used to quantify proton dynamics in solid-state phosphate-based proton conductors that contain hydrogen-bonded networks.  $^1\text{H}$  NMR was also proposed to characterize hydrogen bonding in boron-containing elastomers. However, directly investigating hydrogen bonding in the elastomeric materials proved to be difficult due to extensive broadening of peaks corresponding to hydrogen-bonded sites. Therefore, the focus of this work was shifted to using quadrupolar  $^{11}\text{B}$  NMR to elucidate boron coordination environments in these materials.

Chapter 1 of this thesis provides an overview of hydrogen bonding interactions and describes how they influence structure and proton dynamics in hard and soft solid-state materials. The introductory chapter then discusses the structure, properties and uses of phosphate-based proton conductors and boron-containing elastomers in further detail. In Chapter 2, fundamental properties of solid-state NMR and the inter-nuclear interactions that are probed extensively in this work are described: dipolar coupling, chemical exchange and quadrupolar coupling. Other

experimental techniques that are described in this chapter include: electrochemical impedance spectroscopy (EIS), thermal gravimetric analysis (TGA) and powder X-ray diffraction (PXRD).

Chapters 3 through 6 describe the experimental work that is presented in this thesis. Proton dynamics in intermediate-temperature proton conductors are investigated in Chapters 3 through 5. These materials are proposed as potential electrolyte materials for fuel cells operating between 100 and 400 °C. Chapters 3 and 4 discuss proton dynamics in phosphate solid acids with an emphasis on proton hopping between two unique proton environments in monoclinic  $\text{RbH}_2\text{PO}_4$  (RDP). The suitability of  $\text{R}26_4^{11}$ , a symmetry-based dipolar recoupling pulse sequence, for the analysis of homonuclear dipolar coupling in multi-spin systems is investigated in Chapter 3. Differing site-specific attenuation of proton dipolar coupling in monoclinic RDP leads to the proposal of a dominant proton hopping pathway for the first time. However, it is predicted that an alternate proton hopping pathway, involving both sites, is also present. Proton dynamics corresponding to proton hopping between sites in RDP are investigated using  $^1\text{H}$  exchange spectroscopy and selective inversion experiments in Chapter 4. Tin pyrophosphates, the materials that are presented in Chapter 5, are another class of phosphate-based solid-state materials that may exhibit anhydrous proton conductivity. In this chapter, proton and phosphorous environments in indium-doped tin pyrophosphates are characterized and the effects of indium doping on proton mobility are quantified using a combination of electrochemical impedance spectroscopy and solid-state

NMR. Proton dynamics arising from site-specific exchange are quantified in these materials for the first time.

The work presented in Chapter 6 is a departure from the characterization of proton dynamics in solids via  $^1\text{H}$  NMR due to undiagnostic results during attempts to characterize hydrogen-bonded sites in the elastomeric materials that are discussed in this chapter. Instead,  $^{11}\text{B}$  NMR is used to characterize boron coordination environments in boron-containing silicone elastomers based on the quadrupolar interactions that are present at these centers. These studies show that boronic acid loading and boronic acid packing density significantly impact boron coordination in these materials. Chapter 7 provides an overall summary of the work that is presented in this thesis as well as some direction for future studies.

## **1.2 Hydrogen Bonding**

### **1.2.1 Defining Hydrogen Bonding**

The fundamental characteristics of hydrogen bonds will be outlined in this section as most of the work performed herein concerns the structure of and/or proton dynamics in hydrogen-bonded materials. The molecular interactions that today fall under the category “hydrogen bond” were first discovered in the early years of the twentieth century.<sup>1,2</sup> Hydrogen bonding was initially described as follows: a hydrogen atom that is strongly attracted to two atoms and acts as a bridge between them.<sup>1</sup> This interpretation of hydrogen bonding has since been proven to be insufficient as many examples of hydrogen bonding that do not conform to this definition have been identified.

The inherent diversity amongst hydrogen-bonded systems has been summarized in the following quote by Zewail: “this transfer of a small particle appears deceptively simple, but is in fact complex in nature”.<sup>3,4</sup> It is for this reason that modern definitions of hydrogen bonding strive to be as inclusive as possible such that a wide variety of bond lengths, bond strengths and donor/acceptor pairs can be described.<sup>1-3</sup> Whereas most classical definitions of hydrogen bonding have focused on the necessity of large differences in electronegativity between the donor and acceptor atoms and the proton, it has since been widely accepted that hydrogen bonding really only requires the system to be slightly polar.<sup>2</sup> Therefore, modern definitions of hydrogen bonding tend to be more broad: a hydrogen bond must a) constitute a bond, and b) X-H acts as a proton donor to Y.<sup>2,3</sup>

### 1.2.2 Structure and Energetics of Hydrogen Bonds

Hydrogen bonds can be described as the intermediate state of proton transfer between X and Y moieties:  $X-H \cdots Y$  (Figure 1.1).<sup>1,3</sup> Hydrogen is formally divalent in this configuration.<sup>5</sup> The formation of this bond is therefore dependent on the properties of the donor and acceptor moieties as well as their orientation relative to one another.<sup>3</sup> However, The exact energy of a hydrogen bond can be difficult to determine because it is often on the same order of magnitude as van der Waals forces and solvent effects.<sup>1</sup> Energetics in hydrogen-bonded systems are usually explored computationally under the assumption that the process can be described as proton transfer from X-H to  $H^+-Y^-$ .<sup>1,5</sup> This process is generally illustrated using a double potential well where the height of the well is the activation energy for this exchange process (Figure 1.1).<sup>1,5</sup>

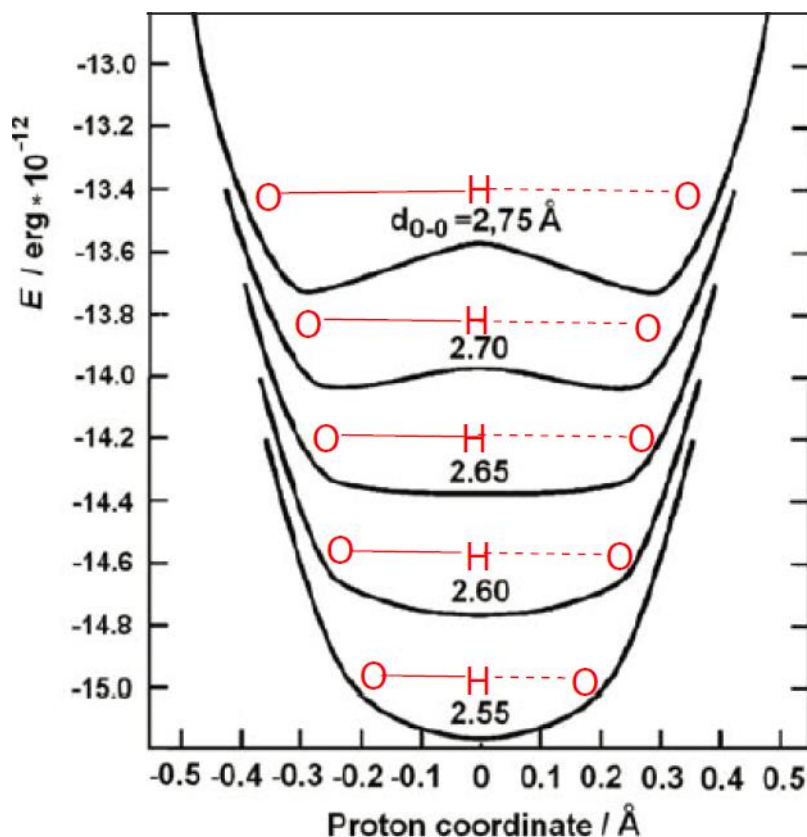


Figure 1. 1. Energy diagram showing potential wells for various oxygen-oxygen distances in O-H...O systems. These diagrams are adapted from computational work presented by Huggins<sup>6</sup> on H-O...H bonds in solid and liquid water. 2.75 Å is a typical oxygen-oxygen distance in this system.<sup>6</sup> The energy barrier in the potential well disappears when the oxygen-oxygen distance decreases to 2.55 Å.<sup>6</sup>

In hydrogen-bonded systems, the X-H distance tends to increase as the H-Y distance decreases.<sup>2</sup> This process continues until the optimal geometry is achieved. The strength of the hydrogen bond, and the subsequent X-Y distance, determine the height of the energy barrier (Figure 1.1).<sup>1-3,5</sup> In the case of short hydrogen bonds, where oxygen-oxygen distance is less than 2.5 Å, the energy barrier can disappear resulting in a single potential well (Figure 1.1).<sup>3,5</sup>

Regardless of the exact height of the potential well, hydrogen bonds are known for being significantly weaker than either ionic or covalent bonds.<sup>2</sup> The

facility with which hydrogen bonds can be broken and formed under mild conditions is important as it is essential for many life-sustaining functions to proceed. For example, hydrogen bonding is used in many enzymatic processes that must occur under physiological conditions to maintain life.<sup>3,7</sup> In this work, the facile reformation and deformation of hydrogen bonds will be important for proton conductivity in solid, crystalline systems where protons travel by hopping between hydrogen-bond-acceptor sites. This method of proton transport, referred to as the Grotthuss mechanism,<sup>8</sup> can occur under mild conditions and makes a significant contribution to proton mobility in the phosphate-based solid-state proton conductors that are discussed in Chapters 3 through 5.

The structure and dynamics of hydrogen-bonded systems are generally studied using computational methods as these allow for both structure and energetics to be modeled.<sup>5</sup> However, physical experiments can also be performed. Hydrogen bonding is commonly detected and analyzed using vibrational spectroscopy (infrared and Raman) because vibrational energies of X-H stretching modes are affected by changes in energetics that occur upon hydrogen bonding.<sup>5</sup> Typical observable effects of hydrogen bonding that can be assessed in infrared and Raman experiments include: an increase in the intensity and the broadness of bands corresponding to X-H stretching.<sup>1,5</sup> This signal is typically found in the 3300  $\text{cm}^{-1}$  region of the spectrum.<sup>9</sup> Dynamic processes pertaining to hydrogen bonding, in solids and in liquids, are typically measured using NMR spectroscopy.<sup>2</sup> Vibrational spectroscopy is not typically used to measure dynamics in extended multi-hydrogen

networks, such as pure water, because other processes and interactions tend to interfere with changes in molecular dipole moments/polarizability.<sup>10</sup> In this work, solid-state NMR is used to measure the dynamics associated with proton hopping in solid-state proton conductors. More information on the NMR theory and the experiments that were used in this thesis is provided in Chapter 2.

### 1.3 Hydrogen Bonding in Hard Solids

Frozen H<sub>2</sub>O, or ice, is one of the most well-studied examples of hydrogen bonding in the solid state. Liquid water is comprised of a hydrogen-bonded network of tetrahedral water molecules (Figure 1.2).<sup>11</sup> This cage-like structure is conserved upon freezing to result in a solid with low atomic density (Figure 1.2).<sup>11</sup> Loose atomic packing in ice enables the solid to float on top of the liquid phase where van der Waals forces dominate resulting in increased packing density (Figure 1.2).<sup>11</sup>

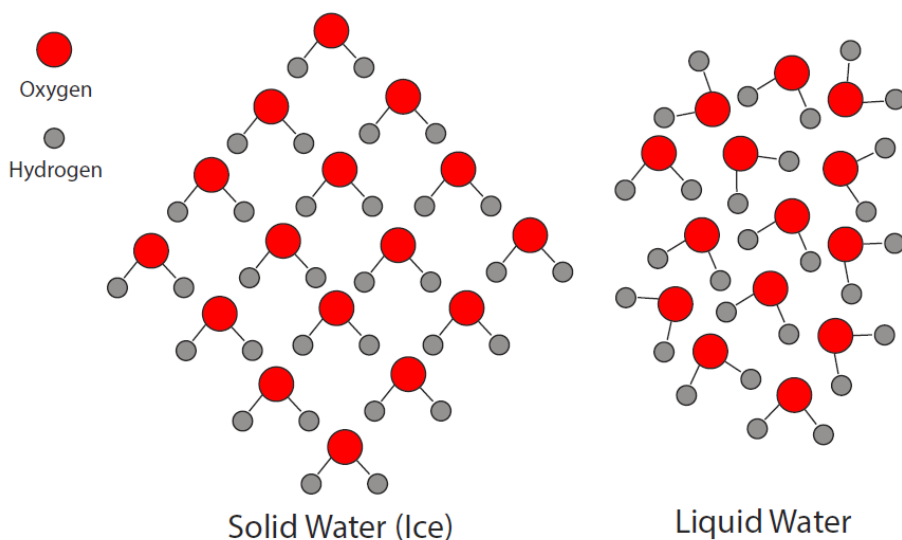


Figure 1. 2. Packing density of water molecules in the solid and liquid states. The cage-like structure is conserved upon freezing resulting in a low-density solid.

In addition to being responsible for bond distances, crystal packing and crystal structure, hydrogen bonding can also introduce pathways for proton dynamics in solid-state systems. For example, in organic-inorganic perovskites, short-range structural disorder is maintained through a hydrogen-bonded network.<sup>12</sup> The disordered hydrogen-bonded network provides a medium through which protons can be conducted via a hopping mechanism.<sup>12</sup> Proton mobility in these systems is expected to be influenced by changes in temperature as hydrogen bond length is sensitive to temperature.<sup>12</sup> It is for this reason that proton conductivity in solid-state phosphate-based proton conductors is heavily influenced by changes in sample temperature and molecular orientation.

### **1.3.1 Fuel Cell Electrolytes: An Application of Connectivity in Hydrogen-Bonded Networks**

Hydrogen fuel cells are electrochemical devices that convert chemical energy from hydrogen fuel sources directly into usable electrical energy.<sup>13-15</sup> Fuel cells are more efficient than internal combustion engines and steam engines but are not as widely used, because these devices require significant improvements to reduce operating costs and improve durability.<sup>13-15</sup> Additionally, the historical low cost and high availability of fossil fuels has further stunted motivation to develop better fuel cell technologies.<sup>16</sup> However, modern concerns surrounding the availability and ethics of these fuel sources has renewed research interest in fuel cells. Fuel cell application in the transportation sector is currently motivated by the automobile industry and the development of fuel cell powered buses and cars in an effort to combat the release of harmful greenhouse gas emissions. Hydrogen-

powered fuel cells emit only water in theory and are environmentally friendly provided that a sustainable source of hydrogen can be found.

Fuel cells in general are comprised of an electrochemically active anode and cathode that are connected by an electrolyte layer (Figure 1.3).<sup>13</sup> The role of the electrolyte layer is to transport the charge carrying species, generally protons but can be carbonates or oxides depending on fuel cell type, from the anode to the cathode such that a power-generating electrochemical reaction can be completed. The nature of each of these components depends on the operating temperature of the fuel cell with different materials being used in low-, intermediate- and high-temperature devices.

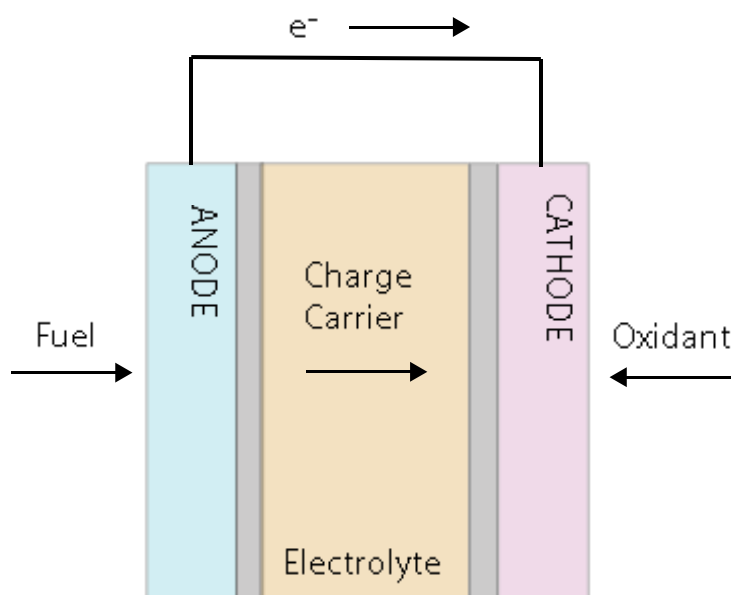


Figure 1. 3. Schematic of a generic fuel cell

Fuel cells can be broadly categorized based on operating temperature. Low-temperature fuel cells (80 to 100 °C) such as proton exchange membrane (PEM) fuel cells are generally comprised of platinum-based electrodes and a

polymer-based electrolyte through which protons are transported between the anode and the cathode.<sup>13,14</sup> The operating temperature of low-temperature fuel cells is a consequence of water being used as a charge carrier in many low-temperature devices. Nafion, the industry standard in conductive polymer membranes, must be fully hydrated to possess good proton conductivity ( $\sim 1$  S/cm). Hydration is necessary because proton transportation relies on having a well-connected water network.<sup>13</sup> However, doping the Nafion membrane with oxides or protic ionic liquids can allow these devices to operate at higher temperatures by reducing the hydration requirements for adequate proton conduction.<sup>13</sup> Advantages of low-temperature fuel cells include fast start-up times and a high power density.<sup>14</sup> However, there are also disadvantages of low-temperature fuel cells which include: water management being critical to maintain optimal device hydration during operation and the platinum catalysts being prone to deactivation via CO adsorption.<sup>13,14</sup> Low-temperature fuel cells are the most likely to be used in vehicular applications due to fast start-up times and smaller device sizes.<sup>14</sup>

High-temperature fuel cells, such as solid oxide fuel cells, operate at temperatures ranging from 600 to 1000 °C. These devices tend to be larger and are best suited to stationary applications due to long start-up times and the need to maintain high operating temperatures.<sup>13</sup> Although high temperatures can be more difficult to maintain and limit the amount of suitable construction materials, these devices can be economical in terms of fuel source and catalyst composition.<sup>13</sup> The high operating temperature means that the hydrogen dissociation reaction can be

catalyzed by nickel or mixed metal oxides instead of noble metals such as platinum.<sup>13</sup> This reduces the cost of the anode relative to devices that operate at lower temperatures. Additionally, CO poisoning is no longer an issue as surface adsorbed CO is reliably oxidized off at elevated temperatures.<sup>13</sup> High tolerance for CO in the fuel feedstock means that low purity fuel sources can be used reducing the need for the production of high grade hydrogen.

Intermediate-temperature fuel cells, which operate between 100 and 400 °C, combine some of the benefits of low- and high-temperature fuel cells. These devices are better able to handle CO in the feedstock than their low temperature counterparts<sup>17</sup> meaning that lower platinum loading and lower grade fuel sources can be used. Significant CO oxidation can be accomplished at temperatures as low as 120 °C. Intermediate-temperature fuel cells can be constructed from a wider variety of materials than high-temperature fuel cells can be.<sup>17</sup> This is because more materials possess sufficient stability and durability in the intermediate-temperature range than in the high-temperature range. The phosphoric acid fuel cell is currently the most widely used type of intermediate-temperature fuel cell.<sup>13</sup> Intermediate-temperature fuel cells could however stand to benefit from the use of solid-state electrolytes to avoid issues associated with flooding and drying out of the electrolyte material. Therefore, proton dynamics in solid-state, intermediate-temperature proton conductors, phosphate solid acids and tin pyrophosphates, are investigated in Chapters 3 through 5 of this thesis.

### **1.3.2 Phosphate-based Proton Conductors as Fuel Cell Electrolytes**

Chapters 3 through 5 of this work investigate proton dynamics in two

classes of solid-state proton conductors: phosphate solid acids and tin pyrophosphates. Proton conduction in both types of material is expected to occur via the Grotthuss mechanism: proton hopping between oxygen sites located on the phosphate tetrahedra.<sup>18,19</sup> Phosphate tetrahedra, a building block of both types of materials, are particularly well-suited to proton conduction because the average oxygen-oxygen distance in this structure ( $\sim 2.5$  Å) results in favourable activation energies for proton hopping ( $\sim 0.5$  eV).<sup>19–21</sup> Advantages for use as proton-conducting electrolytes in fuel cells for each of these classes of materials will be discussed in sub-sections 1.3.2.1 and 1.3.2.2.

### **1.3.2.1 Phosphate Solid Acids as Proton Conductors**

Phosphate solid acids are materials with properties that lie between those of a salt and those of an acid.<sup>22</sup> They contain a hydrogen-bonded network that is comprised of protonated phosphate tetrahedra through which protons are passed between oxygen sites via the formation and deformation of hydrogen bonds (Grotthuss mechanism).<sup>18,22,24</sup> Phosphate solid acids have been well-studied as proton conductors because these materials become particularly good proton conductors when they undergo a phase transition to the superprotonic phase.<sup>18,24</sup> The superprotonic phase is characterized by an extremely disordered hydrogen-bonded network which permits facile proton hopping via the Grotthuss mechanism.<sup>18,24</sup>

$\text{CsH}_2\text{PO}_4$  (CDP) is the most commonly cited example of solid acids as proton conductors based on the well-characterized transformation of this sample to a superprotonic phase.<sup>18,24,30</sup> Proton conductivity in CDP increases by four orders

of magnitude upon transitioning from the monoclinic phase to the cubic phase at 234 °C (Figure 1.4).<sup>18,24</sup> This substantial increase in proton conductivity is a result of the dynamically disordered hydrogen-bonded network that arises from the disordered phosphate tetrahedra and multiple partially occupied proton sites that comprise the cubic phase (Figure 1.4).<sup>18</sup>

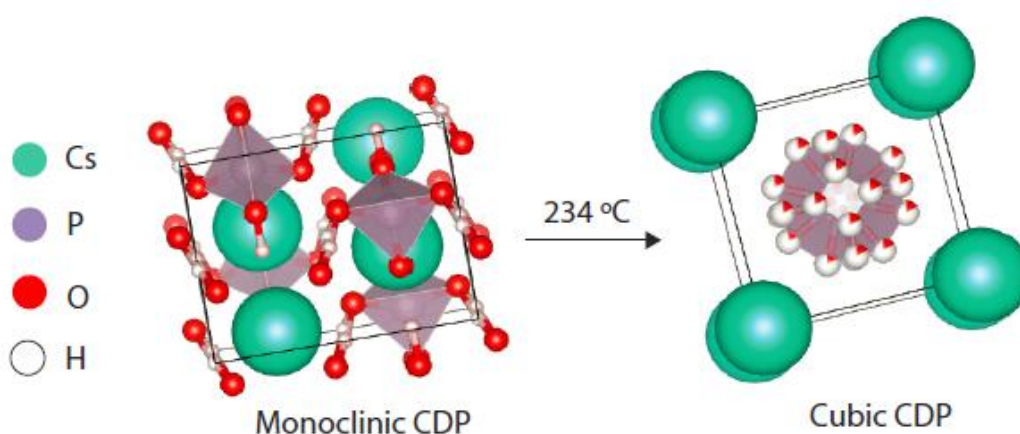


Figure 1. 4. Superprotonic transition from monoclinic CDP to cubic CDP results in significant disordering of the hydrogen-bonded network facilitating proton hopping.

Even though Haile et al. have constructed a laboratory-scale fuel cell based on cubic CDP as a proton conductor, significant controversy surrounding the stability of these phases remains.<sup>24</sup> This controversy is a result of the thermal decomposition temperature for cubic CDP being very close to the phase transition temperature.<sup>31</sup> In fact, high proton conductivity in the fuel cell that was designed by Haile et al.<sup>24</sup> was only maintained through careful control of device temperature and pressure which would not be realistic in a commercial or an industrial fuel cell application. It is for this reason that investigating proton conductivity in other phosphate solid acids, where appreciable proton conductivity can be achieved in

stable phases, is of interest. One such candidate is  $\text{RbH}_2\text{PO}_4$  (RDP) as it has been predicted that RDP may undergo a superprotonic phase transition, analogous to that which is observed in CDP, from the monoclinic to the cubic phase. This phase transition is expected to occur around  $273\text{ }^\circ\text{C}$  and may result in a significant increase in proton conductivity.<sup>23,31</sup> However, as cubic RDP is predicted to be unstable, one of the goals of this thesis is the characterization of changes in proton dynamics that occur following the phase change from the room-temperature tetragonal phase to the monoclinic phase, both of which are stable (Figure 1.5).<sup>21</sup> Monoclinic RDP is what is termed an ionic conductor. This means that structural disorder increases sufficiently such that proton conduction occurs but to a lesser extent (on the order of  $10^{-7}$  to  $10^{-3}$  S/cm) than what is observed in superprotonic conductors.<sup>23,31,32</sup>

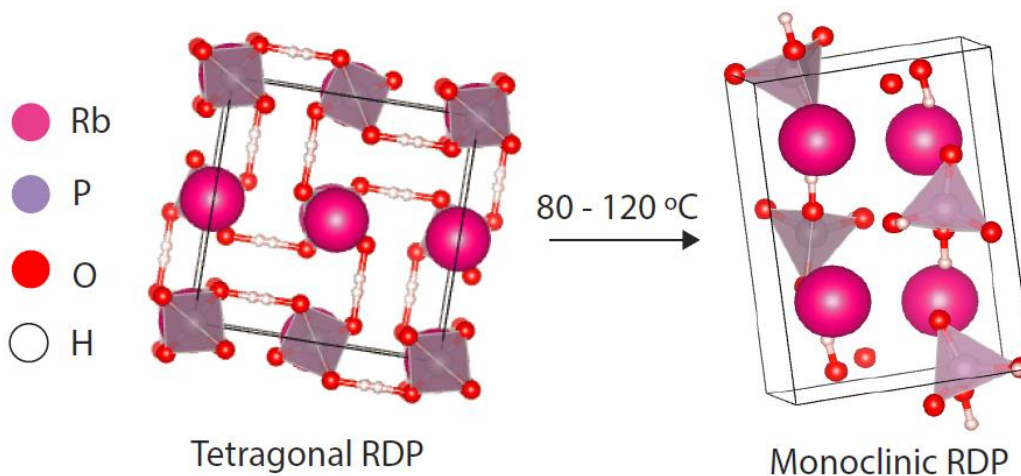


Figure 1. 5. Ionic phase transition from tetragonal to monoclinic RDP. The phase change occurs over a temperature range as opposed to one specific temperature.

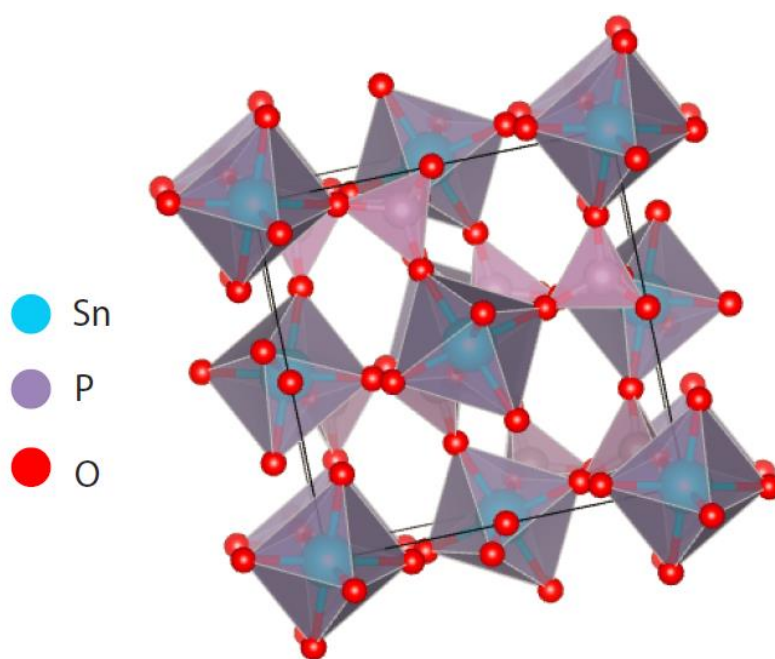
Other types of solid acid proton conductors, such as sulfate solid acids (based on  $\text{SO}_4$  as opposed to  $\text{PO}_4$  tetrahedra), have been proposed for use as solid

state proton conductors.<sup>22</sup> Proton conduction in sulfate solid acids is analogous to proton conduction in phosphate solid acids with protons hopping between acidic tetrahedra due to the formation and deformation of hydrogen bonds.<sup>22</sup> However, sulfate solid acids are generally considered to be more limited in scope than phosphate solid acids are. The operational temperature range for sulfate solid acids is 160 to 200 °C as these materials tend to undergo thermal decomposition at lower temperatures than their phosphate-based counterparts which may be stable at temperatures as high as 300 °C.<sup>22</sup> Additionally, phosphate solid acids, unlike sulfate solid acids, tend to exhibit appreciable proton conductivity below the super protonic phase in stable ionic phases.<sup>23</sup>

Even though thermally stable ionic phases of phosphate solid acids exist, these materials are water soluble and quite fragile when pressed in to solid electrolytes.<sup>22,24</sup> These challenges have been addressed by combining solid acids with inorganic oxides or organic polymers to create composite membranes.<sup>22</sup> However tin pyrophosphates, the materials that are introduced in the following subsection are not subject to these challenges. Tin pyrophosphates are not water-soluble, which is beneficial as intermediate-temperature fuel cell operation may produce gas-phase or liquid water as a by-product.<sup>25</sup> Tin pyrophosphates also tend to exhibit greater mechanical strength when they are pressed into electrolytes than solid acids do and, these materials can also be mixed with polymeric materials to create flexible organic composites.<sup>26</sup>

### 1.3.2.2 Tin Pyrophosphates as Proton Conductors

Tin pyrophosphates, another class of solid-state phosphate-based materials, have also been investigated as potential proton conductors. The prevalence of phosphate-based proton conductors is due to favourable oxygen-oxygen bond distances for proton hopping in phosphate tetrahedra ( $\sim 2.5 \text{ \AA}$ ).<sup>22</sup> Tin pyrophosphates are comprised of phosphate tetrahedra and tin octahedra (Figure 1.6).<sup>29</sup>



Cubic Tin Pyrophosphate

Figure 1. 6. Cubic tin pyrophosphate is comprised of phosphate tetrahedra and tin octahedra. The material is unprotonated in its native state.

Although these materials do not contain native protons, protonation can occur via synthesis with excess phosphoric acid or by doping with lower valence cations.<sup>28</sup> Previous molecular dynamics studies predict that proton conduction in tin pyrophosphate also occurs via the Grotthuss mechanism.<sup>19</sup> However, the

identity of the species that participate in proton conduction is less clear as proton hopping can proceed through phosphoric acid, polyphosphoric acid or between phosphate tetrahedra and tin octahedra depending on the synthetic history of the sample.<sup>17</sup> Hydrogen bonding plays a significant role in proton conduction through each of these media. Proton hopping between phosphate tetrahedra via the Grotthuss mechanism has been observed in liquid phosphoric acid.<sup>33</sup> Thus, it is possible that proton conduction in tin pyrophosphates occurs through phosphoric acid that has been observed on the sample surface or in grain boundaries. In fact, the high proton conductivity ( $\sim 10^{-2}$  S/cm) that has been observed in some tin pyrophosphate samples is commonly attributed to the presence of excess phosphoric acid.<sup>17,28</sup> Additionally, proton conductivity in polyphosphoric acid, a product of thermally-condensed  $\text{H}_3\text{PO}_4$ , is expected to proceed similarly to that which is observed in the phosphate solid acids that are discussed in sub-section 1.3.2.1: proton hopping via the Grotthuss mechanism between phosphate tetrahedra.<sup>34</sup> Proton conductivities on the order of  $10^{-5}$  to  $10^{-3}$  S/cm have been recorded in tin pyrophosphate samples that contain polyphosphates.<sup>28,34</sup> The lowest proton conductivities that have been reported in this class of materials are found in samples that are free from excess phosphoric acid and polyphosphoric acid.<sup>28</sup> Without the assistance of phosphoric acid and its by-products, proton conductivity in tin pyrophosphates is expected to proceed via proton hopping between the hydrogen-bonded sites that are located on the phosphate tetrahedra and hydrogen-bonded sites located on the metal octahedra.<sup>19</sup> Protons in materials where excess

phosphoric acids has been removed originate from cation doping and/or interactions between water/water vapor and defect sites in the pyrophosphate lattice.<sup>29</sup> The stability of these systems has resulted in tin pyrophosphates, like phosphate solid acids, being proposed as intermediate-temperature proton conductors for use in fuel cells. Site-specific proton dynamics and the effects of indium-doping on proton hopping in tin pyrophosphates are discussed in Chapter 5 of this thesis.

#### **1.4 Hydrogen Bonding in Soft Solids**

Elastomers, crosslinked polymers that do not flow but are soft and flexible,<sup>35</sup> owe several of their physical and structural properties to hydrogen bonding.<sup>35,36</sup> In particular, hydrogen bonding has been associated with increased flexibility, increased Young's Modulus (a measure of elasticity derived from the ratio of uniaxial deformation to applied strain) and improved stress resistance.<sup>35,36</sup> However, these materials also contain semi-permanent crosslinks such as ionic bonds, metal-ligand bonds and covalent bonds.<sup>35,37</sup> These stronger linkages are necessary for these materials to maintain sufficient viscosity.<sup>35</sup> As such, elastomers tend to be comprised of a combination of hydrogen bonds and various types of stronger interactions.<sup>37</sup> This combination of bonding modes in elastomers has a significant impact on both the physical properties and the perspective uses of these materials. One of the goals of this work is to investigate the influence of the relative proportions of different bonding modes on the physical properties of these elastomeric materials.

Elastomers have been produced with alternating hydrogen bonds and stronger metal coordination linkages, which makes them more resistant to breakage.<sup>37</sup> In these materials, strain on the system is passed on to sacrificial hydrogen bonds.<sup>37</sup> These linkages break while the stronger coordination bonds remain. The relative proportion of stronger and weaker bonds can be varied to create materials with differing flexibilities.<sup>35,37,38</sup> Alternating stronger and weaker bonds also confers self-healing properties in elastomers. Hydrogen bonding is common in self-healing elastomers as the deformation and reformation energy of hydrogen bonds is low compared to that of ionic or covalent bonds.<sup>39</sup> Hydrogen bonds are also dynamic and are therefore able to move to locations where the material needs to be repaired.<sup>39</sup> Examples of applications where the increased flexibility and the self-healing properties that come with hydrogen bonding are desirable include: seismic isolators for buildings in earthquake-prone areas, waterproof coatings and sealants.<sup>36,38</sup> Hydrogen bonding is expected to be responsible for some of the properties that are observed in the elastomers studied in Chapter 6 of this thesis, namely their flexibility and resistance to strain.

#### **1.4.1 Boronic Acid Functionalized Polydimethylsiloxane**

The elastomeric materials that are discussed in this thesis are formed when polydimethylsiloxane (PDMS) is combined with boronic acid. PDMS, with general form illustrated in Figure 1.7, is the most widely used silicone-based organic polymer due to its unique properties including: high thermal stability, fast curing rate, insulating properties, biocompatibility and non-toxicity.<sup>40</sup> The material has undergone industrial-scale production since the 1940's due to its commercialization

by Dow Corning.<sup>41</sup> PDMS is produced when silica, a product of the high-temperature reduction of sand, is subjected to a flow of methylchloride at 250 – 350 °C and 1 – 5 atm. The resultant dimethyldichlorosilane is hydrolyzed to yield PDMS.<sup>41</sup> Chain extension in PDMS occurs as a result of condensation of terminal Si-OH groups.<sup>41</sup>

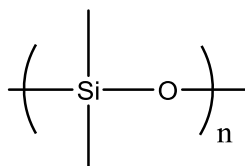


Figure 1. 7. PDMS monomer unit

Long chain PDMS moieties remain linear regardless of molecular weight. Crosslinking, the formation of bonds between polymer chains, must occur in order to introduce three-dimensional structure. As PDMS is relatively inert, the material is usually functionalized to allow crosslinking to occur. At low molecular density, functionalized PDMS chains tend to remain linear and form monolayers.<sup>42</sup> When chain density is increased, chains begin to overlay resulting in the formation of multilayers. The three methods through which silicones are crosslinked in industry are radical reactions, condensation reactions and hydrosilation reactions.<sup>43</sup> Crosslinking via a radical or a hydrosilation reaction requires the presence of organic end groups whereas condensation occurs when PDMS reacts with siloxane.<sup>43</sup> Functionalization of the PDMS chain with vinyl groups allows for crosslinking to occur via a radical reaction.<sup>41</sup> Vinyl-terminated PDMS chains can also be subject to chain extension and crosslinking interactions via platinum-catalyzed addition reactions.<sup>41</sup> The mechanisms for PDMS crosslinking discussed

above are commonly used in the industrial production of elastomers. However, the materials studied in this thesis are comprised of crosslinked vinylphenylboronic acid (VPBA) terminated PDMS chains. Boronic acid functional groups can be reliably added to PDMS chains. Boronic acid groups are protected and then added to PDMS chains via a platinum-catalyzed hydrosilation reaction.<sup>44</sup> The protecting group is then hydrolyzed off which allows crosslinking to occur at the exposed boronic acid end group.<sup>44</sup>

Boronic acid end groups are interesting because they allow for a multitude of different coordination environments. Boronic acids, the product of the double hydrolysis of a borane (three carbons on a boron center), are significantly different than the seemingly analogous carboxylic acids due to their geometry and reactivity.<sup>45</sup> The neutral boronic acid is trigonal planar with  $sp^2$  hybridization (usually  $B(OH)_2$  coordinated to an alkyl or aryl group).<sup>45</sup> However, due to a vacant  $p$ -orbital on the boron center, the boron center acts as a Lewis acid and becomes  $sp^3$  hybridized and tetragonal upon coordination.<sup>45</sup> Moreover, boronic acids are affected by small changes in pH and have a particular affinity for 1,2- and 1,3-diols.<sup>45</sup> These properties make them particularly interesting when considering tunable crosslinking, which leads to modifiable multi-dimensional structures and properties in the resultant elastomers.

Boronic acid termination confers many advantages on the resultant elastomeric materials and, a particularly desirable one is the possibility of tunable crosslinking. Boronic acid functionalization improves the flexibility of the resultant

elastomer. This is because boronic acids can be modified via many well-established scientific procedures such as carbon-carbon bond formation via Suzuki-Miyaura cross coupling and pH sensitive binding at the B-OH groups.<sup>46</sup> Functionalization can result in a variety of coordination environments because boron is stable in three- or four-bond coordination geometries. Coordination centers can be formed under a variety of conditions: hydrogen bonding, Lewis acid/base coordination and dative bonding. The exact bonding mode that occurs is highly dependent on the conditions that the material is exposed to.<sup>45</sup> The behaviour of boronic acid-terminated silicones is tunable under small variations in pH with four-coordinate boron being more favourable at higher pH.<sup>42,44</sup> The presence of certain substrates, particularly diols, can also impact boronic acid coordination as these materials have exhibited a preference for bonding to 1,2- and 1,3-diols.<sup>42</sup> As these changes in conditions are mild and would not normally affect the PDMS backbone, boronic acid functionalization offers opportunities for controlled elastomerization.<sup>42</sup> Additionally, interactions such as hydrogen bonding and Lewis acid/base coordination tend to be reversible. This is important because most industrial methods of silicone production do not allow for modification of the material post-curing.<sup>43</sup>

In addition to offering tunable properties themselves, boronic acid-containing elastomers can be coupled with other stimuli-responsive materials to produce photo- and thermally-responsive materials.<sup>43,45</sup> The ability to selectively bind sugars coupled with the inherent biocompatibility of silicones suggests that

boronic acid-functionalized silicone elastomers have the potential to be used in biomedical devices. One such example is in-vivo glucose detectors for the management of diabetes.<sup>45,47</sup> Boronic acid-containing elastomers also have the potential to be used as cell growth media. Glycoproteins on the cell surface can bind to the boronic acid to provide support during cell growth.<sup>45</sup> The primary advantage of boronic acid-containing cell growth media is that the culture removal is significantly facilitated relative to traditional methods involving proteases that can damage the cells.<sup>45</sup> The addition of saccharides to the culture media results in cell detachment via trans-esterification: the sugar competitively binds to the boronic acid sites reversing the binding process to the cell culture.<sup>45</sup> An additional area of biomedical devices in which boronic-acid containing elastomers may be useful is in the manufacture of contact lenses, popular devices for both vision correction and drug delivery.<sup>45</sup> This is because mucin, the primary component of the ocular tear film, is a glycoprotein containing many saccharide groups that may promote miscibility with a boron-containing material.<sup>48,49</sup> Compatibility between the contact lens and the tear film layer is important as lens comfort is highly dependent on the permeability of the lens to air and moisture.<sup>49</sup> The boronic acid containing-elastomeric materials studied here have the potential to be used in the manufacture of contact lenses because boronic acid binding to polysaccharides can increase miscibility with tear film mucin relative to more traditional hydrogel materials that are not functionalized with boronic acids. Additionally, because these materials crosslink following exposure to water, the insertion/removal of

contact lenses based on boronic acid-containing elastomers could be facilitated by changes in the viscosity of the device upon exposure to water.

### **1.5 Analyses of Hydrogen-Bonded Materials**

The preceding sections show that hydrogen-bonded materials, both hard and soft, play a significant role in many industries from power generation to the production of biomedical devices. Thus, it is critical to develop a better understanding of the structural and dynamic processes that lend these materials their useful properties. Solid-state NMR is the main experimental technique that will be used to analyze solid-state proton conducting materials and elastomeric materials in this work. A brief introduction of the NMR theory and the experiments performed will be detailed in the following chapter. The analyses of phosphate solid acids and tin pyrophosphate will focus on proton dynamics. Hydrogen bonding will not be probed directly in the SiBA samples, but it will be investigated as a potential driving force for boronic acid crosslinking via the characterization of boron coordination environments using quadrupolar  $^{11}\text{B}$  NMR.

### **1.6 References**

1. Fillaux, F. Hydrogen bonding and quantum dynamics in the solid state. *Int. Rev. Phys. Chem.* **19**, 553–564 (2000).
2. Steiner, T. The hydrogen bond in the solid state. *Angew. Chem. Int. Ed.* **41**, 49–76 (2002).
3. Kojić-Prodić, B. & Molčanov, K. The nature of hydrogen bond: New insights into old theories. *Acta Chim. Slov.* **55**, 692–708 (2008).
4. Hynes, J. T., Klinman, J. P., Limbach, H. H. & Schowen, R. L. *Hydrogen-Transfer Reactions*. (Wiley VCH, 2007).
5. Kollman, P. A. & Allen, L. C. THE THEORY OF THE HYDROGEN

- BOND. *Chem. Rev.* **72**, 283–303 (1972).
6. Huggins, M. L. Hydrogen bridges in ice and liquid water. *J. Phys. Chem.* **723–731** (1936). doi:10.1021/j150375a004
  7. Miyake, T. & Rolandi, M. Grotthuss mechanisms: from proton transport in proton wires to bioprotonic devices. *J. Phys. Condens. Matter* **28**, 023001 (2016).
  8. Hassanali, A., Giberti, F., Cuny, J., Kühne, T. D. & Parrinello, M. Proton transfer through the water gossamer. *Proc. Natl. Acad. Sci.* **110**, 13723–13728 (2013).
  9. Mitsuzuka, A., Fujii, A., Ebata, T. & Mikami, N. Infrared Spectroscopy of Intramolecular Hydrogen-Bonded OH Stretching Vibrations in Jet-Cooled Methyl Salicylate and Its Clusters. *J. Phys. Chem. A* **102**, 9779–9784 (1998).
  10. Bakker, H. J. & Skinner, J. L. Vibrational Spectroscopy as a Probe of Structure and Dynamics in Liquid Water. *Chem. Rev.* **110**, 1498–1517 (2010).
  11. Brini, E. *et al.* How Water 's Properties Are Encoded in Its Molecular Structure and Energies. *Chem. Rev.* **117**, 12385–12414 (2017).
  12. Bernasconi, A. *et al.* Ubiquitous Short-Range Distortion of Hybrid Perovskites and Hydrogen-Bonding Role: the MAPbCl<sub>3</sub> Case. *J. Phys. Chem. C* **122**, 28265–28272 (2018).
  13. Carrette, L., Friedrich, K. A. & Stimming, U. Fuel Cells : Principles , Types , Fuels , and Applications. *ChemPhysChem* **1**, 162–193 (2000).
  14. Giorgi, L. & Leccese, F. Fuel Cells : Technologies and Applications. *Open Fuel Cells J.* **6**, 1–20 (2013).
  15. Energy, D. of. FUEL CELL TECHNOLOGIES OFFICE Comparison of Fuel Cell. (2015).
  16. Appleby, A. J. From sir william grove to today: fuel cells and the future. *J. Power Sources* **29**, 3–11 (1990).
  17. Paschos, O., Kunze, J., Stimming, U. & Maglia, F. A review on phosphate based , solid state , protonic conductors for intermediate temperature fuel cells. *J. Phys. Condens. Matter* **23**, 234110 (2011).

18. Kim, G., Blanc, F., Hu, Y. Y. & Grey, C. P. Understanding the conduction mechanism of the protonic conductor  $\text{CsH}_2\text{PO}_4$  by solid-state NMR spectroscopy. *J. Phys. Chem. C* **117**, 6504–6515 (2013).
19. Kreller, C. R. *et al.* Intragranular Phase Proton Conduction in Crystalline  $\text{Sn}_{1-x}\text{In}_x\text{P}_2\text{O}_7$  ( $x = 0$  and  $0.1$ ). *J. Phys. Chem. C* **121**, 23896–23905 (2017).
20. Nelmes, R. J., Meyer, G. M. & Tibballs, J. E. The crystal structure of tetragonal  $\text{KH}_2\text{PO}_4$  and  $\text{KD}_2\text{PO}_4$  as a function of temperature. *J. Phys. C Solid State Phys.* **15**, 59–75 (1982).
21. Kennedy, N. S. J. & Nelmes, R. J. Structural Studies of  $\text{RbH}_2\text{PO}_4$  in its Paraelectric and Ferroelectric Phases. *J. Phys. C Solid State Phys.* **13**, 4841–4853 (1980).
22. Goñi-Urtiaga, A., Presvytes, D. & Scott, K. Solid acids as electrolyte materials for proton exchange membrane (PEM) electrolysis: Review. *Int. J. Hydrogen Energy* **37**, 3358–3372 (2012).
23. Park, J. & Choi, B. Electrical conductivity and impedance characteristics of  $\text{RbH}_2\text{PO}_4$  crystal above room temperature. *Mater. Lett.* **57**, 2162–2167 (2003).
24. Haile, S. M., Chisholm, C. R. I., Sasaki, K., Boysen, D. A. & Uda, T. Solid acid proton conductors: from laboratory curiosities to fuel cell electrolytes. *Faraday Discuss.* **134**, 17–39 (2007).
25. Sato, Y., Shen, Y., Nishida, M., Kanematsu, W. & Hibino, T. Proton conduction in non-doped and acceptor-doped metal pyrophosphate ( $\text{MP}_2\text{O}_7$ ) composite ceramics at intermediate temperatures. *J. Mater. Chem.* **22**, 3973 (2012).
26. Shen, Y., Nishida, M. & Hibino, T. Synthesis and characterization of dense  $\text{SnP}_2\text{O}_7 - \text{SnO}_2$  composite ceramics as intermediate-temperature proton conductors. 663–670 (2011). doi:10.1039/c0jm02596h
27. Szirtes, L., Megyeri, J. & Kuzmann, E. Thermal behaviour of tin (II/IV) phosphates prepared by various methods. *J. Therm. Anal. Calorim.* **99**, 415–421 (2010).
28. Anfimova, T. *et al.* The effect of preparation method on the proton conductivity of indium doped tin pyrophosphates. *Solid State Ionics* **278**,

- 209–216 (2015).
29. Nishida, M. & Tanaka, T. Solid-state NMR study of dopant effects on the chemical properties of Mg-, In-, and Al-doped  $\text{SnP}_2\text{O}_7$ . *Magn. Reson. Chem.* **52**, 163–71 (2014).
  30. Kim, G., Griffin, J. M., Blanc, F., Haile, S. M. & Grey, C. P. Characterization of the Dynamics in the Protonic Conductor  $\text{CsH}_2\text{PO}_4$  by  $^{17}\text{O}$  Solid-State NMR Spectroscopy and First-Principles Calculations : Correlating Phosphate and Protonic Motion. *J. Am. Chem. Soc.* **137**, 3867–3876 (2015).
  31. Li, Z. & Tang, T. High-temperature thermal behaviors of  $\text{XH}_2\text{PO}_4$  (X = Cs, Rb, K, Na) and  $\text{LiH}_2\text{PO}_3$ . *Thermochim. Acta* **501**, 59–64 (2010).
  32. Boysen, D. A., Haile, S. M., Liu, H. & Secco, R. A. Conductivity of Potassium and Rubidium Dihydrogen Phosphates at High Temperature and Pressure. *Chem. Mater.* **16**, 693–697 (2004).
  33. Gervasio, D. *Fuel Cell Science: Theory, Fundamentals, and Biocatalysis*. (John Wiley & Sons, 2010).
  34. Garzon, F. *et al.* Proton Conduction in Inorganic Phosphates. *ECS Trans.* **61**, 159–168 (2014).
  35. Kajita, T., Noro, A. & Matsushita, Y. Design and properties of supramolecular elastomers. *Polymer (Guildf)*. **128**, 297–310 (2017).
  36. Wang, J. *et al.* Significantly Improving Strength and Damping Performance of Nitrile Rubber via Incorporating Sliding Graft Copolymer. *Ind. Eng. Chem. Res.* **57**, 16692–16700 (2018).
  37. Wu, X., Wang, J., Huang, J. & Yang, S. Robust , Stretchable , and Self-Healable Supramolecular Elastomers Synergistically Cross-Linked by Hydrogen Bonds and Coordination Bonds. *ACS Appl. Mater. Interfaces* **11**, 7387–7396 (2019).
  38. Mei, J., Liu, W., Huang, J. & Qiu, X. Lignin-Reinforced Ethylene-Propylene-Diene Copolymer Elastomer via Hydrogen Bonding Interactions. *Macromolecular Materials and Engineering*. 1800689 (2019).
  39. Song, Y., Liu, Y., Qi, T. & Li, G. L. Self-Healing Materials Very Important Paper Towards Dynamic but Supertough Healable Polymers through Biomimetic Hierarchical Hydrogen-Bonding Interactions *Angewandte*. 13838–

13842 (2018). doi:10.1002/anie.201807622

40. Tian, T., Zhang, X. Z., Li, W., Alici, G., Ding, J. Study of PDMS based magnetorheological elastomers. *Journal of Physics*. **412**, 012038 (2013).
41. Colas, A. *Silicones: Preparation, Properties and Performances*. Dow Corning, Life Sciences (2005).
42. Mansuri, E., Zepeda-Velazquez, L., Schmidt, R., Brook, M. A. & DeWolf, C. E. Surface Behavior of Boronic Acid-Terminated Silicones. *Langmuir* **31**, 9331–9339 (2015).
43. Fawcett, A. S., Hughes, T. C., Zepeda-Velazquez, L. & Brook, M. A. Phototunable Cross-Linked Polysiloxanes. *Macromolecules* **48**, 6499–6507 (2015).
44. Pelton, R. *et al.* Facile Phenylboronate Modification of Silica by a Silaneboronate. *Langmuir*, **29**, 594-598 (2013).
45. Brooks, W. L. A. & Sumerlin, B. S. Synthesis and Applications of Boronic Acid-Containing Polymers: From Materials to Medicine. *Chem. Rev.* **116**, 1375–1397 (2016).
46. Brook, M. A., Dodge, L., Chen, Y., Gonzaga, F. & Amarne, H. Sugar complexation to silicone boronic acids. *Chem. Commun.* **49**, 1392 (2013).
47. Zepeda-Velazquez, L., Macphail, B. & Brook, M. A. Spread and set silicone–boronic acid elastomers. *Polym. Chem.* **7**, 4458–4466 (2016).
48. Lu, C., Kostanski, L., Ketelson, H., Meadows, D. & Pelton, R. Hydroxypropyl guar-borate interactions with tear film mucin and lysozyme. *Langmuir* **21**, 10032–10037 (2005).
49. Hodges, R. R. & Dartt, D. A. Tear film mucins: Front line defenders of the ocular surface; comparison with airway and gastrointestinal tract mucins. *Exp. Eye Res.* **117**, 62–78 (2013).

## **Chapter 2: Methodology**

The experimental techniques that were used to perform the work presented in this thesis are introduced in this chapter. This chapter begins with an introduction to solid-state nuclear magnetic resonance (NMR) spectroscopy. This introduction is followed by a detailed discussion of three interactions that are commonly investigated using NMR spectroscopy: dipolar coupling interactions, chemical exchange and quadrupolar coupling interactions. The section on dipolar coupling interactions contains a sub-section on symmetry-based dipolar recoupling techniques. This discussion is adapted from “Quantifying Site-Specific Proton Dynamics in Phosphate Solid Acids by  $^1\text{H}$  Double Quantum NMR Spectroscopy” as published in: *The Journal of Physical Chemistry C*. Copyright 2017 American Chemical Society (G.Y. Foran, D.H. Brouwer and G.R. Goward. 2017, 121, 25641-25650). The remainder of this section discusses heteronuclear dipolar coupling interactions with an emphasis on the cross-polarization experiment. Dipolar nuclei are also discussed in the chemical exchange section which focuses on exchange spectroscopy and selective inversion experiments. The use of multiple quantum magic angle spinning to elucidate coordination environments in complex quadrupolar systems is discussed in the section on quadrupolar coupling interactions. In addition to solid-state NMR, background information on electrochemical impedance spectroscopy, powder X-ray diffraction and thermogravimetric analysis is also provided.

## **2.1 Solid State NMR**

### **2.1.1 Interactions Between Nuclei and An External Magnetic Field**

NMR spectroscopy is an experimental technique that is used to determine chemical properties based on the response of nuclear environments to a strong external magnetic field. Analysis of a system via NMR is dependent on a nuclear property called spin, first proposed by Pauli to explain hyperfine structure in atomic spectra, that arises as a consequence of the mass and charge numbers of a given nucleus.<sup>1,2</sup> For example: nuclei with an odd mass number have a half-integer spin, nuclei with an even mass number but an odd charge have an integer spin and nuclei with an even mass number and an even charge have a spin number of zero and are not NMR active.<sup>1</sup> It should be noted that this section and the two sections following it (2.1, 2.2 and 2.3) discuss dipolar systems (spin = 1/2). Quadrupolar systems, where spin is greater than 1/2, will be addressed exclusively in section 2.4.

Spin ( $I$ ), a quantized nuclear property, causes splitting into energy levels upon exposure to a strong magnetic field (Figure 2.1).<sup>1-3</sup> This phenomenon, which is known as the Zeeman effect, results in  $2I+1$  non-degenerate energy levels that are characterized by a second quantum number,  $m$ , which can take on values between  $-I$  and  $+I$ .<sup>1-3</sup>

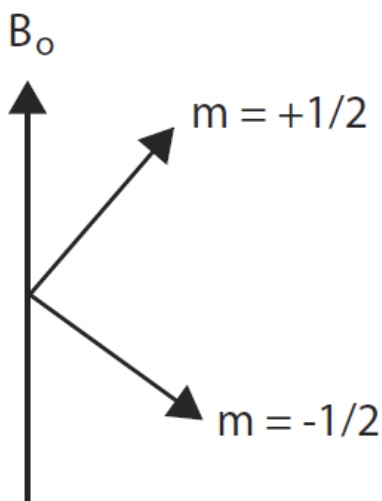


Figure 2. 1. Diagram showing Zeeman splitting of a spin  $\frac{1}{2}$  nucleus in a strong magnetic field ( $B_0$ ).

Upon exposure to a strong magnetic field, spin angular momentum gives rise to the magnetic moment ( $\mu$ ) which is related to the spin angular momentum ( $P = \hbar[I(I+1)]^{1/2}$ ) by the gyromagnetic ratio ( $\gamma$ ), an intrinsic property of the nucleus which is unique to each isotope (Equation 2.1).<sup>1</sup> The  $\gamma\hbar$  term is equal to the product of the nuclear magneton and the nuclear g-factor.

$$\mu = \gamma\hbar[I(I + 1)]^{1/2} \quad (2.1)$$

The energy spacing between nuclear spin states ( $\Delta U$ , which are generated upon Zeeman splitting, is defined in terms of the magnetic moment ( $\mu$ ) and the external magnetic field ( $B_0$ ) (Equation 2.2).

$$\Delta U = -\mu B_0 \quad (2.2)$$

Combining Equations 2.1 and 2.2 yields Equation 2.3 which describes the energy between spin states in terms of the gyromagnetic ratio ( $\gamma$ ), the spin quantum number ( $I$ ) and the external magnetic field ( $B_0$ ).

$$\Delta U = |\gamma\hbar[I(I + 1)]^{1/2}B_o| \quad (2.3)$$

Where  $\Delta U$  is the splitting between the  $(2I+1)$  energy levels that make up the spin system. Therefore, in order to satisfy the Bohr frequency condition, applied electromagnetic radiation that causes a transition between energy levels must have an energy that is equal to  $\Delta U$  (Equation 2.3).<sup>1</sup> The energy difference between spin states generally corresponds to the radiofrequency region of the electromagnetic spectrum.<sup>2</sup> Allowed transitions in NMR spectroscopy are single quantum where the change in  $m$  is equal to  $\pm 1$ . However, double quantum ( $\Delta m = \pm 2$ ) and zero quantum ( $\Delta m = \pm 0$ ) transitions can occur in multi-spin systems.<sup>3</sup> In fact, the generation of DQ NMR signal is exploited in Chapters 3 and 6 of this thesis in order to investigate homonuclear dipolar coupling and quadrupolar coupling interactions respectively.

Since nuclear angular momentum and spin states are quantized, the energy of this system can also be described using the time-dependent Schrödinger equation (Equation 2.4) where  $H$  is the total Hamiltonian and  $\psi$  is the wavefunction.<sup>2</sup>

$$\frac{i\hbar\partial\psi}{\partial t} = H\psi \quad (2.4)$$

As the application of a radiofrequency pulse does not alter the energy levels, the Hamiltonian is assumed to be time-independent.<sup>2</sup> The wavefunction can therefore be written in terms of  $\varphi$ , the time-independent eigenfunction where the eigenvalues ( $E$ ) correspond to the spin energy levels (Equation 2.5).

$$\psi = \varphi e^{(-i\frac{Et}{\hbar})} \quad (2.5)$$

Larmor precession is another consequence of the interaction between the nuclear magnetic moment and a strong magnetic field.<sup>1,2</sup> This phenomenon is similar to the precession of a spinning top in a gravitational field and is therefore generally illustrated as a vector ( $\mu$ ) rotating about the strong magnetic field ( $B_0$ ) at an angle  $\theta$  (Figure 2.2).<sup>1</sup> This description of the Larmor frequency is useful for describing the effect of a second, weaker, magnetic field ( $B_1$ ) on this system. When  $B_1$  is applied perpendicularly to  $B_0$ , there is a torque force ( $T$ ) acting on the magnetic moment ( $\mu$ ) that serves to increase the angle  $\theta$  between  $B_0$  and  $\mu$  (Figure 2.2).<sup>1</sup> This effect is important because it explains why weak magnetic fields, for example applied radiofrequency pulses, can have a significant impact on the orientation of the magnetic moment in a large magnetic field.

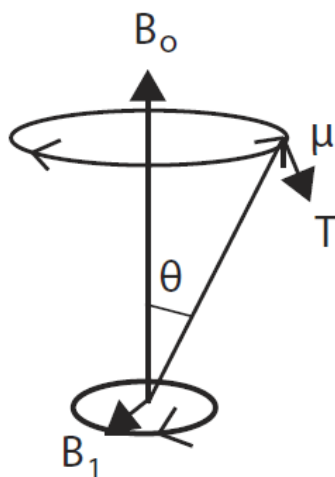


Figure 2. 2. Larmor precession in a strong magnetic field ( $B_0$ ). The presence of a second weak field ( $B_1$ ) perpendicular to  $B_0$  results in torque ( $T$ ) that increases the angle between  $\mu$  and  $B_0$ .

### 2.1.2 Applied Radiofrequency Pulses

NMR spectra are acquired by irradiating the magnetic moment as it precesses about  $B_0$  with plane polarized radio frequency (rf) radiation.<sup>2,4</sup> The rf radiation has an oscillating electromagnetic field ( $B_1$ ) that oscillates perpendicular to  $B_0$  (Figure 2.3).<sup>4</sup> As  $\mu$  precesses about  $B_0$  at a frequency of  $\omega_0$ , the application of an on-resonance pulse ( $\omega_{rf} = \omega_0$ ) results in  $\mu$  becoming effectively stationary with respect to  $B_0$  and experiencing only the effects of  $B_1$ .<sup>4</sup>

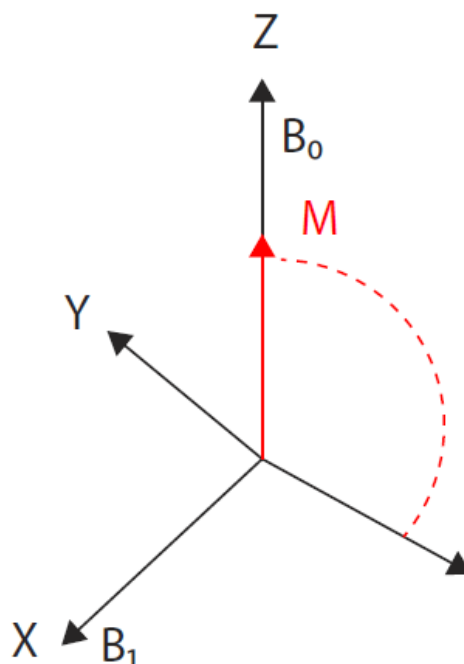


Figure 2. 3. Effects of a rf pulse ( $\omega_{rf}$ ) in the x-direction on the magnetization vector (M).

Nuclei that are in thermal equilibrium with the external static magnetic field ( $B_0$ ) interact with the magnetic component of the rf wave. This interaction results in the magnetization vector (M) being inclined relative to  $B_0$ . The magnetization vector is inclined towards the -y axis as  $B_1$  is perpendicular to  $B_0$ . The degree of inclination depends on the pulse with the most common angles being  $90^\circ$  and  $180^\circ$ .<sup>2,4</sup> This process can be interpreted quantum mechanically as the spins being perturbed away from their equilibrium positions in  $B_0$  when  $B_1$  is applied. In spin  $\frac{1}{2}$  systems,  $90^\circ$  pulses equalize energy level populations and  $180^\circ$  pulses change the most highly populated energy level from  $-1/2$  to  $+1/2$ .<sup>2</sup> It is the  $90^\circ$  pulse which serves to transform longitudinal magnetization that lies along the z-axis into observable transverse magnetization that lies along the y-axis.<sup>2</sup> In spin  $\frac{1}{2}$  nuclei, this is generally the result of a single quantum transition where  $m = \pm 1$ .<sup>2</sup>

### 2.1.3 Mechanisms of Relaxation

Following the application of a rf pulse, the magnetization vector is perturbed away from the equilibrium position. In NMR, the process through which a spin system returns to the equilibrium state under a given set of experimental conditions is termed relaxation.<sup>5</sup> In this case, the term equilibrium is defined by the Boltzmann equation (Equation 2.6). A system is at equilibrium when the population of each spin energy level ( $P_{rr}^{eq}$ ) is that which is predicted based on the Boltzmann equation where  $k_B$  is equal to  $1.30 \times 10^{-23} \text{ JK}^{-1}$  and  $T$  is the temperature of the system.<sup>5</sup>

$$P_{rr}^{eq} = \frac{e^{\left(\frac{-\hbar\omega}{k_B T}\right)}}{\sum_s e^{\left(\frac{-\hbar\omega}{k_B T}\right)}} \quad (2.6)$$

Additional conditions for equilibrium include: all magnetization is longitudinal (aligned along the z-axis) and no coherences are present.<sup>5</sup> Various types of relaxation have a significant role in NMR experiments as relaxation times often determine how quickly rf pulses can be repeated.

Longitudinal ( $T_1$ ) relaxation, also called spin lattice relaxation, is characterized by the flow of energy out of the spin system and into the lattice (degrees of freedom outside of the spin system).<sup>1,5</sup> Following the application of a radio frequency pulse, the magnetization vector is perturbed away from its equilibrium position which is defined as lying along the +z-axis.<sup>5</sup> For example, the magnetization is pushed on to the x-y plane following the application of a  $90^\circ$  pulse

and on to the -z-axis following a  $180^\circ$  pulse.  $T_1$  relaxation is the time that is required to return to the equilibrium position along the +z-axis.<sup>5</sup>  $T_1$  relaxation typically occurs on a timescale of seconds or milliseconds and can be influenced by various properties of the sample.<sup>1</sup> For example, interactions such as dipolar coupling, which provide an additional pathway through which magnetization can be transferred between the spin system and the lattice, tend to result in shorter  $T_1$  relaxation times.<sup>1</sup>  $T_1$  relaxation is relevant in the work presented in this thesis as it was used to determine how frequently pulses could be repeated in all NMR experiments.  $T_1$  relaxation was particularly influential in the selective inversion experiments that were performed on  $\text{RbH}_2\text{PO}_4$  in Chapter 4 as the return to equilibrium following site-specific inversion is governed by a combination of chemical exchange and  $T_1$  relaxation.

Transverse relaxation ( $T_2$ ), also called spin-spin relaxation, is the relaxation of the x and y components of the magnetization vector without energy transfer to the lattice.<sup>1</sup>  $T_2$  relaxation occurs in the transverse direction in the x-y plane after a pulse has been applied to the system. The x and y components of the magnetization vector tend to precess around the transverse plane. This process destroys coherence (magnetization that is oriented in the same direction) and is known to result in line broadening.<sup>5</sup>  $T_2$  relaxation is affected by the orientation of the nucleus with respect to the magnetic field and scalar coupling between electrons.<sup>1</sup>  $T_2$  relaxation was not a significant concern in most of the work presented in this thesis as  $T_2$  relaxation times were long enough such that minimal amounts of signal coherence were lost

during inter-pulse delays. However, some signal loss in the EXSY experiments that were performed on tin pyrophosphate and are presented in Chapter 5 suggests that  $T_2$  relaxation can contribute to signal loss in some dynamic systems.<sup>6,7</sup>

#### **2.1.4 Chemical Shift**

While previous subsections of this report discussed considerations for the generation of coherent magnetization following a rf pulse, this subsection discusses how differences in nuclear environment can be exploited to generate diagnostic spectra. NMR is a valuable technique for the characterization of materials because nuclei that exist in different chemical environments are observed at different parts of the NMR spectrum. These differences in resonance are referred to as chemical shifts.<sup>1</sup> The differing response of various nuclear environments to a strong magnetic field is the result of shielding of the nucleus by electrons.<sup>1</sup> Nuclear shielding is described by a dimensionless quantity called the shielding constant.<sup>1</sup> Chemical shielding is indicative of actual changes in the magnetic field that are felt at the nucleus due to local fields that are the result of interactions between the applied magnetic field and the surrounding electrons.<sup>2</sup> The strength of these local fields is inversely proportional to the distance between the electrons and the nucleus.<sup>4</sup> Therefore, local magnetic fields are generated based on the interaction between the external magnetic field, electrons and other atoms that make up the nearest neighbour coordination sphere of a given nucleus.<sup>4</sup>

Chemical shielding can be normalized against the Larmor frequency or the reference frequency of a standard sample to allow for comparison between magnetic fields and between samples.<sup>2</sup> As the differences in shielding between

nuclear environments tend to be small, this quantity is often reported in parts per million (ppm).<sup>1</sup> The normalization of chemical shielding with respect to a reference sample gives rise to the quantity known as chemical shift which is what is generally reported experimentally. Chemical shifts are also reported in units of parts per million.

### **2.1.5 Solid-State NMR and Magic Angle Spinning**

Samples used in solid-state NMR are typically micro-crystalline powders in which nuclei exist in many different orientations.<sup>4</sup> Many intra- and internuclear interactions, including dipolar and quadrupolar coupling interactions and chemical shift anisotropy, are orientation dependent.<sup>4,8</sup> These interactions, which are averaged out by molecular tumbling in solution-state NMR, provide a lot of information about the system.<sup>4</sup> However, this tends to result in broad lineshapes that are representative of these interactions occurring at slightly different frequencies in crystallites of the same material existing in different orientations. The downside of this is that individual signals become difficult to resolve due to increased overlap between peaks. Spectral resolution can be improved through various experimental techniques. One of these, magic angle spinning (MAS) which is used to improve site resolution in the NMR experiments that are presented in this thesis, will be discussed in this section.

Anisotropic interactions can be averaged out by setting the higher order terms of the Legendre polynomial, contained within the Hamiltonian, equal to zero.<sup>8</sup> Orientation averaging due to molecular tumbling in solution-state samples can be replicated experimentally in solid-state NMR via MAS. This technique

involves spinning the sample at an angle  $\theta$  relative to the external magnetic field ( $B_0$ ) which is illustrated in Figure 2.4.

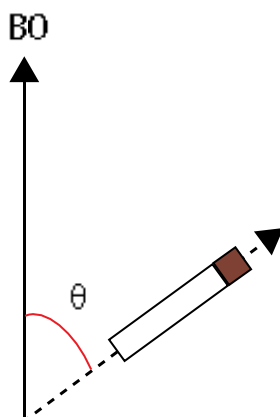


Figure 2. 4. Powder sample packed in a rotor rotating at an angle  $\theta$  relative to the external magnetic field ( $B_0$ ). Broadening due to chemical shift anisotropy and dipolar coupling interactions is significantly reduced when  $\theta$  is equal to  $54.74^\circ$ .

The angle of rotation,  $\theta$ , is set such that chemical shift anisotropy and dipolar coupling interactions are averaged to zero. For both these interactions, the second order term of the Legendre polynomial is the highest that is found in the Hamiltonian for spin  $\frac{1}{2}$  systems (see section 2.2 for an in-depth description of the dipolar coupling interaction).<sup>8</sup> The zero solution to this term is presented in Equation 2.7. The solution to Equation 2.7 is  $54.74^\circ$ , the magic angle. If MAS occurs at a rate that is fast relative to the anisotropic interactions, these are removed from the spectrum.<sup>4</sup> This has been demonstrated experimentally by tracking line width as a function of the angle of the rotation axis relative to the external magnetic field.<sup>8</sup> In this set of experiments, line broadening increased as the angle of rotation diverged from  $54.74^\circ$ .

$$3 \cos^2 \theta - 1 = 0 \quad (2.7)$$

MAS does not completely attenuate broadening and lineshape distortion due to the quadrupolar coupling interaction. The effects of MAS on quadrupolar nuclei are described in detail in section 2.4. However, here it suffices to state that the Hamiltonian that describes the interaction between a quadrupolar nucleus and a strong magnetic field contains higher order Legendre terms with different zero solutions.

## 2.2 Solid-State NMR of Dipolar Nuclei

### 2.2.1 Homonuclear Dipolar Coupling Interactions in spin $1/2$ Nuclei

Dipolar coupling between NMR-active nuclei is a through-space interaction that depends on internuclear distance as well as the orientation of the coupled nuclei with respect to the external magnetic field.<sup>9</sup> The Hamiltonian operator for the homonuclear dipolar coupling interaction (in a strong external magnetic field) between two spins  $j$  and  $k$  of the same type of nucleus (for example  $^1\text{H}$ ) is given by Equation 2.8.

$$\hat{H}_D = D_{jk}(3 \cos^2 \theta - 1) \frac{3\hat{I}_{jz}\hat{I}_{kz} - \hat{I}_j\hat{I}_k}{2} \quad (2.8)$$

Where  $D_{jk}$  is the dipolar coupling constant (in Hz) which is described by Equation 2.9.

$$D_{jk} = \frac{1}{2\pi} \frac{\mu_0}{4\pi} \frac{\gamma_j \gamma_k \hbar}{r_{jk}^3} \quad (2.9)$$

In Equation 2.9,  $r_{jk}$  is the internuclear distance between the two spins,  $\theta$  is the angle between the internuclear vector and the external magnetic field,  $\hat{I}_{jz}$  and  $\hat{I}_{kz}$  are spin operators between spins  $j$  and  $k$  and the external magnetic field,  $\hat{I}_j$  and  $\hat{I}_k$  are the spin operators, and  $\mu_0$  is the magnetic constant.

As nuclei undergo motions, both the distances between the nuclei as well as the orientations of the spins with respect to each other and the magnetic field, can change.<sup>10,11</sup> These atomic and molecular-scale motions typically lead to a reduction of the observed dipolar coupling between spins.<sup>10,11</sup> The reduction of dipolar coupling interactions has a complicated dependence on the rate of proton motion and on the orientation dependence of that motion. For example, a sufficiently rapid and fully isotropic motion will reduce the dipolar interaction to zero. However, in many materials (such as the phosphate-based proton conductors studied in Chapters 3 and 4 of this thesis), the nuclei do not occur as isolated spin pairs related by dipolar coupling, but rather exist as networks of coupled spins.<sup>12,13</sup> Quantification of dipolar couplings in multi-spin networks is much more complicated than the relatively straightforward situation of isolated spin pairs. This situation is usually the case in solid state  $^1\text{H}$  NMR due to the ubiquity of  $^1\text{H}$  atoms, the high natural abundance of  $^1\text{H}$ , and the large gyromagnetic ratio of  $^1\text{H}$  nuclei. Chapter 3 of this thesis explores how multi-spin  $^1\text{H}$  dipolar interactions in solid acid proton-conducting materials can be quantified through advanced solid-state MAS NMR experiments as a function of temperature and be related to the motions that give rise to proton conduction in these materials.

### **2.2.2 Symmetry-Based Dipolar Recoupling in Homonuclear Systems**

In order to obtain chemical shift resolved spectra in solid-state NMR, it is necessary to carry out MAS. However, in doing so, the dipolar coupling interactions are averaged to zero. Dipolar recoupling pulse sequences are designed to interrupt

the spatial averaging of the dipolar interaction with sequences of rotor synchronized rf pulses, so that dipolar couplings are re-introduced and can be quantified under high resolution MAS conditions.<sup>10,14</sup> For recoupling between nuclei of the same type ( $^1\text{H}$ - $^1\text{H}$ ), there are a variety of homonuclear dipolar recoupling pulse sequences available, including the BaBa sequence<sup>15</sup> and a variety of symmetry-based recoupling pulse sequences (e.g. C7, R14, etc).<sup>10,11,14,15</sup> Here, we have employed the R26<sub>4</sub><sup>11</sup> pulse sequence for homonuclear  $^1\text{H}$  dipolar recoupling.<sup>14</sup> The strength of the dipolar coupling interaction is typically quantified by observing the intensities of the DQ coherences that develop under the recoupling pulse sequence as a function of the recoupling time.<sup>11</sup> This is typically referred to as a DQ build up curve. For an isolated pair of dipolar-coupled spins, the DQ build up curve increases according to the strength of the dipolar interaction and then the intensity oscillates at a frequency related to the dipolar coupling constant. By fitting such a DQ build up curve (through simulations<sup>16</sup> or suitable analytical solutions)<sup>10,17</sup> the dipolar coupling constant can be obtained, and then converted into an internuclear distance.

In the case of multi-spin networks (such as phosphate solid acids that are presented in Chapters 3 and 4), the DQ build up curves are much more complicated. The form of the DQ build up curve is strongly geometry-dependent in the sense that the DQ build up curve is quite sensitive to the spatial arrangement of the nuclei relative to each other.<sup>11</sup> Extracting dipolar coupling constants from multi-spin situations is possible in only the simplest cases involving clusters of spins in which much is already known about the geometry of the spins, rather than extended

networks of coupled spins. For most materials of interest, simulating and fitting the DQ build up curves in order to extract quantitative information is usually a futile endeavour due to the complexity of the problem. However, a number of authors have pointed out that the initial rise of the DQ build up curve is largely insensitive to the geometry of the multi-spin system.<sup>10,11,14</sup> By carrying out a normalization of the homonuclear DQ signals, the initial part of the normalized DQ build up curve can be approximated as if it were an isolated spin pair, but with an apparent dipolar coupling constant (Equation 2.10) that is the root-sum-square of the dipolar coupling constants between a central spin  $j$  and all of its neighbours  $k$  (within a defined radius) where  $p_j$  is the site occupancy.

$$D_{app,j} = \sqrt{\sum_k p_j D_{jk}^2} \quad (2.10)$$

To obtain and construct normalized DQ build up curves, two spectra are collected at each value of the dipolar recoupling time  $\tau_{DQ}$ : a “reference” (REF) spectrum and a “double quantum” (DQ) spectrum, the difference being found in the phase cycling used to collect each spectrum which selects different coherence pathways.<sup>11</sup> The normalized DQ build up curves (nDQ) are constructed by calculating the ratio  $nDQ = DQ/MQ$  where MQ, the sum of multiple quantum coherences, is equal to  $DQ+REF$  at each recoupling time. An example of this is shown in Figure 2.5.

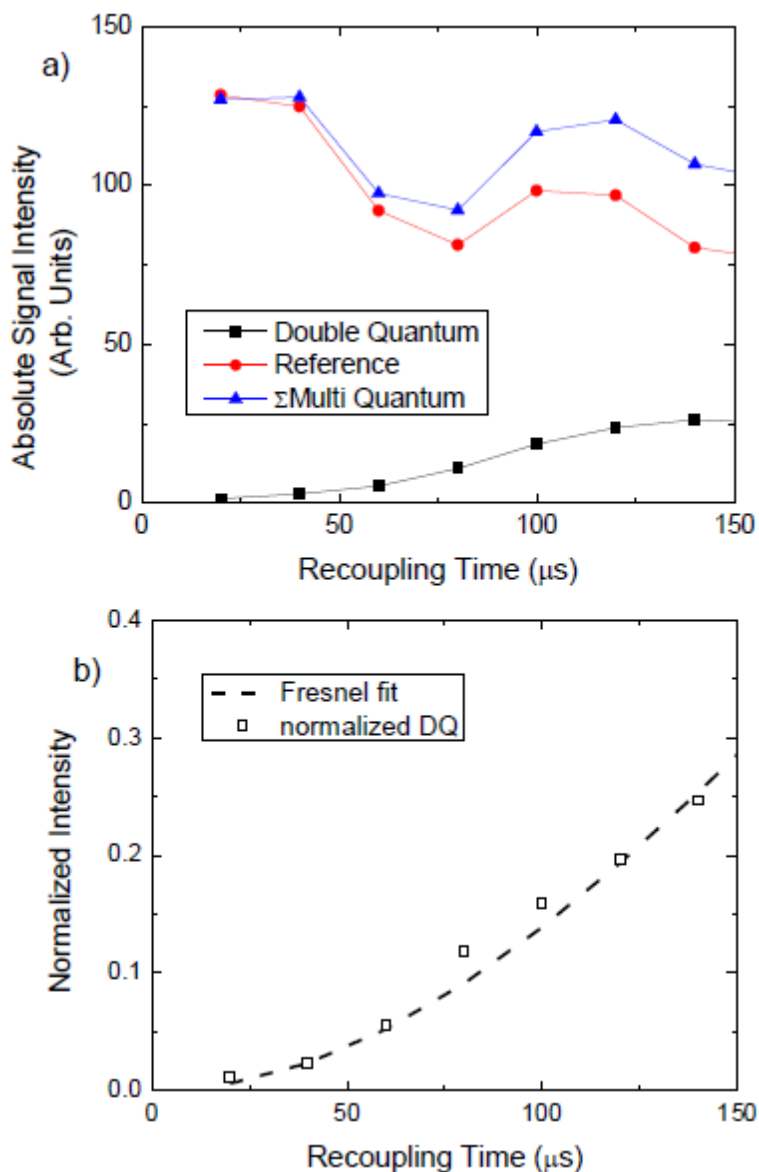


Figure 2. 5. Normalization of DQ intensity from the analysis of calcium hydroxyapatite with the R264<sup>11</sup> pulse sequence on a 7.0 T spectrometer with 13.7 kHz MAS: a) signal intensities of the DQ, reference and MQ spectra, b) Fresnel function fit to the first three points of the normalized DQ build up curve.

A number of functions have been proposed to fit the initial rise of a normalized DQ build up curve, including a quadratic function<sup>18</sup> and a

Gaussian-type function.<sup>11</sup> Here, we employ the Fresnel function analytical solution to the powder averaged DQ signal of an isolated spin pair under gamma-encoded homonuclear dipolar recoupling, as shown in Equation 2.11.

$$nDQ(\tau_{DQ}) = \frac{1}{2} - \frac{1}{x\sqrt{8}} \{F_c(x\sqrt{2}) \cos(2\theta) + F_s(x\sqrt{2}) \sin(2\theta)\} \quad (2.11)$$

In Equation 2.10,  $F_c$  and  $F_s$  are the cosine and sin Fresnel integrals respectively,  $x = \sqrt{2\theta/\pi}$ ,  $\theta = \frac{3}{2}\kappa D_{app}$ , and  $\kappa$  is a scaling factor that is specific to the dipolar recoupling sequence that was used ( $\kappa = 0.1708$  for the R264<sup>11</sup> sequence that is employed in Chapter 3).<sup>14</sup> The dipolar coupling constant has been replaced with the multi-spin apparent dipolar coupling constant,  $D_{app}$  as is defined in Equation 2.10, above. Like the quadratic and Gaussian-type functions referred to above, using the Fresnel function to fit the normalized DQ build up curves is very rapid and depends only on a single parameter  $D_{app}$ .

It is important to point out that since the nDQ build up curves are being fit as if they were behaving as an isolated spin pair but with an apparent dipolar coupling constant  $D_{app}$ , the fit is only valid for the initial rise of the nDQ build up curve (no more than about half way to maximum intensity) before geometry-dependent multi-spin effects become pronounced. An example of a fit with the Fresnel function to the initial part of an nDQ curve is shown in Figure 2.5.

Protons dynamics in phosphate solid acids were probed as a function of temperature (and the subsequent reduction of the dipolar interactions) by fitting the initial parts of normalized DQ build up curves obtained over a range of

temperatures with Equation 2.10. These experimentally determined apparent dipolar coupling constants are referred to in Chapter 3 as  $D_{\text{app}}^{\text{T}}$ . In the absence of motions the experimentally determined values should agree well with the  $D_{\text{app}}^0$  values calculated from the crystal structure, while the presence of dynamics should give rise to  $D_{\text{app}}^{\text{T}}$  values that are less than  $D_{\text{app}}^0$  in some manner that is related to the nature of and rates of motion.

### 2.2.3 Heteronuclear Dipolar Coupling Interactions in spin $\frac{1}{2}$ Nuclei

Heteronuclear dipolar coupling is much like homonuclear dipolar coupling, a through-space interaction that arises from the interacting magnetic moments of proximal nuclei.<sup>19</sup> However, the nuclei,  $j$  and  $k$ , are not identical. The system is therefore described by the Hamiltonian presented in Equation 2.12 where  $D_{jk}$  is the dipolar coupling constant as is described in Equation 2.9. Heteronuclear dipolar coupling also depends on the orientation of the nuclei relative to the external magnetic field and, like homonuclear dipolar coupling, has zero solution at  $54.74^\circ$ . The interaction can therefore also be attenuated by typical MAS.

$$\hat{H} = D_{jk}(3 \cos^2 \theta) \hat{I}_{jz} \hat{I}_{kz} \quad (2.12)$$

### 2.2.4 Approximating Heteronuclear Dipolar Coupling with Cross-Polarization

In Chapter 5 of this thesis, unknown proton signals are correlated to characterized phosphorous environments in indium-doped tin pyrophosphates. This is done via heteronuclear multi-quantum coherence (HMQC) experiments where signal is generated as a result of heteronuclear dipolar coupling.<sup>20</sup> In these experiments, through-bond coupling is investigated via cross polarization (CP).

The CP experiment (Figure 2.6) is characterized by the transfer of magnetization between an abundant spin (I, usually  $^1\text{H}$ ) and a dilute spin (S,  $^{31}\text{P}$  in our case). As the measurement of NMR spectra occurs on the dilute spin, typical advantages of CP include improved spectral resolution of nuclei of low abundance and reduced experimental time as the  $T_1$  value of the abundant spin is used.<sup>1</sup> The primary advantage of CP in the tin pyrophosphate system that is discussed in Chapter 5 is a reduction in experimental time.  $^{31}\text{P}$  is highly abundant but  $^{31}\text{P}$   $T_1$  relaxation at the pyrophosphate site is on the order of 200 s.

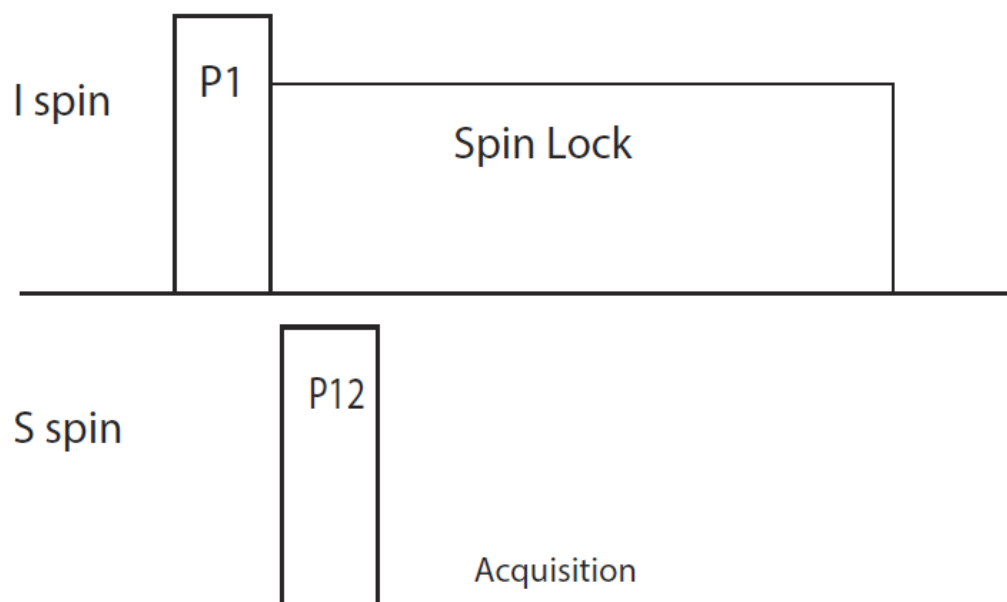


Figure 2. 6. Cross polarization pulse sequence for the transfer of magnetization between an abundant (I) spin and a dilute (S) spin.

The CP experiment begins by applying a  $90^\circ$  pulse (P1) on the I spin channel ( $^1\text{H}$  in this case) which is followed with a pulse that spin locks the  $^1\text{H}$  magnetization along the y-axis.<sup>1,21</sup> A  $90^\circ$  pulse (P12) is applied on the S spin channel (in this case  $^{31}\text{P}$ ) during the spin lock.<sup>1</sup> At this time, both the I and S

magnetization vectors lie along the y-axis.<sup>21</sup> Pulse lengths and power levels for each nucleus are chosen such that the Hartmann-Hahn matching condition (Equation 2.13) is satisfied.<sup>1</sup> When Hartmann-Hahn matching is achieved, both nuclei have equal rates of precession and equal effective energies.<sup>1</sup> This is obtained by setting the  $B_1$  field on each channel such that the difference between the product of  $B_1$  and the gyromagnetic ratio ( $\gamma$ ) for both nuclei is equal to  $n$  times the MAS rate in kilohertz where  $n$  is equal to  $\pm 1$  or  $2$ . This facilitates the transfer of magnetization from the abundant I spin to the dilute S spin.<sup>1</sup> The transfer of magnetization to the S spin continues until the signal from the I spin has decayed via  $T_{1\rho}$  (decay to the lattice).<sup>1</sup>

$$\gamma_I B_{1I} - \gamma_S B_{1S} = nMAS \quad (2.13)$$

Magnetization transfer from the abundant I spins to the dilute S spins is governed by three dynamic processes: the rate of magnetization transfer between the I and S spins ( $k_{IS}$ ), the rate of loss of magnetization transfer from the I spin to the lattice ( $k_I = 1/T_{1\rho}^I$ ) and the rate of loss of magnetization transfer from the S spin to the lattice ( $k_S = 1/T_{1\rho}^S$ ).<sup>22</sup> This system, illustrated in Figure 2.7, produces the observed S magnetization ( $S(t)$ ) as shown in Equation 2.14 where  $I_0$  is the initial magnetization of the I spin, which is equal to the product of the S spin magnetization following a single pulse, and the ratio of the gyromagnetic ratios of the I and S spins.<sup>22</sup>  $T_{1\rho}^S$  can be determined experimentally by adding a spin locking pulse on to the S nucleus during a typical CP experiment (Figure 2.7).<sup>23</sup> The length of the spin lock pulse is varied. Fitting the signal decay as a function of spin lock

time yields the  $T_{1\rho}$  value. Significant lineshape broadening in  $^1\text{H}$  spectra can make it more difficult to measure  $T_{1\rho}^I$  in the same way.<sup>23</sup> However,  $T_{1\rho}^I$  can also be extracted from the CP magnetization (S spin) as this depends on  $T_{1\rho}^I$ .<sup>23</sup>

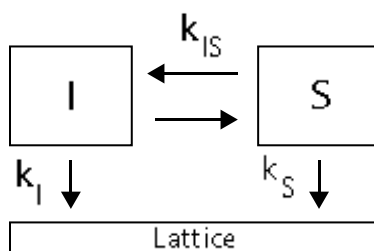


Figure 2. 7. Schematic demonstrating magnetization transfer during a CP experiment. Magnetization is transferred between I and S spins until it is lost to the lattice due to  $T_{1\rho}$  decay.

$$S(t) = I_o \frac{k_{IS}}{(k_{IS} + k_I) - k_I} (e^{-k_I t} - e^{-(k_{IS} + k_S)t}) \quad (2.14)$$

The rate of magnetization transfer,  $k_{IS}$ , can be used to get a quantitative picture of heteronuclear dipolar coupling in a spin system as it is proportional to the square of the dipolar coupling interaction.<sup>22</sup> Although  $k_{IS}$  is not equal to the magnitude of the heteronuclear dipolar coupling interaction, it can be used as a relative comparison to indicate changes in the strength of this interaction.<sup>22</sup> Higher rates of magnetization transfer are indicative of stronger dipolar coupling interactions. As was seen in the homonuclear dipolar case, build up curves can be used as a means of approximately quantifying the strength of the dipolar coupling interaction. While larger  $S(t)$  values are indicative of stronger dipolar coupling interactions, the contact times over which CP intensity is built up can be used to characterize and separate signals in multi-component systems based on their dynamic properties.

## **2.3 Chemical Exchange**

### **2.3.1 Introduction to Chemical Exchange**

In Chapter 4 of this thesis, inter-site proton dynamics in monoclinic  $\text{RbH}_2\text{PO}_2$  are characterized by measuring chemical exchange. In this system, signals that are observed in NMR spectra are representative of specific nuclear environments. Changes to these environments that occur as a result of dynamic processes, such as chemical exchange, can be measured using NMR due to the ability to resolve resonances that differ by fractions of parts per million.<sup>24</sup> Chemical exchange, which can occur either inter- or intramolecularly, is described by defining the sites that are involved and the process by which chemical exchange occurs.<sup>24</sup> In one dimensional (1D) NMR spectra, chemical exchange is typically manifested as coalescence where the rate of chemical exchange can be interpreted based on the degree of peak overlap.<sup>24</sup> The degree of coalescence that is observed depends on the rate at which chemical exchange occurs relative to the difference in Larmor frequency between the exchanging sites.<sup>24</sup> Chemical exchange processes are typically categorized into slow, intermediate and fast regimes. The term slow exchange is used to characterize processes where the rate of exchange is much slower than the difference in Larmor frequency between the exchanging sites. Systems in slow exchange are generally manifested as separate sites that may experience some broadening. For systems in intermediate exchange, the rate of exchange is similar to the differences in Larmor frequencies. NMR spectra of systems in intermediate exchange typically show significant peak overlap and possibly coalescence. The fast exchange regime is characterized by systems where

the rate of exchange is significantly greater than the difference the in Larmor frequencies of the exchanging sites. In these systems, coalescence has already occurred resulting in a single peak that is comprised of two Lorentzian lineshapes that represent the exchanging sites.<sup>24</sup> Peak broadening is not typically observed in rapidly exchanging systems as a result of motional averaging. In this thesis, proton exchange is measured between sites in monoclinic  $\text{RbH}_2\text{PO}_4$  in Chapter 4 and in indium-doped tin pyrophosphates in Chapter 5. In both cases, chemical exchange occurs in the slow regime which is demonstrated by the ability to resolve individual peaks, corresponding to the exchanging sites, in the NMR spectra of both systems.

The theory behind the characteristic lineshape of a system that is experiencing chemical exchange can be derived based on a pair of Bloch equations (Equations 2.15, 2.16) that describe the magnetization ( $M_z$ ) of a spin  $\frac{1}{2}$  nucleus interacting with a strong magnetic field ( $B_0$ ).<sup>24</sup>

$$\frac{du}{dt} + \frac{u}{T_2} - (\omega_o - \omega)v = 0 \quad (2.15)$$

$$\frac{dv}{dt} + \frac{v}{T_2} + (\omega_o - \omega)u = \gamma B_1 M_z \quad (2.16)$$

Where  $B_1$  is the applied rf field,  $\gamma$  is the gyromagnetic ratio,  $T_2$  is the transverse magnetization and  $u$  and  $v$  are magnetization vectors that are perpendicular to  $B_0$ .<sup>24</sup> Vectors  $u$  and  $v$  precess about  $B_0$  at the Larmor frequency ( $\omega_o$ ). Equations 2.15 and 2.16 can be simplified by defining a complex magnetization  $M$  where  $M = u + iv$  to yield Equation 2.17:

$$\frac{dM}{dt} + i(\omega_o - \omega)M + \frac{1}{T_2}M = i\gamma B_1 M_z \quad (2.17)$$

Since the exchange lineshape is the sum of two transitions, it can always be broken down to yield two Lorentzian lineshapes.<sup>24</sup> It is for this reason that an exchanging system, comprised of two equally populated sites (A and B), can be represented by a set of Bloch equations that are similar to those presented above. Adding site exchange to Equation 2.17 results in equations 2.18 and 2.19 where  $\omega_o$  is the Larmor frequency and  $k$  is the rate of chemical exchange between sites A and B.

$$\frac{dM_A}{dt} + i(\omega_o - \omega)M_A - kM_B + kM_A = i\gamma B_1 M_{zA} \quad (2.18)$$

$$\frac{dM_B}{dt} + i(-\omega_o - \omega)M_B - kM_A + kM_B = i\gamma B_1 M_{zB} \quad (2.19)$$

The observable NMR lineshape is the sum of  $M_A$  and  $M_B$  and is linear in  $B_1$ .<sup>24</sup> Each transition has a position and an intensity which are complex numbers with exchange and relaxation components that can be derived using a density matrix approach.<sup>24</sup> This approach will not be described here but the resultant NMR spectrum, based on the Bloch equation derivation presented above, is given by equation 2.20.

$$v = \gamma B_1 M_z \frac{k(2\omega_o)^2}{(\omega_o - \omega)^2(\omega_o + \omega)^2 + 4k^2\omega^2} \quad (2.20)$$

### 2.3.2 Exchange Spectroscopy

Exchange spectroscopy (EXSY), is a commonly used two-dimensional (2D) NMR technique for identifying exchange processes. EXSY works best for exchange processes that occur on the slow to intermediate timescale, like the monoclinic  $\text{RbH}_2\text{PO}_4$  system studied in Chapter 4, as site resolution is needed in order to identify exchange.<sup>24,25</sup> The EXSY pulse sequence, shown in Figure 2.8, is comprised of three  $90^\circ$  pulses. The first pulse serves to frequency label all spins in the system, the labeled spins are allowed to evolve over  $t_1$ .<sup>25</sup> The second and third pulses are similar to a saturation recovery experiment in the sense that all spins are inverted by the second pulse, are allowed to relax during  $t_m$  and are observed following the application of the third pulse.<sup>25</sup>

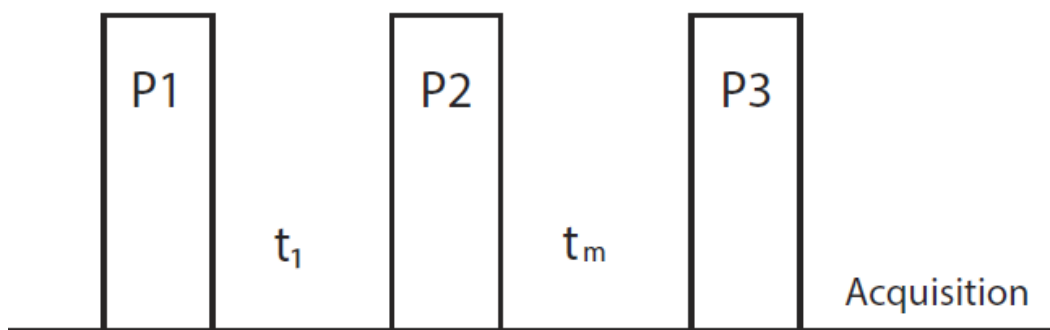


Figure 2. 8. EXSY pulse sequence.

All pulses maintain the frequency labelling that was created by the first pulse after the read pulse has been applied.<sup>25</sup> Signals that are related to chemical exchange between sites appear as cross peaks in the resultant 2D spectrum (Figure 2.9). Due to EXSY and Nuclear Overhauser Effect spectroscopy (NOESY) utilizing

the same pulse sequence, some of the observed crosspeak intensity may result from dipolar coupling interactions as opposed to purely resulting from chemical exchange.<sup>24</sup> Quantitative data can be obtained from EXSY spectra by fitting the 2D spectrum (Figure 2.9) to obtain peak areas for the crosspeaks and the diagonal peaks. Crosspeak areas are normalized relative to the diagonal peak areas and can then be used to extract kinetic data such as rate of exchange (Figure 2.10) and activation energy for the exchange process.<sup>25</sup> The rate of exchange is determined by plotting normalized crosspeak intensity as a function of mixing time. The resultant plot (Figure 2.10) can be fit with an exponential decay function (Equation 2.21) to yield the rate of exchange.

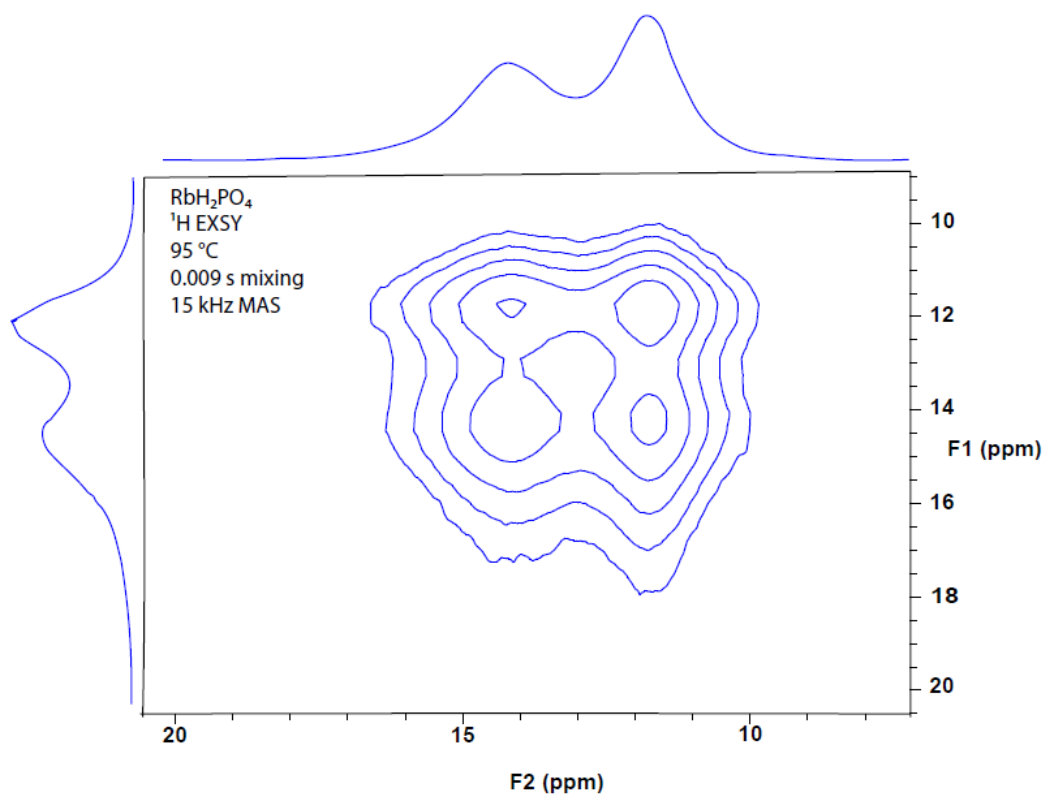


Figure 2. 9. Sample <sup>1</sup>H EXSY spectrum showing crosspeaks which are indicative of exchange. The RbH<sub>2</sub>PO<sub>4</sub> spectrum was acquired at 95 °C with a mixing time of 0.009 s with 15 kHz MAS at 7.0 T.

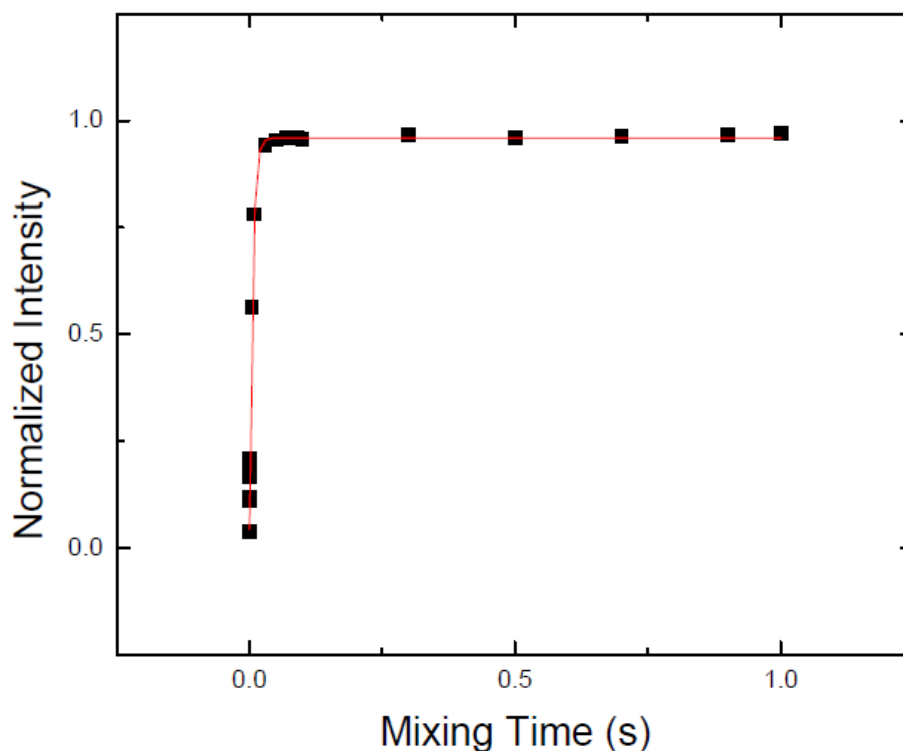


Figure 2. 10. Intensity build up curve for  $\text{RbH}_2\text{PO}_4$   $^1\text{H}$  EXSY experiment collected at  $95^\circ\text{C}$ . Spectra were collected at 7.0 T with 15 kHz MAS.

$$y = y_0 + Ae^{\frac{-x}{\tau}} \quad (2.21)$$

Limitations of data extraction for the EXSY experiment include difficulties associated with obtaining integrated areas from 2D spectra and the need to have sufficient site resolution, or slow enough exchange, to be able to observe crosspeaks and measure site-specific areas.<sup>25</sup>

### 2.3.3 Selective Inversion

Another NMR method by which slow to intermediate chemical exchange can be measured is selective inversion. The selective inversion pulse sequence is comprised of two pulses: a longer selective pulse (P1) where the pulse length and the position of the transmitter frequency are chosen such that a single site is inverted and a higher powered  $90^\circ$  observe pulse (P2) (Figure 2.11). These pulses are

separated by a variable delay time ( $v_d$ ) over which magnetization is exchanged between the inverted site and any non-inverted sites that it may be in exchange with (Figure 2.11).<sup>26</sup>

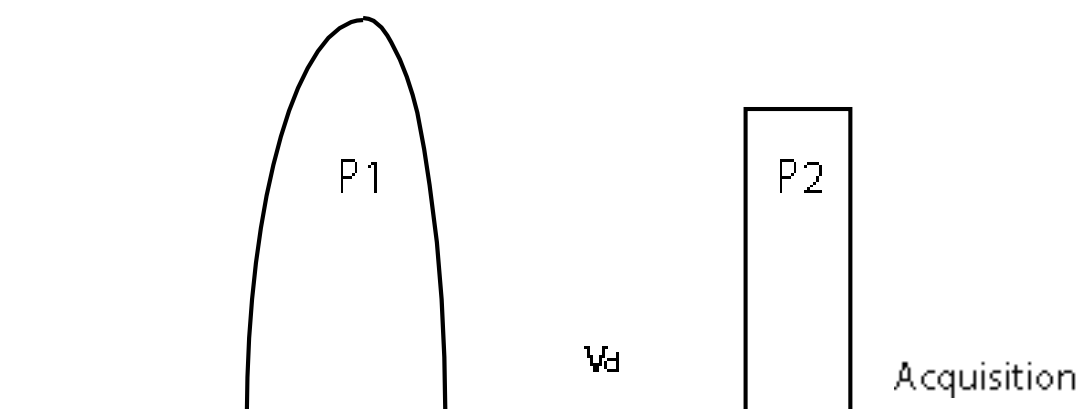


Figure 2. 11. Selective inversion pulse sequence.

The selective pulse is calibrated such that a single site is inverted. This site returns to equilibrium through a combination of exchange and  $T_1$  relaxation.<sup>26</sup> When the experiment is complete, any other sites that are in exchange with the inverted site experience a decrease in intensity that is related to the rate of exchange with the inverted site and the length of the delay ( $v_d$ ) between P1 and P2 (Figure 2.12).<sup>26</sup>

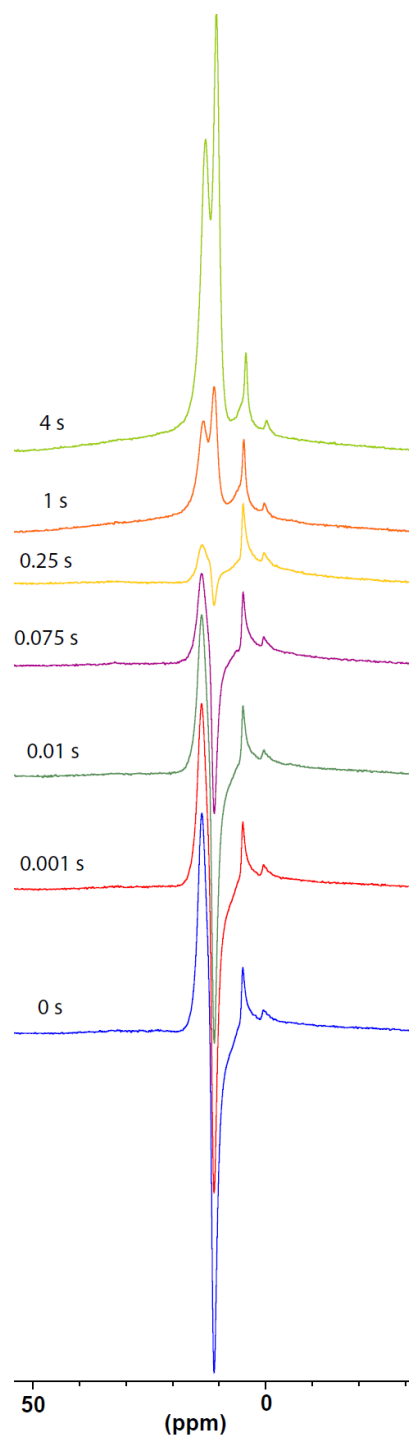


Figure 2. 12. Selective inversion spectra of  $\text{RbH}_2\text{PO}_4$  acquired at 7.0 T with 15 kHz MAS. The 11.5 ppm site was inverted using a 1400 ms selective pulse. Each spectrum is labeled with the  $v_d$  time at which it was collected.

Relaxation back to equilibrium during  $\nu_d$  depends on the exchange mechanism and  $T_1$  relaxation.<sup>26,27</sup> It is for this reason that  $T_1$  is often determined independently.  $T_1$  relaxation can be measured experimentally using the inversion recovery experiment.<sup>1</sup> The pulse sequence for inversion recovery is similar to the pulse sequence used in the selective inversion experiment (Figure 2.11) except that the first pulse, P1, is a non-selective  $180^\circ$  pulse that inverts all signals. Spectral intensity can be plotted as a function of the variable delay time ( $\nu_d$ ) (Figure 2.13) which allows the null time ( $t_{\text{null}}$ ), where the spectral intensity is equal to zero, to be determined by fitting the plot with an exponential function (Equation 2.21).<sup>1</sup>  $T_1$  can then be calculated from  $t_{\text{null}}$  based on the relationship that is described in Equation 2.22.

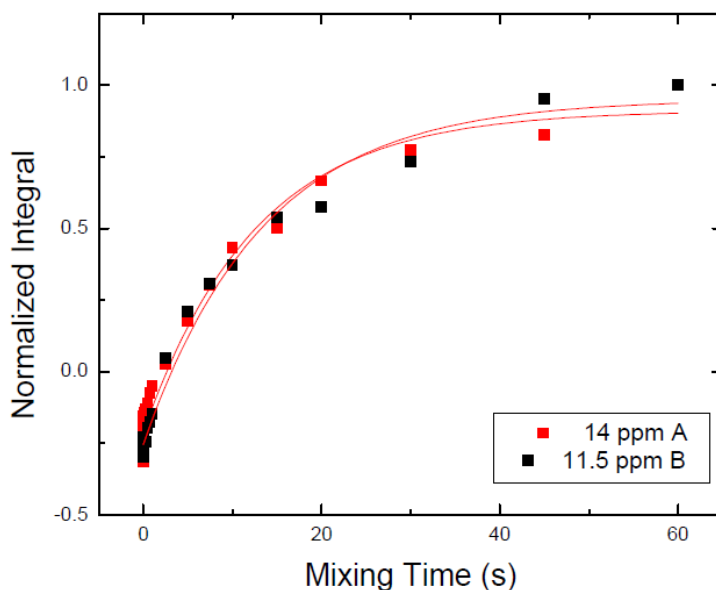


Figure 2. 13. Plot of signal intensity as a function of mixing time following an inversion recovery experiment. The sample analyzed was monoclinic  $\text{RbH}_2\text{PO}_4$  at room temperature with 7.0 T and 15 kHz MAS.

$$T_1 = \frac{t_{null}}{\ln 2} \quad (2.22)$$

A program called CIFIT, which was developed by Dr. Alex D. Bain,<sup>26</sup> was used to extract rate data from the selective inversion experiments that are described in Chapter 4 of this thesis. The CIFIT program fits experimental data according to a model that takes into account both chemical exchange and  $T_1$  relaxation.<sup>27</sup> Equation 2.23 describes a mathematical model of a spin system where  $M_i(t)$  is the magnetization of site  $i$  at time  $t$ ,  $M_i(\infty)$  is the equilibrium magnetization at site  $i$ ,  $k$  is the rate of exchange between sites and  $K$  is the equilibrium constant. The matrix representing  $K$  is independent of  $k$  which allows the rate of exchange to be varied independently during data fitting.<sup>27</sup>

$$\frac{\partial}{\partial t} \begin{pmatrix} M_1(\infty) - M_1(t) \\ M_2(\infty) - M_2(t) \end{pmatrix} = -k \begin{pmatrix} K & -1 \\ -K & 1 \end{pmatrix} \begin{pmatrix} M_1(\infty) - M_1(t) \\ M_2(\infty) - M_2(t) \end{pmatrix} \quad (2.23)$$

The CIFIT program varies the parameters of the equation: initial magnetization, equilibrium magnetization, rate of exchange and  $T_1$ , until the sum of squares of differences between the model and the experimental data is minimized.<sup>27</sup> The best set of parameters are determined using an algorithm called the Marquardt method which takes partial derivatives at each data point with respect to the specified parameters.<sup>27</sup> This approach combines the method of steepest descents (works well when parameters are far from the equilibrium value) with the method of linearization which works well when the parameters are near their equilibrium values.<sup>27</sup> The result is a fit file that can be compared to

experimental data (Figure 2.14). All parameters described in Equation 2.23 can be varied to better represent the experimental data set.

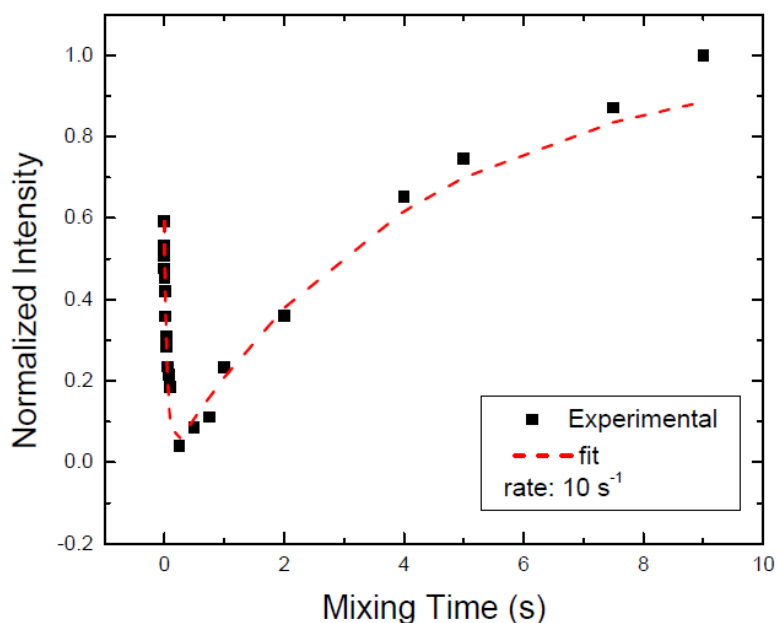


Figure 2. 14. Plot showing normalized intensity of the non-inverted site from a series of selective inversion spectra as a function of  $\nu_d$  (black squares) with the corresponding CIFIT-derived fit (red dashed line). The selective inversion experiment was performed on monoclinic  $\text{RbH}_2\text{PO}_4$  at 44 °C using a 7.0 T spectrometer with 15 kHz MAS.

Like EXSY, selective inversion works best for observing processes that occur on the slow timescale as individual site resolution aides significantly in the selective inversion of single sites.<sup>26</sup> However, the method has been deemed to be more reliably quantitative than EXSY because 1D spectra are more readily integrated than 2D spectra are.<sup>26</sup> Additionally, signal measured in selective inversion experiments is less likely to result from other inter- or intramolecular interactions. The selective inversion experiment is also deemed to be a more efficient method of data collection. This is because several 1D NMR experiments can be collected in the amount of time that it takes to collect one 2D experiment.<sup>26</sup>

This is particularly beneficial in the analyses of  $\text{RbH}_2\text{PO}_4$  where a series of mixing times were collected at several temperatures to observe exchange.

## **2.4 Solid-State NMR of Quadrupolar Nuclei**

### **2.4.1 Interactions and Energetics of Quadrupolar Nuclei**

In Chapter 6 of this thesis, boron coordination environments are assigned in silicone boronate elastomers on the basis that  $^{11}\text{B}$ , which has a natural abundance of about 80 %, is a quadrupolar nucleus. Quadrupolar nuclei are any nuclei that have spin greater than  $\frac{1}{2}$ .<sup>28</sup> These isotopes have an asymmetric distribution of nuclear charge which leaves them vulnerable to the effects of the electric field gradient (EFG).<sup>28</sup> Quadrupolar coupling is a single nucleus interaction which arises from the interaction between the nuclear quadrupole moment and the EFG.<sup>28</sup> The nuclear quadrupole moment is isotope-dependent but the EFG varies depending on the nuclear coordination environment.<sup>28</sup> The EFG is a tensor quantity which can be described using the asymmetry parameter ( $\eta$ ) and the quadrupole coupling constant ( $C_Q$ ). The asymmetry parameter describes the symmetry of the EFG and can have values between 0 (the most symmetrical) and 1 (the least symmetrical).<sup>28</sup>  $C_Q$  describes the magnitude of the interaction between the EFG and the quadrupolar center.<sup>28</sup>  $C_Q$  values range between about 0 and 30 MHz and are highest when the symmetry of the quadrupole environment is the lowest.<sup>28</sup>

The energetics of the nuclear quadrupole interaction can be described by the following Hamiltonian ( $H_Q$ ) (Equation 2.24) where  $eQ$  is the electronic quadrupole moment,  $I$  is the spin quantum number,  $\hat{I}$  is the nuclear spin vector and  $V$  is the EFG tensor.

$$H_Q = \frac{eQ}{2I(2I-1)\hbar} \hat{I} \times V \times \hat{I} \quad (2.24)$$

The magnitude of the quadrupolar interaction is much smaller than the magnitude of the Zeeman interaction. Therefore, the quadrupole interaction can be interpreted as a perturbation on the Zeeman interaction ( $H_Z$ ) (Equation 2.25) which results in first and second order differences in energy level splitting (Figure 2.15).

$$H = H_Z + H_Q \quad (2.25)$$

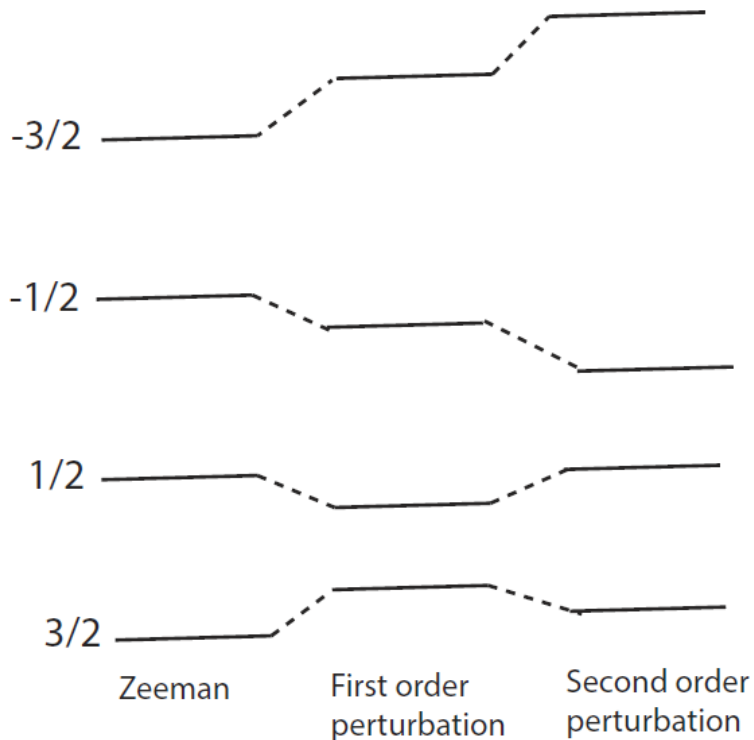


Figure 2. 15. Energy level diagram of a  $I = 3/2$  system subjected to Zeeman splitting and then first and second order quadrupole splitting.

Energy shifts in the Zeeman energy levels that occur as a result of the quadrupolar interaction also affect solid-state NMR spectra.<sup>28</sup> The first order

quadrupolar interactions affects the satellite transitions only, for example:  $1/2 \leftrightarrow 3/2$ .<sup>28</sup> The orientation dependence of the first order quadrupolar interaction results in significant line broadening in solid-state spectra.<sup>28</sup> The second order quadrupolar interaction affects all transitions and results in the unusual lineshapes that are observed in central transition spectra of quadrupolar nuclei.<sup>28</sup> The exact effects of interactions with the EFG on NMR spectra are highly dependent on the symmetry of the nuclear environment.

The quadrupolar interaction has the potential to be a valuable source of structural information in both crystalline and amorphous materials. This is because  $C_Q$  and  $\eta$  are highly dependent on the geometry of the coordination sphere with less symmetric geometries resulting in higher  $C_Q$  values.<sup>29</sup> Perfectly cubic symmetries result in  $C_Q$  values of 0 whereas planar symmetries tend to result in the highest  $C_Q$  values with other geometries lying somewhere in between these extremes.<sup>29</sup>  $C_Q$  and  $\eta$  can be extracted from lineshapes originating from crystalline materials by lineshape fitting, quantum mechanical modeling or some combination of the two.<sup>28,29</sup> This strategy becomes less accurate in the analysis of amorphous materials because characteristic lineshapes get broadened out as a result of a distribution of isotropic chemical shifts and  $C_Q$  values.<sup>29</sup> Coordination environments in amorphous materials, such as the silicone boronate acid elastomers that are analyzed in Chapter 6, can be elucidated using various solid-state NMR techniques that will be discussed in the following sub-section.

### 2.4.2 Challenges in the Elucidation of Coordination Environments in Quadrupolar Systems

The observed NMR frequency for quadrupolar nuclei ( $\omega$ ) depends on both the first and second order quadrupolar interactions which result in line broadening and lineshape distortion respectively.<sup>30</sup> The influence of these interactions is described in Equation 2.26 where  $\omega_Q$  is the quadrupole frequency, A is the isotropic chemical shift, B is the second rank anisotropic term and C is the fourth rank anisotropic term. The terms  $d^2$  and  $d^4$ , the second and fourth order Legendre polynomials, are expanded in Equations 2.27 and 2.28 to give the angular dependence of these interactions.

$$\omega \propto \frac{\omega_Q^2}{\omega_o} [A + Bd^2\theta + Cd^4\theta] \quad (2.26)$$

$$d^2 \propto (3 \cos^2 \theta - 1) \quad (2.27)$$

$$d^4 \propto (35 \cos^2 \theta - 30 \cos^4 \theta + 3) \quad (2.28)$$

It can be observed from Equations 2.27 and 2.28 that the second and fourth order anisotropic terms cannot be removed by spinning the sample at a single MAS axis.<sup>31</sup> The second rank anisotropic term can be removed by spinning at  $54.7^\circ$ , the typical magic angle, which represents the zero solution to  $d^2$ .<sup>32</sup> However, eliminating the fourth rank anisotropic term requires spinning at an angle of either  $30.6^\circ$  or  $70.1^\circ$ .<sup>32</sup> Due to the lineshape broadening and distortion that is caused by the quadrupolar interaction, the presence of more than one nuclear environment results in the overlap of non-equivalent sites.

### 2.4.3 Experimental Techniques for the Resolution Non-Equivalent Sites

Various experimental techniques exist for the resolution of individual sites in quadrupolar NMR and the determination of quadrupolar parameters,  $C_Q$  and  $\eta$ . Two of these techniques, dynamic angle spinning (DAS) and double rotation (DOR) rely on the use of specialized probes that are capable of spinning a sample on more than one axis.<sup>31,33</sup> During DAS experiments, anisotropic terms are refocused by alternately spinning the sample at two angles.<sup>31,33</sup> In addition to the need to use complex equipment, DAS experiments are further complicated by sample properties. Sample  $T_1$  values must be longer than the time required to switch between rotation angles ( $\sim 30$  ms) and spin exchange due to dipolar coupling interactions must be minimal.<sup>33</sup> In DOR, the sample is simultaneously spun at two angles.<sup>31,33</sup> The probe is spun at  $54.7^\circ$ , the regular magic angle, while the rotor is spun at  $30.6^\circ$ .<sup>33</sup> This setup yields isotropic spectra, however rotor synchronized pulses must be used to reduce the quantity of spinning side bands.<sup>33</sup> Additionally, spinning rates are limited to 12 kHz (for the probe) and 2 kHz (for the rotor) due to the mechanical demands of simultaneously spinning at two angles.<sup>33</sup> Additional experimental techniques, satellite transition magic angle spinning (STMAS) and multiple quantum magic angle spinning (MQMAS) were developed with the purpose of obtaining the isotropic chemical shift,  $C_Q$  and  $\eta$  while utilizing regular MAS probes.

Satellite transition magic angle spinning (STMAS) utilizes the relative positions of the satellite and central transitions to determine isotropic chemical shift and quadrupolar parameters.<sup>34</sup> A satellite transition is any single quantum transition

that is not the central transition.<sup>34</sup> These transitions tend to be ignored in most NMR techniques as they are broadened by the first order quadrupolar interaction.<sup>34</sup> However, this broadening is less than that which is experienced by the central transition.<sup>34</sup> Satellite transitions are highly sensitive to the MAS angle and can therefore offer improved spectral resolution provided that the magic angle is precisely calibrated.<sup>34</sup> STMAS is a 2D experiment where an isotropic spectrum is generated from the excitation of a satellite transition and the subsequent coherence transfer to the central transition.<sup>34</sup> First order quadrupolar effects in the satellite (F1) dimension are averaged to zero with a precisely calibrated magic angle and a rotor synchronized evolution time.<sup>34</sup> The resonance frequencies along each dimension are the sum of the isotropic chemical shift and the isotropic and anisotropic second order quadrupolar effects. However, because both frequencies contain the same anisotropic part, the superposition of the resonance frequencies yields a ridge-shaped peak in the 2D spectrum. Data processing of the 2D spectrum yields the isotropic spectrum in the F1 dimension and the anisotropic spectrum in the F2 dimension.<sup>34</sup>

Multiple quantum magic angle spinning (MQMAS) is another experimental technique that can be used to resolve individual quadrupolar sites and determine quadrupolar parameters. MQMAS is similar to STMAS except that coherence is generated as a result of a multiple quantum transition and then transferred to the single quantum central transition.<sup>31</sup> MQMAS is generally considered to be less sensitive than STMAS because single quantum transitions can be executed more

efficiently than multiple quantum transitions can.<sup>35</sup> However, STMAS is more sensitive to experimental conditions as the first order quadrupolar interaction can be re-introduced if any of the following conditions are not met: the magic angle is not set within  $0.002^\circ$ , the spectral width in the F1 dimension does not match the spinning frequency or the spinning frequency is not stable.<sup>35</sup> Additionally, lineshapes tend to be broadened in STMAS spectra as a result of higher order quadrupolar effects, interactions with spin  $\frac{1}{2}$  nuclei and molecular re-orientation under MAS, all of which do not affect MQMAS spectra.<sup>35</sup> Due to the increased possibility of line broadening, MQMAS was chosen for the analysis of the silicone boronate elastomers that is presented in Chapter 6. These materials are amorphous and contain multiple boron sites which makes reduced line broadening essential for the resolution of non-equivalent sites.

#### **2.4.4 Multiple Quantum Magic Angle Spinning**

The MQMAS experiment can produce spectra that are free from quadrupolar and dipolar anisotropies through a combination of magic angle spinning and multi-quantum excitation. Second rank quadrupolar effects are averaged out by magic angle spinning whereas fourth rank broadening can be averaged out via time domain refocusing that occurs during multiple quantum excitation.<sup>31,36</sup> The MQMAS technique is based on the fact that the broadening that is experienced by symmetric multi-quantum transitions ( $-3/2$  to  $3/2$  in a spin  $3/2$  system) due to second order quadrupolar effects is related to broadening that is experienced by the central transition due to second order quadrupolar effects by a ratio.<sup>37</sup> The detection of a purely isotropic signal is dependent on the coherence

pathway that is selected during multi-quantum excitation and the subsequent reconversion to single quantum coherence.<sup>31,36</sup> In  $^{11}\text{B}$ , the spin  $3/2$  system studied in Chapter 6, the ideal coherence transfer pathway is  $0 \rightarrow -3 \rightarrow -1$ .<sup>31</sup> The result is a ridge lineshape for each site with a slope that is given by the ratio of the second order broadening of the multi-quantum and central transitions.<sup>37</sup> As in STMAS, data processing yields a 2D spectrum with a conventional MAS spectrum along the F2 axis and a spectrum with only isotropic patterns along the F1 axis.<sup>36</sup>

MQMAS spectra of boron-containing elastomers were acquired using a three-pulse sequence (Figure 2.16).

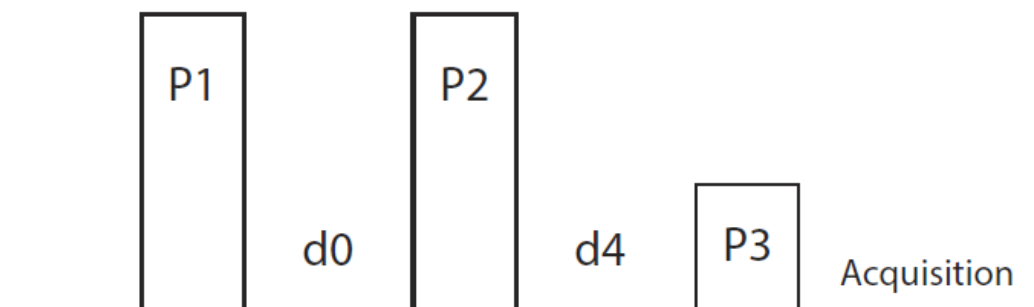


Figure 2. 16. Three-pulse MQMAS sequence.

The first pulse (P1) is a high power ( $\sim 300$  W) short ( $\sim 3$   $\mu\text{s}$ ) excitation pulse that serves to generate multi-quantum coherence.<sup>37</sup> P1 is followed by a delay (d0) during which multi-quantum coherence is allowed to evolve.<sup>37</sup> P2 is another high power ( $\sim 300$  W) short ( $\sim 1$   $\mu\text{s}$ ) reconversion pulse that is used to transform the multi-quantum coherence into detectable single-quantum coherence.<sup>37</sup> P2 is followed by a second delay period (d4) during which the single-quantum coherence

is phased by passing through a z-filter. The read pulse (P3) is a longer ( $\sim 20 \mu\text{s}$ ) low powered ( $\sim 0.5 \text{ W}$ ) pulse. The P3 pulse length is chosen so that it is selective for the excitation of the central transition only.<sup>37</sup>

In the resultant 2D spectrum, the quadrupolar interaction is conserved in the direct dimension.<sup>38</sup> Following data processing, an isotropic spectrum can be observed in the indirect dimension.<sup>38</sup> The absence of quadrupole contributions to the lineshape in the indirect dimension means that previously overlapped peaks are resolved.<sup>38</sup> The difference in chemical shifts in the direct and indirect dimensions can be used to extract quadrupolar parameters for each site.<sup>38</sup> The ratio between the chemical shift in the direct dimension ( $\delta_{MQ}$ ) and the chemical shift in the indirect dimension ( $\delta_{iso}$ ) is described in Equation 2.29. The term  $\delta_{qis}$ , reflective of the change in chemical shift caused by the quadrupolar interaction is defined in Equation 2.30 as a function of the spin ( $I$ ), the quadrupolar coupling constant ( $C_Q$ ), the Larmor frequency ( $\omega_o$ ) and the asymmetry parameter ( $\eta$ ).<sup>37</sup>

$$\delta_{MQ} = \delta_{iso} - \frac{10}{17} \delta_{qis} \quad (2.29)$$

$$\delta_{qis} = -\frac{3(4I(I+1)-3)}{(4I(2I-1))^2} \times \frac{C_Q^2}{\omega_o^2} \left(1 + \frac{\eta^2}{3}\right) \times 10^5 \quad (2.30)$$

As this relationship (Equation 2.30) is defined in terms of the quadrupolar parameters ( $C_Q$  and  $\eta$ ) the quadrupolar product (Equation 2.31), which is a ratio of these, can be calculated based on the difference between  $\delta_{MQ}$  and  $\delta_{iso}$ .<sup>39</sup> The relationship between the quadrupolar product ( $P_Q$ ) and the difference in chemical shift in the indirect and direct dimensions ( $\delta_{iso}-\delta_{MQ}$ ) is illustrated in Equation 2.32

where  $\omega_o$  is the Larmor frequency,  $I$  is the spin quantum number and  $f(I)$  is a coefficient that is equal to 4 in spin 3/2 systems.<sup>37,38</sup>

$$P_Q = C_Q^2 \left( 1 + \frac{\eta^2}{3} \right) \quad (2.31)$$

$$P_Q = \frac{(\delta_{iso} - \delta_{DQ}) \times \omega_o \times 10^{-6}}{\frac{1}{17} \times \left[ \frac{(4I(2I+1))^2}{3(4I(I+1)-3)} + 3 \right] \times \frac{3}{10} \times \left( \frac{1}{2I(2I-1)} \right)^2} \quad (2.32)$$

Values of  $\eta$  must lie between 0 and 1.<sup>39</sup> Therefore,  $P_Q$  provides a range of  $C_Q$  for each site in the MQMAS spectrum.  $C_Q$  is largest when  $\eta = 0$  and smallest when  $\eta = 1$ . Lineshape fitting of individual peaks from the projection of the indirect dimension were fit to extract exact values of  $C_Q$  and  $\eta$  from these ranges. The MQMAS-derived fits were verified by using the same quadrupole parameters to fit regular quadrupolar MAS spectra from three different magnetic fields: 7.0, 11.7 and 20.0 T (Appendix A.2 to A.4).

## 2.5 Additional Experimental Techniques

### 2.5.1 Electrochemical Impedance Spectroscopy

Electrochemical impedance spectroscopy (EIS) is a popular experimental technique that is used to measure the electrical properties of materials.<sup>40</sup> EIS is suitable for the measurement of the motion of charge carriers in both solids and liquids.<sup>40</sup> In this work, EIS is used to measure proton motion in solid state proton conductors such as phosphate solid acids and tin pyrophosphates (Chapters 3 to 5). Impedance, a measure of the circuit characteristics that impede the flow of charge carriers through a circuit, is measured by applying an alternating current perturbation and measuring the resultant phase shift in the in the constant

alternating current relative to the applied signal.<sup>40</sup> Impedance is mathematically represented by a complex number that is composed of resistance and reactance.<sup>40</sup> Where resistance ( $Z'$ ) is the frequency-independent real component of impedance and reactance ( $Z''$ ) is the frequency-dependent imaginary component. Raw data is typically comprised of both real and imaginary components.

Impedance ( $Z$ ) can be mathematically derived based on Ohm's law as it is analogous to resistance but is described using alternating current ( $I_t$ ) and alternating potential ( $E_t$ ) (Equation 2.33).<sup>40</sup>

$$Z = \frac{E_t}{I_t} \quad (2.33)$$

Both  $E_t$  and  $I_t$  can be expressed as a function of time (Equations 2.34 and 2.35). Where  $E_o$  and  $I_o$  are the potential and current when  $t=0$  and  $\omega$  is the angular frequency in Hertz.<sup>40</sup> In linear systems, the response signal,  $I_t$ , is phase shifted by  $\theta$ .

$$E_t = E_o \sin \omega t \quad (2.34)$$

$$I_t = I_o \sin(\omega t - \theta) \quad (2.35)$$

Combining Ohm's law with Euler's law yields (Equation 2.36):

$$Z(\omega) = \frac{E_t}{I_t} = \frac{E_o e^{i\omega t}}{I_o e^{i(\omega t - \theta)}} \quad (2.36)$$

EIS data can be represented using Nyquist (Figure 2.17) and Bode (Figure 2.18) plots.<sup>41</sup> The Nyquist plot (Figure 2.17) represents imaginary impedance,  $Z''(\omega)$ , as a function of real impedance ( $Z'(\omega)$ ) on the complex plane.<sup>41</sup> The Bode plot (Figure 2.18) can represent either  $\log|Z|$  or phase angle ( $\theta$ ) as a function of  $\log$

of the frequency ( $\log(\omega)$ ).<sup>41</sup> Nyquist plots are useful because the shape of the curve allows for qualitative evaluation of the data upon visual inspection.<sup>41</sup> However, Bode plots offer a more complete interpretation of the data because both impedance and phase difference can be monitored as a function of frequency.<sup>41</sup> Impedance data is typically interpreted by fitting the curves in the Nyquist and Bode plots to an equivalent circuit model. These models can be increasingly complex and include combinations of resistors, capacitors and inductors.<sup>41,42</sup> The plots presented in Figures 2.17 and 2.18 are representative of Nyquist and Bode plots for a capacitor and a resistor that are connected in series. The properties of these curves change based on the elements of the equivalent circuit that are present and how they are connected (in series, in parallel, nested...).

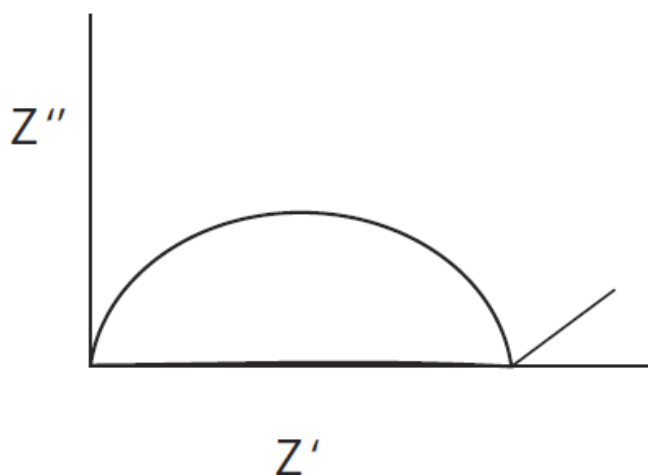


Figure 2. 17. Sample Nyquist plot for a capacitor and a resistor that are connected in series.

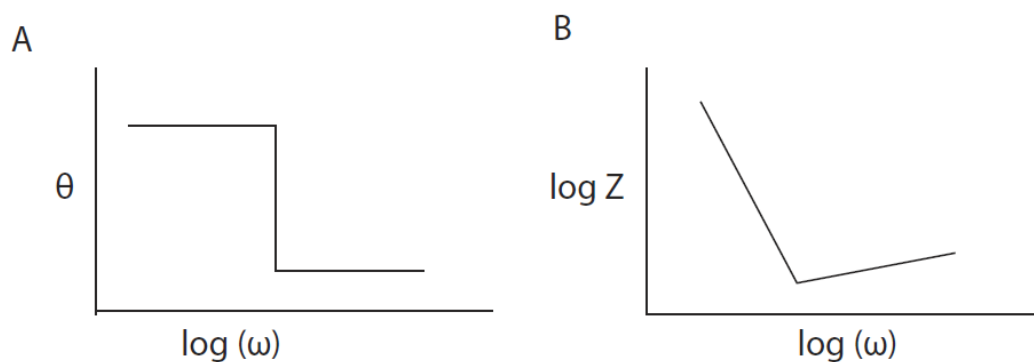


Figure 2. 18. Sample Bode plots, phase angle as a function of  $\log \omega$  (A) and  $\log Z$  as a function of  $\log \omega$  (B) for a capacitor and a resistor that are connected in series.

In Chapters 3-5, solid-state proton conductors are prepared for EIS analysis by being pressed into pellets with a width of 1-3 mm and a diameter of 10 mm. Impedance is measured across these samples using the two-terminal set up. In the two-terminal set up, working and working sense electrodes and, counter and reference electrodes are connected to create two electrodes that are then connected on either side of the cell. The two-terminal method is chosen over the four-terminal method due to the fragility of these samples which makes pressing pellets significantly easier than casting membranes. However, it is noted that the two-terminal set up is limited to systems with relatively high resistance ( $>10^6 \Omega$ ) due to interfacial resistance and polarization that arise from voltage drop being measured across the same electrodes that constant current is flowing through.<sup>43</sup> This issue is eliminated when the four-terminal method is used because the electrodes that are used to measure voltage are separated from those that are used to measure current.<sup>43</sup>

Proton conductivity ( $\sigma$ ) of the solid-state disks in S/cm was determined based on the Nyquist plot using Equation 2.36 where  $d$  is the width of the pellet,  $A$  is the area of the pellet and  $R$  is the resistance.<sup>42,44</sup>

$$\sigma = \frac{d}{AR} \quad (2.36)$$

The resistance is the high frequency intercept on the Nyquist plot.<sup>42</sup> The surface area of the disk was calculated according to Equation 2.37 where  $r$  is the radius of the disk in cm.

$$A = \pi r^2 \quad (2.37)$$

### 2.5.2 Powder X-ray Diffraction

Powder X-ray diffraction (PXRD) is an experimental technique that is commonly used to characterize crystalline solids, identify phases and mixtures and determine unit cell dimensions. The term “powder” generally refers to samples containing randomly oriented crystalline domains.<sup>45</sup> The technique is non-destructive and is based on the interaction between incident X-rays and planes in a crystalline lattice.<sup>45</sup> Diffraction can be described as deviations in light propagation from the trajectories that are predicted based on optical geometry.<sup>46</sup> In order for diffraction to be observed, the scattering surface must be similar in size to the incident wavelength.<sup>46</sup> The distance between neighbouring atomic unit cells is on the order of hundreds of nanometers. It is for this reason that X-rays, which have wavelengths of a similar magnitude, are employed to investigate symmetry in atomic systems.<sup>46</sup> X-ray diffraction operates on the premise that a wave propagating in a homogeneous medium will continue to propagate at the same rate and in the same

direction due to the law of conservation of momentum.<sup>46</sup> When inhomogeneities in the propagation medium are encountered, momentum is no longer conserved and the wave experiences changes in the rate and/or direction of propagation.<sup>46</sup> These changes in wave propagation are known as scattering.

The diffraction of X-rays in a crystal lattice can be modeled using the diffraction of a plane wave ( $Y$ ) (Equation 2.38) at a defined scattering point in a non-homogeneous medium with translational symmetry. The plane wave described in Equation 2.36 oscillates in time ( $t$ ) and space ( $r$ ) and is described in terms of wave amplitude ( $Y_0$ ), wave vector ( $k$ ) and wave angular frequency ( $\omega_w$ ). The phase of this wave,  $\varphi$ , is defined by  $\varphi = kr - \omega_w t$ .

$$Y = Y_0 e^{i(kr - \omega_w t)} \quad (2.38)$$

Scattering occurs when a propagating wave encounters a scatter site ( $r_s$ ) which is described in Equation 2.39 in terms of three non-coplanar translational vectors ( $a_x$ ) and integers ( $n_x$ ).

$$r_s = n_1 a_1 + n_2 a_2 + n_3 a_3 \quad (2.39)$$

The incident plane wave has the same amplitude at all scattering points but can differ in phase by a factor of  $2\pi$ .<sup>46</sup> Following a scattering event, the phase ( $\varphi$ ) changes in terms of its wave vector ( $k$ ) and location in space ( $r$ ).<sup>46</sup> Wave vectors of the incident ( $k_i$ ) and scattered ( $k_f$ ) waves differ by a factor of  $2\pi$  relative to the scatter site  $r_s$ . This scenario results in the quasi-momentum conservation law that defines specific angles,  $2\theta$ , between the incident and scattered wave vectors where diffraction can occur.<sup>46</sup> The diffraction vectors are presented in Figure 2.19 where

H is the diffraction vector that is represented in reciprocal space by reciprocal vectors ( $b_x$ ) and Miller indices (hkl) (Equation 2.40).<sup>46</sup>

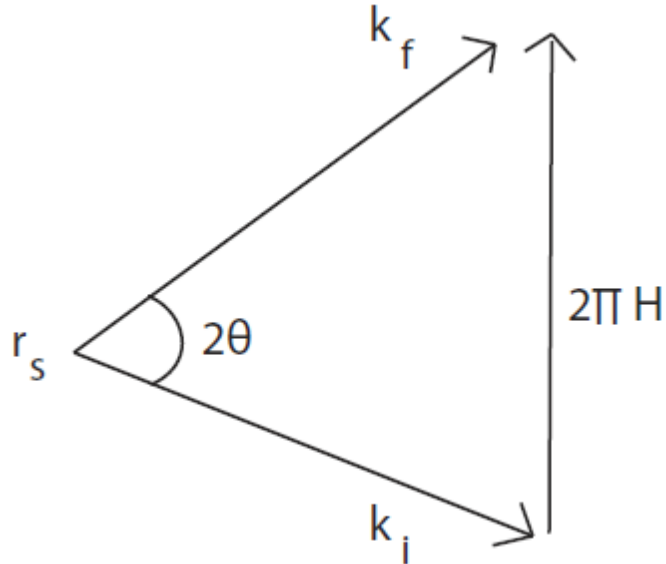


Figure 2. 19. Relationship between the incident ( $k_i$ ) and scattered ( $k_f$ ) waves following interaction with a scatter site in a non-homogeneous medium.

$$H = hb_1 + kb_2 + lb_3 \quad (2.40)$$

Solving the vector triangle presented in Figure 2.19 results in Equation 2.41 where  $\lambda$  is the incident wavelength.

$$2\pi|H| = \frac{4\pi \sin \theta}{\lambda} \quad (2.41)$$

Through Miller indices, the diffraction vector H is related to real crystallographic positions. The spacing between these crystallographic planes is defined by the term d which is the reciprocal of H.<sup>46</sup> Substituting d into Equation 2.39 yields the Bragg diffraction law (Equation 2.42) which is the relationship

between possible directions for the propagation of diffracted waves and the interplanar spacing (or d-spacing) in crystals.<sup>46</sup>

$$\lambda = 2d\sin\theta \quad (2.42)$$

During PXRD experiments, X-rays are generated from a cathode tube and are filtered and collimated to produce an intense monochromatic beam.<sup>45</sup> The atomic level planes in the sample act as a grating upon which the incident beam is diffracted. This interaction produces constructive interference, resulting in a diffraction peak, when Bragg's law (2.42) is satisfied.<sup>45</sup> In crystalline samples, where atoms are arranged periodically, the diffracted wave produces sharp peaks whose position and intensity are correlated to atomic positions.<sup>45</sup> This is not the case in amorphous samples where atomic distribution tends to result in destructive interference. All possible diffraction peaks can be observed in a powder sample by scanning through a range of  $2\theta$  angles.<sup>45</sup> This is because finely-ground powder samples contain a random mixture of all possible crystal orientations. Diffraction patterns differ between materials and between different phases of the same material due to differences in d-spacing.<sup>45</sup> Materials and phases can be identified through comparison to reference powder patterns. PXRD was used in this work to identify whether desired phases of synthesized phosphate solid acids (Chapters 3 and 4) and tin pyrophosphates (Chapter 5) were produced.

### **2.5.3 Thermogravimetric Analysis**

Thermogravimetric analysis (TGA) is an analytical technique that is used to measure changes in sample mass as a function of either temperature or time.<sup>47</sup> In

this thesis, the technique was used to confirm boronic acid loading in silicone boronic acid elastomers. During analysis, the sample is contained in a pre-weighted pan that is supported by a precision balance.<sup>47</sup> During the experiment, the sample is placed inside a furnace and is subjected to a temperature program under controlled atmospheric conditions.<sup>47</sup> The atmosphere can be reactive or inert.<sup>48</sup> Commonly used temperature programs include temperature ramping at a constant rate and heating followed by holding at a constant temperature.<sup>48</sup> Sample mass is continuously measured as a function of either temperature or time depending on the nature of the temperature program.<sup>47,48</sup> Changes in sample mass can be correlated to various changes in the sample including: chemical reactions, redox reactions, phase changes, decomposition events, evaporation of volatile components and dehydration.<sup>47,48</sup>

Thermal events are indicated by the presence of a step in the TGA curve with each process corresponding to one or more steps.<sup>48</sup> Steps are typically analyzed by drawing a horizontal tangent at the beginning and ending of the step and calculating the difference in mass.<sup>48</sup> Percent mass loss can then be used to characterize the thermal event. For example, volatile components can be identified based on their mass. In this work, silicone boronate acid elastomers are subjected to a temperature ramp under argon atmosphere for the purpose of identifying decomposition events.

## 2.6 References

1. Harris, R. K. *Nuclear Magnetic Resonance Spectroscopy*. (Pitman Publishing INC, 1983).

2. MacKenzie, K.J.D., Smith, M. . *Multinuclear Solid-State NMR of Inorganic Materials*. (Elsevier Science Ltd, 2002).
3. Keeler, J. 2. NMR and Energy Levels. in *Understanding NMR Spectroscopy* 2-1-2-21 (2004).
4. Antzutkin, O. N. *et al. Solid State NMR Spectroscopy Principals and Applications*. (Blackwell Publishing Ltd, 2002).
5. Keeler, J. Chapter 8. Relaxation. 1–24 (2004). Available at: [http://www-keeler.ch.cam.ac.uk/lectures/understanding/chapter\\_8.pdf](http://www-keeler.ch.cam.ac.uk/lectures/understanding/chapter_8.pdf). (Accessed: 26th February 2019)
6. Kleckner, I. R. & Foster, M. B. An Introduction to NMR-based Approaches for Measuring Protein Dynamics. *Biochim Biophys Acts* **1814**, 942–968 (2011).
7. Reich, H. J. 8.1 Relaxation in NMR Spectroscopy. 1–13 (2017).
8. Andrew, E. R. Magic angle spinning in solid state n.m.r. spectroscopy. *Phil. Trans. R. Soc. Lond. A* **299**, 505–520 (1981).
9. Reichert, D. & Saalwachter, K. Dipolar Coupling: Molecular-Level Mobility. in *Encyclopedia of Magnetic Resonance* (2008). doi:10.1002/9780470034590.emrstm1020
10. Pileio, G. *et al.* Analytical theory of  $\gamma$ -encoded double-quantum recoupling sequences in solid-state nuclear magnetic resonance. *J. Magn. Reson.* **186**, 65–74 (2007).
11. Saalwächter, K.  $^1\text{H}$  multiple-quantum nuclear magnetic resonance investigations of molecular order in polymer networks. II. Intensity decay and restricted slow dynamics. *J. Chem. Phys.* **120**, 454–464 (2004).
12. Kim, G., Griffin, J. M., Blanc, F., Haile, S. M. & Grey, C. P. Characterization of the Dynamics in the Protonic Conductor  $\text{CsH}_2\text{PO}_4$  by  $^{17}\text{O}$  Solid-State NMR Spectroscopy and First-Principles Calculations : Correlating Phosphate and Protonic Motion. *J. Am. Chem. Soc.* **137**, 3867–3876 (2015).
13. Kreller, C. R. *et al.* Intragranular Phase Proton Conduction in Crystalline  $\text{Sn}_{1-x}\text{In}_x\text{P}_2\text{O}_7$  ( $x = 0$  and  $0.1$ ). *J. Phys. Chem. C* **121**, 23896–23905 (2017).
14. Kristiansen, P. E., Carravetta, M., Lai, W. C. & Levitt, M. H. A robust pulse sequence for the determination of small homonuclear dipolar couplings in magic-angle spinning NMR. *Chem. Phys. Lett.* **390**, 1–7 (2004).

15. Feike, M. *et al.* Broadband Multiple-Quantum NMR Spectroscopy. *J. Magn. Reson. Ser. A* **122**, 214–221 (1996).
16. Bak, M., Rasmussen, J. T. & Nielsen, N. C. SIMPSON: A general simulation program for solid-state NMR spectroscopy. *J. Magn. Reson.* **213**, 366–400 (2011).
17. Rienstra, C. M. *et al.* Determination of multiple torsion-angle constraints in U-<sup>13</sup>C, <sup>15</sup>N-labeled peptides: 3D <sup>1</sup>H-<sup>15</sup>N-<sup>13</sup>C-<sup>1</sup>H dipolar chemical shift NMR spectroscopy in rotating solids. *J. Am. Chem. Soc.* **124**, 11908–11922 (2002).
18. Strojek, W., Kalwei, M. & Eckert, H. Dipolar NMR strategies for multispin systems involving quadrupolar nuclei: <sup>31</sup>P{<sup>23</sup>Na} rotational echo double resonance (REDOR) of crystalline sodium phosphates and phosphate glasses. *J. Phys. Chem. B* **108**, 7061–7073 (2004).
19. Levitt, M. H. *Spin Dynamics: Basics of Nuclear Magnetic Resonance*. (John Wiley & Sons, 2008).
20. Saalwächter, K. Proton multiple-quantum NMR for the study of chain dynamics and structural constraints in polymeric soft materials. *Prog. Nucl. Magn. Reson. Spectrosc.* **51**, 1–35 (2007).
21. Kolodziejcki, W. & Klinowski, J. Kinetics of Cross-Polarization in Solid-State NMR : A Guide for Chemists. *Chem. Rev.* **102**, 613–628 (2002).
22. Fyfe, C. A., Brouwer, D. H. & Tekely, P. Measurement of NMR Cross-Polarization (CP) rate constants in the slow CP regime: Relevance to structure determinations of zeolite-sorbate and other complexes by CP magic-angle spinning NMR. *J. Phys. Chem. A* **109**, 6187–6192 (2005).
23. Foerster, H. *et al.* Relaxation Measurements. in *User Manual* 202–229 (2009).
24. Bain, A. D. Chemical exchange in NMR. *Prog. Nucl. Magn. Reson. Spectrosc.* **43**, 63–103 (2003).
25. Bain, A. D. Chemical Exchange. in *Annual Reports on NMR Spectroscopy* (ed. Web, G.) 23–48 (Elsevier Ltd, 2008). doi:10.1016/S0066-4103(07)63002-6
26. Bain, A. D. & Fletcher, D. A. S elective-inversion experiments applied to chemical exchange in coupled spin systems. *Mol. Phys.* **95**, 1091–1098 (1998).
27. Bain, A. D. *The cifit program*. (2000).
28. Autschbach, J., Zheng, S. & Schurko, Robert, W. Analysis of Electric Field

- Gradient Tensors at Quadrupolar Nuclei in Common Structural Motifs. *Concepts Magn. Reson. A* **36**, 84–126 (2010).
29. Kentgens, A. P. M. A practical guide to solid-state NMR of half-integer quadrupolar nuclei with some applications to disordered systems. *Geoderma* **80**, 271–306 (1997).
  30. Frydman\_MQMAS3\_optimization.pdf.
  31. Frydman, L. & Harwood, J. S. Isotropic Spectra of Half-Integer Quadrupolar Spins from Bidimensional Magic-Angle Spinning NMR. *J. Am. Chem. Soc.* **117**, 5367–5368 (1995).
  32. Ashbrook, S. Introduction to Quadrupolar NMR Interactions in NMR.
  33. Freude, D. Quadrupolar Nuclei in Solid-state Nuclear Magnetic Resonance. *Encycl. Anal. Chem.* 12188–12224 (2000). doi:10.1002/9780470027318.a6112
  34. Gan, Z. Satellite transition magic-angle spinning nuclear magnetic resonance spectroscopy of half-integer quadrupolar nuclei. *J. Chem. Phys.* **114**, 10845–10853 (2001).
  35. Takahashi, T., Kanehashi, K., Shimoikeda, Y., Nemoto, T. & Saito, K. Practical comparison of sensitivity and resolution between STMAS and MQMAS for  $^{27}\text{Al}$ . *J. Magn. Reson.* **198**, 228–235 (2009).
  36. Frydman, L., Grant, D. M. & Harris, R. K. Fundamentals of Multiple-Quantum Magic-Angle Spinning NMR on Half-Integer Quadrupolar Nuclei Magic-Angle Spinning NMR on Half-Integer Quadrupolar Nuclei. *Encyclopedia of Nuclear Magnetic Resonance. Volume 9: Advances in NMR* **9**, 262–274 (2002).
  37. Foerster, H. *et al.* Basic MQ-MAS. in *User Manual* 213–230 (Bruker Biospin GmbH, 2009).
  38. A. Medek, J.S. Harwood & L. Frydman. Multiple-Quantum Magic- Angle Spinning NMR: A New Method for the Study of Quadrupolar Nuclei in Solids. *J. Am. Chem. Soc.* **117**, 12779–12787 (1995).
  39. Johnston, K. E. *et al.* The polar phase of  $\text{NaNbO}_3$ : A combined study by powder diffraction, solid-state NMR, and first-principles calculations. *J. Am. Chem. Soc.* **132**, 8732–8746 (2010).
  40. Zia, A. I. & Mukhopadhyay, S. C. Impedance Spectroscopy and Experimental Setup. in *Electrochemical Sensing: Carcinogens in Beverages, Smart Sensors, Measurements and Instrumentation* 21–37 (2016). doi:10.1007/978-3-319-32655-9

41. Lasia, A. *Electrochemical Impedance Spectroscopy and its Applications*. (2014).
42. Lvovich, V. F. Selected Examples of Impedance Analysis Applications. in *Impedance Spectroscopy: Applications to Electrochemical and Dielectric Phenomena* 281–318 (John Wiley & Sons, 2015).
43. Lee, C. H., Park, H. B., Lee, Y. M. & Lee, R. D. Importance of Proton Conductivity Measurement in Polymer Electrolyte Membrane for Fuel Cell Application. *Ind. Eng. Chem. Res.* **44**, 7617–7626 (2005).
44. Qi, Y. *et al.* Increased proton conductivity of metal – organic framework micro- film prepared by a facile salt-free approach. *J. Mater. Chem. A* **2**, 8849–8853 (2014).
45. Dutrow, B. L. & Clark, C. M. *Geochemical Instrumentation and Analysis, X-ray Powder Diffraction*. 1 (2019). Available at: [http://serc.carleton.edu/research\\_education/geochemsheets/techniques/XRD.html](http://serc.carleton.edu/research_education/geochemsheets/techniques/XRD.html). (Accessed: 4th April 2019)
46. Zolotoyabko, E. *Basic Concepts of X-Ray Diffraction*. (Wiley-VCH Verlag GmbH & Co., 2014).
47. Cai, J. *et al.* Processing thermogravimetric analysis data for isoconversional kinetic analysis of lignocellulosic biomass pyrolysis: Case study of corn stalk. *Renew. Sustain. Energy Rev.* **82**, 2705–2715 (2018).
48. Bottom, R. Thermogravimetric Analysis. in *Principals and Applications of Thermal Analysis* (ed. Gabbott, P.) 87–118 (Blackwell Publishing Ltd, 2008).

### **Chapter 3: Quantifying Site-Specific Proton Dynamics in Phosphate Solid Acids by $^1\text{H}$ Double Quantum NMR Spectroscopy**

This chapter discusses the use of symmetry-based double quantum (DQ) filtered solid-state NMR for the recoupling of homonuclear dipolar coupling interactions in complex multi-spin systems: phosphate solid acids. It was shown that dipolar coupling interactions corresponding to specific proton environments could be quantified. Site specific attenuation of the dipolar coupling interaction lead to the identification of a preferred proton hopping pathway in multi-site monoclinic  $\text{RbH}_2\text{PO}_4$  (RDP).

This work was adapted from “Quantifying Site-Specific Proton Dynamics in Phosphate Solid Acids by  $^1\text{H}$  Double Quantum NMR Spectroscopy” as published in: *The Journal of Physical Chemistry C*. Copyright 2017 American Chemical Society (G.Y. Foran, D.H. Brouwer and G.R. Goward. 2017, 121, 25641-25650). All sample preparation and analysis were performed by G.Y. Foran at McMaster University. D.H. Brouwer assisted in the initial set up of the DQ NMR experiments and in the calculation of the apparent dipolar couplings. The initial drafts of the manuscript were prepared by G.Y. Foran and were edited in collaboration with G.R. Goward.

#### **3.1 Introduction**

Phosphate solid acids are materials that are comprised of an alkali cation and a phosphate oxyanion that have properties that lie between those of a salt and those of an acid.<sup>1</sup> These materials have been identified as possible intermediate temperature range proton conductors due to their ability to conduct protons

anhydrously via the Grotthuss mechanism.<sup>1,2</sup> Relatively high proton conductivities, on the order of  $10^{-2}$  S/cm, have been achieved under ideal conditions making phosphate solid acids potential membrane electrolyte assembly (MEA) materials for use in proton exchange membrane (PEM) fuel cells.<sup>1-4</sup>  $\text{CsH}_2\text{PO}_4$  (CDP) is probably the most famous example of the use of phosphate solid acids as MEAs in intermediate-temperature fuel cells. A working laboratory-scale fuel cell was created around a CDP electrolyte by Haile et al.<sup>2</sup> This device took advantage of the monoclinic to cubic phase transition in CDP which occurs at 234 °C.<sup>2,5</sup> This phase change has been described as superprotonic, meaning that proton conductivity in the material increases by several orders of magnitude after it has occurred.<sup>2,3</sup> The structural basis of the superprotonic phase change is that the level of disorder in the hydrogen-bonded network surrounding the phosphate tetrahedra increases such that proton hopping via the Grotthuss mechanism becomes substantially more favorable.<sup>1-3</sup>

Despite the successful construction of a fuel cell based on a CDP electrolyte, controversy surrounding the stability of superprotonic phases has been extensively documented.<sup>2,5</sup> It is often argued that superprotonic phases of solid acids are not reliable proton conductors because humidity and pressure must be tightly controlled in order to prevent the decomposition or melting of the material.<sup>2,5</sup> The need for tightly controlled sample conditions somewhat limits the types of experiments that can be performed on these highly conductive phases. It is for this reason that this work focuses on changes in proton dynamics in materials with ionic proton

conducting phases.<sup>5</sup> Stable phases of phosphate solid acids will be studied to gain a better understanding of the mechanics of proton conduction in these materials. To this end, proton conductivity and accompanying changes in proton dynamics as a function of temperature will be quantified in the following solid acid proton conductors:  $\text{KH}_2\text{PO}_4$  (KDP) and  $\text{RbH}_2\text{PO}_4$  (RDP) as well as in calcium hydroxyapatite,  $\text{Ca}_{10}(\text{PO}_4)_6(\text{OH})_2$ , (CaHA), a non-conductive material. Particular attention will be paid to the analysis of RDP. This material undergoes a phase change from the tetragonal to the monoclinic phase in the temperature range that is accessible via the NMR experiments performed in this work. It is hoped that the analysis of RDP will show that multiple motional pathways can be differentiated using site-selective NMR techniques.

Molecular-level dynamics in phosphate solid acids have been previously studied via NMR. These studies have focused primarily on the determination of molecular structure and the characterization of local dynamics involved in proton transport. Kim et al.<sup>6,7</sup> have characterized two unique processes contributing to proton transport via the Grotthuss mechanism in CDP: proton exchange via proton hopping between hydrogen-bonded sites and proton exchange via phosphate oxyanion rotation. Activation energies for these processes have been determined via variable temperature proton and phosphorus NMR.<sup>3</sup> Structural models of these processes have been constructed using a combination of  $^{17}\text{O}$  NMR and computational methods.<sup>6</sup> One of the goals of their work was to determine whether proton motion in phosphate solid acids can be attributed to proton hopping,

phosphate rotation or a combination of these processes. Monoclinic RDP has been previously investigated using solid-state NMR by Vijayakumar et al.<sup>7</sup> at 21.0 T. Under these conditions, three distinct proton sites were resolved.<sup>7</sup> Two of these resonances were assigned to the protons occupying sites along the disordered hydrogen-bonded network located on the b-axis in the crystal structure (Figure 3.1).<sup>7</sup> The remaining resonance was assigned to the proton occupying the ordered hydrogen-bonded network located on c-axis (Figure 3.1).

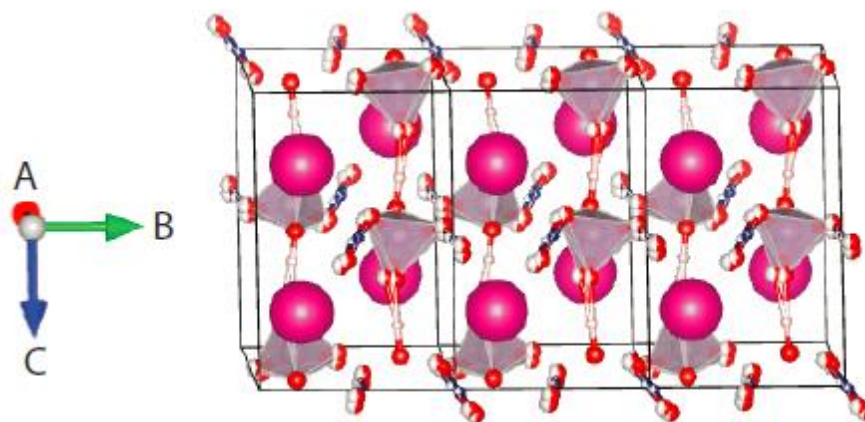


Figure 3. 1. Monoclinic RDP with b- and c-axes labelled.

Proton dynamics were determined from Arrhenius plots of longitudinal relaxation ( $T_1$ ) data and were attributed to phosphate tetrahedra rotation.<sup>7</sup> Anion dynamics have also been investigated in RDP by Traer et al.<sup>8</sup> via  $^{31}\text{P}$  centerband-only detection of exchange (CODEX) NMR experiments, where rotation of the phosphate tetrahedra was found to occur on the millisecond timescale. Proton hopping was not explicitly discussed in either of these works, but we believe that it may make significant contributions to proton dynamics in solid acids, particularly

at temperatures well below the superprotonic transition. Previous double quantum (DQ) NMR studies probing both proton and rubidium environments in RDP and rubidium methane phosphonate were performed by Vijayakumar et al.<sup>4</sup> where dipolar recoupling methods were used to determine the relative strength of proton-proton dipolar coupling interactions.<sup>4</sup> Although proton-proton interactions were the focus of these previous studies, site-specific proton-proton dipolar coupling has yet to be quantified in these materials. It is expected that the analysis of site-specific proton homonuclear dipolar coupling data will provide new insight in the assignment of motional processes to unique proton sites in multi-site systems.

## **3.2 Experimental**

### **3.2.1 Sample Preparation**

KDP and RDP were prepared by dissolving 1.00 g of the corresponding carbonate in a stoichiometric amount of phosphoric acid as was described by Kim et al.<sup>6</sup> A minimal amount of de-ionized water was added to completely dissolve any remaining solid. The solid acid samples were precipitated out of solution via the addition of small amounts of methanol. The resultant crystals were filtered and then dried in a vacuum oven at 80 °C for several hours. The CaHA sample was purchased from Sigma Aldrich and dried in a furnace at 600 °C for several hours prior to use.

RDP was prepared in the tetragonal phase and was converted into the monoclinic phase via additional heating to 130 °C. Powder X-ray diffraction (PXRD) and solid-state NMR were used to confirm that this procedure resulted in a transition to the monoclinic phase (Figure 3.2). Spectra confirming the conversion

to the monoclinic phase could be collected up to several hours after the removal of the sample from the oven, demonstrating the meta-stability of this phase.

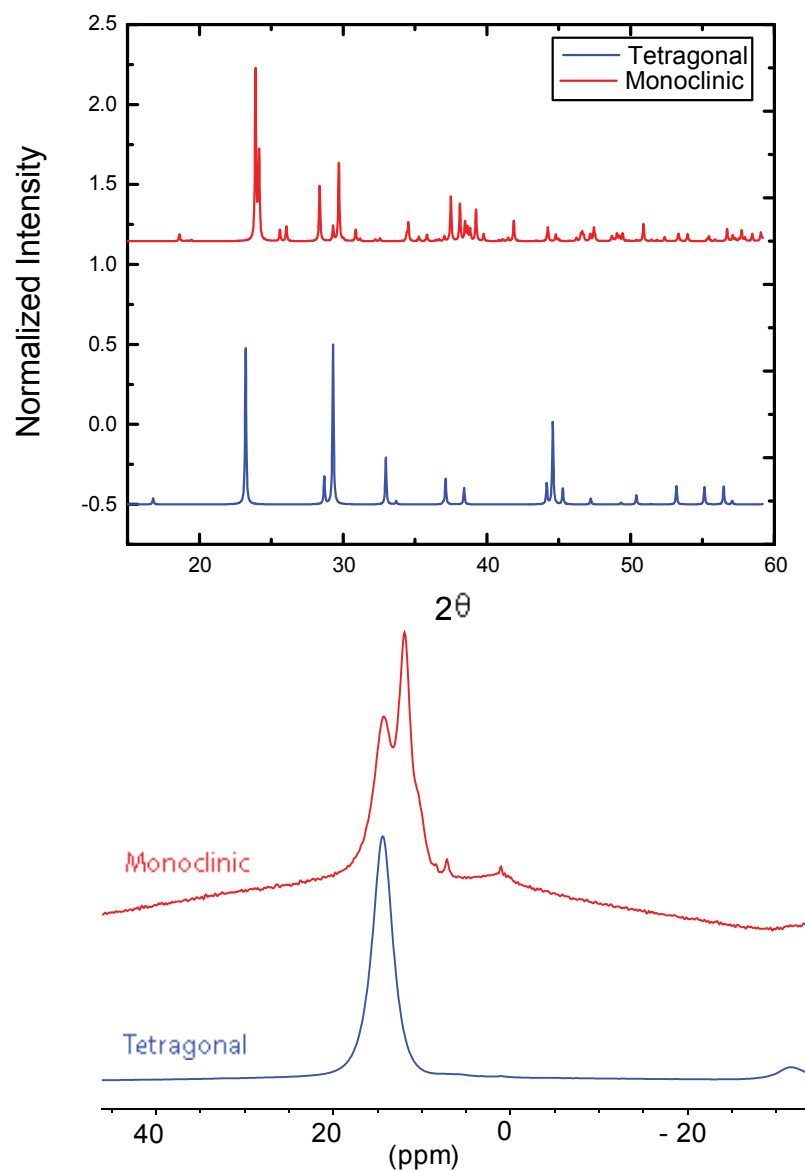


Figure 3. 2. PXR D pattern (step size =  $0.017^\circ$ ) and proton NMR spectra (7.0 T, 13.7 kHz MAS) showing the phase transition from the tetragonal (blue) to the monoclinic (red) phase in RDP following overnight heating to  $130^\circ\text{C}$ .

### 3.2.2 Impedance Spectroscopy

Powdered KDP and RDP samples were pressed uniaxially for 15 minutes

at 5000 psi to yield pellets with a diameter of 14 mm and a width of 1.5-3 mm. Pellets were sintered at 130 °C overnight and then gold coated for one minute on each side. CaHA pellets were prepared similarly but were pressed at 12000 psi and were sintered at 300 °C. Impedance measurements were taken using a Gamry Interface 1000 potentiostat with constant voltage and frequencies ranging from 100000 to 10 Hz. Pellets were contained within a two-electrode cell where they were pressed between two metal disks allowing current to flow through them widthwise. Measurements were taken in ten-degree increments between 50 and 170 °C. Sample temperature was equilibrated for one hour prior to each measurement.

### **3.2.3 Powder X-ray Diffraction**

Powdered samples were mounted on a disk using a mixture of Vaseline and toluene. These samples were analyzed at room temperature between 15 and 60° (2 $\theta$ ) in steps of 0.017°. All PXRD measurements were performed using a 0.154 nm Cu source.

### **3.2.4 NMR Measurements**

All NMR experiments were performed on a 7.0 T wide-bore Ascend spectrometer using a 4 mm double-resonance magic angle spinning (MAS) probe. Samples were packed in a 4 mm thick-walled rotor and spun at a rate of 13.7 kHz. Spectra were referenced to adamantane (1.63 ppm) for a 2.5  $\mu$ s  $\pi/2$  pulse at a power level of 100 W. All DQ experiments were performed using the R264<sup>11</sup> symmetry-based dipolar recoupling pulse sequence. Variable temperature experiments were performed between -7 and 107 °C. 107 °C was the highest temperature that could

be reliably obtained with the employed experimental set-up. Sample temperature was calibrated based on the response of a mixture of  $\text{Sm}_2\text{Sn}_2\text{O}_7$  and  $\text{SnO}_2$  to probe heating under MAS conditions.<sup>9</sup> Experimental temperature was accurate to  $\pm 4$  °C based on the transition to the monoclinic phase began at 76 °C as opposed to 80 °C as has been previously described.<sup>10</sup>

### **3.3 Results and Discussion**

#### **3.3.1 Proton Conductivity in Systems Containing Phosphate Tetrahedra**

Bulk proton conductivity in RDP, KDP and CaHA was measured using electrochemical impedance spectroscopy (EIS) (Figure 3.3). As expected, CaHA is a poor proton conductor with no observed increase in proton conductivity with increasing sample temperature (Figure 3.3). In contrast, proton conductivity in both KDP and RDP increases by about four orders of magnitude (Figure 3.3). As signal intensity in DQ NMR is correlated to the magnitude of the dipolar coupling interaction (Chapter 2),<sup>11</sup> it is expected that increased proton motion will result in observable signal attenuation. However, as no break or step is observed in the conductivity trend, these materials are expected to act as ionic conductors. This behaviour is consistent with previous studies of these materials.<sup>5,12,13</sup>

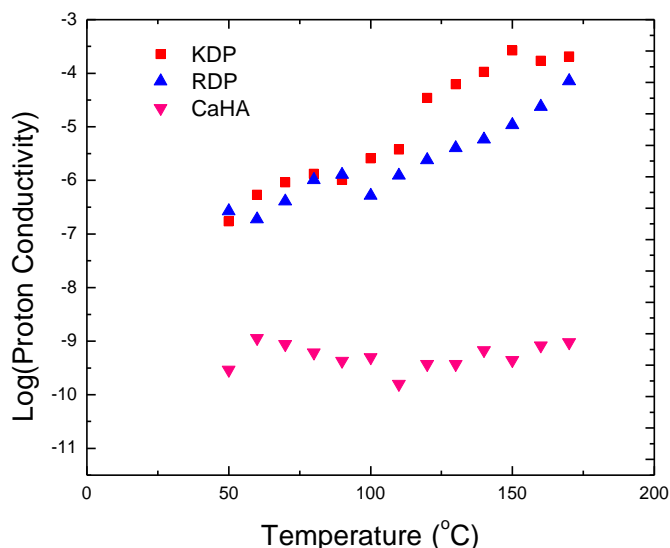


Figure 3. 3. Proton conductivity of KDP, RDP and CaHA measured via EIS between 50 and 170 °C.

A limitation of EIS is that the technique measures all processes that contribute to proton conduction across the entire sample. Proton conductivity measurements obtained via this technique encompass local proton motion through all sites as well as additional proton motion that can be attributed to conductivity through grain boundaries and other long-range effects. Therefore, solid-state NMR, a site-specific technique will be utilized to elucidate proton motion in individual chemical environments.

### 3.3.2 Overview of Site-Specific Proton Motion

$1D\ ^1H$  NMR was used to elucidate proton environments in each sample of interest: CaHA, KDP and RDP (Figure 3.4).

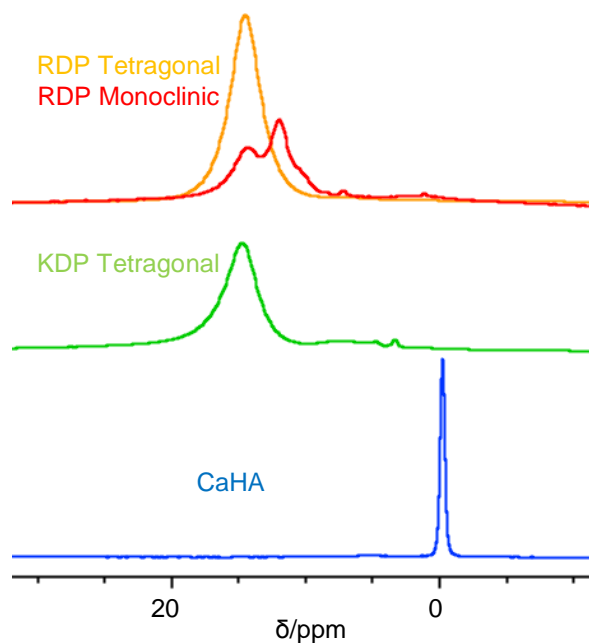


Figure 3. 4. 1D  $^1\text{H}$  NMR of CaHA, KDP and RDP acquired at room temperature at 7.0 T with 13.7 kHz MAS.

$D_{\text{app}}^0$  for the static phases of these materials were calculated using proton-proton distances which were determined based on the respective crystal structures (Equation 3.1).

$$D_{\text{app}}^0 = \sqrt{\sum_k p_j D_{jk}^2} \quad (3.1)$$

Where  $D_{\text{app}}^0$  is calculated based on the root sum square of the individual proton-proton dipolar coupling interactions ( $D_{jk}$ ) and  $p$  is the occupancy factor of each protonated site.  $D_{\text{app}}^0$  was found to stabilize once the size of the coordination sphere reached 15 Å as can be observed for tetragonal KDP and RDP in Figure 3.5.

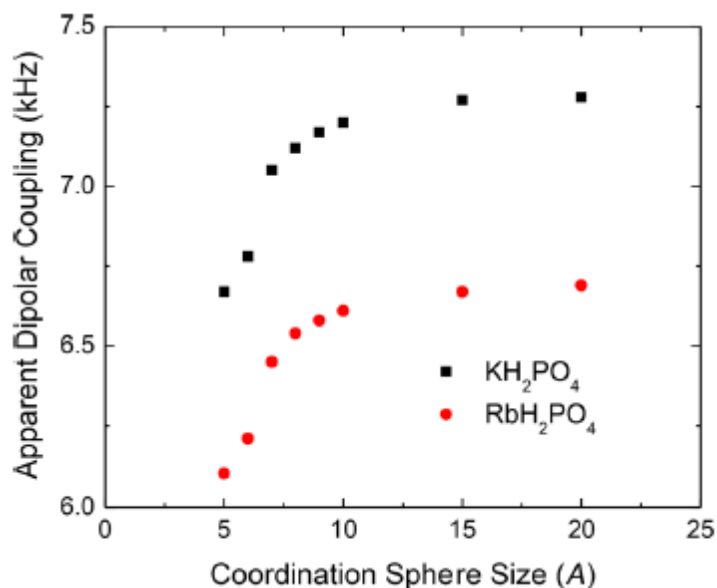


Figure 3. 5. Calculated  $D_{\text{app}}^0$  in tetragonal KDP and RDP as a function of coordination sphere size.

DQ build-up curves were acquired for each of the samples presented in Figure 3.4. These curves were constructed by plotting the normalized intensity of the DQ filtered signal as a function of recoupling time (Chapter 2.2). The experimentally determined apparent dipolar coupling ( $D_{\text{app}}^T$ ) was compared to  $D_{\text{app}}^0$  at each temperature to determine the extent of attenuation relative to the pristine phase.  $D_{\text{app}}^0$  for these materials ranges from 3-8 kHz. Within this range of dipolar coupling the build-up of DQ intensity occurs within 0.1 to 0.3 ms. This sets the timescale over which proton dynamics are expected to be observed. Thus, when the attenuation of the DQ curves is interpreted, the lower limit on the rate of ion hopping is being assessed. At correlation times faster than 100  $\mu\text{s}$  the build-up curves will show attenuation.<sup>14,15</sup> Much slower than this, attenuation is not expected. And right in this range intermediate motional behaviour, similar to the

coalescence point of a standard variable temperature 1D NMR experiment, is expected.<sup>14-16</sup> It is important to note that trends in apparent dipolar coupling, as opposed to individual dipolar coupling constants are being extracted.

### 3.3.3 Calcium Hydroxyapatite: A non-conductive reference

CaHA, a common bio-composite material, is the main component of bones and teeth.<sup>17</sup> The material is used here as a reference to test the suitability of using DQ NMR to quantify apparent proton dipolar coupling in phosphate solid acids. This non-conductive material is chosen as it contains hydrogen-bonded protons and phosphate tetrahedra making it an ideal structural analogue for the materials of interest. At room temperature, CaHA is expected to be in the monoclinic phase which possesses a single proton environment located around 0 ppm (Figure 3.4).<sup>17</sup> The DQ NMR build-up experiment was performed at room temperature on the dehydrated sample yielding a  $D_{\text{app}}^{\text{T}}$  of 2.97 kHz. This differed by 4 % from  $D_{\text{app}}^0$ , calculated using a 15 Å coordination sphere, 3.08 kHz. The difference between  $D_{\text{app}}^{\text{T}}$  and  $D_{\text{app}}^0$  was determined to be within the error of the DQ method. The agreement between  $D_{\text{app}}^{\text{T}}$  and  $D_{\text{app}}^0$  for CaHA demonstrated that symmetry-based recoupling techniques can be used to quantify  $D_{\text{app}}^{\text{T}}$  in complex multi-spin systems.

### 3.3.4 KH<sub>2</sub>PO<sub>4</sub>: A Single Proton Site with Dynamics

DQ NMR was performed on KDP to determine whether  $D_{\text{app}}^{\text{T}}$  could be reliably measured in a dynamic multi-spin system. The conductive nature of KDP (Figure 3.3) suggests that  $D_{\text{app}}^{\text{T}}$  should attenuate with increasing temperature as protons become more mobile. The attenuation of  $D_{\text{app}}^{\text{T}}$  with increasing temperature

is demonstrated in Figure 3.6 where DQ intensity is built up more slowly as sample temperature is increased.

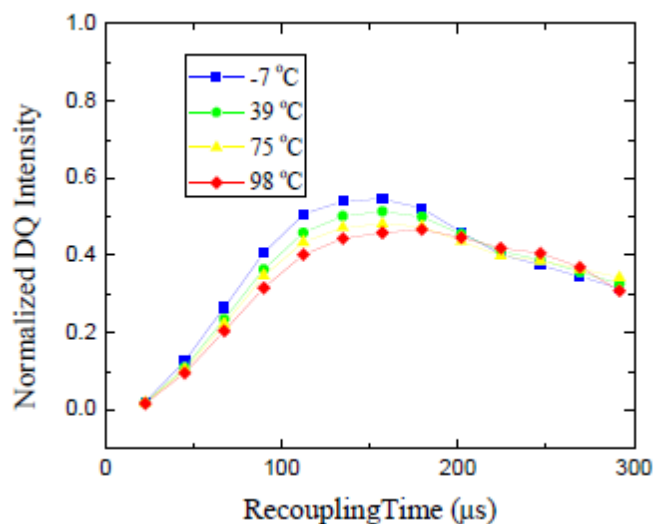


Figure 3. 6. The rate of buildup of DQ intensity as a function of recoupling time in KDP.

At  $-7\text{ }^{\circ}\text{C}$ , the lowest temperature measured by DQ NMR,  $D_{\text{app}}^{\text{T}}$  was  $7.07\text{ kHz}$  which differed from  $D_{\text{app}}^0$  by only  $1.5\%$ . This is within error of the static case and signifies that proton mobility is limited at low temperature. Overall,  $D_{\text{app}}^{\text{T}}$  decreases by  $15\%$  between  $-7$  and  $107\text{ }^{\circ}\text{C}$  (Figure 3.7). However, it is important to note that other factors, in addition to proton dynamics, might impact  $D_{\text{app}}^{\text{T}}$ . Thermally induced unit cell expansion was thought to be the most significant of these factors. In order to account for this, the change in the value of  $D_{\text{app}}^0$  based on the expansion of the unit cell as a function of temperature was considered using coefficients for thermal expansion in tetragonal KDP as provided by Cook.<sup>18</sup> The calculations were performed according to Equation 3.2 where  $dl$  is the calculated change in size,  $L_0$  is the length of the crystallographic dimension as provided by

Nelmes et al.<sup>19</sup> at -146 °C,  $\alpha$  is the coefficient of thermal expansion and  $\Delta T$  is the change in temperature.

$$dl = L_o \alpha \Delta T \quad (3.2)$$

These calculations show that  $D_{\text{app}}^0$  is expected to decrease by 1.25 % over the temperature range that was analyzed by DQ NMR. As  $D_{\text{app}}^T$  decreased by a total of 15 % (Figure 3.7), thermally induced lattice expansion was not determined to contribute significantly to the observed decrease in the apparent dipolar coupling constant. A similar treatment is applied below for the two RDP phases, based on their known unit cell parameters at the temperatures of interest.

Transverse or  $T_2$  relaxation (loss of magnetization in the x-y plane) was verified as a further cross-check into the causes of attenuation of the DQ build-up curves. The  $\Sigma$ MQ data sets (sum of the DQ and ref intensities) for KDP were analyzed. All curves were normalized to the corresponding back-extrapolated zero recoupling time intensity. True  $T_2$  relaxation can be analyzed only when the full pulse sequence has been completed, which for R264<sup>11</sup> corresponds to four rotor periods of recoupling time.<sup>11,20</sup> Comparing the signal intensity from the initial data point and the four rotor period data point shows that the overall decrease in intensity with the oscillations at shorter recoupling times is insignificant as they are the result of higher-order effects caused by an incomplete pulse sequence. Normalized intensities collected at temperatures between -7 and 75 °C were the same within error but at higher temperatures, 91 to 107 °C, normalized intensity decreased with increasing temperature. The Curie effect was thought not to be a significant cause

of  $T_2$  signal decay as Nelmes et al.<sup>19</sup> have reported that tetragonal KDP is paraelectric. These changes were instead interpreted to indicate that a  $T_2$  minimum is being approached in the slow motion regime<sup>11</sup> where system dynamics are slower than both the MAS rate and  $1/D_{\text{app}}^T$ .  $T_1$  effects were minimal as KDP signal intensity did not change significantly as the sample was heated. Further heating (in the absence of sample decomposition) is expected to result in a  $T_2$  minimum beyond which fast limit averaging will be observed.<sup>11</sup>

Having considered both the influence of  $T_2$  relaxation and unit cell expansion on the DQ recoupling build-up curves, it can be concluded that changes in the build-up curves as a function of temperature can be robustly interpreted as changes in local proton dynamics. In particular, the KDP experiment showed that the R264<sup>11</sup> pulse sequence can be used to quantify changes in proton motion in a dynamic, multi-spin system containing a single type of proton environment.

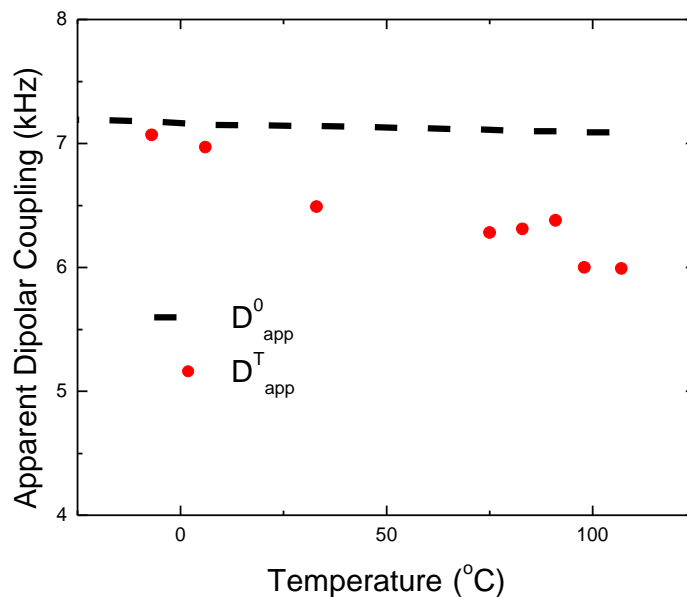


Figure 3. 7.  $D_{app}^T$  in KDP measured between -7 and 107 °C at 7.0 T with 13.7 kHz MAS compared to  $D_{app}^0$ .

### 3.3.4 RbH<sub>2</sub>PO<sub>4</sub>: Two Proton Sites with Dynamics

Room temperature RDP is similar to KDP in the sense that both materials are in the tetragonal phase with a single proton environment (Figure 3.4).<sup>10</sup> As the sample temperature is increased, a second proton environment at 11.7 ppm is observed (Figure 3.8) which is consistent with the beginning of the formation of the monoclinic phase (Figure 3.1).<sup>5,10</sup> Two proton environments in monoclinic RDP have been described in previous studies by the Goward group; a high frequency resonance, which is weakly split at 21.0 T, (14.2 ppm & 13.8 ppm) and a lower frequency resonance at 11.7 ppm (Figure 3.1). These resonances are correlated with specific sites in the crystal lattice.<sup>7</sup> Our chemical shift assignments are based on the previous assignment by Vijayakumar et al.<sup>7</sup> which states that increasing oxygen-oxygen distance results in a lower chemical shift. The resonance at 14 ppm,

labelled site A in Figure 3.8, has an oxygen-oxygen distance of 2.49 Å.<sup>21</sup> Meanwhile, the resonance at 11.7 ppm, labelled site B in Figure 3.8, has an oxygen-oxygen distance of 2.50 Å.<sup>21</sup>

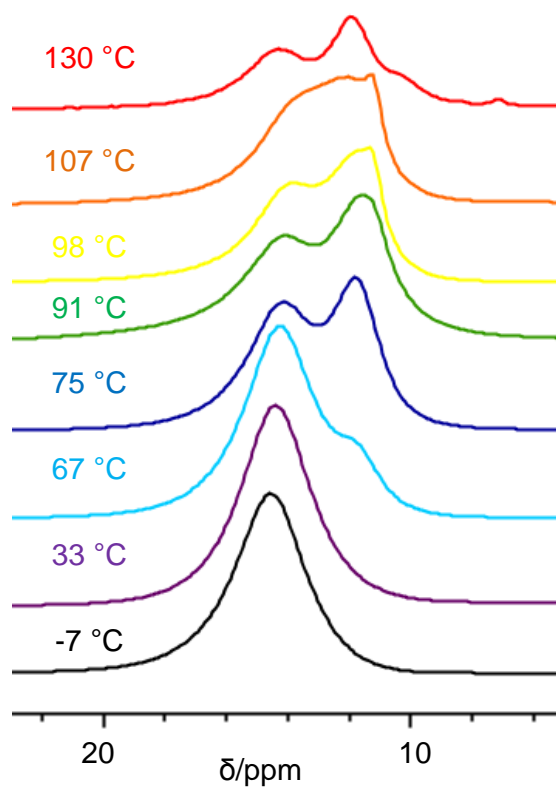


Figure 3. 8. <sup>1</sup>H NMR spectra of RDP acquired between -7 and 130 °C at 7.0 T with 13.7 kHz MAS demonstrating the transition between the tetragonal and monoclinic phases.

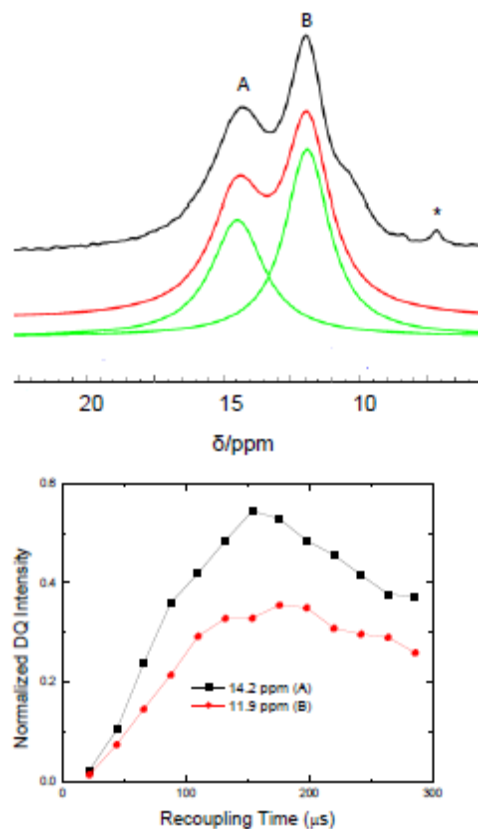


Figure 3. 9. Top:  $^1\text{H}$  NMR spectrum of monoclinic RDP at 7.0 T and 13.7 kHz MAS demonstrating deconvoluted individual peaks. Bottom: DQ build-up curves with fitting at both sites: A at 14.2 ppm and B at 11.7 ppm.

In the present study, the combination of a phase change and a new multi-site phase presented a challenge. The presence of two distinct proton chemical shifts above 76 °C is either indicative of the tetragonal and monoclinic phases being present simultaneously as part of a solid-solid phase transition or the monoclinic phase only, with its two chemically distinct protons. It is also clear in Figure 3.8 that individual proton sites are not well resolved at this field strength, which introduces error in the fitting required to calculate  $D_{\text{app}}^{\text{T}}$  while the sample is undergoing the phase change. For this reason, two distinct samples were created:

one in the tetragonal phase, and a second thermally treated sample in the metastable monoclinic phase. The latter sample was fully converted to the monoclinic phase at 130 °C, as evidenced by PXRD and solid-state NMR (Figure 3.2). The presence of two resolved proton sites in the monoclinic phase presents an opportunity to resolve individual apparent dipolar couplings using DQ NMR. Site-specific resolution in the thermally treated sample results in separate DQ build-up curves (Figure 3.9) allows  $D_{\text{app}}^{\text{T}}$  to be evaluated at each chemically distinct  $^1\text{H}$  site. This is an interesting and potentially useful advantage of the DQ methodology described herein.

Normalized DQ build-up curves were constructed for the 14.2 and 11.7 ppm sites in monoclinic RDP (Figure 3.9). These sites were sufficiently resolved to yield distinct DQ build-up curves allowing  $D_{\text{app}}^{\text{T}}$  to be quantified at each site. The ability to quantitatively determine proton dipolar coupling in tetragonal RDP and both proton environments in monoclinic RDP (Figure 3.9) means that changes in the  $D_{\text{app}}^{\text{T}}$  can be tracked as a function of temperature through the tetragonal to monoclinic phase change (Figure 3.10). Figure 3.10 shows  $D_{\text{app}}^0$  and  $D_{\text{app}}^{\text{T}}$  between -7 and 67 °C for the tetragonal phase, and then between 83 and 107 °C for the monoclinic phase.  $D_{\text{app}}^0$  in RDP differs between the tetragonal and monoclinic phases due to differences in proton-proton distances in the respective crystal structures (Figure 3.10).<sup>21-23</sup> The shortest proton-proton distance in tetragonal RDP is 3.34 Å resulting in a  $D_{\text{app}}^0$  of 6.9 kHz.<sup>22</sup> The shortest proton-proton distances in monoclinic RDP are 3.16 and 4.78 Å at site A and site B respectively resulting in

stronger and weaker dipolar coupling interactions respectively (Figure 3.10).<sup>21</sup>

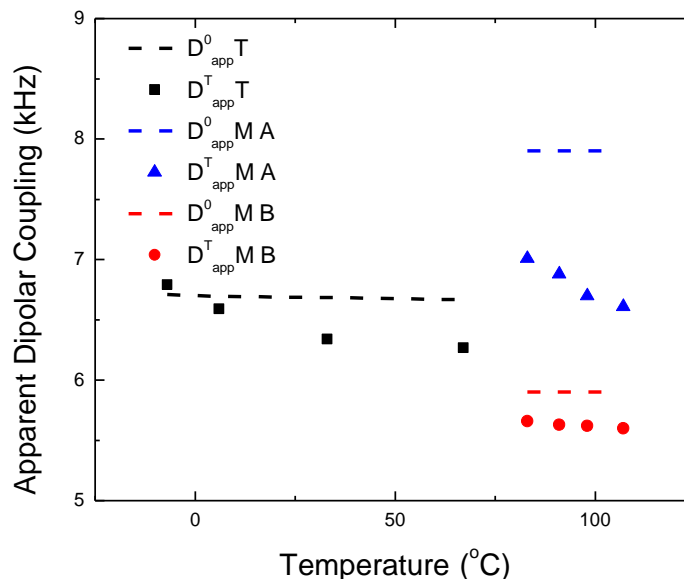


Figure 3. 10.  $D_{app}^T$  in tetragonal (T) and monoclinic (M) RDP calculated from DQ build-up curves resulting from experiments performed at 7.0 T and 13.7 kHz MAS.

The RDP sample is in the tetragonal phase between  $-7$  and  $76$  °C (Figure 3.8). Over this temperature range,  $D_{app}^T$  decreases from 6.8 to 6.3 kHz, corresponding to a difference in maximum correlation time of 150 to 160  $\mu$ s (Figure 3.10). The trend of decreasing  $D_{app}^T$  with increasing temperature in tetragonal RDP is similar to what was observed in tetragonal KDP (Figure 3.7):  $D_{app}^T$  is equivalent to  $D_{app}^0$  within error at low temperature and is then attenuated with increasing temperature as is consistent with increasing proton conductivity.  $D_{app}^T$  decreases by a total of 8 % prior to transitioning to the monoclinic phase (Figure 3.10). This is a greater change in  $D_{app}^T$  than would be expected from thermal expansion alone.

Intriguingly, the two proton sites in the monoclinic phase respond

differently to increasing sample temperature. The attenuation of  $D_{\text{app}}^T$  at the two sites is clearly distinct, with 18% attenuation at the 14.2 ppm site, in contrast with almost negligible attenuation of 3% for the 11.7 ppm site at the highest temperature measured in this study (Figure 3.10). The  $D_{\text{app}}^0$  values can be used to set the upper limit on the associated proton correlation times in monoclinic RDP: of  $\tau_c \leq 200 \mu\text{s}$ . It must be noted, that although apparent proton dipolar coupling is attenuated with increasing temperature, the surprising lack of coalescence excludes the possibility that these sites are in fast exchange with one another. The monoclinic RDP proton sites are separated by 700 Hz. Due to the lack of coalescence, the peak separation, corresponding to a correlation time of  $\tau_c \geq 1400 \mu\text{s}$ , can be taken as the lower limit for the correlation time for proton hopping between the two types of proton environments in this system. As chemical exchange between protons in the 11.7 and 14.2 ppm sites is not detected on the timescale of this experiment, the difference in response at the two proton sites, must be interpreted in another way.

### **3.3.5 Proton Hopping Pathways in $\text{RbH}_2\text{PO}_4$**

Site specific apparent proton dipolar couplings were calculated based on the monoclinic RDP crystal structure. This allows interactions between like- and distinct-sites to be compared with the purpose of determining whether the observed proton dynamics are site-dependent. Like-site and distinct-site apparent dipolar coupling could not be determined directly via NMR without performing multi-dimensional experiments. Nevertheless, values calculated based on the position of individual proton sites in the monoclinic crystal structure<sup>21,23</sup> were used to better

understand the motional relationships between protons in monoclinic RDP. These quantities are summarized in Table 3.1. The phase II variant of the monoclinic structure exists between 44 and 104 °C and is characterized by a doubling along the c-axis (relative to phase I) and disordered hydrogen-bonded protons along the b-axis.<sup>21</sup> The phosphate tetrahedra are connected through a two-dimensional network of hydrogen bonds along the b-c plane.<sup>21</sup> Based on both our own and previous studies of the RDP phases, we anticipate that the relative proton-proton internuclear distances, which dictate the values of  $D_{\text{app}}^0$  at the A and B proton sites, also play an important role in determining the influence of site-specific dynamics on  $D_{\text{app}}^T$ .

Table 3. 1. Site-Specific Apparent Proton Dipolar Coupling Calculated Based on the Crystal Structure of Monoclinic RDP

	<b>Total (kHz)</b>	<b>H<sub>B</sub> (11.7 ppm) (kHz)</b>	<b>H<sub>A1</sub> (13.8 ppm) (kHz)</b>	<b>H<sub>A2</sub> (14.2 ppm) (kHz)</b>
<b>H<sub>B</sub> (11.7 ppm)</b>	5.9	3.33	3.34	3.41
<b>H<sub>A1</sub> (13.8 ppm)</b>	7.9	4.79	1.59	6.08
<b>H<sub>A2</sub> (14.2 ppm)</b>	7.9	4.83	6.08	1.59

\*14.2ppm and 13.8ppm sites are not resolved at 7 T, but are resolved in previous work at 21 T<sup>7</sup>

Table 3.1 shows that site A protons which have resonances of 13.8 and 14.2 ppm at 21.0 T with 25 kHz MAS (which are both found at 14.2 ppm in this work) are more strongly coupled to one another (6.08 kHz) than they are to the 11.7 ppm site B proton (3.8 kHz). The site A protons exist within disordered hydrogen bonds along the b-axis<sup>21</sup> and exhibit partial site occupancy (Figure 3.1).

The 11.7 ppm site corresponds to the site B protons<sup>7</sup> which exist in ordered hydrogen bonds along the c-axis (Figure 3.1).<sup>21</sup> As the  $D_{\text{app}}^0$  values in Table 3.1 describe the static structure only,  $D_{\text{app}}^T$  values (Figure 3.10) were used to interpret the impact of dynamics on the two proton sublattices.

The substantial attenuation of  $D_{\text{app}}^T$  at the 14.2 ppm site suggests that the disordered site A protons are significantly more mobile than the well-ordered site B protons as temperature increases. Proton transport mechanisms have been investigated by both Kim<sup>6</sup> & Vijayakumar,<sup>7</sup> using solid-state NMR strategies. Proton motion via the Grotthuss mechanism can occur through two main pathways in phosphate solid acids: rotation of the phosphate tetrahedra or inter-site proton hopping.<sup>6</sup> In the work of Vijayakumar et al.<sup>7</sup> the interbond proton migration model was used to suggest that site B protons reorient along the c-axis via a two-fold rotation and that site A protons reorient along the b-axis via a three-fold rotation.<sup>7</sup> The three-fold rotation of the site A protons was thought to be more favorable as the oxygen atoms are required to travel a shorter distance. Rotation of the phosphate tetrahedra was observed by Traer et al.<sup>8</sup> in CDP, RDP and KDP but this process was found to occur on the order of milliseconds which is much slower than the dynamics observed here.

Meanwhile, structural data from Magome et al.<sup>21</sup> suggests that the site A protons are optimally positioned to migrate along the b-axis by hopping between disordered hydrogen-bonded sites. Hopping between the disordered A sites is thought to be more favourable than hopping between the B sites as proton-proton

distances are shorter: 3.16 Å relative to 4.78 Å.<sup>21</sup> <sup>17</sup>O NMR experiments performed by Kim et al.<sup>6</sup> showed that proton hopping can occur at temperatures as low as room temperature. It is noted that while proton hopping was described, no site-specific <sup>1</sup>H transport data was reported. Kim et al.<sup>6</sup> found that the rotation of the phosphate tetrahedra was not observed until 147 °C. As this temperature was outside of the scope of this work, the attenuation of  $D_{\text{app}}^T$  that was observed here at site A was attributed to proton hopping between the disordered site A protons themselves (Figure 3.11). Proton hopping was found to be significant enough to cause a 18 % reduction in apparent dipolar coupling constant at site A. A reduction of only 3 % was observed at site B. The lesser influence of proton dynamics on the overall apparent dipolar coupling of site B was attributed to larger proton-proton distances and more ordered hydrogen bonds existing along the c-axis.<sup>21</sup> These structural characteristics were thought to make proton hopping less favourable for site B protons. Differences in the favourability of proton hopping are believed to account for the experimentally observed differences in the extent of attenuation of  $D_{\text{app}}^T$  at the ordered site B protons (11.7 ppm) and the disordered site A protons (14.2 ppm) which was quantified here for the first time.

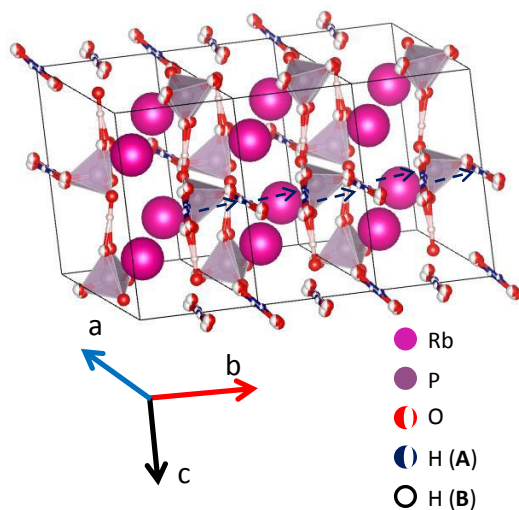


Figure 3. 11. Site A protons (blue and white) hop between disordered hydrogen-bonded sites along the b-axis in phase II monoclinic RDP. The atoms partially occupy two sites and form disordered hydrogen bonds. The adjacent phosphorous tetrahedra exist in two possible orientations creating a disordered network of oxygen (red and white) which the protons are hydrogen bonded to. Proton hopping occurs at the A site and follows the pathway indicated by the blue arrows. This process is facilitated by the disorder of the hydrogen bonded network and the proton-proton internuclear distance. It is noted that the site B protons (white) are bonded to oxygen which exist in one possible orientation resulting in ordered hydrogen bonds along the c-axis. Proton motion was observed at a lesser extent at the B site.

### 3.4 Conclusion

Symmetry-based dipolar recoupling solid-state NMR experiments were used to study site-specific dipolar coupling in several multi-spin systems: no dynamics, one proton environment with dynamics and two proton environments with dynamics. This technique reliably showed increased proton motion via attenuation of  $D_{\text{app}}^T$  in the dynamic systems. More importantly, the use of a site-specific technique for the determination of apparent dipolar coupling was most useful in a multi-site system such as monoclinic RDP as distinct behaviour was

revealed at each proton site. Notably,  $D_{\text{app}}^{\text{T}}$  decreased by 18 % at the 14.2 ppm site and 3 % at the 11.7 ppm site. Connections made to previously published neutron diffraction data<sup>19</sup> allowed the greater decrease in  $D_{\text{app}}^{\text{T}}$  at the 14.2 ppm site to be attributed to proton hopping along the b-axis in phase II monoclinic RDP between the disordered type-A protons for the first time. The distinction of mobility amongst the A and B sublattices would not have been possible without site-specific resolution of proton dipolar coupling that was afforded by the R26<sub>4</sub><sup>11</sup> pulse sequence and the ability to extract apparent proton dipolar couplings directly from the experimental build-up curves.

### 3.5 References

1. Goñi-Urtiaga, A., Presvytes, D. & Scott, K. Solid acids as electrolyte materials for proton exchange membrane (PEM) electrolysis: Review. *Int. J. Hydrogen Energy* **37**, 3358–3372 (2012).
2. Haile, S. M., Chisholm, C. R. I., Sasaki, K., Boysen, D. A. & Uda, T. Solid acid proton conductors: from laboratory curiosities to fuel cell electrolytes. *Faraday Discuss.* **134**, 17–39 (2007).
3. Kim, G., Blanc, F., Hu, Y. Y. & Grey, C. P. Understanding the conduction mechanism of the protonic conductor CsH<sub>2</sub>PO<sub>4</sub> by solid-state NMR spectroscopy. *J. Phys. Chem. C* **117**, 6504–6515 (2013).
4. Vijayakumar, M., Traer, J. W., Britten, J. F. & Goward, G. R. Investigations of the phase transition and proton dynamics in rubidium methane phosphonate studied by solid-state NMR. *J. Phys. Chem. C* **112**, 5221–5231 (2008).
5. Li, Z. & Tang, T. High-temperature thermal behaviors of XH<sub>2</sub>PO<sub>4</sub> (X = Cs, Rb, K, Na) and LiH<sub>2</sub>PO<sub>3</sub>. *Thermochim. Acta* **501**, 59–64 (2010).
6. Kim, G., Griffin, J. M., Blanc, F., Haile, S. M. & Grey, C. P. Characterization of the Dynamics in the Protonic Conductor CsH<sub>2</sub>PO<sub>4</sub> by <sup>17</sup>O Solid-State NMR Spectroscopy and First-Principles Calculations : Correlating Phosphate and Protonic Motion. *J. Am. Chem. Soc.* **137**, 3867–3876 (2015).

7. Vijayakumar, M., Bain, A. D. & Goward, G. R. Investigations of Proton Conduction in the Monoclinic Phase of  $\text{RbH}_2\text{PO}_4$  Using Multinuclear Solid-State NMR. *J. Phys. Chem. C* **113**, 17950–17957 (2009).
8. Traer, J. W., Soo, K. J., Vijayakumar, M. & Goward, G. R. Elucidating the Time Scale and Geometry of Phosphate and Phosphonate Rotation in Solid Acid Electrolytes Using Multinuclear NMR. *J. Phys. Chem. C* **115** 6064–6072 (2011).
9. van Moorsel, G.-J. M. P., van Eck, E. R. H. & Grey, C. P.  $\text{Pr}_2\text{Sn}_2\text{O}$  and  $\text{Sm}_2\text{Sn}_2\text{O}_7$  as High-Temperature Shift Thermometers in Variable Temperature  $^{119}\text{Sn}$  MAS NMR. *J. Magn. Reson.* **113**, 159–163 (1995).
10. Botez, C. E. *et al.* High-temperature crystal structures and chemical modifications in  $\text{RbH}_2\text{PO}_4$ . *J. Phys. Condens. Matter* **21**, 325401 (2009).
11. Saalwächter, K. Proton multiple-quantum NMR for the study of chain dynamics and structural constraints in polymeric soft materials. *Prog. Nucl. Magn. Reson. Spectrosc.* **51**, 1–35 (2007).
12. Haile, S. M., Chisholm, C. R. I., Sasaki, K., Boysen, D. A. & Uda, T. Solid acid proton conductors : from laboratory curiosities to fuel cell electrolytes. *Faraday Discuss.* **134**, 17–39 (2007).
13. Park, J. & Choi, B. Electrical conductivity and impedance characteristics of  $\text{RbH}_2\text{PO}_4$  crystal above room temperature. *Materials Letters* **57**, 2162–2167 (2003).
14. Pileio, G. *et al.* Analytical theory of  $\gamma$ -encoded double-quantum recoupling sequences in solid-state nuclear magnetic resonance. *J. Magn. Reson.* **186**, 65–74 (2007).
15. Saalwächter, K.  $^1\text{H}$  multiple-quantum nuclear magnetic resonance investigations of molecular order in polymer networks. II. Intensity decay and restricted slow dynamics. *J. Chem. Phys.* **120**, 454–464 (2004).
16. Reichert, D. & Saalwächter, K. Dipolar Coupling: Molecular-Level Mobility. in *Encyclopedia of Magnetic Resonance* (2008). doi:10.1002/9780470034590.emrstm1020
17. Pourpoint, F. *et al.* Calcium Phosphates and Hydroxyapatite: Solid-State NMR Experiments and First-Principles Calculations. *Appl. Magn. Reson.* **32**, 435–457 (2007).

18. Cook, W. R. Thermal Expansion of Crystals with  $\text{KH}_2\text{PO}_4$  Structure. *J. Appl. Phys.* **38**, 1637–1642 (1967).
19. Nelmes, R. J., Meyer, G. M. & Tibballs, J. E. The crystal structure of tetragonal  $\text{KH}_2\text{PO}_4$  and  $\text{KD}_2\text{PO}_4$  as a function of temperature. *J. Phys. C Solid State Phys.* **15**, 59–75 (1982).
20. Kristiansen, P. E., Carravetta, M., Lai, W. C. & Levitt, M. H. A robust pulse sequence for the determination of small homonuclear dipolar couplings in magic-angle spinning NMR. *Chem. Phys. Lett.* **390**, 1–7 (2004).
21. Magome, E., Komukae, M. & Machida, M. Neutron Diffraction Study of Ferrielectric Phase Transition in Monoclinic  $\text{RbD}_2\text{PO}_4$ . *J. Phys. Soc. Japan* **76**, 8–13 (2007).
22. Kennedy, N. S. J. & Nelmes, R. J. Structural Studies of  $\text{RbH}_2\text{PO}_4$  in its Paraelectric and Ferroelectric Phases. *J. Phys. C Solid State Phys.* **13**, 4841–4853 (1980).
23. Hagiwara, T., Itoh, K. & Nakamura, E. Structure of Monoclinic Rubidium Dideuterium Phosphate,  $\text{RbD}_2\text{PO}_4$ , in the Intermediate Phase. *Acta Crystallogr.* **40**, 718–720 (1984).

#### **Chapter 4: An Alternate Pathway for Proton Hopping in Monoclinic RbH<sub>2</sub>PO<sub>4</sub>**

This chapter is an extension to the work that was done regarding proton dynamics in monoclinic RbH<sub>2</sub>PO<sub>4</sub> (RDP) which was presented in Chapter 3. Double quantum (DQ) NMR was used to probe site-specific attenuation of proton dipolar coupling at two distinct proton environments: site A protons which exist in a disordered hydrogen-bonded network along the b-axis and site B protons that exist in an ordered hydrogen-bonded network along the c-axis (Figure 3.10, 3.11). Exchange between site A protons was found to be the most favourable dynamic pathway based on the significant attenuation of homonuclear dipolar coupling at this site. However, we are also aware of the possibility of exchange between protons at sites A and B. Therefore, Chapter 4 focuses on confirming the existence of proton exchange between these environments and quantifying the rate of this process.

To this end, <sup>1</sup>H exchange spectroscopy (EXSY) and selective inversion NMR methods were performed to investigate the exchange process in monoclinic RDP. Activation energies for this process were extrapolated based on the rate information obtained from each experimental method. My contributions to this work include performing the <sup>1</sup>H EXSY and selective inversion NMR experiments and processing the resulting data. The CIFIT program (a program written in C for selective inversion fitting)<sup>1</sup>, created and developed by Dr. A. D. Bain, was used in the analyses of the selective inversion data to determine rates of proton exchange.

#### 4.1 Introduction

Both catalyst efficiency and resistance to CO poisoning in proton exchange membrane (PEM) fuel cells can be improved if the average operating temperature of the device is increased to 100-200 °C from the typical 80 °C.<sup>2</sup> Operation within this elevated temperature range is not feasible for most current devices as these utilize Nafion-based membrane electrolyte assemblies (MEAs). Nafion-like polymers must be hydrated in order to achieve the extremely high proton conductivity for which they are renown ( $\sim 1$  S/cm).<sup>3</sup> The enhancement of these devices is therefore dependent on the construction of a MEA that allows for anhydrous proton conduction.<sup>3</sup>

Phosphate solid acids are a class of solid-state materials that conduct protons anhydrously and could potentially be used to construct a MEA for use in intermediate temperature fuel cells. In this vein, Haile et al.<sup>4</sup> created a working laboratory-scale fuel cell using a  $\text{CsH}_2\text{PO}_4$  (CDP)-based MEA. CDP becomes an excellent proton conductor ( $\sim 10^{-2}$  S/cm) around 234 °C when the material undergoes a phase transition from the monoclinic phase to the cubic phase.<sup>4-6</sup> This increase in proton conductivity is a result of cubic phase CDP being a superprotonic conductor. Superprotonic phases are extremely good proton conductors and are characterized by increased disorder in the hydrogen-bonded network that surrounds the phosphate tetrahedra.<sup>4,6,7</sup> The increase in hydrogen bond disorder tends to facilitate proton transport via the Grotthuss mechanism in these materials.<sup>8</sup> RDP, a phosphate solid acid with phase transitions that are analogous to those observed in

CDP, has been identified as another potential proton-conducting material for use in anhydrous PEM fuel cells.

Tetragonal RDP, the room temperature phase, undergoes a quasi-reversible phase transition to the monoclinic phase between 80 and 120 °C.<sup>5,8-10</sup> It is anticipated that the subsequent transition to the cubic phase, occurring around 273 °C, will result in a superprotonic material analogous to that which has been observed for CDP.<sup>4,5,11</sup> However, there has been significant debate regarding the stability of the reported cubic phase with some researchers stating that the transition to the cubic phase is a decomposition event instead of a true phase transition.<sup>5,11</sup> With this in mind, we have decided to focus our study of proton dynamics in RDP on the monoclinic phase. The monoclinic phase has the advantage of being stable between 130 and 270 °C and meta-stable at the lower temperatures that make up our NMR-accessible experimental temperature range. Additionally, the ability to resolve two distinct proton environments (Figure 3.9) allows for the characterization and quantification of multiple potential dynamic pathways. These proton sites, with chemical shifts of 14.2 and 11.7 ppm respectively, are labelled A and B (Figure 4.1).

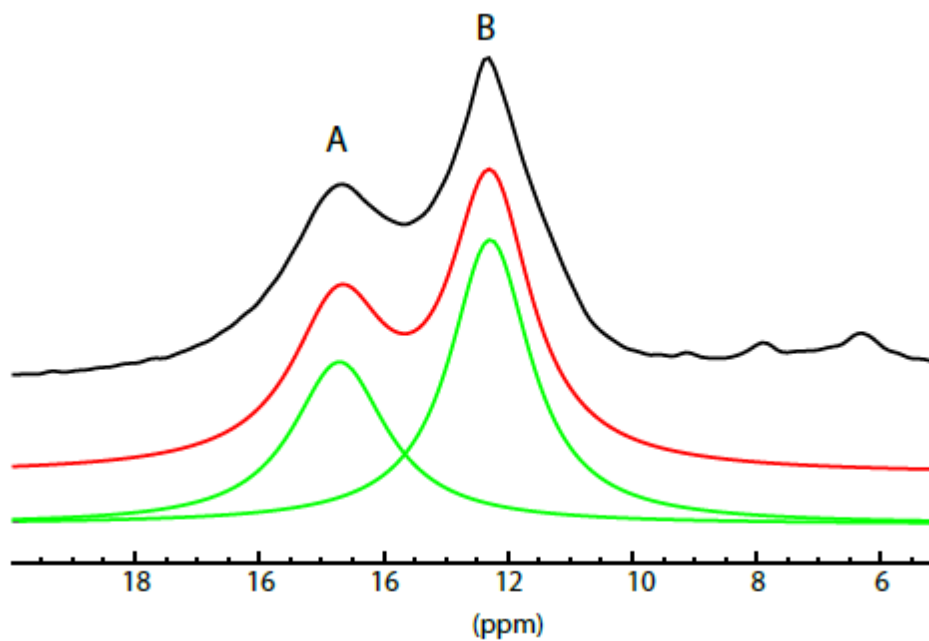


Figure 4. 1.  $^1\text{H}$  NMR of monoclinic RDP acquired at 7.0 T with 13.7 kHz MAS.

We have previously investigated proton dynamics in monoclinic RDP via solid-state NMR using symmetry-based DQ techniques to extract site-specific apparent dipolar couplings for both proton sites (Chapter 3).<sup>12-14</sup> It was found that site A to site A proton hopping is the preferred pathway for proton transport in monoclinic RDP.<sup>12</sup> The preference of site A to site A proton hopping over site A to site B proton hopping was attributed to site A protons occupying relatively disordered sites in the crystal lattice.<sup>12,15</sup> However, we anticipate that site A to site B proton hopping is still likely to occur in monoclinic RDP. This assumption is based on a two-dimensional (2D) DQ NMR correlation study performed by Vijayakumar et al.<sup>14</sup> where cross-peaks indicate that site A protons are correlated to both site A and site B protons through dipolar coupling interactions.

It is therefore reasonable to assume that site A and site B protons are in exchange with one another. However, our previous DQ NMR study imposed certain limits on the timescale on which proton exchange between these sites can occur. Firstly, peaks corresponding to these sites did not coalesce over the -7 to 107 °C temperature range used in these experiments.<sup>12</sup> These peaks were separated by 700 Hz which sets the minimum correlation time for this motion to 0.0014 s. Secondly, proton exchange between site A and site B must occur on a slower timescale than the dominant proton motion: hopping between site A protons. An exact correlation time for this motion was not obtained in our previous study as apparent dipolar coupling is a measure of the overall proton mobility at a given site and is not diagnostic of specific transport mechanisms.<sup>16</sup> In this work, proton exchange between site A and site B will be identified and quantified using <sup>1</sup>H EXSY and selective inversion NMR methods. It is expected that kinetic parameters describing this process, exchange rate and activation energy, will be obtained.

## **4.2 Experimental**

### **4.2.1 Sample Preparation**

RDP was prepared, as described by Boysen et al.<sup>17</sup>, by dissolving stoichiometric quantities of phosphoric acid and rubidium carbonate in minimal amounts of deionized water. The product was precipitated by the addition of methanol. This synthesis method yields tetragonal RDP at room temperature. The tetragonal sample was converted to the monoclinic phase by overnight heating at 130 °C in air.

#### 4.2.2 Electrical Impedance Spectroscopy

RDP pellets with a diameter of 14 mm and a width of 1-2 mm were uniaxially pressed at 5000 psi for a total of 15 minutes. The resultant pellets were sintered overnight at 130 °C and were gold coated for one minute on each side prior to use. Conductivity measurements were performed using a two-electrode cell. All measurements were taken inside an oven where the assembly was equilibrated at the desired temperatures for one hour. All experiments were performed using a Gamry 1000 potentiostat where the frequency was varied between 100000 and 10 Hz.

#### 4.2.3 Solid State NMR

All <sup>1</sup>H EXSY and selective inversion experiments were performed on a Bruker Advance 7.0 T wide-bore spectrometer using a 4 mm double-resonance probe. Spectra were referenced to adamantane (1.63 ppm) for a 4 μs π/2 pulse at 40 W. A 4 μs 40 W π/2 pulse was used to perform the EXSY experiments. Spectra were collected with a 10 s recycle delay. Mixing time was varied between 0.0001 and 0.5 s. The selective inversion experiments were comprised of a long, low power selective pulse and a non-selective π/2 pulse. The pulse length and transmitter frequency for the selective pulse were calibrated based on the site that was being inverted. The non-selective π/2 pulse was calibrated to 4 μs at 40 W. Mixing time was varied between 0.0001 and 9.0 s. Both EXSY and selective inversion experiments were performed at temperatures within the -7 to 107 °C range that was accessible with our experimental setup. All temperatures were calibrated based on

the response of a mixture of  $\text{Sm}_2\text{Sn}_2\text{O}_7$  and  $\text{SnO}_2$  to probe heating under MAS conditions.<sup>18</sup> Temperature calibrations were accurate to  $\pm 5$  °C.

#### 4.3 Results

At 7.0 T, the  $^1\text{H}$  spectrum of monoclinic RDP is comprised of two signals. The signal at 14.2 ppm corresponds to site A and a second signal at 11.7 ppm corresponds to site B (Figure 4.1). These signals were assigned to specific proton environments within the monoclinic crystal structure based on the effects of increasing oxygen-oxygen bond distance on proton chemical shift (Figure 4.2).<sup>14</sup> Site A protons lie along the b-axis where O-HA $\cdots$ O distance is 2.49 Å and site B protons lie along the c-axis where O-HB $\cdots$ O distance is 2.50 Å.<sup>15</sup>

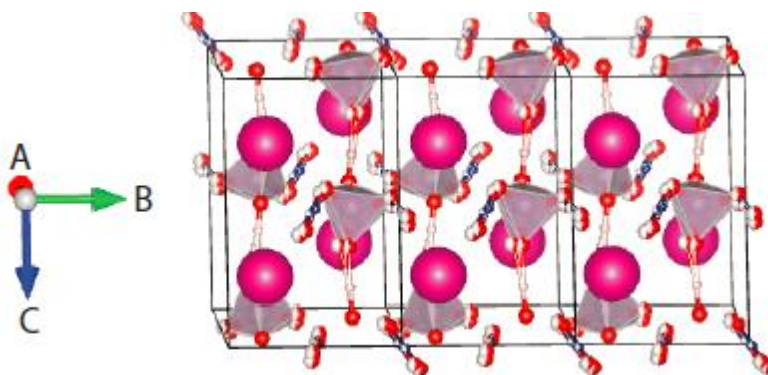


Figure 4. 2. Crystal structure of monoclinic RDP illustrating the b- and c-axis.

##### 4.3.1 Proton EXSY in Monoclinic $\text{RbH}_2\text{PO}_4$

$^1\text{H}$  EXSY experiments were performed on monoclinic RDP at four temperatures: 80, 85, 90 and 95 °C. Eleven different mixing times were chosen over a timescale spanning 0.0001 to 0.5 s. The experimental timescale was chosen such that it was significantly shorter than  $T_1$  (spin-lattice relaxation) for monoclinic RDP ( $\sim 4$  s) in order to minimize the impact of  $T_1$  on the measured exchange rate.<sup>19,20</sup> Cross-peaks were observed at each temperature and at all mixing times confirming

that proton hopping between site A and site B is a viable pathway for proton exchange in monoclinic RDP (Figure 4.3).

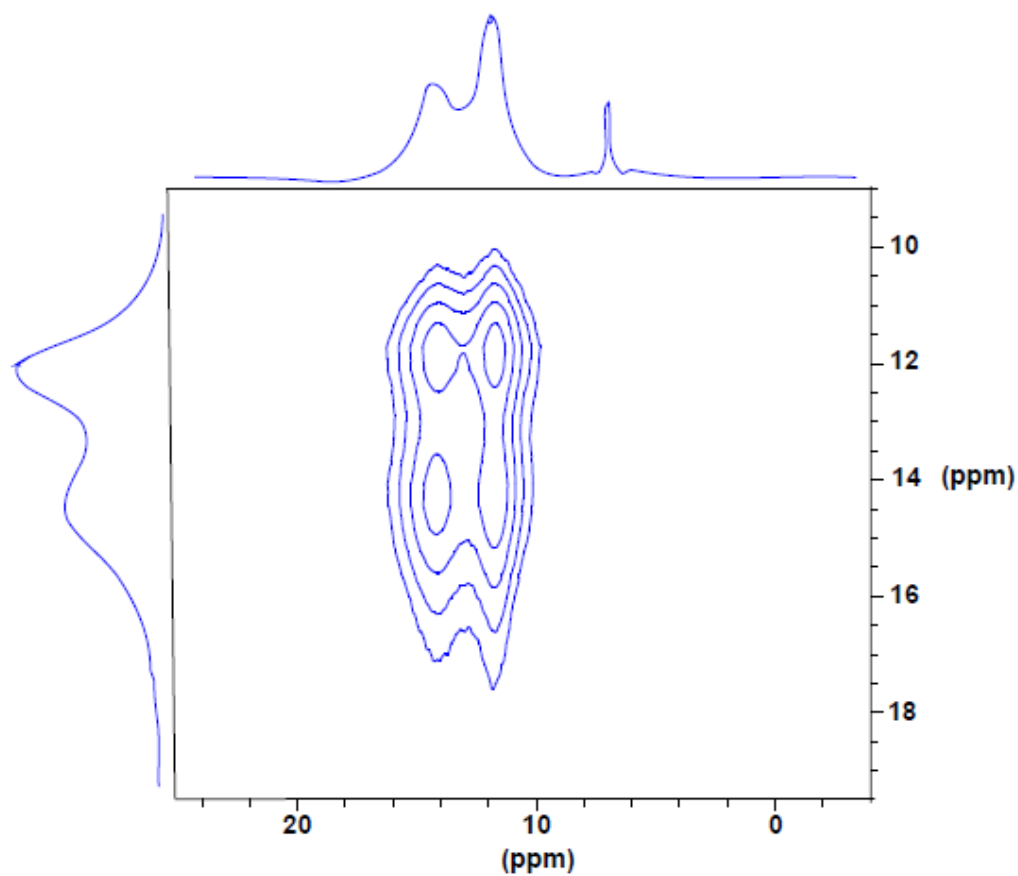


Figure 4. 3.  $^1\text{H}$  EXSY of monoclinic RDP acquired at 7.0 T with 15 kHz MAS. The EXSY mixing time was 0.01 s. Sample temperature was 95 °C.

Exchange between site A and site B was evaluated based on the relative intensities of the crosspeaks. This was done by integrating the crosspeaks and the diagonal peaks and then normalizing the integrated area of the crosspeaks relative to the area of the diagonal peaks. Normalized intensities were plotted as a function of mixing time (Figure 4.4). The resultant build-up curves were fit using a first-

order exponential decay function (Equation 4.1) to extract the rate of exchange at each temperature (Figure 4.5).

$$y = y_0 + Ae^{-x/t} \quad (4.1)$$

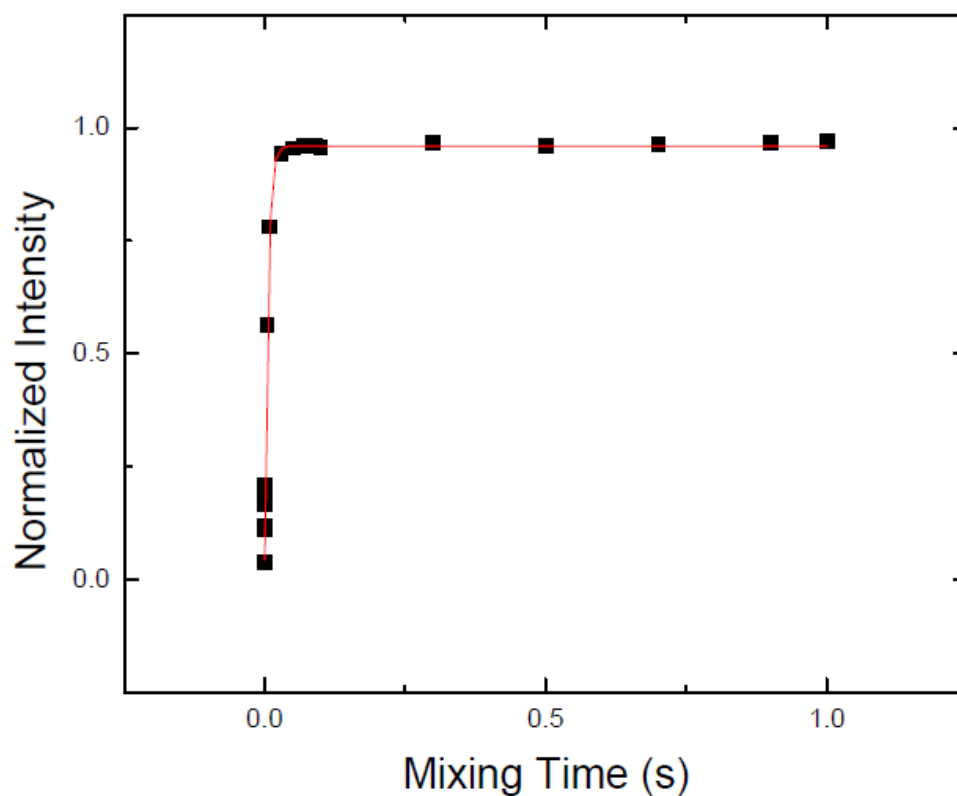


Figure 4. 4. Normalized integrated crosspeak intensity for a monoclinic RDP sample analyzed at 95 °C and plotted as a function of mixing time. The EXSY build-up curve was fit using a first-order exponential decay function.  $^1\text{H}$  spectra were acquired at 7.0 T with 15 kHz MAS.

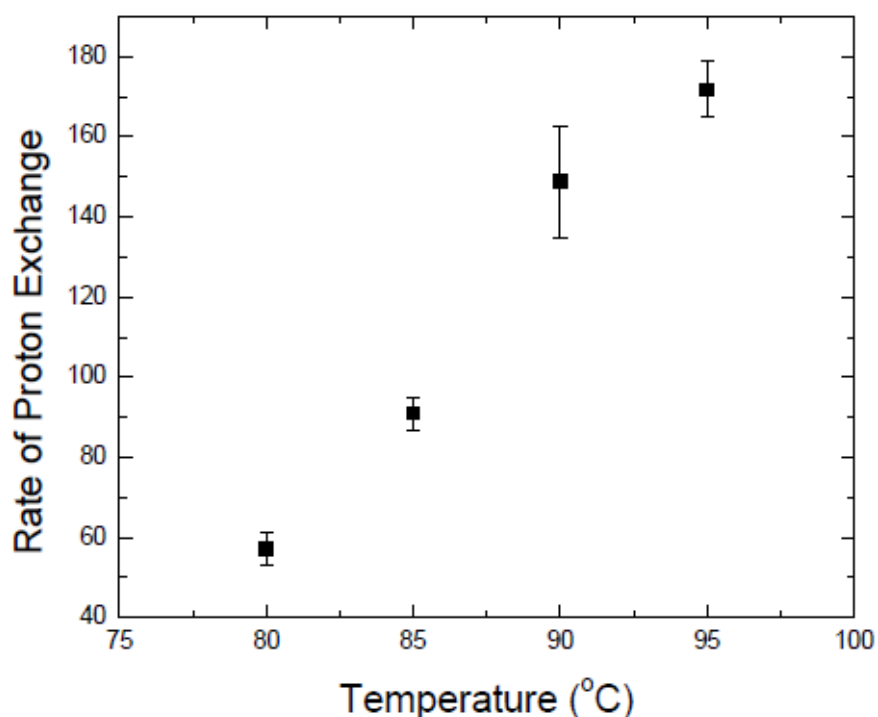


Figure 4. 5. Rate of proton exchange between site A and site B in monoclinic RDP determined via  $^1\text{H}$  EXSY from 80 to 95 °C plotted as a function of sample temperature.  $^1\text{H}$  EXSY spectra were acquired at 7.0 T with 15 kHz MAS.

As shown in Figure 4.5, the rate of proton exchange increased with temperature.<sup>11,12</sup> The rate of proton exchange between site A and site B in monoclinic RDP increased from  $57\text{ s}^{-1}$  at 80 °C to  $172\text{ s}^{-1}$  at 95 °C. Measured rates of proton exchange were used to calculate an activation energy of  $0.72 \pm 0.09\text{ eV}$  for site A to site B proton exchange (Figure 4.6). The experimentally determined activation energy agrees, within error, with the activation energy determined by Boysen et al. via electrochemical impedance spectroscopy (EIS):  $0.77 \pm 0.03\text{ eV}$ .<sup>17</sup> Differences between these activation energies can be attributed to the fact that EIS

measures bulk proton conductivity across a material and EXSY measures site-specific exchange.

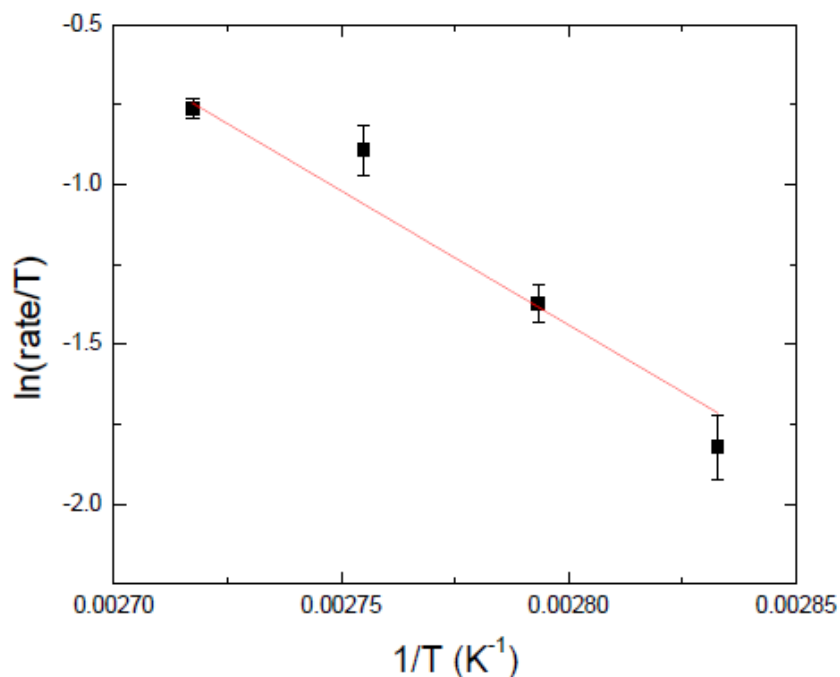


Figure 4. 6. Eyring plot of the rate of A-B proton exchange in monoclinic RDP between 80 and 95 °C. Rates of proton exchange were determined from  $^1\text{H}$  EXSY spectra acquired at 7.0 T with 15 kHz MAS.

#### 4.3.2 Proton Selective Inversion in Monoclinic $\text{RbH}_2\text{PO}_4$

Selective inversion experiments were performed on monoclinic RDP at temperatures between 0 and 107 °C. Site B was inverted for most of these experiments. However, the inversion of site A and the partial inversion of the site B were performed at one low, one intermediate and one high temperature to verify the reproducibility of the selective inversion experiment. Figure 4.7 shows a collection of representative spectra of each type of selective inversion experiment performed at 91 °C.

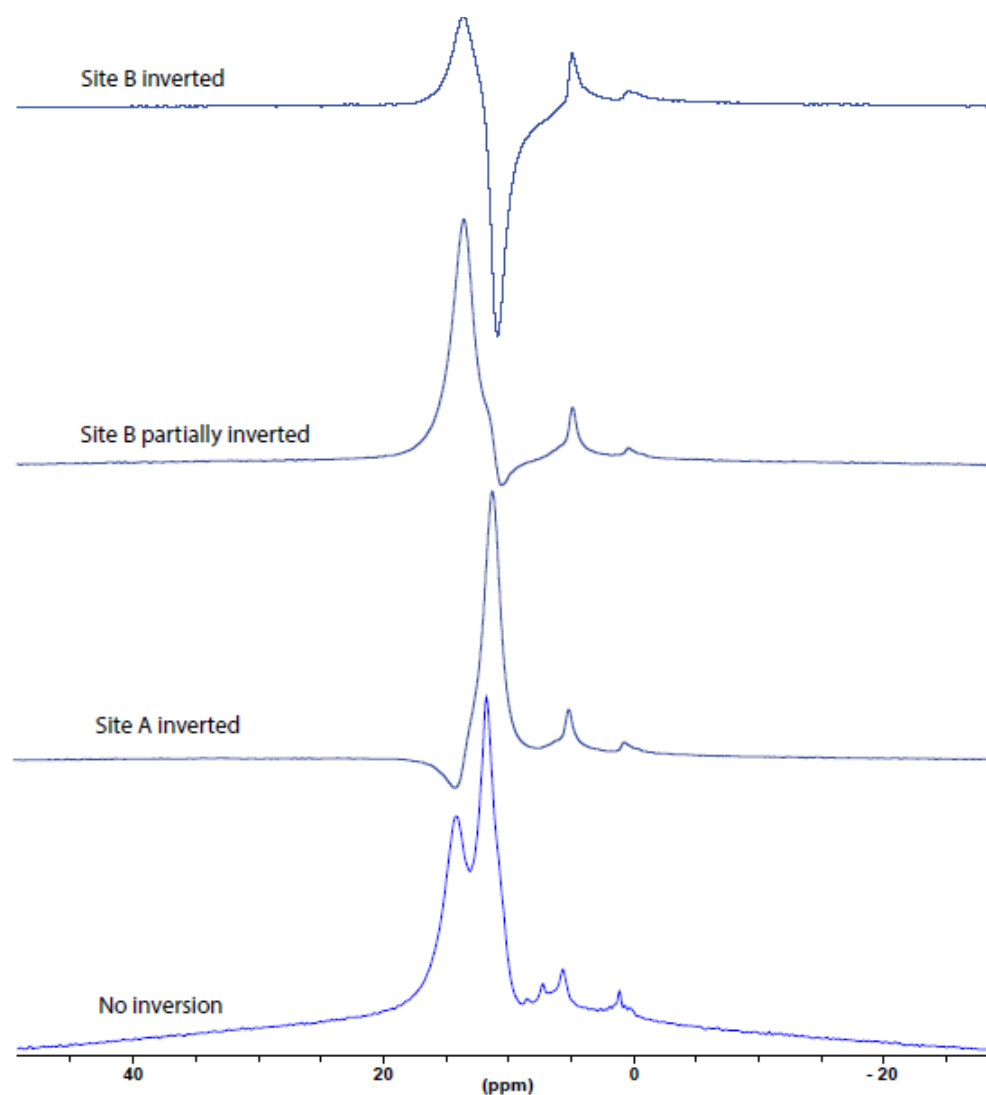


Figure 4. 7. Three conditions of site-selective inversion in monoclinic RDP performed at 7.0 T with 15 kHz MAS.

Site A and site B peaks were integrated via two methods: individual peak fitting (Figure 4.8 A, C, E) and “block” integration (Figure 4.8 B, D). Individual peak fitting involves deconvoluting the lineshape into peaks and then integrating each peak. “Block integration” involves integrating everything between two points on the chemical shift axis. Two integration methods were used to better account for

the errors that arise in selectively inverting one site and integrating peaks in a system that does not have baseline resolution of all sites.

Peak areas from both sites were normalized relative to the intensity of the fully relaxed system. The area of the non-inverted site was plotted as a function of mixing time (Figure 4.8). The transient well observed in Figure 4.8 indicates that inverting site B impacts the intensity of site A, which demonstrates that proton exchange occurs between site A and site B.<sup>21</sup> A summary of each integration and peak fitting method is provided in Table 4.1. Transient well depth and shape were analyzed using the CIFIT program where both proton exchange between site A and site B and  $T_1$  relaxation are considered to interpret the resultant spectral intensities.<sup>22</sup> The CIFIT program uses experimental data to fit the transient well and determine the rate of proton exchange under a given set of experimental parameters. In order to accurately account for  $T_1$  relaxation,  $T_1$  values for monoclinic RDP were determined separately using a non-selective inversion experiment (Chapter 2, Figure 2.13).  $T_1$  values were  $4.0 \pm 0.1$  s for site A and  $4.6 \pm 0.1$  s for site B. Relaxation is anticipated to be faster at site A due to stronger proton-proton dipolar coupling interactions.  $T_1$  relaxation is proportional to the square of the magnitude of the dipolar coupling interaction as this interaction provides a pathway through which energy can be transferred between the lattice and the spins.<sup>23</sup>

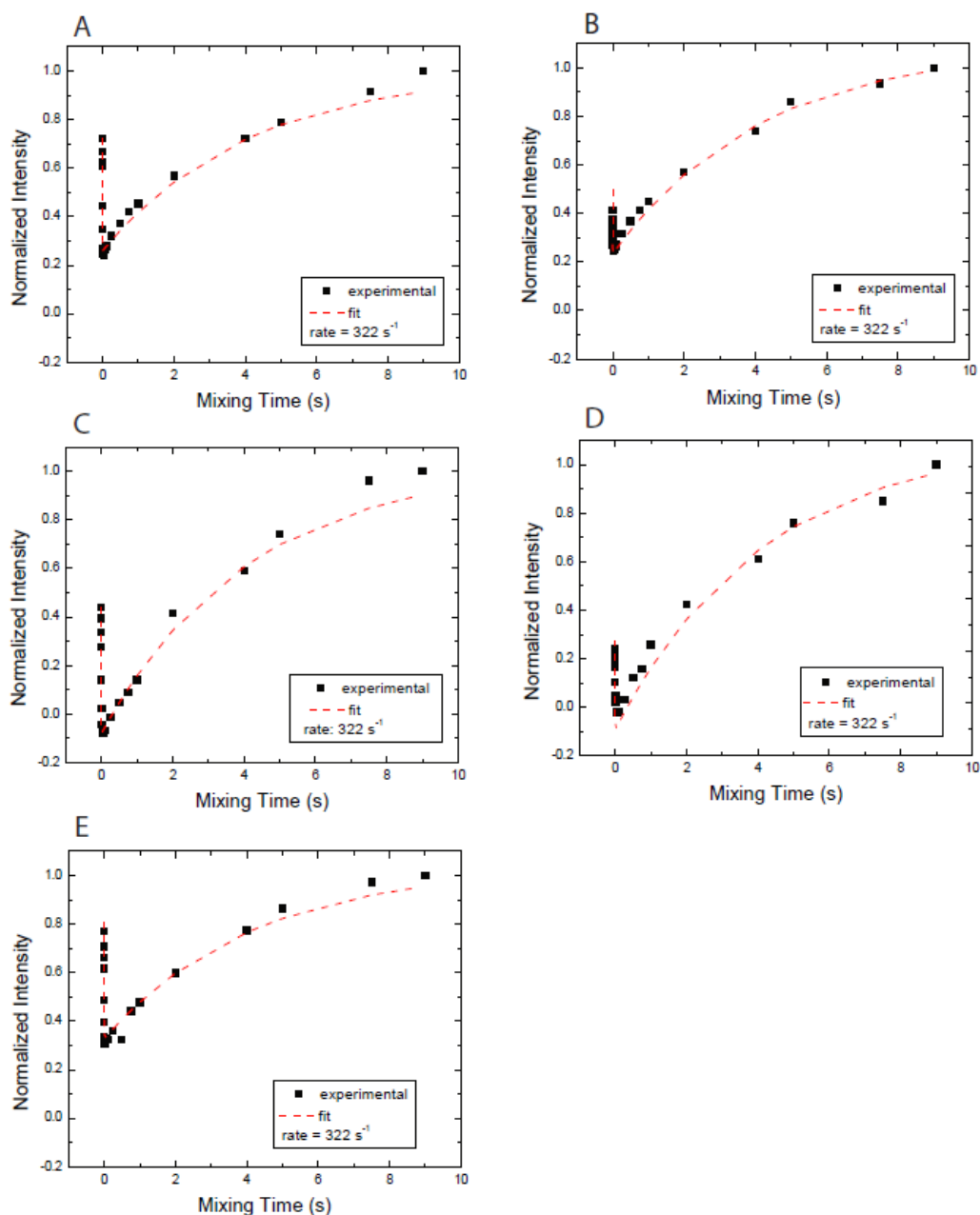


Figure 4. 8. Normalized intensity of the non-inverted peak (experimental) and the CIFIT model (fit) as a function of mixing time for three different inversion methods: invert site A (A, B), invert site B (C, D), partially invert site B (E). All selective inversion experiments were performed at  $91 \text{ }^\circ\text{C}$  at 7.0 T with 15 kHz MAS.

Table 4. 1. Rates of Proton Exchange and Activation Energy Obtained via Variations on the Selective Inversion Experiment.

Experiment	Figure 4.8 Curve	Rates at...			Activation Energy (eV)
		20 °C	52 °C	91 °C	
Site A inverted, peak integration	A	1.8	13	322	$0.7 \pm 0.1$
Site A inverted, block integration	B	1.8	12	322	$0.66 \pm 0.09$
Site B inverted, peak integration	C	3.0	14	322	$0.6 \pm 0.1^*$
Site B inverted, block integration	D	1.8	13	322	$0.66 \pm 0.06$
Site B partially-inverted, peak integration	E	1.6	12	322	$0.67 \pm 0.09$

\*Activation energy is calculated based on three data points only

Similar rates of proton exchange could reliably be obtained using all three inversion conditions and both integration methods (Figure 4.8). The only exception to this was block integration of the spectra acquired via partial inversion of site B (not shown), where the CIFIT-derived model did not converge with the experimental data. The lack of convergence of these data sets was attributed to ambiguity of selecting integration ranges for the partially inverted spectra. As the experimentally determined rates of proton exchange were deemed to be reproducible, these quantities were used to calculate activation energy for proton exchange between site A and site B using an Eyring plot (Figure 4.9). The activation energy for this process was calculated to be  $0.56 \pm 0.03$  eV based on eleven data points acquired by inverting site B (Figure 4.9). Similar rates of proton

exchange and activation energies were obtained under all three inversion conditions and both peak integration methods (Table 4.1).

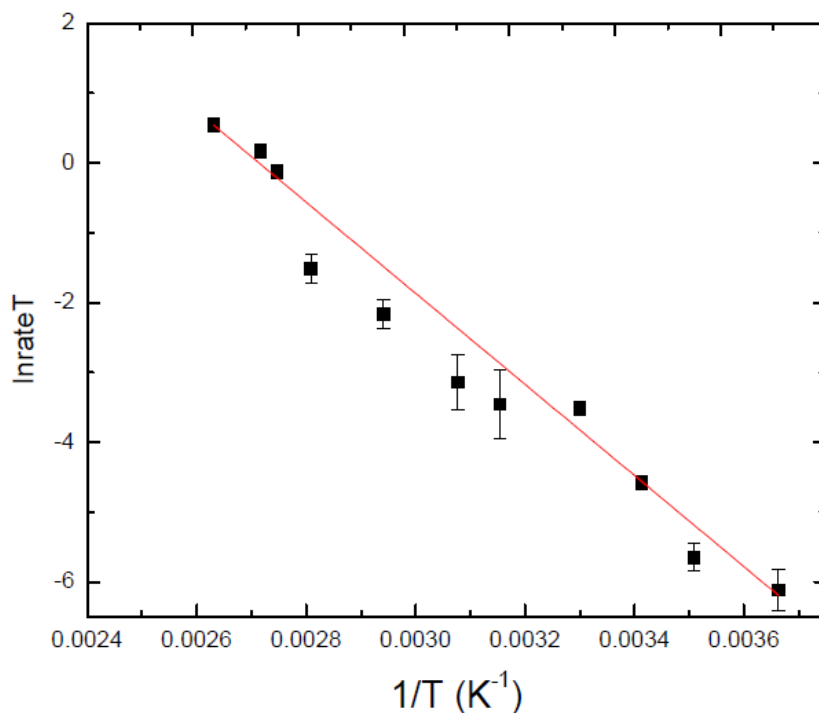


Figure 4. 9. Eyring plot for the determination of activation energy for proton exchange between A and B sites in monoclinic RDP. All spectra were collected by inverting site B at 7.0 T with 15 kHz MAS.

#### 4.3.3 Proton Conductivity in Monoclinic RDP

In addition to the NMR experiments presented above, activation energy for proton exchange between sites A and B in monoclinic RDP was also investigated using EIS (Figure 4.10). An Arrhenius plot was constructed based on proton conductivity measured as a function of temperature (Figure 4.10). The calculated activation energy was  $0.85 \pm 0.05$  eV which agrees within error with the activation energy for proton transport in monoclinic RDP that was measured by Boysen et al.<sup>17</sup>:  $0.77 \pm 0.03$  eV. Unlike the solid-state NMR experiments presented above, EIS

measures bulk proton conductivity, thus the reported activation energy is representative of all contributions to long-range proton motion in monoclinic RDP and is not selective for proton hopping between site A and site B.<sup>24</sup>

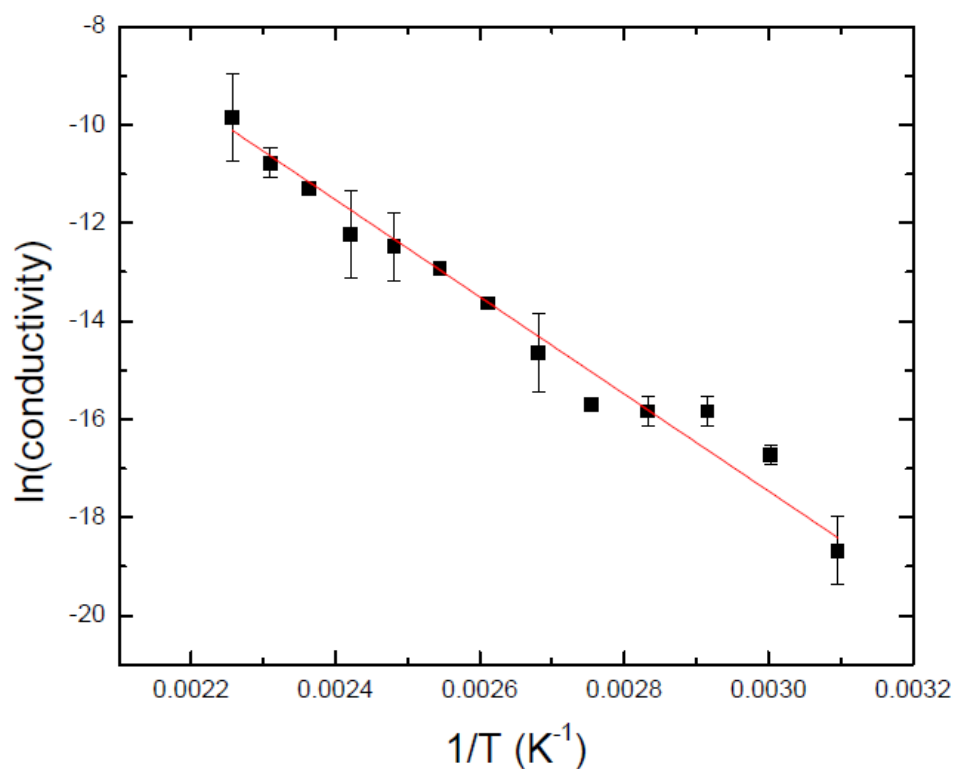


Figure 4. 10. Arrhenius plot for the determination of activation energy of proton transport in monoclinic RDP constructed based on EIS proton conductivity measurements.

#### 4.4 Discussion

The activation energy for proton exchange between site A and site B in monoclinic RDP was determined experimentally using three different techniques: EIS, <sup>1</sup>H EXSY and <sup>1</sup>H selective inversion (Table 4.2).

Table 4. 2. Activation Energy for Proton Exchange in Monoclinic RDP

Experiment	Activation Energy (eV)
EIS	$0.85 \pm 0.05$
$^1\text{H}$ EXSY	$0.72 \pm 0.09$
$^1\text{H}$ Selective Inversion	$0.56 \pm 0.03$

Activation energies for proton exchange between site A and site B in monoclinic RDP as calculated based on EIS and  $^1\text{H}$  EXSY experiments agree within error (Table 4.2). However, the activation energy that was calculated based on the  $^1\text{H}$  selective inversion experiments is much lower. The nature of each type of experiment is considered to evaluate which experimentally determined activation energy best represents proton exchange between site A and site B in monoclinic RDP.

EIS is a technique that measures the total proton conductivity across a sample. Therefore, proton conductivities measured via EIS include contributions from all processes that are involved in moving protons from one side to the other.<sup>24</sup> This means that the activation energy that was calculated from the EIS data is in no way selective for proton exchange between site A and site B. Other processes that may contribute to the observed activation energy include: proton exchange between A sites (previously characterized via DQ NMR in Chapter 3)<sup>12</sup> and grain boundary effects.<sup>25,26</sup> Since the b-axis, along which proton exchange between A site protons occurs, is more disordered than the c-axis, along which site B protons are found, it is likely that the activation energy of proton exchange between A sites is lower than the activation energy of proton exchange between site A and site B.<sup>10,15</sup> This is because systems with disordered hydrogen-bonded networks tend to have lower

activation energies for proton exchange than well-ordered systems do.<sup>4,6</sup> However, grain boundary effects are known to increase the activation energy for proton conduction in solid materials.<sup>25,26</sup> Positive charges tend to get stuck in the grain boundary cores resulting in layers that are devoid of protons.<sup>25</sup> The lack of protons results in decreased proton mobility across the grain boundaries relative to the bulk, thereby increasing activation energy for proton transport in the material.

Both the <sup>1</sup>H EXSY and selective inversion NMR experiments are selective for proton exchange between site A and site B. Therefore, considerations for competing proton transport processes are not as relevant when comparing data from these two NMR methods. It can however be argued that the selective inversion experiment quantifies proton exchange more accurately. The EXSY experiment is a reliable method to establish that proton exchange occurs.<sup>20</sup> However, since the pulse sequence in the EXSY experiment is the same as the one in the nuclear Overhauser effect spectroscopy (NOESY) experiment, the chemical exchange process competes with the nuclear Overhauser effect.<sup>20</sup> The nuclear Overhauser effect arises from through-space interactions between proximal nuclei. This is a concern in monoclinic RDP since the magnitude of the homonuclear dipolar coupling constants between protons at site A and site B are between 3 and 4 kHz.<sup>12,20</sup> Additionally, 2D integration is generally more challenging to perform than one dimensional (1D) integration.<sup>20</sup> This means that signal intensities at each site, upon which our calculations are based, tend to be more accurately measured in the selective inversion experiments as opposed to the EXSY experiments. It was

therefore determined that the activation energy for proton exchange between the A and B sites in monoclinic RDP is most accurately represented by the selective inversion method,  $0.56 \pm 0.03$  eV.

In addition to the above experimental considerations, properties of the RDP samples that were used for the EIS, EXSY and selective inversion experiments and their potential effects on the measured activation energies must be evaluated. The RDP samples that were used for the EIS and EXSY experiments started out in the room-temperature tetragonal phase and were heated, over the course of the EIS and EXSY experiments, to yield the monoclinic phase. However, for the selective inversion experiments, the sample was converted to the metastable monoclinic phase via pre-heating. Lineshape analysis of the sample that was used in the selective inversion experiments confirms that the sample stayed in the monoclinic phase while this work was performed.

These differences in sample preparation may contribute to differences in the experimentally determined activation energies. Activation energies as determined by EIS and EXSY were  $0.85 \pm 0.05$  eV and  $0.72 \pm 0.09$  eV respectively. These are higher than the activation energy as determined by selective inversion,  $0.56 \pm 0.03$  eV. It is anticipated that some of the data points collected via EIS (50 to 180 °C) are representative of the tetragonal phase and the transition between the tetragonal and monoclinic phases. EXSY data was collected between 80 and 90 °C and could include some data points that are representative of the transition between tetragonal and monoclinic phases. It can therefore be proposed that proton

conduction is less favourable in tetragonal RDP resulting in higher activation energies for proton transport. This theory is supported by the data presented in Chapter 3 of this thesis where Figure 3.10 shows a lesser attenuation in dipolar coupling constant in the tetragonal RDP than in monoclinic RDP.

#### 4.5 Conclusions

Proton exchange between site A and site B in monoclinic RDP was investigated using  $^1\text{H}$  EXSY and selective inversion methods. It was confirmed that proton exchange does occur between the disordered site A and the well-ordered site B. This process was quantified by determining the rate of proton exchange and the activation energy for the process. The proton exchange data acquired via selective inversion was deemed to best represent the kinetics of this process, with an activation energy of  $0.56 \pm 0.03$  eV, as this method probed the fewest competing processes. This work demonstrates that multiple pathways for proton transport exist in RDP. As both A to A and A to B proton exchange readily occurs in monoclinic RDP, it can be assumed that both pathways would contribute to proton conduction in the intermediate temperature range. Despite having lower overall proton conductivity than superprotonic CDP or fully hydrated Nafion, monoclinic RDP would be an ideal proton conductor in the 100 to 200 °C temperature range as adequate conductivity can be achieved in the absence of hydration or a phase change.

#### 4.6 References

1. Bain, A. D. & Cramer, J. A. Slow Chemical Exchange in an Eight-Coordinated Bicentered Ruthenium Complex Studied by One-Dimensional Methods . Data Fitting and Error Analysis. *J. Magn. Reson. Ser. A* **118**, 21–

27 (1996).

2. Carrette, L., Friedrich, K. A. & Stimming, U. Fuel Cells : Principles , Types , Fuels , and Applications. *ChemPhysChem* **1**, 162–193 (2000).
3. Goñi-Urtiaga, A., Presvytes, D. & Scott, K. Solid acids as electrolyte materials for proton exchange membrane (PEM) electrolysis: Review. *Int. J. Hydrogen Energy* **37**, 3358–3372 (2012).
4. Haile, S. M., Chisholm, C. R. I., Sasaki, K., Boysen, D. A. & Uda, T. Solid acid proton conductors: from laboratory curiosities to fuel cell electrolytes. *Faraday Discuss.* **134**, 17–39 (2007).
5. Li, Z. & Tang, T. High-temperature thermal behaviors of  $\text{XH}_2\text{PO}_4$  (X = Cs, Rb, K, Na) and  $\text{LiH}_2\text{PO}_3$ . *Thermochim. Acta* **501**, 59–64 (2010).
6. Kim, G., Blanc, F., Hu, Y. Y. & Grey, C. P. Understanding the conduction mechanism of the protonic conductor  $\text{CsH}_2\text{PO}_4$  by solid-state NMR spectroscopy. *J. Phys. Chem. C* **117**, 6504–6515 (2013).
7. Kim, G., Griffin, J. M., Blanc, F., Haile, S. M. & Grey, C. P. Characterization of the dynamics in the protonic conductor  $\text{CsH}_2\text{PO}_4$  by  $^{17}\text{O}$  solid-state NMR spectroscopy and first-principles calculations: Correlating phosphate and protonic motion. *J. Am. Chem. Soc.* **137**, 3867–3876 (2015).
8. Gaydamaka, A. A., Ponomareva, V. G. & Bagryantseva, I. N. Phase composition , thermal and transport properties of the system based on the mono- and dihydrogen phosphates of rubidium. *Solid State Ionics* **329**, 124–130 (2019).
9. Botez, C. E. *et al.* High-temperature crystal structures and chemical modifications in  $\text{RbH}_2\text{PO}_4$ . *J. Phys. Condens. Matter* **21**, 325401 (2009).
10. Kennedy, N. S. J. & Nelmes, R. J. Structural Studies of  $\text{RbH}_2\text{PO}_4$  in its Paraelectric and Ferroelectric Phases. *J. Phys. C Solid State Phys.* **13**, 4841–4853 (1980).
11. Park, J. & Choi, B. Electrical conductivity and impedance characteristics of  $\text{RbH}_2\text{PO}_4$  crystal above room temperature. *Mater. Lett.* **57**, 2162–2167 (2003).
12. Foran, G. Y., Brouwer, D. H. & Goward, G. R. Quantifying Site-Specific Proton Dynamics in Phosphate Solid Acids by  $^1\text{H}$  Double Quantum NMR

- Spectroscopy. *J. Phys. Chem. C* **acs.jpcc.7b06034** (2017).  
doi:10.1021/acs.jpcc.7b06034
13. Vijayakumar, M., Traer, J. W., Britten, J. F. & Goward, G. R. Investigations of the phase transition and proton dynamics in rubidium methane phosphonate studied by solid-state NMR. *J. Phys. Chem. C* **112**, 5221–5231 (2008).
  14. Vijayakumar, M., Bain, A. D. & Goward, G. R. Investigations of Proton Conduction in the Monoclinic Phase of  $\text{RbH}_2\text{PO}_4$  Using Multinuclear Solid-State NMR. *J. Phys. Chem. C* **113**, 17950–17957 (2009).
  15. Magome, E., Komukae, M. & Machida, M. Neutron Diffraction Study of Ferrielectric Phase Transition in Monoclinic  $\text{RbD}_2\text{PO}_4$ . *J. Phys. Soc. Japan* **76**, 8–13 (2007).
  16. Reichert, D. & Saalwachter, K. Dipolar Coupling: Molecular-Level Mobility. in *Encyclopedia of Magnetic Resonance* (2008).  
doi:10.1002/9780470034590.emrstm1020
  17. Boysen, D. A., Haile, S. M., Liu, H. & Secco, R. A. Conductivity of Potassium and Rubidium Dihydrogen Phosphates at High Temperature and Pressure. *Chem. Mater.* **16**, 693–697 (2004).
  18. van Moorsel, G.-J. M. P., van Eck, E. R. H. & Grey, C. P.  $\text{Pr}_2\text{Sn}_2\text{O}$  and  $\text{Sm}_2\text{Sn}_2\text{O}_7$  as High-Temperature Shift Thermometers in Variable Temperature  $^{119}\text{Sn}$  MAS NMR. *J. Magn. Reson.* **113**, 159–163 (1995).
  19. Davis, L. J. M. *et al.*  $^6\text{Li}$  1D EXSY NMR spectroscopy: A new tool for studying lithium dynamics in paramagnetic materials applied to monoclinic  $\text{Li}_2\text{VPO}$  4F. *J. Phys. Chem. C* **115**, 22603–22608 (2011).
  20. Bain, A. D. & Fletcher, D. A. Selective-inversion experiments applied to chemical exchange in coupled spin systems. *Mol. Phys.* **95**, 1091–1098 (1998).
  21. Smiley, D. L., Davis, L. J. M. & Goward, G. R. An improved understanding of  $\text{Li}^+$  hopping pathways and rates in  $\text{Li}_3\text{Fe}_2(\text{PO}_4)_3$  using selective inversion  $^6\text{Li}$  NMR spectroscopy. *J. Phys. Chem. C* **117**, 24181–24188 (2013).
  22. Bain, A. D. *The cifit program*. (2000).
  23. Keeler, J. Chapter 8. Relaxation. 1–24 (2004). Available at: <http://www->

keeler.ch.cam.ac.uk/lectures/understanding/chapter\_8.pdf. (Accessed: 26th February 2019)

24. Lasia, A. *Electrochemical Impedance Spectroscopy and its Applications*. (2014).
25. Chang, C. S., Lubomirsky, I. & Kim, S. Complete Mechanistic Elucidation of Current–Voltage Characteristics of Grain Boundaries in a Proton-Conducting Solid Electrolyte. *J. Phys. Chem. C* **123**, 4396–4400 (2019).
26. Wang, B., Bi, L. & Zhao, X. S. electrolyte for proton-conducting solid oxide fuel cells. *J. Power Sources* **399**, 207–214 (2018).

### **Chapter 5: Proton Dynamics in Tin Pyrophosphates**

This chapter describes proton dynamics in indium-doped tin pyrophosphates. Tin pyrophosphates are a class of hydrogen-bonded solid-state proton conductors in which proton dynamics are difficult to analyze as a result of the proton content of these materials being highly dependent on the synthetic history of the sample. Tin pyrophosphate samples were originally prepared with the intention of quantifying proton dynamics using symmetry-based dipolar recoupling techniques, as was done for phosphate solid acids in Chapter 3. However, these methods were not suitable for characterizing homonuclear proton dipolar coupling interactions in the tin pyrophosphate samples. Unlike phosphate solid acids, which contain structural protons at regular intervals, protons in tin pyrophosphate are the result of defect site protonation and/or cation doping which makes them dispersed. Therefore, proton dipolar coupling interactions tend to be weak resulting in insufficient signal to probe proton dynamics in these materials using dipolar recoupling-based NMR methods.

As a result of this challenge, proton dynamics were instead probed using a combination of one dimensional  $^1\text{H}$  NMR,  $^1\text{H}$  EXSY and conductivity measurements. These experiments showed that proton conduction increases with indium addition up to 20 % but that indium doping does not change the activation energy for proton conduction. This suggests that indium doping does not change the mechanism of proton motion in these materials (hopping between hydrogen-bonded sites on the metal octahedra to hydrogen-bonded sites on the phosphate

tetrahedra). Instead, observed increases in proton conductivity are believed to be the result of the increasing proton concentration.

The indium-doped tin pyrophosphate samples that are studied in this chapter were prepared and characterized by G. Foran. The work presented in the chapter is unpublished but a manuscript, which will be written by G. Foran and edited in collaboration with Dr. G. R. Goward, is in progress.

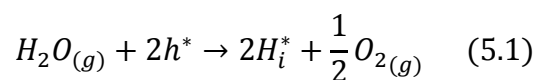
## 5.1 Introduction

Phosphoric acid fuel cells are currently the most commercially successful variety of intermediate-temperature (100-400 °C) fuel cell.<sup>1-3</sup> These devices consist of a supported phosphoric acid electrolyte that is responsible for proton conduction between the anode and the cathode, both of which are made from carbon-supported platinum.<sup>1</sup> Proton conduction through the phosphoric acid electrolyte occurs via the Grotthuss mechanism where protons are passed between phosphate tetrahedra via the formation and deformation of hydrogen bonds.<sup>4</sup> Although the phosphoric acid fuel cell has been used for decades, intermediate-temperature fuel cells can potentially be made more robust by adopting a solid-state electrolyte.<sup>2,5</sup> This is because liquid electrolytes must be monitored to prevent issues related to flooding and drying out, both of which would compromise fuel cell performance.<sup>1,5,6</sup> Tin pyrophosphates have been investigated as potential materials for solid-state electrolytes in intermediate-temperature fuel cells.

Tin pyrophosphates, solid-state materials that are comprised of a cubic network of tin octahedra and corner-sharing phosphate tetrahedra have been

proposed as potential intermediate-temperature proton conductors.<sup>2,5,7</sup> These materials have been shown to yield moderate proton conductivities in the 100 to 350 °C range which would extend the operational temperature range when compared to phosphoric acid fuel cells, which typically operate around 200 °C.<sup>1,2,7</sup> Higher operating temperatures would potentially increase both the proton conductivity and resistance to CO poisoning of these devices.<sup>1</sup> Additionally, tin pyrophosphates are thermally stable up to about 850 °C and are not water soluble.<sup>2,8</sup> These characteristics may result in increased stability relative to phosphate solid acids, another class of solid-state proton conductors, which have also been proposed as electrolytes for use in intermediate-temperature fuel cells.<sup>6,9</sup> However, creating a useable solid-state fuel cell electrolyte from tin pyrophosphate requires careful consideration as sample preparation and handling have been shown to have a significant impact on the proton conductivity of these materials.

Tin pyrophosphates as proton conductors is an interesting idea because these materials do not contain structural protons. It is for this reason that protons must be added to the material in some way. Protons can be incorporated into the pyrophosphate lattice through the interaction between water vapor (during synthesis, from atmosphere) and defect sites such as electron holes (Equation 5.1) and oxygen vacancies (Equation 5.2).<sup>7,10,11</sup>





Electron holes ( $h^*$ ) are generated when an electron escapes the valence band. An interstitial proton ( $H_i^*$ ) can then be incorporated, through interaction with water vapor, to charge balance the deficient site (Equation 5.1).<sup>11</sup> Electron holes are thought to be the cause of protonation in undoped tin pyrophosphate as this material has been previously shown to behave as a semi-conductor.<sup>3,7</sup> Protonation of the doped materials is expected to occur primarily through the generation of oxygen vacancies.<sup>3,7</sup> Oxygen vacancies ( $V_{\ddot{o}}$ ) are created when oxygen is removed from the lattice ( $O^x_o$ ) and is incorporated into the water vapor phase (Equation 5.2).<sup>11</sup> The vacancy can be filled with interstitial protons ( $OH_o^*$ ) (Equation 5.2).<sup>11</sup> These protons are expected to occupy hydrogen bonded interstitial sites on either the Sn-O-P or the P-O-P bridges (Figure 5.1).<sup>12</sup>

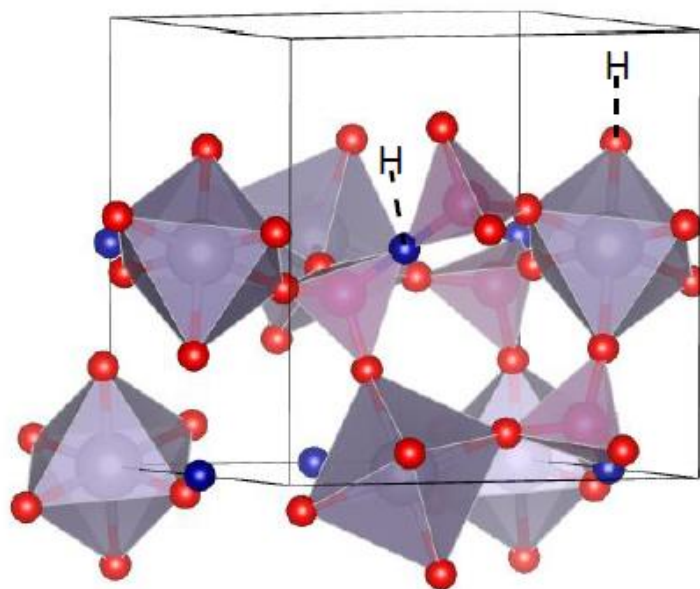


Figure 5. 1. Partial cubic tin pyrophosphate unit cell with interstitial protons added at the Sn-O-P and P-O-P bridge sites.

The most energetically favourable positions for interstitial protons is to be hydrogen bonded to the Sn-O-P and P-O-P bridges that connect tin octahedra and phosphate tetrahedra in the cubic structure (Figure 5.1).<sup>12,13</sup> Proton motion between these sites is believed to occur via the formation and deformation of hydrogen bonds.<sup>12</sup> The energetics of this process have been previously described via molecular dynamics simulations that were performed by Kreller et al.<sup>12</sup> The lowest energy pathway for proton motion is hopping between the Sn-O-P octahedral sites (Figure 5.1). The activation energy for this process has been calculated to be  $0.25 \pm 0.02$  eV.<sup>12</sup> However, this motion alone is unlikely to result in long-range proton transport because metal octahedra in cubic tin pyrophosphate are not corner-sharing.<sup>14</sup> Motions that would result in long-range proton transport include:

hopping between P-O-P sites and hopping from P-O-P to Sn-O-P sites.<sup>12</sup> These processes have activation energies of about  $1.5 \pm 0.2$  and  $0.5 \pm 0.1$  eV respectively.<sup>12</sup> The relatively low P-O-P to Sn-O-P energy barrier results from the geometry of the hydrogen bond transition state (Figure 5.1) where the hydrogen is simultaneously bonded to oxygen on both the P-O-P and M-O-P polyhedra. In this coordination mode, the oxygen-hydrogen distance is approximately 1.3 Å which in turn reduces the oxygen-oxygen distance from 3.8 to 2.5 Å.<sup>12</sup> As hydrogen bonding to the P-O-P site is less energetically favourable than bonding to the Sn-O-P site (the P-O-P bond is stronger), it has been proposed that bonding to the P-O-P site is an intermediate state that allows for proton transfer between non-bridging octahedral sites.<sup>12</sup> It can therefore be anticipated that protons tend to collect at Sn-O-P sites and exist transiently at P-O-P sites during motion.

Protons can be purposely added to tin pyrophosphate through synthetic methods. This has been done for the purpose of increasing proton conductivity in these materials. One method of protonation is to synthesize the material in the presence of excess phosphoric acid.<sup>7</sup> Excess phosphoric acid is expected to exist in grain boundaries post-synthesis and may provide a medium through which long-range proton conduction becomes possible. The presence of excess phosphoric acid can also result in the generation of a protonated, amorphous polyphosphate phase through which protons can be conducted.<sup>15</sup> Disadvantages of these methods for enhancing proton conductivity are that the resultant polyphosphate phase is amorphous and tends to vary between syntheses. Structural variability in the

proton-conducting phase would make it difficult to determine the mechanisms that are responsible for proton transport in these materials.

A more reliably controlled method of introducing protons into tin pyrophosphate is to replace a fraction of the tin (4+) with lower valence metals, often cations with 3+ or 2+ charges. This is done by substituting part of the tin oxide for another metal oxide during synthesis. This strategy increases the quantity of interstitial protons in the system as these are needed to balance the effective negative charge that is generated at the metal (M) octahedral (M-O-P) site when tin is replaced.<sup>7,10</sup> Studies have shown that hydrogen bonding to the  $M^{2+/3+}$ -O-P site is energetically more favourable than hydrogen bonding to the Sn-O-P site.<sup>12</sup> As the likelihood of hydrogen bonding to the P-O-P site remains largely unaffected by the incorporation of small amounts of foreign cations, it is assumed that the greatest impact of doping with lower valence metals is an increased tendency for protons to occupy the M-O-P sites.<sup>12</sup> If the fraction of tin that is replaced is relatively low, long-range cubic structure should be maintained and proton conductivity can be evaluated based on the structure of the cubic phase.

The majority of the NMR studies that have previously been performed on tin pyrophosphates have focused on characterizing the protonated phosphorous environments that exist in these materials.<sup>10,16</sup> Three varieties of protonated phosphate environments were previously identified by Nishida et al.<sup>10</sup> through a combination of  $^{31}\text{P}$  direct detection and  $^1\text{H}$ - $^{31}\text{P}$  cross polarization (CP) experiments.

In Nishida's work, signals at -12, -31 and -37 ppm were assigned to polyphosphoric acid, protonated pyrophosphate and unprotonated pyrophosphate respectively based on their chemical shifts in the directly detected spectra and their relative intensities in the CP spectra (Figure 5.2). The signal at -12 ppm is significantly attenuated in the CP spectrum as a result of high proton mobility through the polyphosphate phase.<sup>10</sup> The signal at -37 ppm is absent from the CP spectrum as it corresponds to pyrophosphate that does not interact with protons.<sup>10</sup> The most intense signal in the CP spectrum is the peak at -31 ppm which corresponds to protonated pyrophosphate where heteronuclear dipolar coupling interactions are strongest as a result of protons being less mobile in this phase than in the polyphosphoric acid phase.<sup>10</sup>

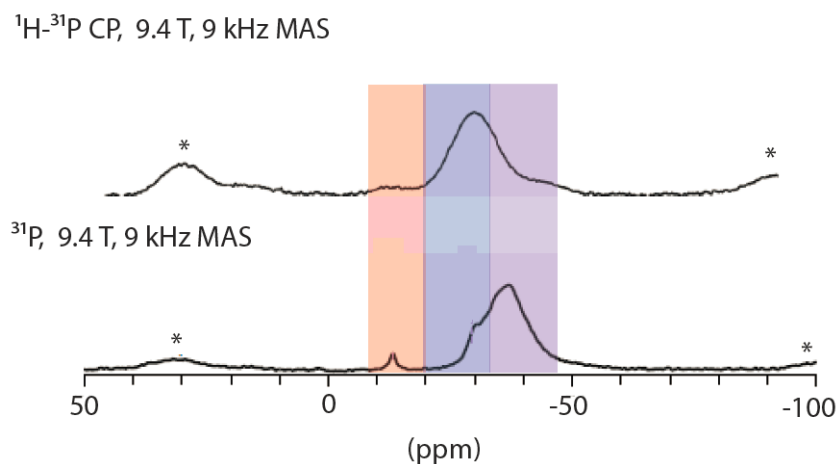


Figure 5. 2.  $^1\text{H}$ - $^{31}\text{P}$  CP and  $^{31}\text{P}$  spectra of  $\text{SnP}_2\text{O}_7$  adapted from Nishida et al.<sup>10</sup> with protonated phosphorous environments colour-coded: polyphosphoric acid (red), protonated pyrophosphate (blue) and unprotonated pyrophosphate (purple). Spectra were acquired at 9.4 T with 9 kHz MAS.

In addition to the characterization of protonated phosphorous environments, previous studies have highlighted the need for careful sample preparation. Studies

by Anfimova et al.<sup>7</sup> have shown that sample washing time and drying temperature have a significant impact on proton conductivity in tin pyrophosphate samples. As high proton conductivities have been associated with adsorbed phosphoric acid and/or polyphosphoric acid,<sup>3</sup> Nishida et al.<sup>10</sup> took additional measures to ensure that reproducible NMR spectra were obtained. These include sample drying at 600 °C, packing samples into rotors inside of a glovebox, utilising a rotor with an O-ring sealed cap and excluding any wet samples from their analyses.<sup>10</sup> Reducing the quantity of impurity phases present in the pyrophosphate samples through synthetic methods and sample storage was integral to obtaining reproducible data for analysis in this work. However, in addition to characterizing protonated phosphorous environments in tin pyrophosphate samples, proton conductivity measurements and solid-state NMR are used to quantify proton dynamics in indium-doped tin pyrophosphate samples. Solid-state NMR is particularly well-suited to the study of tin pyrophosphate samples as individual protonated environments can be resolved. This allows for the quantification of site-specific proton dynamics as was previously done for phosphate solid acids, another class of phosphate-based solid-state proton conductors that were analyzed in previously published work.<sup>17</sup>

## **5.2 Experimental**

### **5.2.1 Tin Pyrophosphate Synthesis**

Tin pyrophosphate samples were prepared by combining phosphoric acid and tin oxide in a 2.8 to 1 phosphorous to metal ratio based on the acid-oxide synthesis method that was described by Anfimova et al.<sup>7</sup> The mixture was dispersed

in water and then heated until a viscous paste was formed. The paste was heated overnight at 650 °C. The resultant solid was ground into a powder and was washed with water until the rinsate was pH neutral. The sample was then dried at 650 °C for a second time. The sample was promptly stored in the glovebox following the second heating step to limit exposure to atmospheric water prior to NMR analysis. The indium-doped samples were prepared similarly but with 5 to 20 % of the tin fraction being replaced with indium. Indium was added as indium oxide.

### **5.2.2 Powder X-ray Diffraction**

Samples prepared for powder x-ray diffraction (PXRD) analysis were ground and then adhered to a flat disk using a mixture of toluene and Vaseline. Diffraction patterns were acquired under ambient conditions over a range of diffraction angles spanning 15 to 60  $2\theta$  with a step size of 0.017  $2\theta$  at a rate of 0.35° per minute. X-ray excitation was performed using a 0.154 nm Cu source. All samples that were used in PXRD experiments were stored and analyzed under ambient conditions.

### **5.2.3 Electrochemical Impedance Spectroscopy**

Ground tin pyrophosphate powders were uniaxially pressed to yield disks that were 10 mm in diameter and 1 to 3 mm wide. The disks were sintered at 120 °C and were gold-coated (30 nm) on both sides. Electrochemical impedance spectroscopy (EIS) measurements were performed using a two-electrode cell. Proton conductivities were measured between 50 and 150 °C with samples being allowed to equilibrate for one hour at temperature prior to measurements being

taken. EIS measurements were taken at a constant potential of 50 V. Frequencies were varied between 1000000 and 10 Hz. All EIS samples were stored and analyzed under ambient conditions.

#### **5.2.4 Solid-State NMR**

Solid state  $^1\text{H}$  NMR experiments: variable-temperature one dimensional (1D) experiments and exchange spectroscopy (EXSY) were performed at 7.0 T with 15 kHz MAS using a 4 mm two-channel wide-bore probe. A  $4.7 \mu\text{s}$   $^1\text{H}$   $\pi/2$  pulse was calibrated at 40 W. Temperature calibration was performed based on changes in chemical shift of a mixture of  $\text{Sm}_2\text{Sn}_2\text{O}_7$  and tin oxide as a function of temperature.<sup>18</sup> Samples were equilibrated at temperature for ten minutes prior to performing the experiments. Sample temperatures were found to be accurate to  $\pm 4$  °C. 1D phosphorous NMR and dipolar coupling-based  $^1\text{H}$ - $^{31}\text{P}$  heteronuclear multi-quantum coherence (HMQC) experiments were performed at 20.0 T where the resonance frequency for  $^{31}\text{P}$  is 344.14 MHz. Samples were spun at 30 kHz using a 1.9 mm two-channel probe.  $\pi/2$  Pulse lengths of 2.8 and 8.75  $\mu\text{s}$  were calibrated at 40 W for proton and phosphorous respectively. All samples that were used in the NMR experiments were stored and packed into rotors in an argon-filled glovebox.

### **5.3 Results and Discussion**

#### **5.3.1 Tin Pyrophosphate Synthesis**

The tin pyrophosphate samples discussed here were synthesized in the presence of excess phosphoric acid (2.8:1 phosphate to metal ratio as opposed to the 2:1 stoichiometric ratio). Although this was originally done to align with a

previously published procedure where the aim was to produce a material that contained conductive species such as phosphoric acid and polyphosphoric acid,<sup>7</sup> it was found that cubic phase tin pyrophosphate could not be produced if a stoichiometric quantity of phosphoric acid was used. Excess phosphoric acid is required for the synthesis of tin pyrophosphate to proceed to completion because phosphoric acid is prone to evaporation due to the high temperatures that are needed to produce pyrophosphate.<sup>3</sup> Therefore, syntheses were carried out with excess phosphoric acid to prevent the formation of phosphate-deficient species.

In addition to investigating phosphoric acid requirements for tin pyrophosphate synthesis, fractions of indium doping that would result in cubic phase tin pyrophosphate were also studied. Indium was added in 5 % increments between 5 and 30 %. PXDR data showed that when indium loading exceeded 20 %, cubic tin pyrophosphate was no longer produced (Figure 5.3). Instead, PXRD powder patterns indicated the presence of an amorphous phase with some peaks corresponding to indium oxide (Figure 5.3).

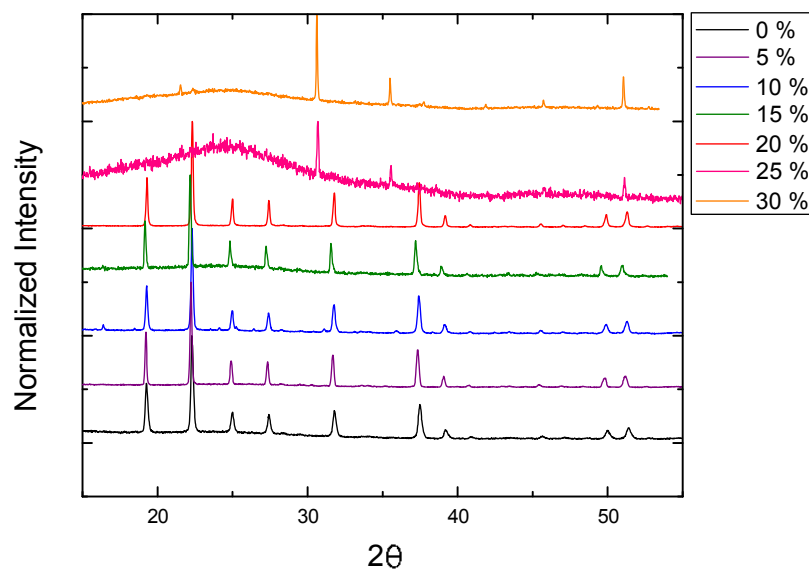


Figure 5. 3. PXRD patterns of tin pyrophosphate samples with 0 to 30 % indium doping. The powder patterns were acquired at room temperature using a 0.134 nm Cu source with a 0.017  $2\theta$  step size at a rate of 0.35°/min.

It is believed that replacing tin sites with indium results in some disruption of the cubic tin pyrophosphate lattice.  $\text{In}^{3+}$  cations have larger atomic radii than  $\text{Sn}^{4+}$  cations, 94 pm versus 83 pm,<sup>19</sup> which would result in changes in bond lengths at the M-O-P octahedral centers. At lower indium loadings, below 20 %, these disruptions are minimal as the corresponding PXRD powder patterns suggest that long-range order is maintained (Figure 5.3). However, when indium loading surpasses 20 % long-range order is disrupted resulting in powder patterns that indicate the formation of an amorphous sample (Figure 5.3). As proton hopping in tin pyrophosphate is facilitated by a shortening of the oxygen-oxygen bond length between P-O-P and M-O-P sites in the cubic phase,<sup>12</sup> it is anticipated that significant structural distortion would reduce proton conductivity in these samples.

It is for this reason that indium doping was limited to 20 % in the study of proton dynamics in tin pyrophosphates that is presented here.

Despite significant evidence that the long-range cubic tin pyrophosphate structure is conserved when indium doping is below 20 %, it must be noted that the diffraction pattern corresponding to the sample with 15 % indium loading shows that this material is somewhat more amorphous than the other tin pyrophosphate samples (Figure 5.3). This is evidenced by the increased distortion of the powder pattern baseline relative to that of the other samples. As the reflections corresponding to cubic phase tin pyrophosphate are still present in this sample, it is anticipated that the overall long-range structure has been conserved with the observed amorphousness corresponding to the presence of some differences in crystallite orientation. It is anticipated that these structural differences will be observable via NMR.

In addition to indium doping, another aspect of tin pyrophosphate synthesis that is considered here is the presence of additional conductive species that arise from synthesis with excess phosphoric acid: phosphoric acid and polyphosphoric acid. Phosphoric acid is a good proton conductor, as is evidenced by the existence of the phosphoric acid fuel cell which uses membrane-bound phosphoric acid as an electrolyte.<sup>1,4,20</sup> Polyphosphoric acids are also expected to participate in proton conduction, as these materials are comprised of polymerized chains of phosphate tetrahedra that may be protonated.<sup>15</sup> In fact, some authors have suggested that

proton conductivity in tin pyrophosphate samples, in which significant proton conductivity has been observed ( $\sim 10^{-2}$  S/cm),<sup>7,15</sup> is actually attributable to polyphosphoric acid species and/or absorbed phosphoric acid.<sup>3</sup> Therefore, in order to ensure that proton dynamics that are measured here result from the pyrophosphate phase, samples were washed and subjected to additional heating prior to analysis.

Washing the sample in water is expected to remove phosphoric acid.<sup>7</sup> This was confirmed both by measuring the pH of the rinsate and the absence of a characteristic peak at 0 ppm in the <sup>31</sup>P NMR spectra. Additional heating is expected to aid in the degradation of polyphosphoric acid.<sup>7</sup> In addition to these protocols, samples that were used for NMR analysis are stored in the glovebox to minimize hydration and/or protonation from atmospheric exposure. Figure 4 shows that these measures have contributed to reducing the quantity of protons that are present in a tin pyrophosphate sample. This is gauged based on the relative intensity of a background peak, where constant intensity is assumed, that is found at 1 ppm in the <sup>1</sup>H spectra, following additional heating and glovebox storage (Figure 5.4). The other significant difference between these proton spectra is a peak at 7 ppm in the sample that was not stored in the glovebox. This signal was attributed to polyphosphoric acid as it was significantly attenuated following heating and glovebox storage.

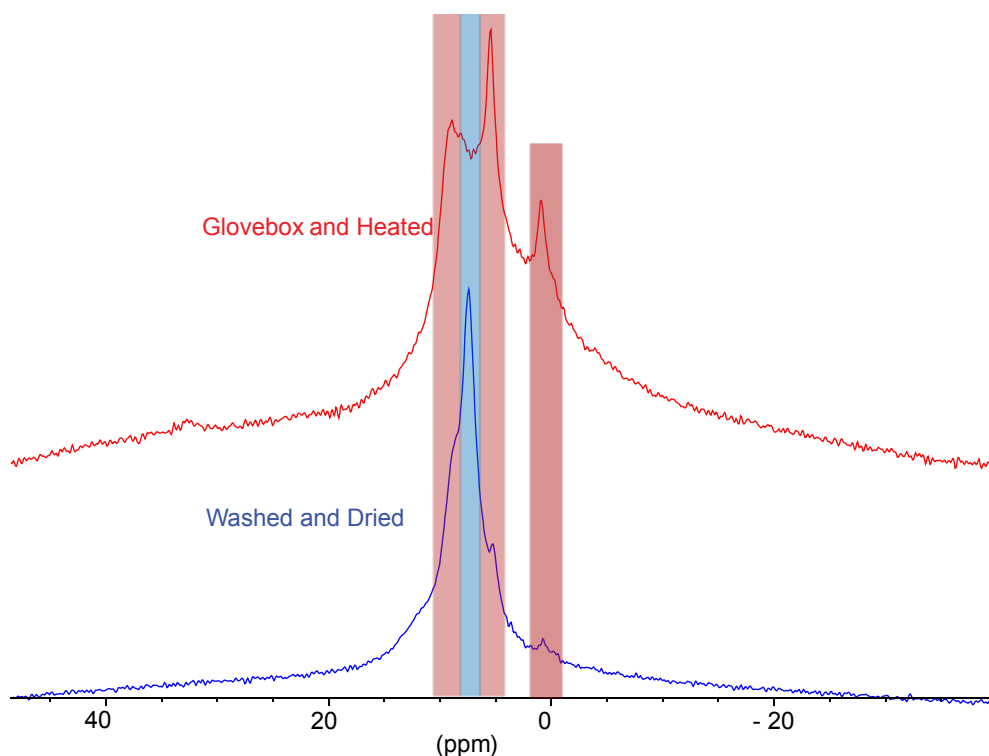


Figure 5. 4.  $^1\text{H}$  NMR spectrum of undoped tin pyrophosphate with and without additional heating and glovebox storage at 7.0 T and 15 kHz MAS.

### 5.3.2 Tin Pyrophosphate Structure

$^{31}\text{P}$  NMR spectra of tin pyrophosphate samples doped with 0 to 20 % indium (Figure 5.5) contain two main groups of peaks, one centered at -30 ppm and another that is centered at -37 ppm. These sites are assigned to protonated pyrophosphate (Figure 5.6) and bulk pyrophosphate (Figure 5.6) respectively based on peak assignments for tin pyrophosphate that were presented by Nishida et al.<sup>10</sup> However, unlike in Nishida's work, each site in Figure 5 is comprised of two distinct peaks. This is a result of improved spectral resolution caused by increased magnetic field strength from 9.4 T (Nishida's work) to 20.0 T (this work).

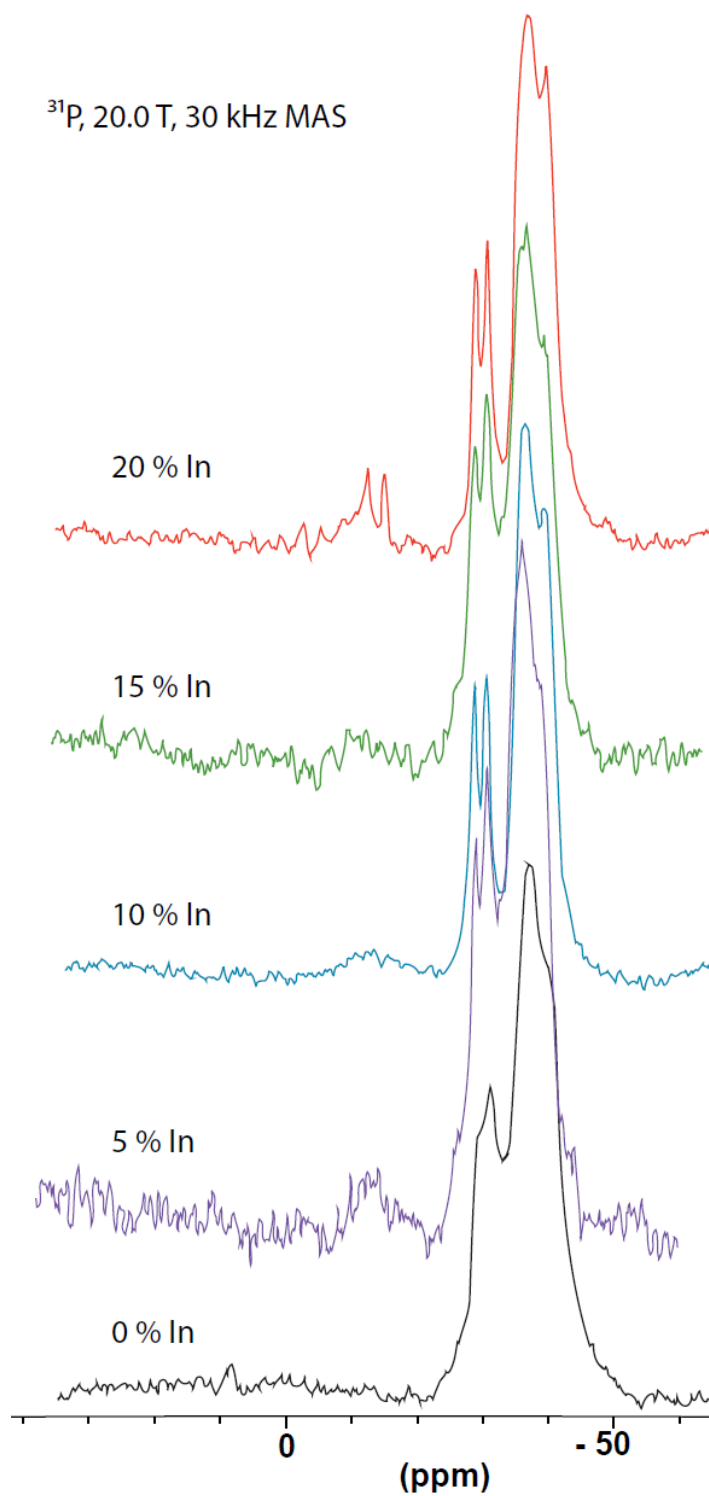


Figure 5. 5.  $^{31}\text{P}$  spectra of tin pyrophosphates with 0 to 20 % indium loading acquired at 20.0 T with 30 kHz MAS.

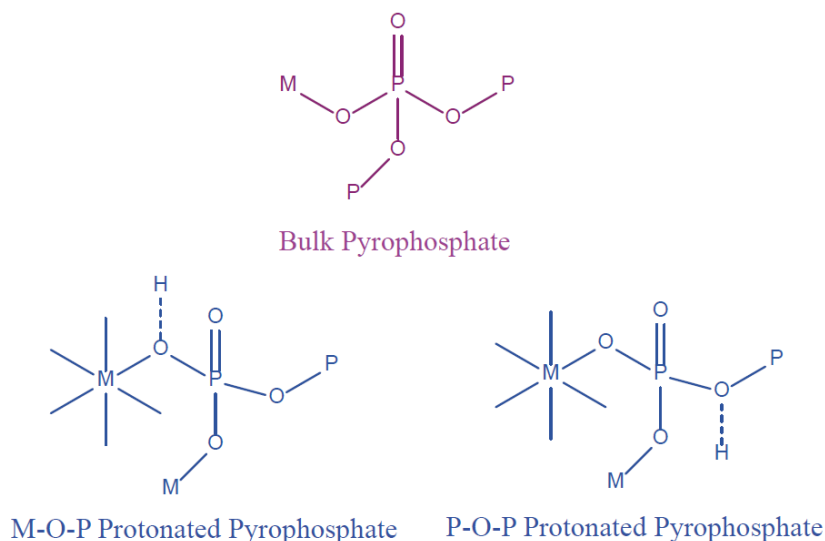


Figure 5. 6. Molecular structures for bulk and protonated pyrophosphates. Pyrophosphate protonation occurs via hydrogen bonding to the M-O-P or the P-O-P bridge. In this schematic, M represents both tin and indium centers.

The  $^{31}\text{P}$  spectra presented in Figure 5.5 are similar regardless of indium doping with the relative proportion of protonated pyrophosphate being about 20 % in all cases. This is somewhat counterintuitive as proton content is expected to increase with indium doping. This was also observed in the work of Nishida et al.<sup>10</sup> where a significant peak corresponding to protonated pyrophosphate can be found in spectra of undoped tin pyrophosphate (Figure 5.2). Spectra shown in Figure 5.5, as well as those that were acquired by Nishida et al.<sup>10</sup>, were collected with a recycle delay of 200 s. These results suggest that  $^{31}\text{P}$  longitudinal ( $T_1$ ) relaxation may change as a function of indium loading and that significant signal can result from the protonation of defect sites (electron holes) in the undoped sample.

Increased indium doping is expected to result in an overall increase in  $^{31}\text{P}$   $T_1$  relaxation time. This is because  $T_1$  relaxation can be facilitated through

processes such as dipolar coupling and molecular mobility<sup>21</sup> which are expected to be impeded by indium addition. As  $\text{In}^{3+}$  has a larger atomic radius than  $\text{Sn}^{4+}$ , indium doping could result in changes to the local structure, namely the lengthening of bonds in the M-O-P octahedra. Although the PXRD data suggests that this level of indium doping does not affect long-range structure, changes in homonuclear phosphorous apparent dipolar coupling (which is most heavily impacted on the local scale) could result. In addition, phosphorous are expected to remain relatively stationary in these materials meaning  $T_1$  relaxation time would also not be decreased by motional processes.<sup>12</sup> Insufficient relaxation time would result in decreased signal from peaks corresponding to protonated pyrophosphate. Measurement of  $^{31}\text{P}$   $T_1$  relaxation in these materials shows that  $T_1$  relaxation times for sites corresponding to protonated pyrophosphate increase from 80 s in the undoped sample up to 160 s in the sample with 20 % indium loading. These results suggest that performing direct detection experiments with long recycle delays is essential for the characterization of these materials based on the proportion of protonated pyrophosphate. To this end, direct detection experiments were performed with a 1000 s recycle delay (exceeding the  $5 \cdot T_1$  requirement for all samples). These experiments showed that the relative proportion of protonated pyrophosphate increased from 8 % in the undoped sample to 64 % in the sample with 20 % indium loading. These experiments demonstrated that increased indium doping increases proton concentration in the doped tin pyrophosphate samples.

In addition to peak assignment based on changes in relative intensity with increasing indium loading, the -30 ppm site could also be assigned to protonated pyrophosphate based on the results of  $^1\text{H}$ - $^{31}\text{P}$  HMQC experiments. In these experiments, the presence of crosspeaks shows that proton peaks, which are believed to correspond to protonated M-O-P and P-O-P sites, are correlated to the phosphorous peaks at -30 ppm but not those at -37 ppm (Figure 5.7). This supports the above assignment that was based on chemical shifts that were reported by Nishida et al.<sup>10</sup>

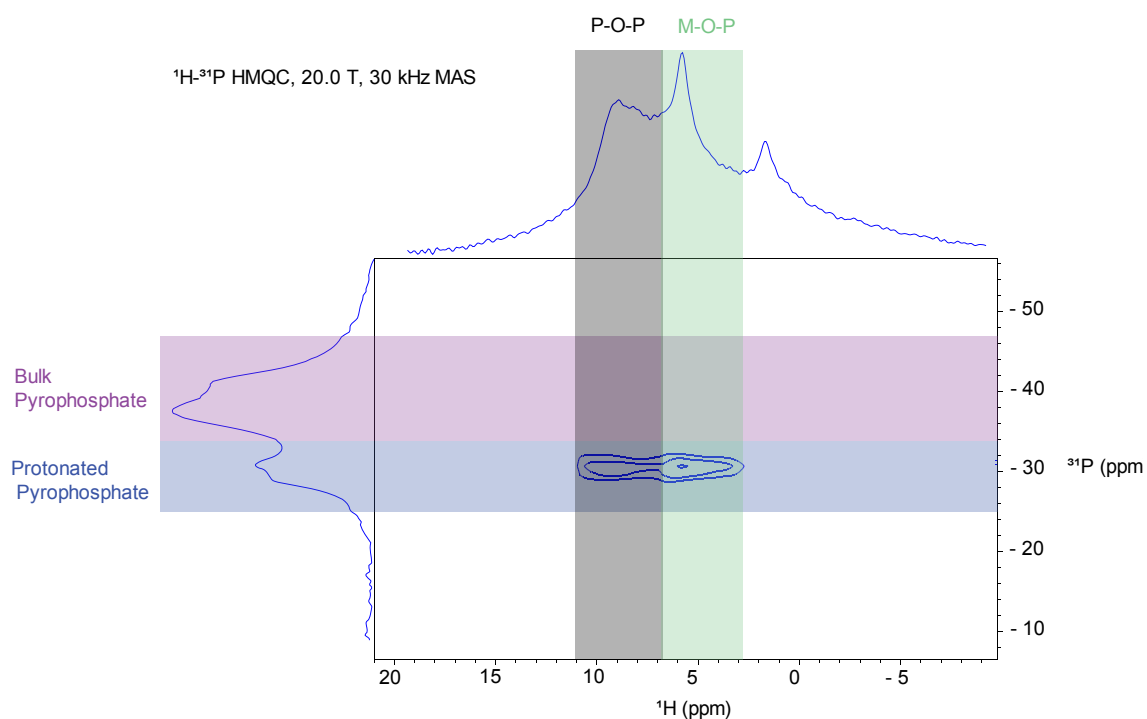


Figure 5. 7.  $^1\text{H}$ - $^{31}\text{P}$  HMQC spectrum of undoped tin pyrophosphate acquired at 20.0 T with 30 kHz MAS.

It was predicted that the influence of indium doping on tin pyrophosphate samples could also be discerned by considering the 1D  $^1\text{H}$  spectra. The primary

advantage of evaluating the effects of indium doping on the proton network is to assess changes in proton dynamics caused by either changes to the mechanism of proton transport and/or by increasing proton concentration. The proton spectra contain two major peaks at 9.0 and 5.5 ppm which are hypothesized to correspond to M-O-P and P-O-P proton environments (Figure 5.6). Analyses of the  $^1\text{H}$  spectra revealed significant changes in linewidth and spectral intensity with indium addition (Figure 5.8). Most notably, the peak at 5.5 ppm increases in both intensity and area relative to the 9.0 ppm site. These changes suggest that indium doping increases the quantity of protons that are present in the tin pyrophosphate samples. It must however be noted that the general trend in increasing spectral intensity at the 5.5 ppm site with indium doping is somewhat broken when the sample with 15 % indium doping is considered. In this case, the  $^1\text{H}$  lineshape is affected by increased amorphousness or the presence of more than one crystallographic orientation as was predicted based on the PXRD results. Other differences between  $^1\text{H}$  spectra can be attributed to differences in lower intensity signals coming from residual polyphosphoric acid. Although measures were taken to reduce the quantity of this phase,  $^1\text{H}$  and  $^{31}\text{P}$  NMR suggest the presence of small amounts. However, lineshape changes with indium doping are observed in the proton spectra as the addition of indium is expected to increase, not decrease as was predicted for phosphorous, the rate of  $T_1$  relaxation. Indium doping is expected to increase proton concentration as protons are added with each indium ion for charge balancing purposes. Increased proton concentration would result in either increased  $^1\text{H}$

apparent dipolar coupling or increased proton mobility, both of which would provide additional pathways for  $T_1$  relaxation.<sup>21</sup>

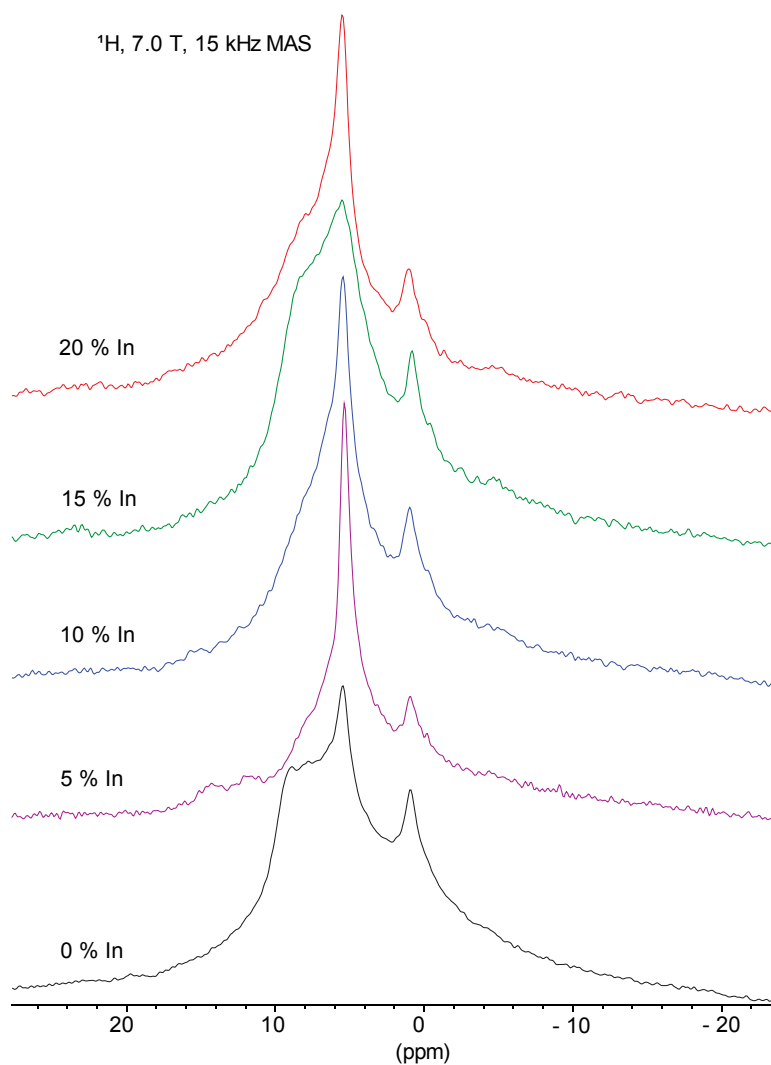


Figure 5. 8.  $^1\text{H}$  spectra of tin pyrophosphate with 0 to 20 % indium loading acquired at 7.0 T with 15 kHz MAS.

The fact that more significant changes were observed at the 5.5 ppm site than at the 9.0 ppm site upon indium addition is interesting and may be useful in assigning these sites to M-O-P and P-O-P proton environments. Protons are

expected to be more likely to occupy the M-O-P site as indium doping increases because more deficient metal octahedral sites would need to be charge balanced. Changes in peak intensity and peak area therefore suggest that the 5.5 ppm site corresponds to the M-O-P environment. As a result of differing activation energies for proton motion at the M-O-P and P-O-P sites, a site-specific investigation of proton dynamics was proposed as a means of site assignment. Molecular dynamics simulations (performed by Kreller et al.<sup>12</sup>) suggest that proton mobility can be expected to be greater at the M-O-P sites than at the P-O-P sites. This is because the activation energy for proton hopping between M-O-P sites ( $0.25 \pm 0.02$  eV) is lower than the activation energy for proton hopping between P-O-P and M-O-P sites ( $0.5 \pm 0.1$  eV).<sup>12</sup> Therefore, we endeavoured to quantify site-specific proton dynamics at both sites.

As peak narrowing is typically associated with increased motion, <sup>1</sup>H linewidths and T<sub>1</sub> relaxation times were assessed to assign the observed signals to either M-O-P or P-O-P proton sites based on the anticipated mobility of each type of site. <sup>1</sup>H linewidths were measured by fitting individual sites in the 1D <sup>1</sup>H spectra. Each spectrum was fit with three proton sites: one at 9.0 ppm, one at 5.5 ppm and one at 1.0 ppm (Figure 5.9). Proton mobility was evaluated by measuring the full-width half-maximum (FWHM) of each peak.

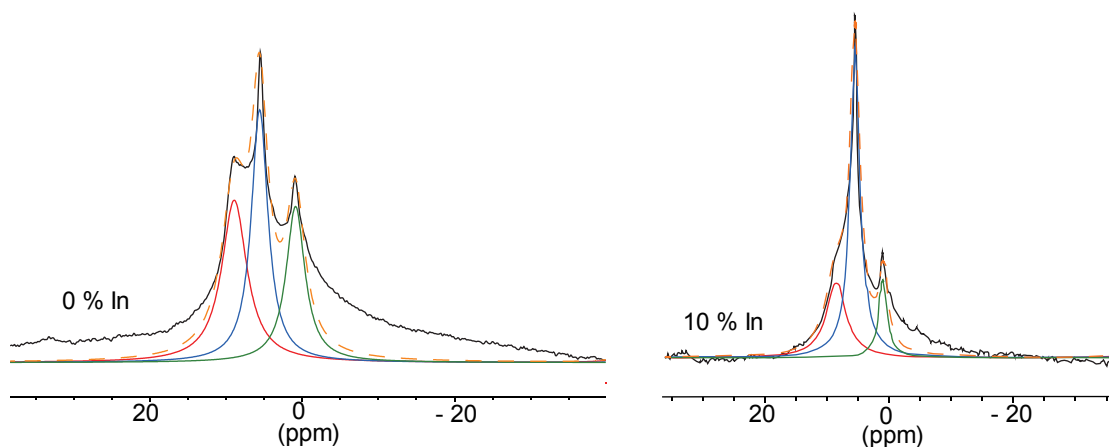


Figure 5. 9.  $^1\text{H}$  spectra of 0 % and 10 % indium-doped tin pyrophosphates acquired at 7.0 T with 15 kHz MAS. Each spectrum was fit with three proton sites at 9.0, 5.5 and 1.0 ppm. The acquired spectrum is represented by a solid line. The fit is represented by a dashed line.

FWHM were measured at the 5.5 and 9.0 ppm sites as a function of temperature. Changes in FWHM differed significantly between the 9.0 and 5.5 ppm sites. While FWHM of the 9.0 ppm site remained relatively constant as sample temperature increased, FWHM of the 5.5 ppm site decreased by a few ppm over the same temperature range (Figure 5.10). These changes were also observed in the sample with 15 % indium loading making FWHM an adequate method of characterizing site-specific proton mobility in all tin pyrophosphate samples that are considered here.

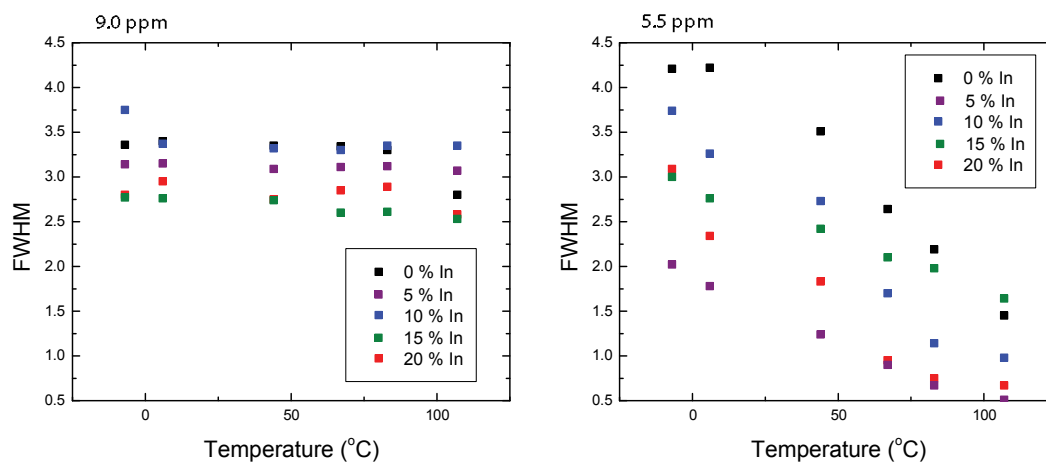


Figure 5. 10. FWHM as a function of temperature for indium-doped tin pyrophosphate samples. Spectra were acquired at 7.0 T with 15 kHz MAS.

Substantial changes in FWHM at the 5.5 ppm site as a function of temperature support our earlier hypothesis that the 5.5 ppm peak corresponds to the M-O-P proton environment. Protons at the M-O-P site are expected to be more mobile as a result of the relatively low energy for proton hopping between hydrogen-bonded sites at the metal octahedral center ( $0.25 \pm 0.02$  eV).<sup>12</sup> The FWHM of the 9.0 ppm site remained relatively constant which suggests that protons occupying this environment are less mobile. Decreased mobility at the 9.0 ppm site was also confirmed by measuring  $T_1$  at both the 5.5 and 9.0 ppm sites. At all indium loadings,  $T_1$  was around 10 s for the 9.0 ppm site and 1 s for the 5.5 ppm site (Figure 5.11). Sites with lower mobility tend to require more time for  $T_1$  relaxation to occur.<sup>22</sup>

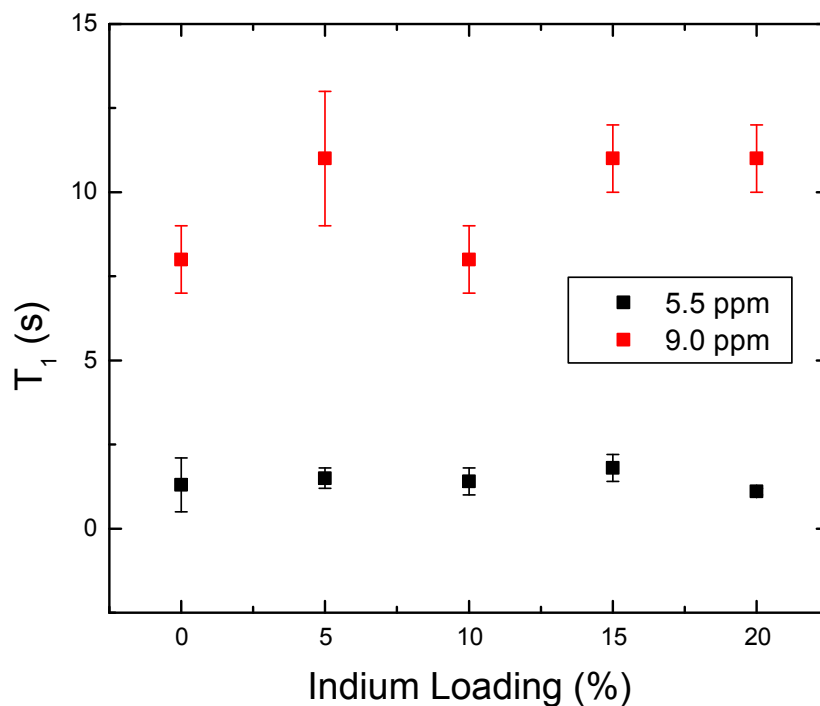


Figure 5. 11. Proton  $T_1$  values for 5.5 and 9.0 ppm sites in indium-doped tin pyrophosphate measured at room temperature with 15 kHz MAS at 7.0 T.

Two measures of proton dynamics show that the 9.0 ppm site can be correlated with the P-O-P tetrahedral site which has a higher activation energy for proton hopping ( $0.5 \pm 0.1$  eV).<sup>12</sup> Although tracking FWHM as a function of temperature and  $T_1$  measurements allowed M-O-P and P-O-P sites to be differentiated, additional experiments are required to quantitatively evaluate proton dynamics in these materials. Therefore, conductivity measurements and two dimensional (2D) EXSY experiments were performed with the goals of quantifying both long-range proton conductivity and inter-polyhedron proton transfer more specifically.

### 5.3.3 Proton Dynamics in Tin Pyrophosphates

Proton conductivity was measured in tin pyrophosphate samples with 0 to 20 % indium doping (Figure 5.12) via EIS. Overall, proton conductivity increased by about two and a half orders of magnitude between 50 and 150 °C in all samples. Measured proton conductivities were relatively low when compared to some of the values that have previously been reported,  $10^{-10}$  to  $10^{-6}$  S/cm as opposed to  $10^{-2}$  S/cm.<sup>7</sup> These measurements may however be consistent with the studied materials being relatively pure as it has been stated that extremely high proton conductivities in tin pyrophosphates may not result from proton conduction through the pyrophosphate phase.<sup>3,13</sup> High proton conductivities in tin pyrophosphates are instead believed to be the result of proton conduction through other, more conductive, phases that tend to be found in tin pyrophosphate samples as a result of synthesis with excess phosphoric acid: phosphoric acid and polyphosphoric acid.<sup>3,13,15,23</sup> Polyphosphoric acid impurities are amorphous and are generally found adsorbed to the tin pyrophosphate surface or in grain boundaries.<sup>7</sup> This phase is protonated and has been shown to provide an alternate pathway for proton conduction other than through the crystalline pyrophosphate phase.<sup>15,23</sup> In this work, steps including additional heating and glovebox storage, were taken to minimize the amount of polyphosphoric acid that is present (Figure 5.3) in order to facilitate the analysis of proton dynamics in the pyrophosphate phase specifically. These steps were successful in reducing the amount of polyphosphate phase that is

present but have also reduced proton conductivity in these materials relative to previously reported values.<sup>7</sup>

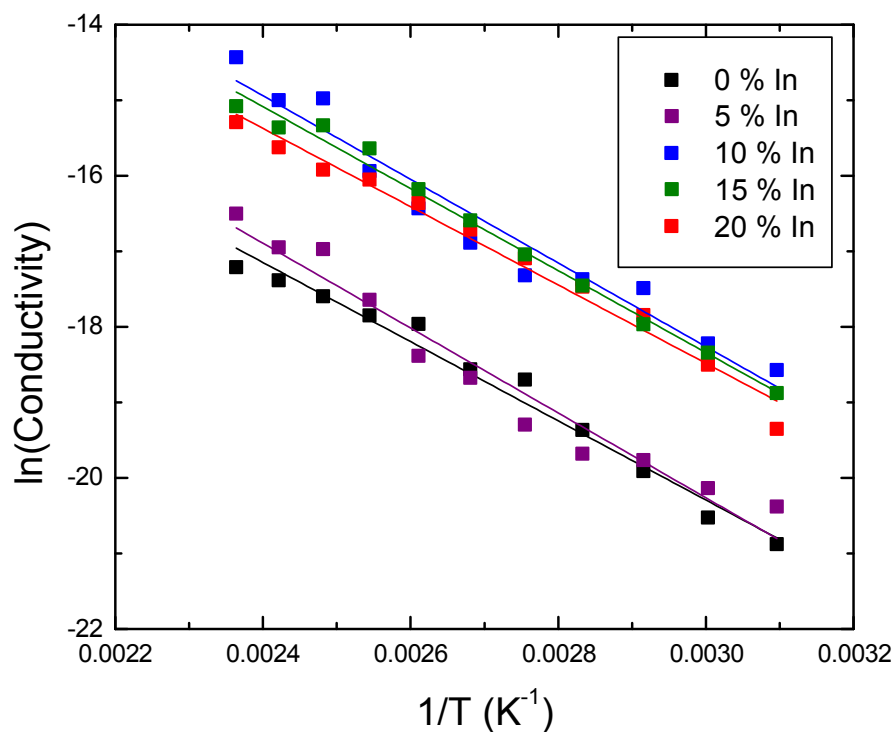


Figure 5. 12. Proton conductivity of tin pyrophosphate samples doped with 0 to 20 % indium measured via EIS between 50 and 150 °C. The lines represent linear fits which were used to calculate activation energies for proton conduction in these materials.

However, what is consistent with previously reported data is that, in all cases, proton conductivity in the indium-doped samples is greater than proton conductivity in the undoped sample. This suggests that adding indium to tin pyrophosphate increases proton mobility in these materials. Despite increasing proton conductivity, activation energies for proton mobility that were calculated

based on the conductivity data were the same within error at all indium loadings (Figure 5.13). Equivalence between the activation energies suggests that increases in proton conductivity that result from increased indium loading are not caused by changes to the mechanism of proton conduction but are instead caused by increasing the concentration of the mobile species (in this case protons). This phenomenon is described in Equation 5.3 where conductivity ( $\sigma$ ) is expressed as a function of the charge carrier concentration ( $c$ ), charge carrier charge ( $q$ ) and charge carrier mobility ( $u$ ).<sup>24</sup>

$$\sigma = cqu \quad (5.3)$$

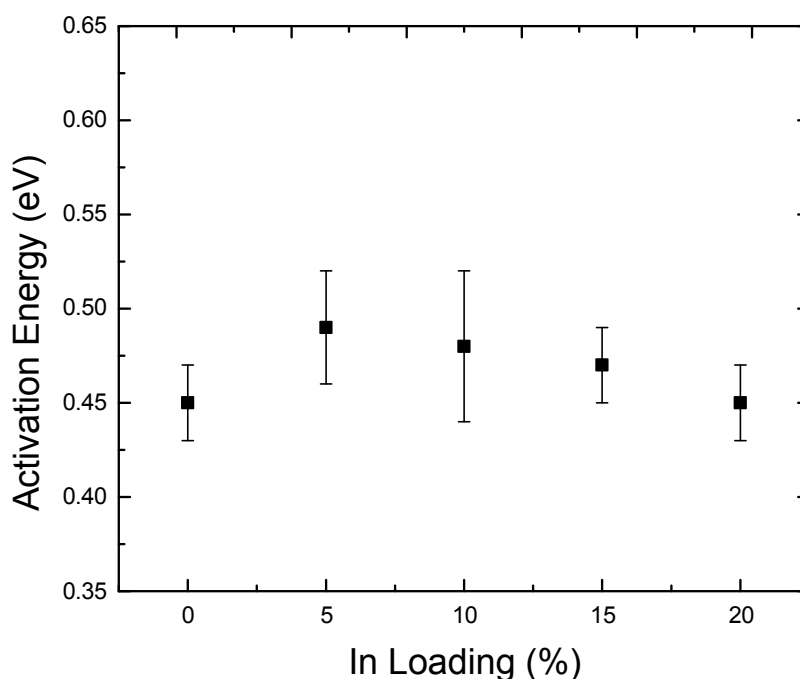


Figure 5. 13. Activation energy for proton conduction in tin pyrophosphate as a function of indium loading. Activation energies were calculated based on proton conductivity data acquired between 50 and 150 °C.

Despite the observation of increased proton conductivity in the indium-doped samples, proton conductivity seemed to plateau once indium loading reached 10 % (Figure 5.12). There are a few possibilities as to why proton conductivity in tin pyrophosphate did not increase linearly with indium doping. It is possible that increased indium doping changes the oxygen-oxygen bond length between P-O-P and M-O-P sites in cubic tin pyrophosphate as a result of  $\text{In}^{3+}$  cations having a larger atomic radius than  $\text{Sn}^{4+}$  cations. This explanation is however unlikely because PXRD diffraction patterns demonstrate that long-range crystallographic order is maintained with up to 20 % indium loading (Figure 5.3). Differences in proton conductivities may also result from different quantities of polyphosphoric acid being present as the amount of polyphosphoric acid that is formed does not depend on indium addition. EIS measures proton conductivity across a whole material and does not differentiate between conductivity through poly- and pyrophosphates. It is also possible that increasing the quantity of charge-deficient sites increases proton affinity for M-O-P sites. The feasibility of the latter explanation will be evaluated in the next section where solid-state NMR will be used to probe inter-polyhedron proton transfer more directly. As sites corresponding to M-O-P and P-O-P proton environments are relatively well-resolved in the 1D spectra, 2D EXSY experiments were used to measure site-specific proton exchange.

EXSY, a 2D NMR technique that is commonly employed to measure chemical exchange, was used to specifically probe inter-polyhedron proton hopping in tin pyrophosphate samples. EXSY was chosen for the investigation of site-

specific proton dynamics in this system as a result of insufficient signal being obtained when dipolar coupling-based NMR experiments were employed. It is hypothesized that relatively low proton concentrations and/or high proton dispersion in the doped samples resulted in both weak  $^1\text{H}$ - $^1\text{H}$  and  $^1\text{H}$ - $^{31}\text{P}$  dipolar coupling interactions making experiments such as symmetry-based dipolar recoupling and cross polarization inadequate methods for the characterization of proton dynamics in this system. The purpose of these experiments was to gauge whether the rate of inter-polyhedron proton exchange is affected by indium doping. In EXSY experiments, exchange is typically indicated by the presence of crosspeaks. However, in the tin pyrophosphate samples that were studied here, well-resolved crosspeaks were only observed for samples with 5 and 10 % indium loading (Figure 5.14 B, C).

$^1\text{H}$  EXSY, 7.0 T, 15 KHz MAS

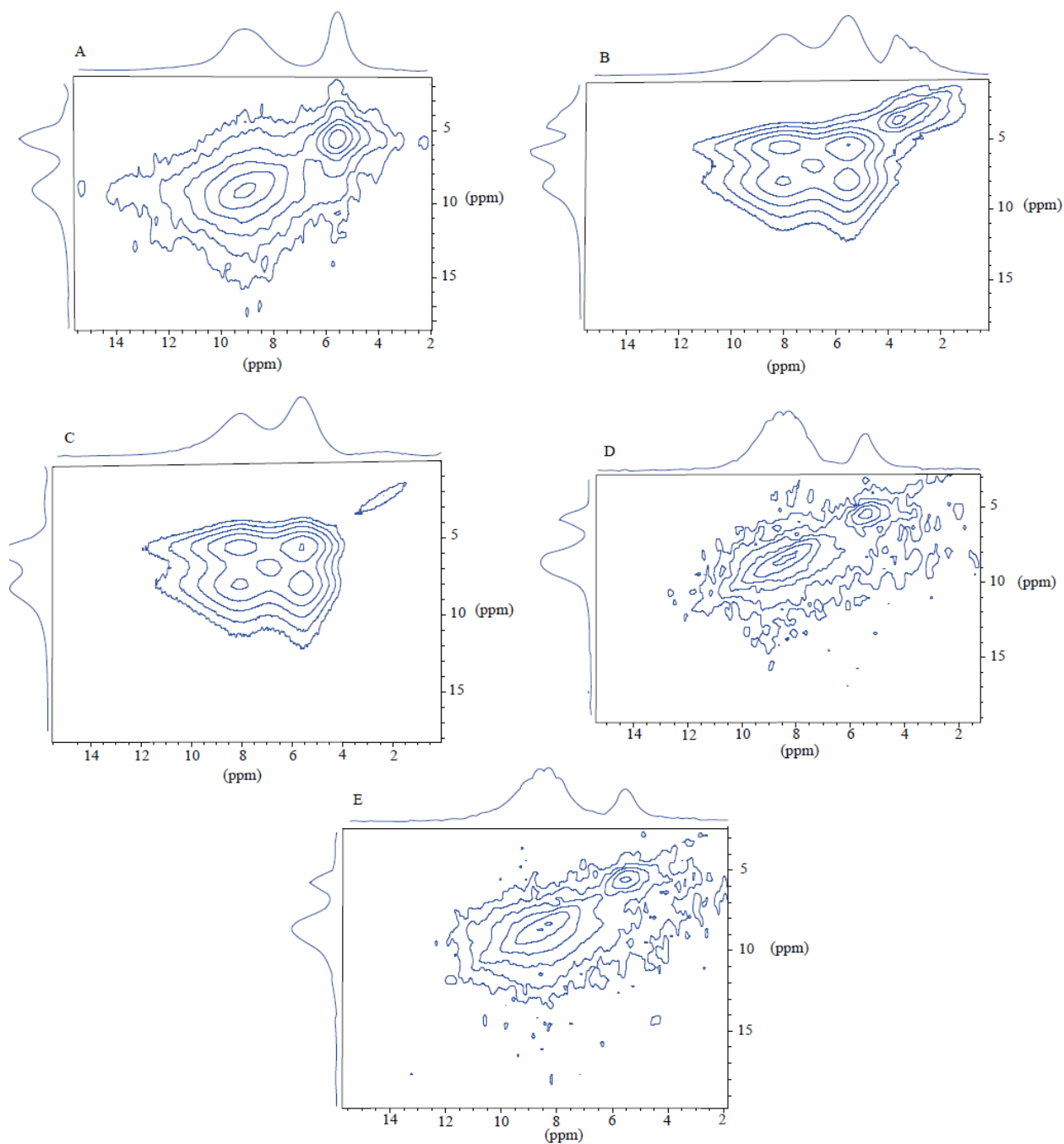


Figure 5. 14.  $^1\text{H}$  EXSY spectra of tin pyrophosphates with 0 to 20 % (A to E) indium loading. All spectra were acquired at 7.0 T with 15 kHz MAS. Sample temperature was 90 °C and mixing time was 0.05 s.

In addition to not observing crosspeaks in the 2D EXSY spectra at higher indium loadings, signal in the F1 dimension of the EXSY spectra decayed more rapidly (after about 20 slices versus after 42 slices) upon indium addition. This suggests that  $^1\text{H}$  transverse ( $T_2$ ) relaxation time decreases upon indium doping.<sup>25,26</sup> As  $T_2$  relaxation time is decreased by increased molecular motion,<sup>25,26</sup> it can be inferred that the rate of proton exchange in tin pyrophosphate increases upon indium addition. Although, as differences in the time required for the F1 signal to decay did not differ significantly between the doped samples (all were between 18 and 22 slices with no pattern resulting from indium loading) changes in  $T_2$  relaxation time are not the only reason that crosspeaks were not observed in the EXSY spectra when indium loading is between 15 and 20 %. The possibility of coalescence was therefore investigated to explain the absence of crosspeaks in these systems.

Coalescence occurs when the rate of chemical exchange is greater than the peak separation between exchanging sites.<sup>27,28</sup> In order to better measure peak separation and understand why crosspeaks were only observed at indium loadings between 5 and 10 % when the EIS data suggest that inter-polyhedron proton exchange should occur in all the tin pyrophosphate samples, 1D projections were extracted from the  $^1\text{H}$  EXSY spectra. The projections, which are presented in Figure 15, are displayed alongside the corresponding 1D data sets such that peaks could be assigned to M-O-P and P-O-P proton environments.

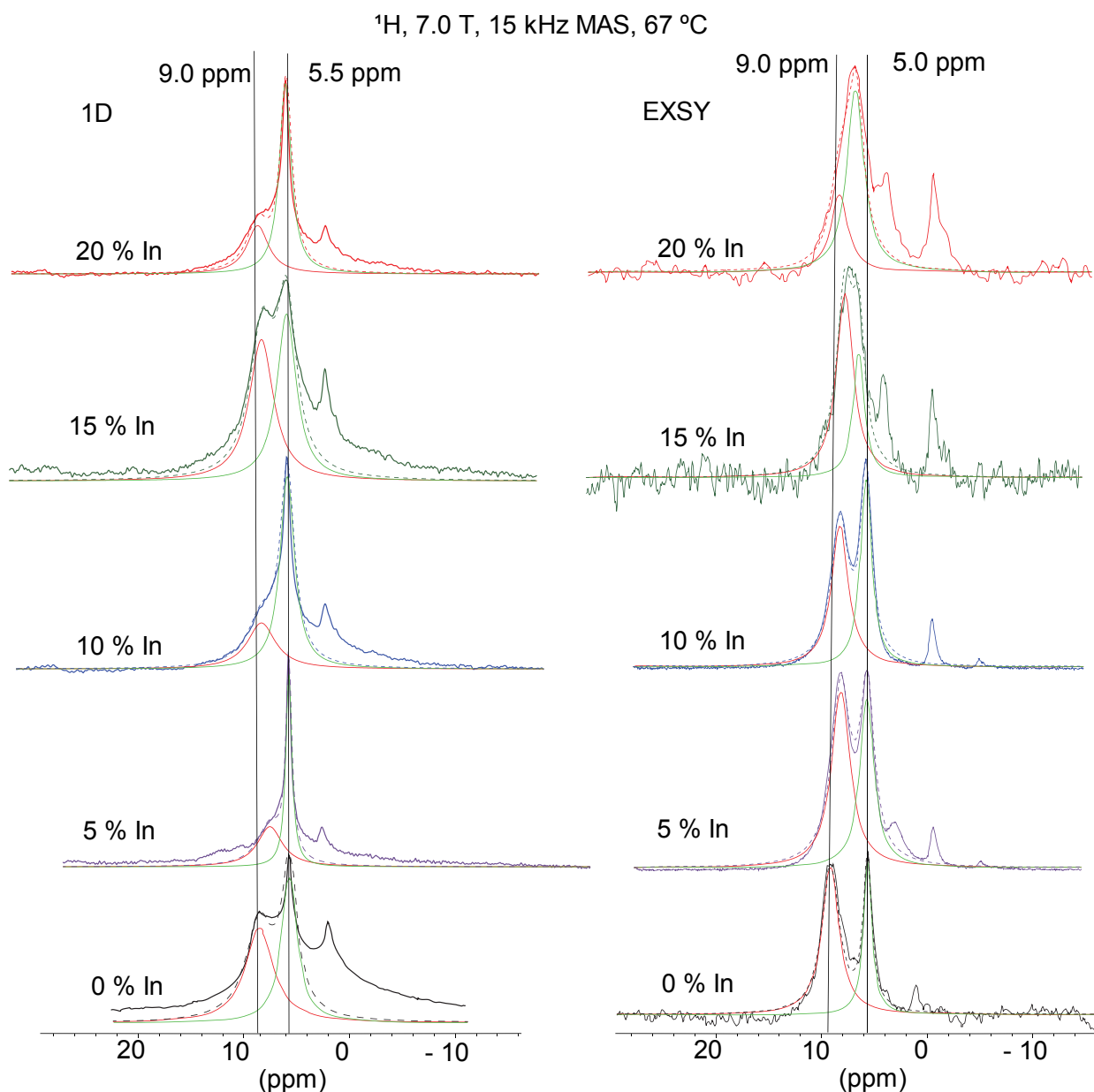


Figure 5. 15. 1D projections taken from EXSY spectra of tin pyrophosphates acquired with a mixing time of 0.1 s compared with 1D spectra. All spectra were collected at 7.0 T with 15 kHz MAS. Sample temperature was 67 °C. Lineshape fitting at the M-O-P and P-O-P sites is displayed.

The 1D projections from the EXSY spectra show that the separation between peaks corresponding to M-O-P and P-O-P proton environments tends to

decrease as indium loading increases (Figure 5.15). The distance between M-O-P and P-O-P sites can be used to gauge the maximum correlation times for proton exchange in each tin pyrophosphate sample. Peak separation is greatest in the undoped sample (1074 Hz) which sets the maximum correlation time for proton exchange in this sample at about 0.0009 s. As indium doping is increased, peaks corresponding to the M-O-P and P-O-P sites approach one another thereby increasing the maximum correlation times for proton exchange. Peak separations of 750 and 732 Hz in the samples with 5 and 10 % indium loading put the maximum correlations times for proton exchange in these samples at about 0.0013 s. Peak separations in samples with 15 and 20 % indium loading are 388 and 448 Hz which increases maximum correlation times to 0.0026 and 0.0022 s respectively. This indicates that the maximum rate of proton hopping roughly increases with indium doping, suggesting that inter-polyhedron proton exchange is more favourable at higher indium loadings.

Crosspeaks are observed in the EXSY spectra of the tin pyrophosphates with 5 and 10 % indium loading (Figure 5.14). As the appearance of crosspeaks is dependent on the rate of chemical exchange being in the slow regime, we can anticipate that the rate of proton exchange is slower than the maximum correlation time that is given by the peak separation. In order to verify this, crosspeak intensities were measured via peak integration, normalized relative to the intensity of the diagonal peaks and used to construct build up curves from which rates of proton exchange could be extracted (Figure 5.16 A, B). Rates of proton exchange

were calculated by fitting the EXSY build up curves with an exponential function (Equation 5.4), where  $y$  is the normalized crosspeak intensity,  $A$  is a pre-exponential factor,  $y_0$  is the normalized crosspeak intensity at zero mixing time,  $x$  is the mixing time and  $t$  is the correlation time. The rate of proton exchange is the inverse of the correlation time.

$$y = y_0 + Ae^{\frac{-x}{t}} \quad (5.4)$$

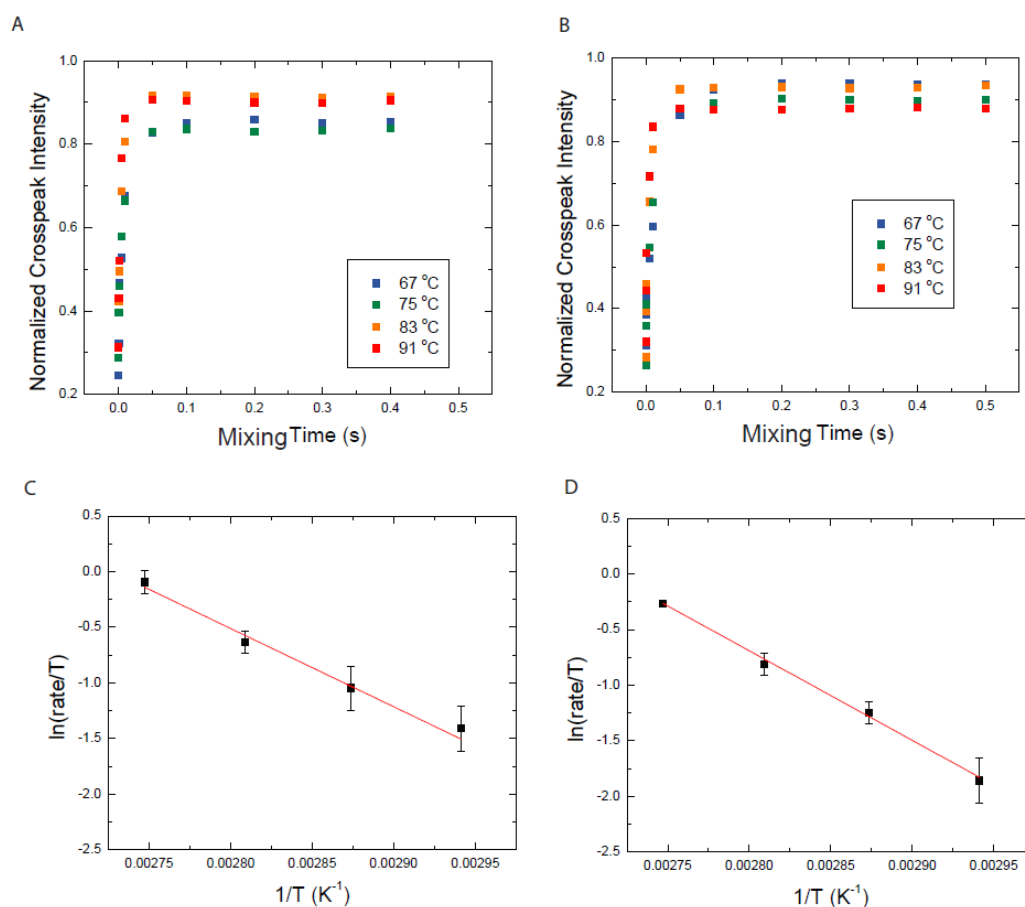


Figure 5. 16. Normalized crosspeak intensity build up curves for tin pyrophosphate samples with 5 and 10 % indium loading (A, B) and the respective Eyring plots (C, D).

Rates of proton exchange between M-O-P and P-O-P sites were similar, within error, for the 5 % and 10 % indium doped samples at each temperature (Figure 5.16 C, D). Additionally, the rates of proton exchange are slower than the maximum rates of proton exchange that are imposed by the peak separations in the 1D EXSY projections ( $331 \pm 40$  Hz vs.  $750 \pm 10$  Hz at 5 % indium loading and  $279 \pm 10$  Hz vs.  $732 \pm 10$  Hz at 10 % indium loading) which confirms that inter-polyhedron proton exchange occurs in the slow regime in these samples. The rate data also allowed activation energies for proton exchange to be calculated for both samples. The activation energies were  $0.61 \pm 0.09$  eV at 5 % indium loading and  $0.69 \pm 0.02$  eV at 10 % indium loading. As was observed in the EIS data, the activation energies were the same within error. It however must be noted that the magnitude of the error bars for these values is quite different. The error on the activation energy at 5 % indium loading is higher as a result of increased error in build-up curve fitting at lower temperature (Figure 5.16 C). This is caused by having fewer points with normalized intensities between 0.7 and 0.8 in the build-up curve and could be remedied by collecting additional data points at mixing times between 0.05 and 0.1 s. However, it can still be concluded that activation energies do not change significantly with indium loading which suggests that increased proton mobility is a result of increased proton concentration and is not caused by changes in the proton conduction mechanism as was concluded from the conductivity data.

Activation energies for proton exchange that were calculated based on the EXSY data were around 0.65 eV which is about 0.2 eV higher than the activation energies that were calculated based on the conductivity data. This is a result of the EXSY experiment being selective for M-O-P to P-O-P proton hopping whereas the EIS experiment measures total proton conductivity across the sample and is not selective for any one proton transport process. This, coupled with the fact that the samples that were analyzed via EIS were not stored in the glovebox, suggests that processes such as proton conduction through polyphosphoric acid and/or proton conduction through adsorbed water could be contributing to the observed activation energies. It is therefore concluded that activation energies that were calculated based on data from the EXSY experiment are more representative of proton conduction in the tin pyrophosphate phase.

Exact rates of proton exchange could not be determined based on the EXSY data for the undoped sample and samples with 15 and 20 % indium doping. It is predicted that the rate of inter-polyhedron proton exchange in the undoped sample is very slow relative to the peak separation resulting in crosspeaks with intensities that are too low to resolve via the EXSY experiment. At higher indium loading, where peak separation decreases to 388 and 448 Hz, it is anticipated that crosspeak intensities are lost in the intensity of the approaching diagonal peaks which makes them difficult to observe and quantify. Therefore, all that can be said regarding inter-polyhedron proton transfer in these samples is that the absence of coalescence places that maximum correlation times at 0.0009 s, 0.0027 s and 0.0022 s for the

undoped, 15 % indium and 20 % indium samples respectively. It is anticipated that selective inversion, another technique that is used to quantify chemical exchange, may be more successful in extracting rate data from these systems as this experiment is less reliant on well-resolved spectra.<sup>27</sup>

#### **5.4 Conclusion**

Tin pyrophosphates are complex materials whose potential as solid-state proton conductors is heavily reliant on the synthetic history of the sample. Therefore, the samples that were presented in this thesis were treated to remove impurity phases such as phosphoric acid and polyphosphoric acid that have previously been proposed to contribute to measured proton conductivities. <sup>1</sup>H and <sup>31</sup>P NMR experiments, which were performed to characterize protonated phosphorous environments in these materials, revealed two proton environments corresponding to hydrogen-bonded positions on the phosphate tetrahedra and the metal octahedra in protonated tin pyrophosphate.

The identification of two distinct proton environments allowed for site-specific proton dynamics to be determined in these materials for the first time. EXSY experiments showed that maximum correlation time for inter-polyhedron proton exchange increases as a function of indium loading. Activation energies for proton transport in these materials were also calculated based on the EXSY data and proton conductivity measurements. These remained relatively constant as a function of indium loading which suggests that observed increases in proton conductivity are a result of increased proton concentration and are not caused by changes to the proton conduction mechanism.

## 5.5 References

1. Carrette, L., Friedrich, K. A. & Stimming, U. Fuel Cells : Principles , Types , Fuels , and Applications. *ChemPhysChem* **1**, 162–193 (2000).
2. Sato, Y., Shen, Y., Nishida, M., Kanematsu, W. & Hibino, T. Proton conduction in non-doped and acceptor-doped metal pyrophosphate ( $\text{MP}_2\text{O}_7$ ) composite ceramics at intermediate temperatures. *J. Mater. Chem.* **22**, 3973 (2012).
3. Paschos, O., Kunze, J., Stimming, U. & Maglia, F. A review on phosphate based , solid state , protonic conductors for intermediate temperature fuel cells. *J. Phys. Condens. Matter* **23**, 234110 (2011).
4. Gervasio, D. *Fuel Cell Science: Theory, Fundamentals, and Biocatalysis*. (John Wiley & Sons, 2010).
5. Shen, Y., Nishida, M. & Hibino, T. Synthesis and characterization of dense  $\text{SnP}_2\text{O}_7 - \text{SnO}_2$  composite ceramics as intermediate-temperature proton conductors. 663–670 (2011). doi:10.1039/c0jm02596h
6. Haile, S. M., Chisholm, C. R. I., Sasaki, K., Boysen, D. A. & Uda, T. Solid acid proton conductors: from laboratory curiosities to fuel cell electrolytes. *Faraday Discuss.* **134**, 17–39 (2007).
7. Anfimova, T. *et al.* The effect of preparation method on the proton conductivity of indium doped tin pyrophosphates. *Solid State Ionics* **278**, 209–216 (2015).
8. Szirtes, L., Megyeri, J. & Kuzmann, E. Thermal behaviour of tin (II/IV) phosphates prepared by various methods. *J Therm. Anal. Calorim.* **99**, 415–421 (2010).
9. Kim, G., Griffin, J. M., Blanc, F., Haile, S. M. & Grey, C. P. Characterization of the Dynamics in the Protonic Conductor  $\text{CsH}_2\text{PO}_4$  by  $^{17}\text{O}$  Solid-State NMR Spectroscopy and First-Principles Calculations : Correlating Phosphate and Protonic Motion. *J. Am. Chem. Soc.* **137**, 3867–3876 (2015).
10. Nishida, M. & Tanaka, T. Solid-state NMR study of dopant effects on the chemical properties of Mg-, In-, and Al-doped  $\text{SnP}_2\text{O}_7$ . *Magn. Reson. Chem.* **52**, 163–71 (2014).
11. Nalini, V. Synthesis , Structure , and Proton Conductivity of Meta- and Pyrophosphates Vajeeston Nalini Dissertation for the degree of Doctor of Philosophy Functional Energy Related Materials in Oslo ( FERMiO ) Centre for Materials Science and Nanotechnology ( SMN ). (2010).

12. Kreller, C. R. *et al.* Intragranular Phase Proton Conduction in Crystalline  $\text{Sn}_{1-x}\text{In}_x\text{P}_2\text{O}_7$  ( $x = 0$  and  $0.1$ ). *J. Phys. Chem. C* **121**, 23896–23905 (2017).
13. Toyoura, K., Terasaka, J., Nakamura, A. & Matsunaga, K. A first-principles study on proton conductivity of acceptor-doped tin pyrophosphate. *J. Phys. Chem. C* **121**, 1578–1584 (2017).
14. Chernaya, V. V *et al.* Synthesis and Investigation of Tin ( II ) Pyrophosphate  $\text{Sn}_2\text{P}_2\text{O}_7$ . *Chem. Mater.* **17**, 284–290 (2005).
15. Kreller, C. R., Wilson, M. S., Mukundan, R., Brosha, E. L. & Garzon, F. H. Stability and Conductivity of  $\text{In}^{3+}$ -Doped  $\text{SnP}_2\text{O}_7$  with Varying Phosphorous to Metal Ratios. *ECS Electrochem. Lett.* **2**, F61–F63 (2013).
16. Nishida, M., Tanaka, T. & Kanematsu, W. Solid-state NMR study on changes of phosphate and proton species in metal pyrophosphate composite ( $\text{MP}_2\text{O}_7\text{-MO}_2$ ) ceramics. *Magn. Reson. Chem.* **55**, 570–578 (2017).
17. Foran, G. Y., Brouwer, D. H. & Goward, G. R. Quantifying Site-Specific Proton Dynamics in Phosphate Solid Acids by  $^1\text{H}$  Double Quantum NMR Spectroscopy. *J. Phys. Chem. C* [acs.jpcc.7b06034](https://doi.org/10.1021/acs.jpcc.7b06034) (2017). doi:10.1021/acs.jpcc.7b06034
18. van Moorsel, G.-J. M. P., van Eck, E. R. H. & Grey, C. P.  $\text{Pr}_2\text{Sn}_2\text{O}_7$  and  $\text{Sm}_2\text{Sn}_2\text{O}_7$  as High-Temperature Shift Thermometers in Variable Temperature  $^{119}\text{Sn}$  MAS NMR. *J. Magn. Reson. Ser. A* **113**, 159–163 (1995).
19. Yamagiwa, N. Visual Exhibition of Atomic Radius. *Let's Visualize the Chemistry!* 1 (2005). Available at: [www.f.u-tokyo.ac.jp/~kanai/document/img/ionic\\_radius.pdf](http://www.f.u-tokyo.ac.jp/~kanai/document/img/ionic_radius.pdf). (Accessed: 15th April 2019)
20. Yasuda, T. & Watanabe, M. Protic ionic liquids: Fuel cell applications. *MRS Bull.* **38**, 560–566 (2013).
21. Keeler, J. Chapter 8. Relaxation. 1–24 (2004). Available at: [http://www-keeler.ch.cam.ac.uk/lectures/understanding/chapter\\_8.pdf](http://www-keeler.ch.cam.ac.uk/lectures/understanding/chapter_8.pdf). (Accessed: 26th February 2019)
22. Keeler, J. 2. NMR and Energy Levels. in *Understanding NMR Spectroscopy* 2-1-2–21 (2004).
23. Lee, K. *et al.* Intermediate temperature fuel cells vis an ion-pair coordinated polymer electrolyte. *Energy Environ. Sci.* **11**, 979–987 (2018).
24. Bruce, P. G. *Solid State Electrochemistry*. (Cambridge University Press, 1995).

25. Kleckner, I. R. & Foster, M. B. An Introduction to NMR-based Approaches for Measuring Protein Dynamics. *Biochim Biophys Acts* **1814**, 942–968 (2011).
26. Reich, H. J. 8.1 Relaxation in NMR Spectroscopy. 1–13 (2017).
27. Bain, A. D. Chemical exchange in NMR. *Prog. Nucl. Magn. Reson. Spectrosc.* **43**, 63–103 (2003).
28. Bain, A. D. Chemical Exchange. in *Annual Reports on NMR Spectroscopy* (ed. Web, G.) 23–48 (Elsevier Ltd, 2008). doi:10.1016/S0066-4103(07)63002-6

## **Chapter 6: Solid-State NMR Study of Boron Coordination Environments in Boron-Containing Polymers**

This chapter discusses the use of solid-state NMR to probe boron coordination environments in boron-containing polymers: silicone boronate acids (SiBA) and commercial Silly Putty. The original intention of this research was to use solid-state  $^1\text{H}$  NMR to characterize hydrogen bonding in SiBA elastomers as these interactions had been previously confirmed via infrared spectroscopy. However, peaks corresponding to hydrogen-bonded centers could not be identified using  $^1\text{H}$  NMR as these signals were significantly broadened. Solid-state  $^{11}\text{B}$  NMR was proven to be an ideal diagnostic method to investigate boron coordination environments in these boron-containing polymers.

There are two main advantages to using solid-state NMR to investigate boron coordination environments in these systems. The first is that lineshapes from quadrupolar nuclei such as  $^{11}\text{B}$  vary significantly depending on their coordination environment. Additionally, the technique is applicable for non-crystalline systems. The ability to perform experiments at high magnetic field and the use of advanced multiple-quantum MAS (MQMAS) NMR pulse sequences allow multiple, overlapping boron coordination environments to be elucidated. After successfully characterizing three- and four-coordinate boron environments in SiBA elastomers, the MQMAS technique was employed to characterize boron coordination environments in a commercial Silly Putty sample.

A portion of this chapter, the discussion of boron coordination environment in SiBA elastomers, is adapted from “Solid State NMR Study of Boron

Coordination Environments in Silicone Boronate (SiBA) Polymers” which was published in *Macromolecules* copyright 2019 American Chemical Society (G. Y. Foran, K. J. Harris, M. A. Brook, B. Macphail and G. R. Goward. **2019**, 52(3), 1055-1064). The SiBA materials analyzed here were prepared by B. Macphail. All NMR experiments were performed by G. Y. Foran. K. J. Harris assisted in the set up and the analyses of the  $^{11}\text{B}$  MQMAS experiments. The infra-red spectrum and Young’s Modulus measurements were acquired by B. Macphail. The initial draft of the manuscript was prepared by G. Y. Foran and was then edited in collaboration with M. A. Brook (SiBA properties and synthesis) and G. R. Goward (solid-state  $^{11}\text{B}$  NMR).

## 6.1 Introduction

The introduction of boronic acid groups onto a silicone backbone dramatically changes the properties of the polymer. In addition to the conversion of mobile oils into elastomeric materials, the presence of the boronic acid enhances the hydrophilic nature of the materials. The SiBA and Silly Putty materials discussed here are non-Newtonian fluids. Meaning that the functional boronic acid groups exist in a dynamic equilibrium between free boronic acids and boronic acid dimers, which act as crosslinks;<sup>1,2</sup> the changing interactions allow the materials to flow under their own weight at a rate that depends upon the weight fraction of boronic acids.<sup>3</sup>

SiBA are reliably synthesized via a two-step process in which vinylphenylboronic acid (VPBA) is first protected by a dimethyl-L-tartrate group

and then grafted onto the a polydimethylsiloxane (PDMS) backbone via a platinum-catalyzed hydrosilylation reaction;<sup>4</sup> both telechelic (boronic acids on the ends of polymer chains)<sup>4</sup> (Figure 6.1-**B-i**) and pendant (boronic acids along the chains at different densities)<sup>4</sup> (Figure 6.1-**B-ii**) materials were prepared.<sup>3</sup> The initial products of this process are oils but, upon exposure to moisture, the protecting groups undergo hydrolysis, freeing the boronic acid-functionalized end groups that then interact to form elastomeric films via a ‘spread and set’ process.<sup>3</sup>

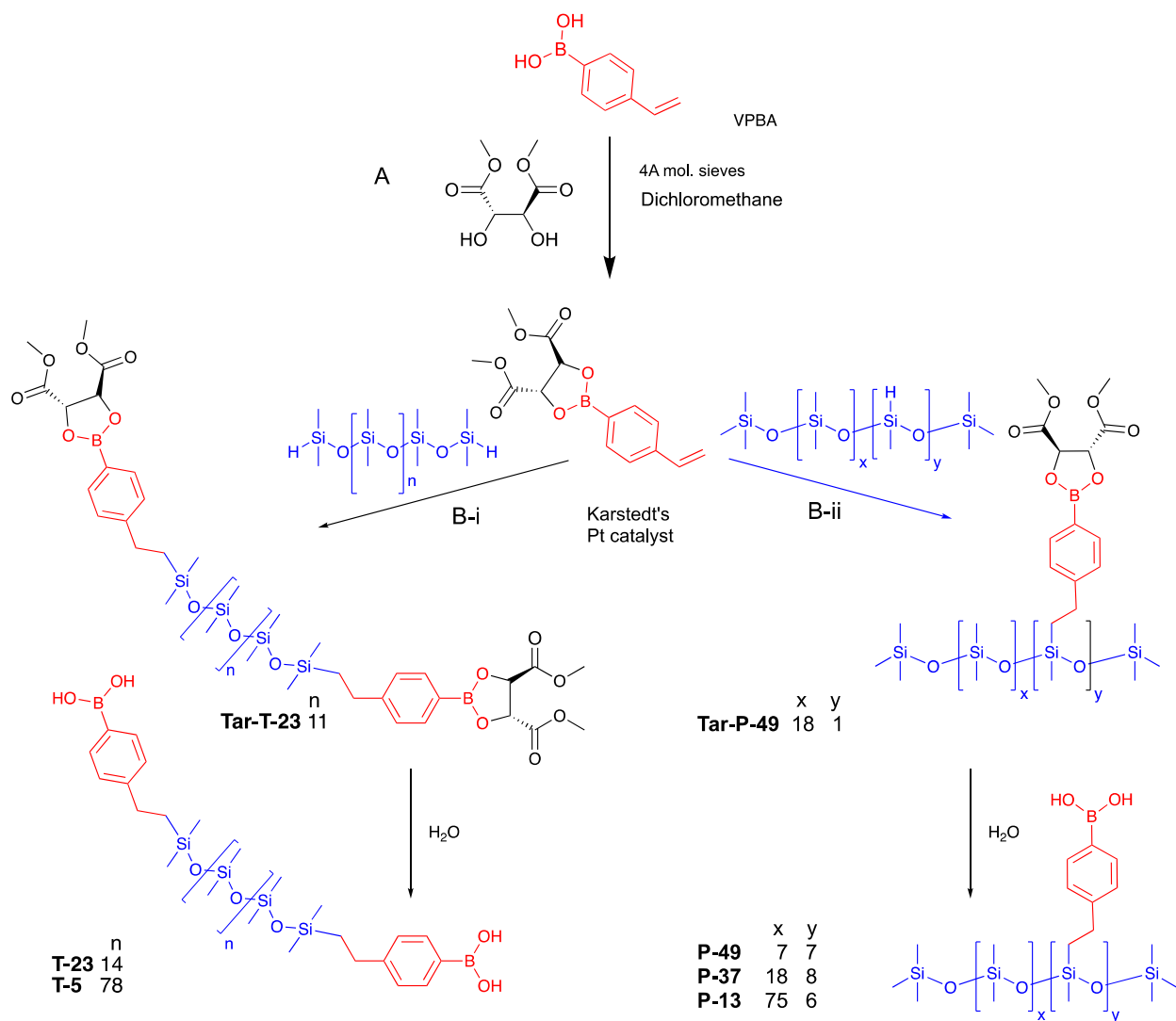


Figure 6. 1. The two-step synthesis of SiBA: (A) protection with dimethyl-L-tartrate followed by (B) hydrosilylation of the protected VPBA to yield telechelic (B-i) and pendant (B-ii) protected Tar-SiBA. (C) The addition of moisture results in hydrolysis of the protecting group to yield SiBA elastomers. Possible crosslink bonding modes are illustrated in Figure 6.3.

The most common precedent material for SiBA elastomers is the unusual polymer formed when silicones are combined with boric acid to form ‘silly putty’ or ‘funny putty’. The precise mechanism of crosslinking interaction in these materials has been the subject of some debate in the literature. Crosslinking

processes have been proposed to involve hydrogen bonding through OH groups, dative crosslinking between boronic acids, dative bonding (covalent bonding where bond electrons come from the same atom) between boronic acids and oxygen atoms on the silicone backbone, and/or covalent bonds at a three- or four-coordinate boron center (Figure 2.A-C). The interactions that are responsible for crosslinking in Silly Putty will also be investigated in this chapter.

Interactions between boronic acid and silicones have previously been investigated in polysaccharides,<sup>1</sup> such as guar, that have been mixed with borate,  $B(OH)_4$ .<sup>5</sup> Polymerization occurs when borate condenses with diols on the polysaccharide (Figure 2.D). A second condensation reaction can also occur, resulting in either intermolecular bonding (crosslinking) or intramolecular bonding (ring formation) (Figure 2.E). Gel formation in this system was found to be dependent on a minimum borate concentration.<sup>5</sup> This example illustrates that the extent of crosslinking at the boron center can be influenced by the relative proportion of boronic acid that is present in the material.

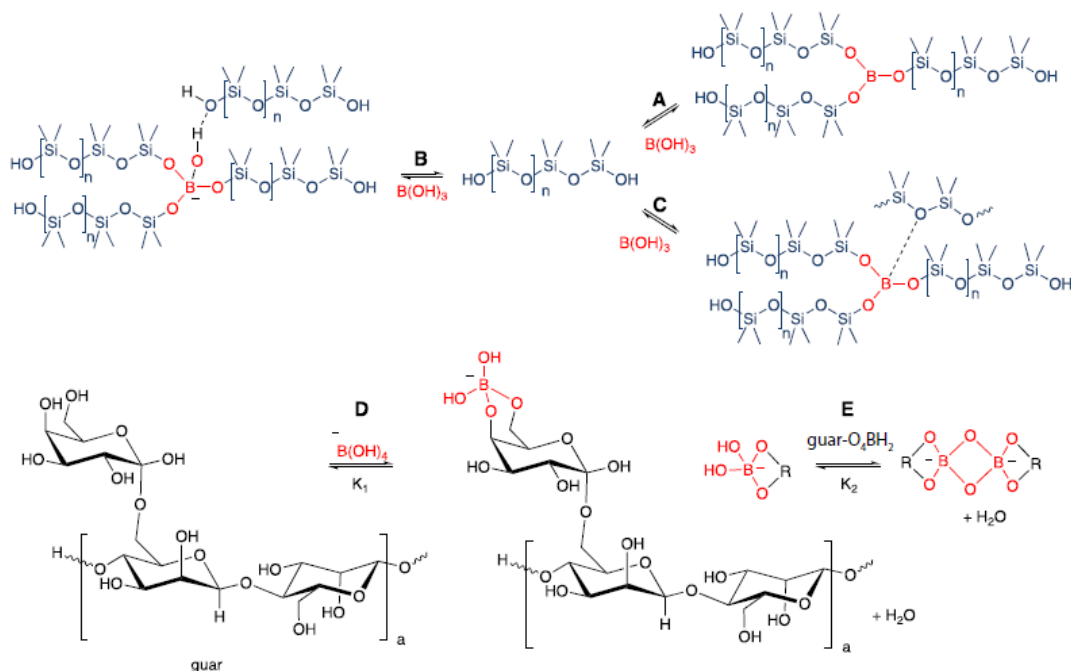


Figure 6. 2. Elastomers can be formed via the condensation of boric acid with PDMS. Crosslinking via three- (A) and four- (B, C) coordinate centers is shown. Gel formation via the condensation of borate with guar polysaccharide. Single (D) and double (E) condensation reactions are possible with  $k_2$  being twice as large as  $k_1$ .

The mechanical properties of SiBA elastomers, for example, Young's Moduli, show a direct correlation with boronic acid density on the polymer, which implicates boronic acids in the crosslinking process, similar to the case with guar and borate.<sup>6</sup> It was initially assumed that crosslinking in SiBA involves 1:1 hydrogen bonding between boronic acid groups that leads to chain extension (and an increase in viscosity), in addition to crosslinking provided by dative bonding between boronic acid sites (Figure 6.3).<sup>3,6</sup> However, the exact nature of the bonding remains poorly understood.

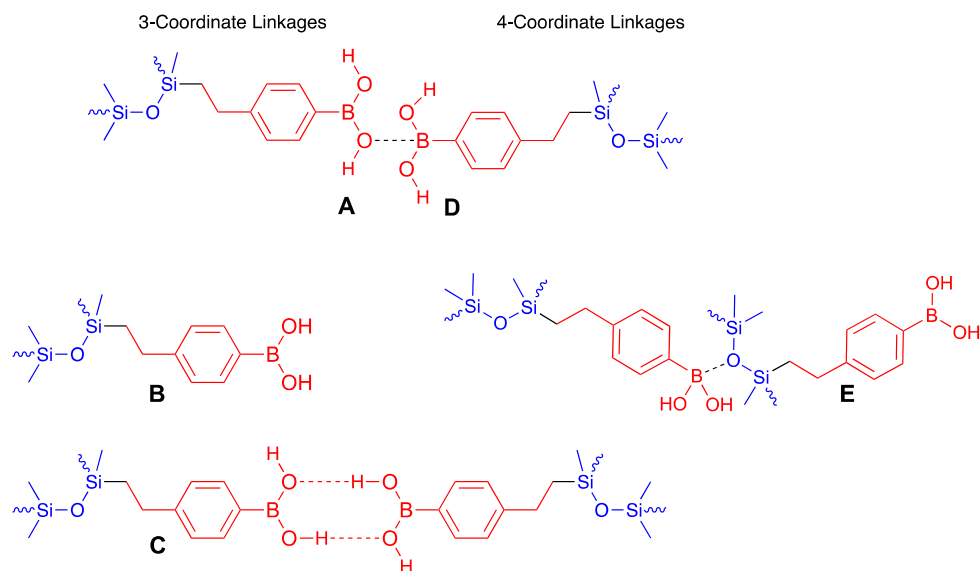


Figure 6. 3. Possible boronic acid binding motifs. Three-Coordinate: A dative bonding between boronic acids, B free boronic acid, C hydrogen-bonded boronic acids. Four-Coordinate: D dative bonding between a boronic acids, E dative bonding between a boronic acid and oxygen on the PDMS backbone.

Boronic acid derivatives represent a promising alternative to traditional organic polymers,<sup>7</sup> particularly in the field of macromolecular chemistry where these materials are known for their ability to self-assemble via reversible covalent bonding.<sup>8-10</sup> However, further investigation into the boron coordination environments that exist in SiBA elastomers is essential as several modes of covalent bonding including: boroxine formation (B-O trimers resulting from the dehydration of boronic acid), Lewis acid/base coordination, spiroborate (boron compounds with two oxygen-based chelating ligands) formation and esterification are possible.<sup>11</sup> Additionally, non-covalent interactions such as hydrogen bonding can have a significant role in the structure of these supramolecular assemblies.<sup>11</sup> To this end,

solid-state  $^{11}\text{B}$  NMR will be employed to elucidate boron coordination environments in SiBA elastomers.

Solid-state NMR was applied to probe the characteristics of the boron centers in SiBA elastomers because the technique has been used successfully in non-crystalline systems.<sup>12,13</sup>  $^{11}\text{B}$  is a quadrupolar nucleus and therefore possesses an asymmetric distribution of its nuclear charge causing it to interact anisotropically with the electric field gradient (EFG).<sup>14</sup> The resultant lineshape is therefore highly dependent on the symmetry of the nuclear environment.  $^{11}\text{B}$  tends to exist in either three-coordinate trigonal planar or four-coordinate tetrahedral environments. The differing symmetry of these environments allows them to be identified by lineshape fitting.<sup>15</sup>  $^{11}\text{B}$  solid-state NMR has previously been used in the characterization of both minerals,<sup>15</sup> and glasses.<sup>12,16</sup>  $^{11}\text{B}$  solid-state NMR has also been used to investigate boron coordination environments in other well-understood systems including boron-doped  $\text{TiO}_2$  and boron-containing small molecules.<sup>17,18</sup> Solid-state  $^{11}\text{B}$  NMR is not typically used to study polymers due in part to the inherent challenge of employing quadrupolar NMR techniques in mobile and amorphous materials. However, Kobera et al.<sup>19</sup> have employed the technique to study less mobile systems such as cured alkali-catalyzed phenol-formaldehyde resins. Quantum chemical calculations were performed concurrently with solid-state NMR for the purpose of confirming experimentally derived quadrupolar parameters in some of these studies.<sup>18,19</sup> However, as this technique depends on the use of optimized structures, quantum chemical calculations were not deemed to be an

efficient technique for the analysis of boron coordination in SiBA elastomers as the amorphous nature of these materials makes it impossible to obtain crystal structures.

These studies have shown that typical quadrupole coupling constant ( $C_Q$ ) values for trigonal planar boron range from 2 to 3 MHz with much lower  $C_Q$  values being reported for tetrahedral environments due to increased symmetry around the  $^{11}\text{B}$  nucleus.<sup>12,15</sup> The asymmetry parameter ( $\eta$ ), which depends on the symmetry of the ligands in the immediate coordination sphere, ranges between 0 and 1.<sup>20</sup> Here,  $^{11}\text{B}$  NMR is used to elucidate the tendencies toward three- versus four-coordinate boron centers in the SiBA elastomers of interest and in a commercial Silly Putty sample.

## 6.2 Experimental

### 6.2.1 Synthesis of SiBAs

SiBA polymers were synthesized according to a previously published procedure.<sup>2-4</sup> Pendant samples were prepared with 49%, 37% and 13% boronic acid, respectively (**P-49**, **P-37**, **P-13**), while telechelic SiBA samples were produced with boronic acid loadings of 23% and 5% (**T-23**, **T-5**). Weight fraction was calculated as  $\text{CH}_2\text{CH}_2\text{C}_6\text{H}_4\text{B}(\text{OH})_2/\text{total molecular weight}$  after hydrolysis. The specifications for each are listed here with x, y and n labels corresponding to the PDMS chain lengths presented in Figure 6.1: 49% **P-49** ( $x = 7$ ,  $y = 7$ ), 37% **P-37** ( $x = 18$ ,  $y = 8$ ) and 13% **P-13** ( $x = 75$ ,  $y = 6$ ) respectively (Figure 6.1.B-ii).

Telechelic SiBA were produced with boronic acid loadings of 23% **T-23** (n = 12) and 5% **T-5** (n = 76).

### 6.2.2 Thermal gravimetric analysis

Thermal gravimetric analysis (TGA) was performed on 5-10 mg SiBA samples using a Mettler Toledo TGA-DSC 3+ system. Samples were heated from 30 to 800 °C at a rate of 10 °C per minute. The experiments were performed under argon flow.

### 6.2.3 Solid-State NMR

<sup>11</sup>B NMR spectra were collected at three different magnetic fields: 7.0, 11.7 and 20.0 T with spinning speeds of 15, 30 and 30 kHz, respectively. Background suppression, achieved through the use of an echo-containing pulse sequence, was used to limit the contribution of signals from boron contained within the probe to the experimentally observed spectra. Samples were referenced to an external aqueous solution of boric acid (19.6 ppm) in all cases.<sup>13</sup> At 7.0 T, spectra were collected using a 4.5 μs 90° pulse at 40 W using a 4 mm wide-bore probe with 15 kHz MAS. At 11.7 T, spectra were collected using a 15 μs 90° pulse at 8.9 W using a 2.5 mm probe with 30 kHz MAS. At 20.0 T, spectra were collected using a 10 μs 90° pulse at 7.24 W using a 1.9 mm probe with 30 kHz MAS. Selective pulses were used to acquire spectra at 20.0 and 11.7 T, non-selective pulses were used at 7.0 T due to significant line broadening at the lower magnetic field. All experiments were performed at room temperature. Spectra of **T-5** at 7.0 T and 20.0 T were collected without spinning due to difficulties associated with achieving a stable MAS rate for this low viscosity sample.

In addition to the background suppressed spectra, multiple quantum magic angle spinning (MQMAS) spectra were collected at 20.0 T with 30 kHz MAS. The spectra were collected using a three-pulse sequence comprised of an excitation pulse (1.2  $\mu$ s, 275 W), a reconversion pulse (3.6  $\mu$ s, 275 W) and a selective pulse (17.5  $\mu$ s, 0.58 W). Due to the relatively low signal intensity obtained via triple quantum excitation and the presence of multiple unique boron chemical environments in the material, the success of this technique was highly dependent on the use of a magnet with sufficiently high field. In this case, MQMAS data were only successfully acquired at 20.0 T.

## 6.3 Results and Discussion

### 6.3.1 $^{11}\text{B}$ MQMAS NMR

Boric acid, a fully characterized compound that, in crystalline form, is comprised of ordered planar  $\text{B}(\text{OH})_3$  layers, was used here as a model three-coordinate boron sample. Lineshape fitting yielded:  $C_Q = 2.5$  MHz and  $\eta = 0.1$  (Figure 6.4A). This is consistent with data presented by MacKenzie and Smith for trigonal planar boron centers with three identical ligands.<sup>15</sup> Tetrahedral four-coordinate boron environments tend to be highly symmetrical.<sup>20,21</sup> This configuration minimizes interaction with the EFG which results in very low  $C_Q$  values.<sup>20,21</sup> Tetrahedral boron centers with four identical ligands tend to crystallize with enough symmetry such that they interact minimally with the EFG. As a result, these samples appear to give rise to only isotropic spectra under MAS conditions.<sup>20</sup> Therefore, quadrupolar parameters cannot be reliably extracted from these lineshapes. The  $^{11}\text{B}$  lineshape for datolite, a mineral that contains  $\text{BO}_4$  tetrahedra,

has a negligible  $C_Q$  value (Figure 6.4**B**).<sup>22</sup> However, tetrahedral centers that are not surrounded by four identical ligands, such as the crosslinked sites in the elastomers studied here, tend to have small  $C_Q$  values (typically around 0.5 MHz).<sup>15</sup> These lineshapes, like the one presented in Figure 6.4**B**, are difficult to fit directly when the high magnetic fields that are necessary to distinguish individual sites are employed. MQMAS is used here to measure and extract values for the quadrupole product ( $P_Q$ ) which is a combination of the quadrupole coupling constant ( $C_Q$ ) and the asymmetry parameter ( $\eta$ ) (Equation 6.1).

$$P_Q = C_Q^2 \left( 1 + \frac{\eta^2}{3} \right) \quad (6.1)$$

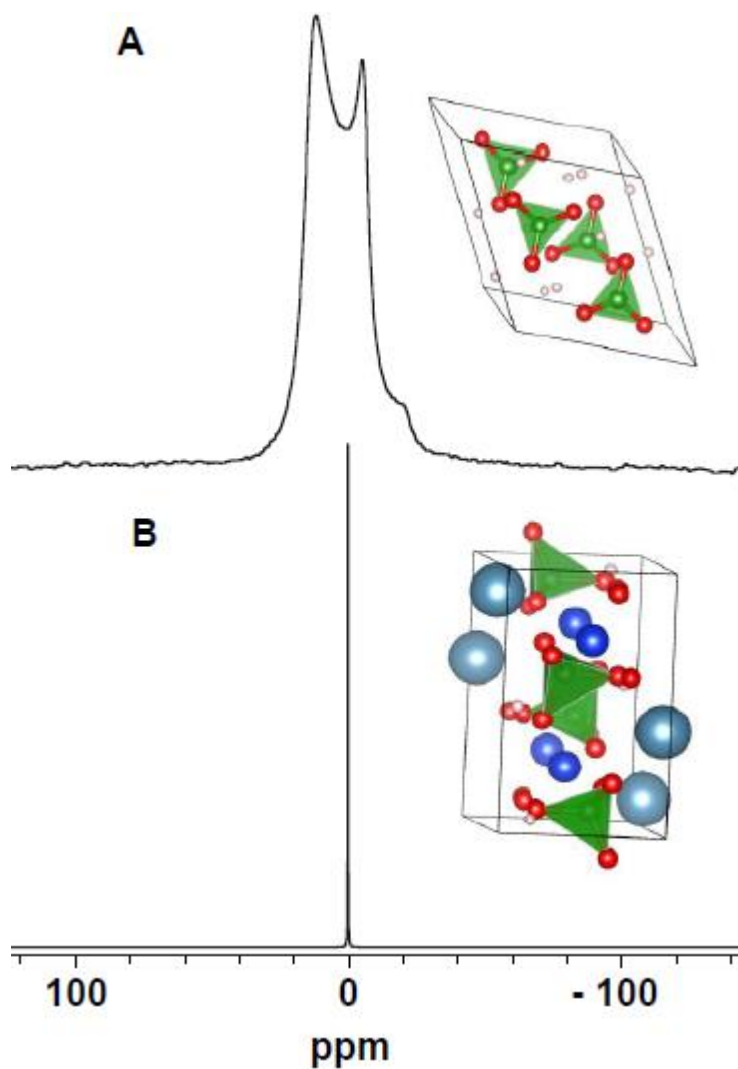


Figure 6. 4.  $^{11}\text{B}$  spectra of boric acid (A) and datolite (B). A was acquired experimentally at 7.0 T with 15 kHz spinning. B is a simulated spectrum that was created based on data obtained by Hansen et al.<sup>22</sup>

Line broadening, caused by distributions of chemical shift and EFG parameters, tends to complicate lineshape fitting, as it is difficult to disentangle superimposed peaks.<sup>20,21</sup> Unlike with dipolar coupling, anisotropy found in  $^{11}\text{B}$  spectra can only be partially improved by MAS alone. Typical MAS NMR, where the sample is spun at  $54.7^\circ$  relative to the external magnetic field, removes the line

broadening due to the first-order anisotropic term. Removing the second anisotropic term requires spinning the sample at an angle of  $37.4^\circ$  or  $79.1^\circ$ .<sup>20</sup> Simultaneously spinning a sample at two different angles is difficult and requires specialized probes.<sup>14</sup> In this work and much more commonly, improved resolution of non-chemically equivalent boron sites in our elastomers is obtained by increasing the magnetic field strength in addition to performing two-dimensional (2D)  $^{11}\text{B}$  MQMAS experiments. Increasing the external magnetic field strength tends to reduce the overlap of peaks from non-chemically equivalent sites because the quadrupolar interaction is inversely proportional to the strength of the magnetic field.<sup>21</sup> Although peak overlap is reduced, the resultant line narrowing removes the quadrupolar features making it difficult to characterize boron sites as three- or four-coordinate.<sup>23</sup> 2D MQMAS is employed such that the information contained in the EFG can be obtained based on differences in chemical shift in the direct ( $F_2$ ) and indirect ( $F_1$ ) dimensions.<sup>24</sup> The 2D experiment produces a spectrum where the  $F_2$  dimension retains the anisotropic quadrupolar interaction and the  $F_1$  dimension shows the isotropic transitions.<sup>23</sup> The lineshape in the  $F_2$  dimension is the same as that which is observed in conventional MAS NMR experiments,<sup>23,24</sup> whereas isotropic lineshapes can be observed in the  $F_1$  dimension following data processing.<sup>23–25</sup> The absence of quadrupole-induced line broadening in the  $F_1$  dimension means that previously overlapped peaks are separated from each other.<sup>23–25</sup> Analyses of the MQMAS data and lineshape fitting allow us to obtain EFG parameters which can then be used to draw analogies to previously studied

crystalline and glassy systems (Figure 6.4) to interpret the  $^{11}\text{B}$  data, and to thereby characterize the bonding environments in the SiBA elastomers.<sup>12,15,25,26</sup> Here we demonstrate that different boron coordination environments in these elastomeric materials can be distinguished based on their quadrupolar lineshapes and quadrupolar parameters.<sup>20,21</sup>

### **6.3.2 Boron Coordination Environments in SiBA Elastomers**

SiBA materials were prepared in two different structural motifs, pendent and telechelic (Figure 6.1), with different boronic acid loadings that were calculated based on the mass of grafted boronic acid relative to the total mass of the sample. Boronic acid loading was readily verified via thermogravimetric analysis (TGA) (Figure 6.5). When subjected to thermal degradation in an inert atmosphere between 400 and 650 °C, long chain PDMS, the parent polymer of SiBA, undergoes a single-step degradation which can be attributed to the breaking/reforming of Si-O bonds.<sup>27</sup> The products resulting from the degradation reaction, mostly cyclic tetramers ((Me<sub>2</sub>SiO)<sub>4</sub>), are volatile, causing significant mass loss.<sup>27</sup> VPBA, the parent boron-containing material, undergoes two decomposition events which result in a total mass loss of 72 % (shown in Figure 6.5). The decomposition profile of the SiBA materials more closely matched the decomposition profile of PDMS, as a single decomposition event is observed (Figure 6.5). The percent mass loss increases with decreasing boronic acid loading, which suggests that most of the observed mass loss is a result of the degradation of the PDMS backbone. The

resultant mass is comprised of decomposed boronic acid and can be used to rank the elastomeric materials based on their boronic acid content.

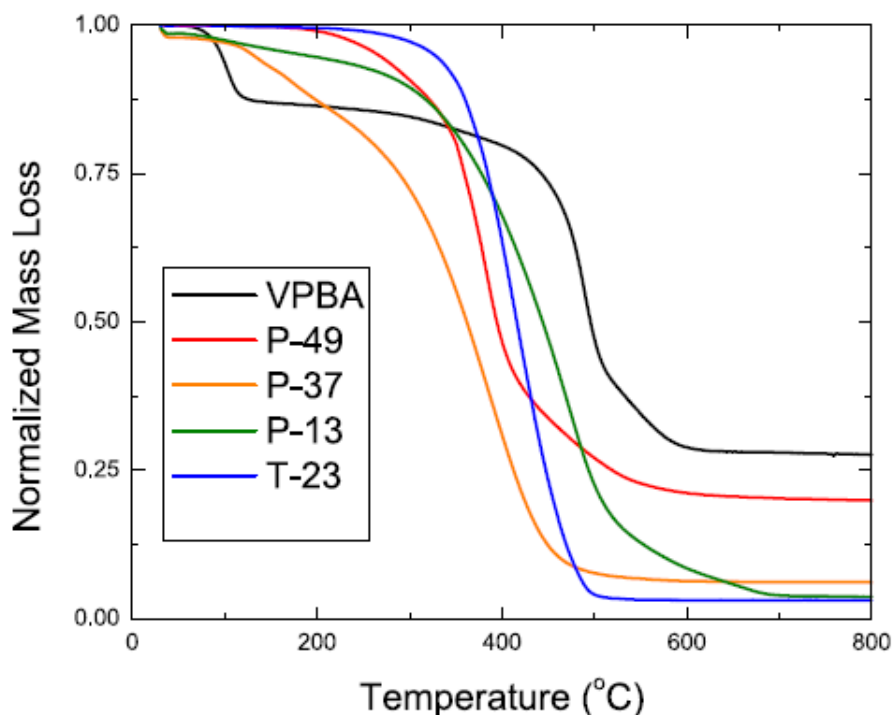


Figure 6. 5. Thermogravimetric decomposition profiles of VPBA and SiBA materials acquired between 30 and 800 °C with a 10 °C/min heating rate under an argon atmosphere. **T-5** was not analyzed via TGA due to low viscosity.

It was previously demonstrated that, after exposure to water, pendant SiBA materials have larger Young's moduli (**P-53** 2285, **P-37** 2192, **P-13** 2149 kPa) than the telechelic SiBA materials (**T-23** 171 and **T-5** 154 kPa),<sup>6</sup> due to higher crosslink densities in the pendant samples. Dimethylsilicones are not capable of self-crosslinking. Therefore, the crosslinking in SiBA is associated with the boronic acid group; note that the tartrate-protected SiBA compounds, e.g., **Tar-T-23** and **Tar-P-49** (Figure 6.1) are oils. Differences in crosslink density can potentially be

attributed to two factors: the weight percent boronic acid and the relative positioning of the boronic acid groups. Previous work, based on only two SiBA samples, proposed that the spacing between boronic acids was ultimately more important.<sup>6</sup>

Here, the crosslinked boron sites were examined using solid-state NMR with site-specific resolution to facilitate a more quantitative analysis of the relative proportion of four-coordinate boron and, therefore, the nature of crosslinking. That is, the influence of boronic acid spacing, telechelic or pendant, and boronic acid loading on crosslinking can be determined. An assignment of the structural nature of various boron coordination environments is also of interest. Several possibilities for boronic acid dimer interactions include: B-OH $\cdots$ O-B hydrogen bonds (Figure 6.3C); B-O-B covalent bonds (Figure 6.3 D); a mixture of the two; and Lewis acid/base interactions between boron and oxygen atoms on silicone chains (Figure 6.3E). It was anticipated that the quantification of three- and four-coordinate boron environments may be used to determine the most likely structural motifs in the crosslinked elastomers.

Background suppressed  $^{11}\text{B}$  spectra are collected at three different magnetic fields: 7.0, 11.7 and 20.0 T (Figure 6.6 A-C). At lower fields, non-equivalent boron sites are superimposed upon one another making it difficult to deconvolute the number of boron sites present in each material and their respective coordination numbers (Figure 6.6A, B). It can however be concluded that multiple boron

coordination environments are present as appropriate lineshape fitting cannot be achieved using a single quadrupolar lineshape.

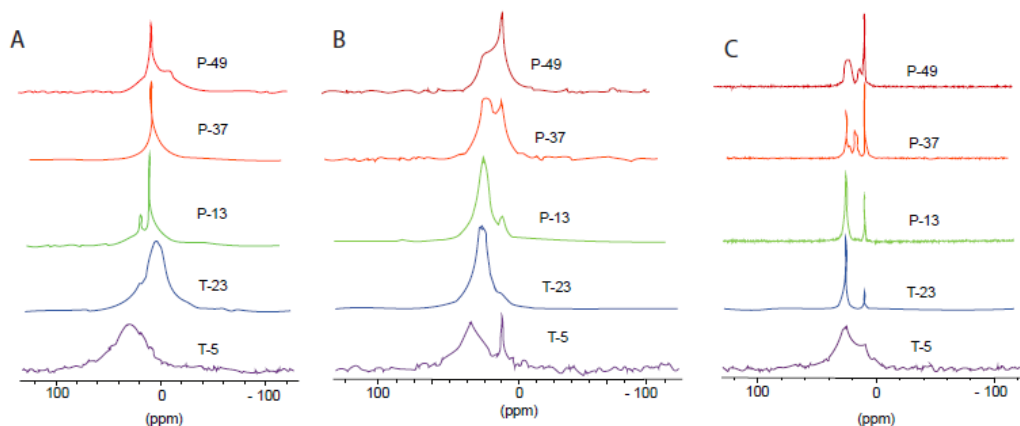


Figure 6.6. Background suppressed  $^{11}\text{B}$  spectra of each elastomer collected at a magnetic field of 7.0 T with 15 kHz MAS (A), 11.7 T with 30 kHz MAS (B) and 20.0 T with 30 kHz MAS (C). The spectra of the **T-5** sample were collected without spinning at 7.0 and 20.0 T (A, C).

Spectra that were collected at 20.0 T are sufficiently well-resolved to reveal individual boron sites (Figure 6.6C). Three distinct groups of sites can be observed in **P-49** and **P-37** (Figure 6.6C). At lower boron loadings, two distinct groups of sites are observed (Figure 6.6C). It can be reasonably assumed that the narrow peak, located around 9 ppm, corresponds to a four-coordinate boron environment and that the sites with the highest chemical shifts (20 to 30 ppm range) correspond to three-coordinate boron environments. These assumptions are made based on typical chemical shift ranges for three- and four-coordinate boron centers.<sup>15</sup> However, due to overlap in typical chemical shift ranges and the general lack of quadrupolar lineshape features at higher fields, the sites with chemical shifts between 13 and

20 ppm in **P-49** and **P-37** cannot readily be assigned to a particular type of coordination environment. Additional NMR techniques must be used to more accurately characterize these sites using quadrupolar parameters such that boron coordinate environments can be proposed.

To this end, MQMAS NMR was performed at 20.0 T with 30 kHz MAS (Figure 6.7). The purpose of this experiment was to separate chemically non-equivalent sites and to obtain more easily verifiable values for the quadrupolar parameters of each site. The quadrupolar product ( $\rho$  from Equation 6.1) is calculated for each site based on the differences between the chemical shifts in the direct and indirect dimensions. As the value of  $\eta$  is fixed between 0 and 1, a range of quadrupolar parameters with which a peak can be fit is obtained. Five distinct boron sites are fit in **P-49** (Figure 6.8).

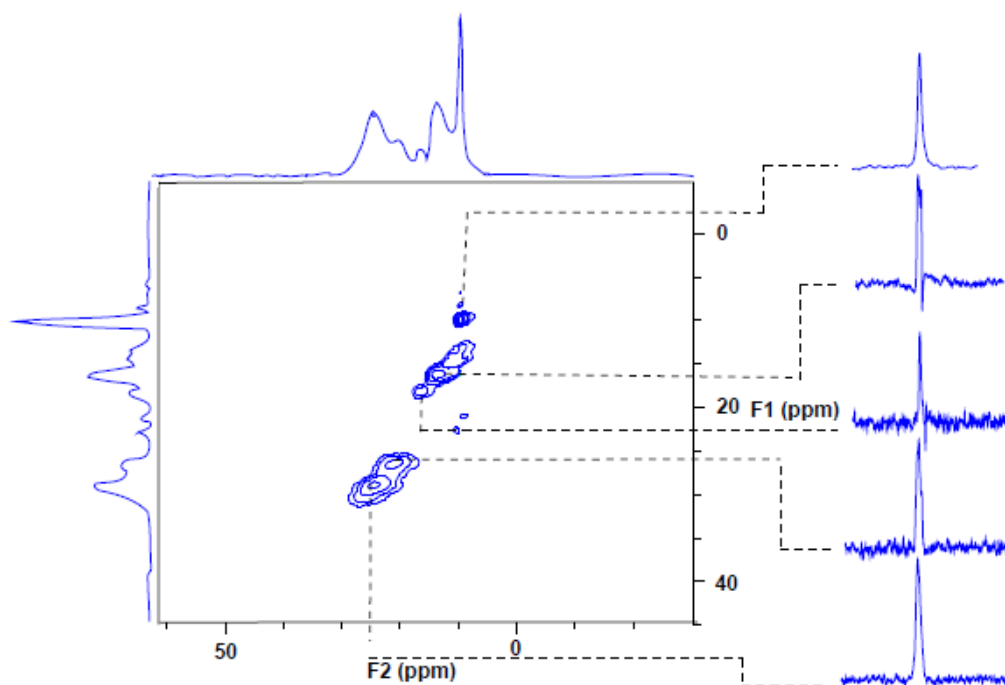


Figure 6. 7. Sheared MQMAS  $^{11}\text{B}$  spectrum of **P-49** collected at 20.0 T with 30 kHz MAS. The differences in chemical shift between the direct and indirect dimensions were used to calculate  $C_Q$  and  $\eta$  for each site. Isotropic projections for each site are shown on the right.

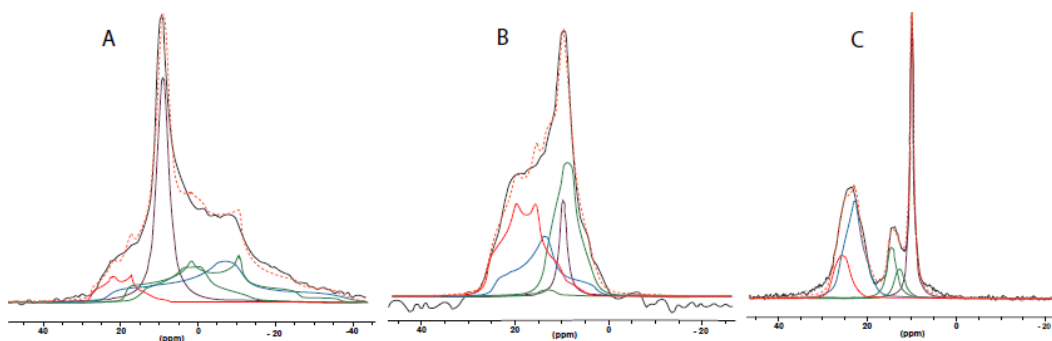


Figure 6. 8. Lineshape fits for **P-49** spectra at 7.0 (A), 11.7 (B) and 20.0 (C) T based on quadrupolar parameters derived from the MQMAS experiment. Sites are colour-coded based on structural motif as seen in Figure 6.9.

Values of  $C_Q$  and  $\eta$  were obtained by fitting the F2 projection lineshapes from the MQMAS data (Table 6.1). Sites with isotropic chemical shifts between 24 and 27 ppm have  $C_Q$  values ranging from 2.5 to 2.9 MHz. Sites with isotropic chemical shifts between 14.5 and 17 ppm have  $C_Q$  values ranging from 1.5 to 2.1 MHz. Both of these groups of sites correspond to three-coordinate boron environments which tend to have  $C_Q$  values ranging from 1.5 to 3.5 MHz depending on the symmetry of the boron center.<sup>15</sup> The site with an isotropic chemical shift of 9.3 ppm has a  $C_Q$  of 0.64 MHz. This site is therefore attributed to an asymmetric four-coordinate boron center. Errors for the lineshape fitting of the MQMAS data were small (~10 %) as the lineshapes from the F2 projections were narrow and individually resolved. The experiment was not attempted on the elastomeric materials with lower boron loading over concerns for achieving appreciable signal. MQMAS experiments tend to yield significantly less signal relative to what can be achieved in a typical 1D NMR experiment.<sup>28</sup> However, based on data from the elastomers with higher boron loading, it can be concluded that the materials with

lower boron loading contain two boron sites with chemical shifts between 20 and 30 ppm and a four-coordinate boron site with a chemical shift around 9 ppm.

Table 6. 1. Lineshape Fitting Parameters for **P-49** Calculated based on an MQMAS Spectrum

20 T					
Site	1	2	3	4	5
$\delta$ (ppm)	$9.8 \pm 0.1$	$15.9 \pm 0.3$	$17.5 \pm 0.3$	$24.1 \pm 0.3$	$26.8 \pm 0.2$
$C_Q$ (MHz)	$0.64 \pm 0.03$	$2.0 \pm 0.1$	$1.6 \pm 0.2$	$2.9 \pm 0.1$	$2.7 \pm 0.2$
$\eta$	$0.9 \pm 0.1$	$0.8 \pm 0.1$	$0.6 \pm 0.2$	$0.8 \pm 0.1$	$0.6 \pm 0.1$
LB (Hz)	$270 \pm 20$	$350 \pm 40$	$420 \pm 30$	$360 \pm 60$	$290 \pm 40$
Coordination	4	3	3	3	3
11.7 T					
Site	1	2	3	4	5
$\delta$ (ppm)	$10.2 \pm 0.5$	$13.7 \pm 0.7$	$15.9 \pm 1$	$24.5 \pm 2$	$26.5 \pm 2$
$C_Q$ (MHz)	$0.64 \pm 0.03$	$2.0 \pm 0.1$	$1.6 \pm 0.2$	$2.9 \pm 0.1$	$2.7 \pm 0.2$
$\eta$	$0.9 \pm 0.1$	$0.8 \pm 0.1$	$0.6 \pm 0.2$	$0.8 \pm 0.1$	$0.6 \pm 0.1$
LB (Hz)	$300 \pm 90$	$250 \pm 70$	$150 \pm 40$	$260 \pm 70$	$200 \pm 60$
Coordination	4	3	3	3	3
7 T					
Site	1	2	3	4	5
$\delta$ (ppm)	$10.4 \pm 0.5$	$15.2 \pm 0.8$	$20.5 \pm 1.5$	$23.1 \pm 2$	$28.4 \pm 3$
$C_Q$ (MHz)	$0.64 \pm 0.03$	$2.0 \pm 0.1$	$1.6 \pm 0.2$	$2.9 \pm 0.1$	$2.7 \pm 0.2$
$\eta$	$0.9 \pm 0.1$	$0.8 \pm 0.1$	$0.6 \pm 0.2$	$0.8 \pm 0.1$	$0.6 \pm 0.1$
LB (Hz)	$300 \pm 90$	$250 \pm 80$	$80 \pm 10$	$300 \pm 80$	$100 \pm 20$
Coordination	4	3	3	3	3

Similar quadrupole parameters were therefore used to fit the 1D spectra of the elastomers with lower boron loading. Errors in lineshape fitting were greater in samples with lower boron loading as MQMAS spectra were not collected. Lineshape fitting for all SiBA materials at each magnetic field can be found in the Appendix (Appendix A.1 to A.4). As was performed for **P-49**, the same quadrupole

parameters and number of sites were used to fit each lineshape at each magnetic field to confirm the suitability of the MQMAS NMR-derived fits. Errors in the determination of line broadening and chemical shift were greater at lower magnetic field due to significant superposition of non-equivalent sites.

The three- and four-coordinate environments as confirmed by MQMAS, are used to determine the structure of each boron site. Each structural motif, presented in Figure 6.3, is linked to specific lineshapes of the  $^{11}\text{B}$  spectra, illustrated in Figure 6.9. The motif labels A-E are retained between Figure 6.3 and Figure 6.9. Motif colour codes are conserved between Figure 6.9 and 6.8. It is well understood that the boronic acid groups are responsible for crosslinking in these materials.<sup>3,6</sup> The transformation from oil to elastomer upon the removal of the tartrate protecting group (Figure 6.1) has been documented via infrared (IR) spectroscopy (Appendix A.5). Elastomer formation is indicated by the presence of a peak at  $3300\text{ cm}^{-1}$  which corresponds to a hydrogen-bonded O-H stretching vibration.<sup>29</sup> It can be concluded that hydrogen bond formation is one of the methods of boron crosslinking that occurs during the formation of SiBA elastomers from the oil precursors (Figure 6.9C). As hydrogen bonding was identified via IR in **T-23** (Appendix A.5), one of the three-coordinate boron sites with chemical shifts between 20 and 30 ppm must correspond to the hydrogen-bonded dimer (Figure 6.9C). Non-Newtonian fluids are characterized by a tendency to exist in an equilibrium between the dimerized and free states.<sup>30</sup> As the elastomers with lower boron loading tend to have the lowest viscosities, it can be assumed that the second three-coordinate site with a chemical

shift between 20 and 30 ppm corresponds to free boronic acid (Figure 6.9B). As boronic acid dimerization is typically associated with lower  $C_Q$  values,<sup>31</sup> the site with an isotropic chemical shift of 26.6 ppm is assigned to the dimerized structure (Figure 6.9C). The site with a chemical shift of 24.0 ppm is therefore assigned to the free boronic acid (Figure 6.9B).

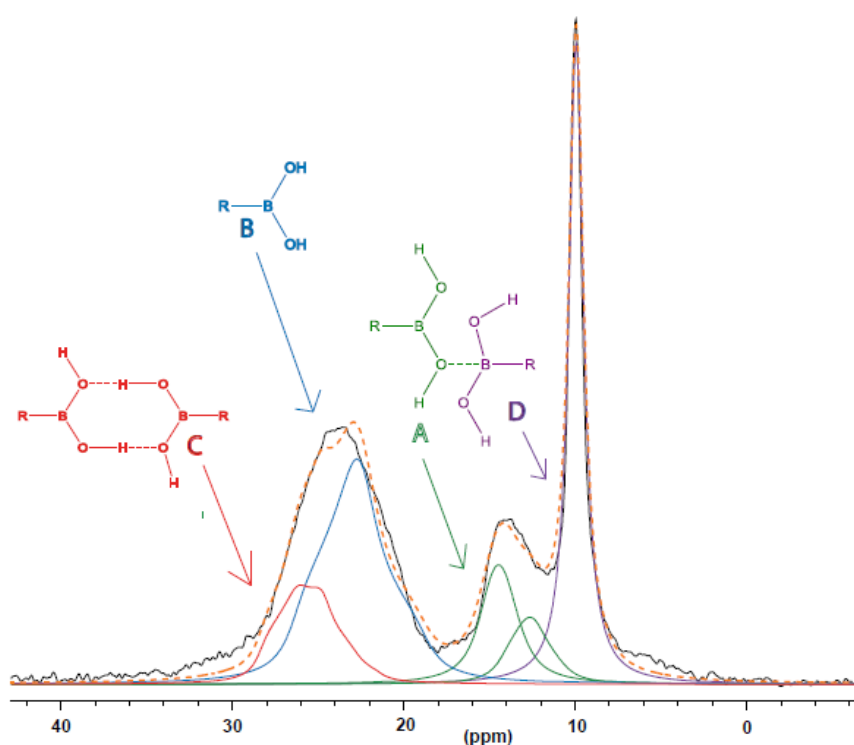


Figure 6. 9. 1D spectrum of **P-49** acquired at 20 T with 30 kHz MAS. The lineshape is fit using the quadrupole parameters that were obtained from MQMAS NMR with the dashed line showing the sum of the fits. Each site is labelled with the corresponding boron coordination environment from Figure 6.3 with the symbol R being used to denote the VPBA group and the PDMS chain.

An additional set of three-coordinate boron peaks exists between 13 and 20 ppm in **P-49** and **P-37** (Figure 6.6 C). These sites were assigned to the three-coordinate boron environment that exists when a B-O-B dative bond is formed

(Figure 6.3A, Figure 6.9A). These sites are not observed in **P-13**, **T-23** and **T-5** (Figure 6.6C) due to fewer four-coordinate boron sites being formed in elastomers with lower boron loadings. These sites are believed to correspond to dimers, instead of free boronic acids, as dimerized boronic acid sites tend to have lower  $C_Q$  values.<sup>31</sup>  $C_Q$  values for the dimerized structure described in Figure 6.9A were around 2 MHz as opposed to the 3 MHz that was observed for free boronic acid Figure 6.9B. It is anticipated that these sites (18.2 ppm and 1.54 MHz, 16.3 ppm and 2.03 MHz) correspond to strong and weakly bound dimers respectively based on the difference in  $C_Q$  between these sites.

An alternative explanation for the crosslinking in SiBA elastomers involves the formation of boroxines. Boroxines are B–O trimers resulting from the dehydration of boronic acids.<sup>32</sup> Normally, the formation equilibrium lies far to the side of boronic acids in the presence of water but, of course, many of the boronic acid groups will reside within a silicone environment, which could have a very low water content. Boroxines derived from phenyl boronic acids exhibit a notable change in chemical shift of the ortho to boron aryl protons in the  $^1\text{H}$  NMR spectrum, from about 7.7 ppm in the absence of boroxines to 8.1 ppm when boroxines are present.<sup>33</sup>  $^1\text{H}$  NMR spectra of **T-23** and **P-13** (Appendix A.6) contain signals at 7.7 ppm and do not contain signals beyond 8 ppm suggesting that boroxines are not present in these materials. Boroxines can also be identified by strong characteristic signals in the IR spectrum at 1340, 1300 and 700  $\text{cm}^{-1}$  resulting from  $E'$  and  $A_2''$  vibrational modes.<sup>34</sup> These are not present in the IR spectrum of

**T-23** (Appendix A.5). Both the IR and  $^1\text{H}$  NMR data indicate that boroxines are not one of the boron coordination modes that are present in the SiBA elastomers.

Quantum chemical calculations are often coupled with MQMAS NMR studies of quadrupolar systems to support the experimentally derived quadrupolar parameters:  $C_Q$  and  $\eta$ . For example, Perras and Bryce performed quantum chemical calculations to support their analyses of several well understood boron containing small molecules.<sup>18</sup>  $C_Q$  and  $\eta$  were reliably determined via quantum chemical calculations but the isotropic chemical shift was not.<sup>18</sup> The significant variance between the isotropic chemical shift as determined by MQMAS NMR and quantum chemical calculations makes this technique non-ideal for use in the analysis of the SiBA elastomers as isotropic shifts are difficult to compare due to significant peak overlap at even high magnetic fields (Figure 6.6 C). Additionally, efficient use of quantum chemical calculations relies on a well-defined crystal structure. SiBA elastomers are amorphous making it impossible to obtain crystal structures. Therefore, quantum chemical calculation is a non-ideal method for the analyses of these materials.

The structure of the four-coordinate boron site is also of interest. Dative bonding may occur via either a B-O-B bond between two boronic acids (Figure 6.3D) or via a B-O-Si bond between a boronic acid and an oxygen on the PDMS backbone (Figure 6.3E). The structure of the four-coordinate site was investigated by tracking the relative proportion of four-coordinate boron as a function of boronic acid loading (Figure 6.10A). B-O-B bonding is expected to become more

favourable when more boronic acid is present whereas B-O-Si bonding is not dependent on having available neighbouring boronic acid groups. Unlike for spin  $\frac{1}{2}$  nuclei, the integrated area of NMR signals usually cannot be used to directly quantify populations of quadrupolar nuclei. This is because differences in  $C_Q$  result in individual sites not being uniformly excited by each radiofrequency pulse.<sup>35</sup> Therefore, excitation is dependent on the spin of the nucleus of interest as well as the symmetry of the nuclear environment at each individual site.<sup>35</sup> However, due to the significant decrease in the strength of the quadrupolar interaction at higher field,<sup>21</sup> it is believed that normalized integrated areas of the four-coordinate boron peaks acquired at 20.0 T may be used to determine the relative proportion of four-coordinate boron in the SiBA elastomers (Figure 6.10A).

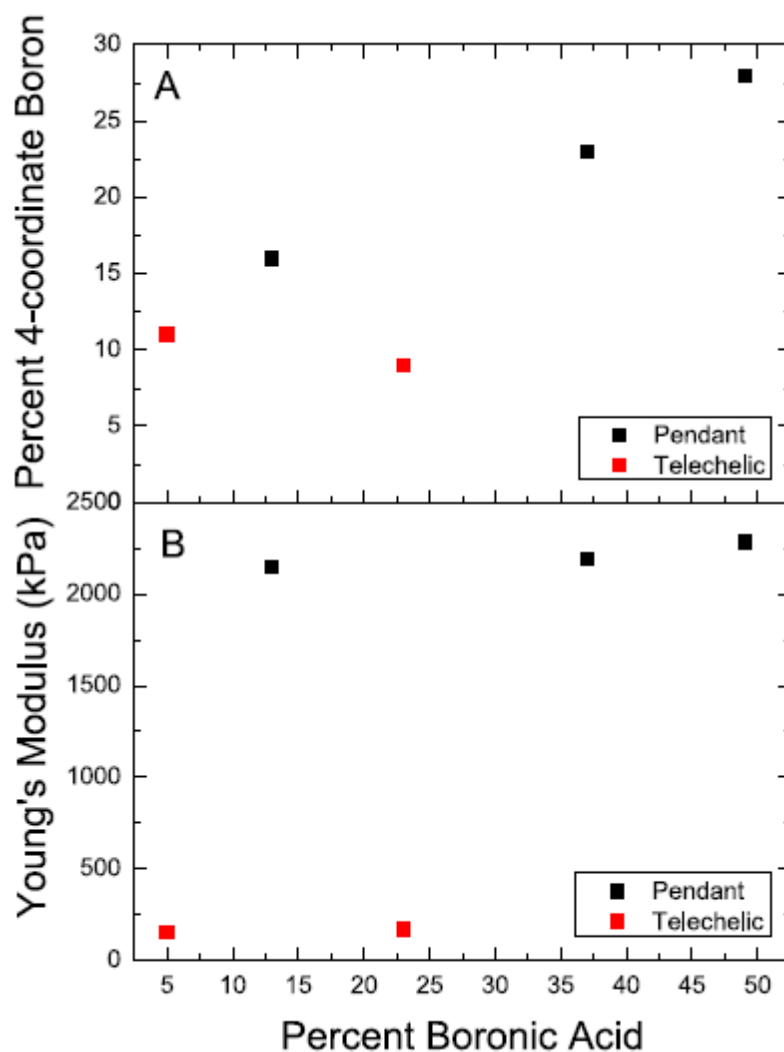


Figure 6. 10. A) Relative proportion of four-coordinate boron, and B) Young's modulus as a function of boronic acid loading.

In general, the relative proportion of four-coordinate boron tends to increase with increasing boronic acid loading. The highest proportion of four-coordinate boron is found in **P-49** and **P-37**, which have significantly higher boronic acid loadings than the other samples (Figure 6.10A). Percent four-coordinate boron decreases substantially when boronic acid loading decreases to 13% in the pendant

SiBA samples and again when pendent SiBA are compared with telechelic SiBA (Figure 6.10A). Although the relationship between boronic acid loading and the relative proportion of four-coordinate boron is not linear, the observed trend suggests that dative bonding is more favourable when more boronic acid is present and that dative bonding is more likely to occur when boronic acid packing density is higher (pendent vs. telechelic). These findings show that conditions which place boronic acid groups closer together result in a greater incidence of dative bonding (Figure 6.3D). The influence of the proximity of boronic acid groups on dative bonding suggests that dative bonding occurs via the formation of B-O-B rather than B-O-Si bonds (Figure 6.3D vs. E).

The quantitative data presented in Figure 6.10 suggests that boronic acid packing density (pendent vs. telechelic) may be the more influential factor in determining the incidence of dative bonding in SiBA elastomers. The increased likelihood of dative bonding in elastomers containing pendant boronic acids is demonstrated when **P-13** and **T-23** are compared. **T-23** contains a higher percentage of boronic acid but has a lower relative proportion of four-coordinate boron centers (Figure 6.10A). The difference between elastomers with pendant and telechelic boronic acids is most intriguing. Pendant boronic acids have fewer degrees of freedom of motion as a consequence of the flanking polymer chains, on both sides, when compared to telechelic compounds, which are tethered on one end. The difference between elastomers with pendant and telechelic boronic acids is most clearly illustrated when Young's moduli of these samples are compared

(Figure 6.10B).<sup>6</sup> The Young's moduli of the pendant samples are an order of magnitude larger than those of the telechelic samples (Figure 6.10B) indicating that the pendant samples are significantly more rigid than the telechelic samples. The increased tendency for four-coordinate boron centers to form in the pendant elastomers suggests that four-coordinate crosslinks may be 'more efficient' with pendant boronic acids than with telechelic moieties, possibly because the equilibrium between free and dimerized boronic acids favors the four-coordinate boron in the former case.

### 6.3.3 Boron Coordination Environments in Commercial Silly Putty

"Silly Putty" is the commercial name for Dow Corning's 3179 dilatant compound where a dilatant is a material that exhibits increased viscosity as the shear rate is increased.<sup>36</sup> Dow Corning's Silly Putty is comprised primarily of PDMS (~69 %) and silica (~17 %).<sup>36,37</sup> However, the material also contains titanium dioxide (1 %), glycerin (1 %), boric acid (3 %) and Thixatrol (a polyamide modified hydrogenated castor oil derivative) (9 %).<sup>36</sup> Silly Putty's unusual properties are due in part to the viscoelasticity that is inherent to high molecular weight PDMS polymers and in part to the weak crosslinks that form between boric acid crosslinkers and the PDMS polymer chains.<sup>36,37</sup> The presence of boric acid gives Silly Putty the properties of an elastic solid, however the exact nature of crosslinking in Silly Putty has garnered some debate.<sup>38</sup> It has long been believed that hydrogen bonding between boric acid and PDMS polymer chains is responsible for crosslinking in Silly Putty.<sup>19,36,38</sup> This assumption is based on the widely

accepted reversibility of hydrogen bonds.<sup>36,37</sup> In actuality, crosslinking in Silly Putty is the result of esterification between boric acid and hydroxyl-terminated PDMS.<sup>38</sup> The boronate ester bond has been deemed reversible enough to result in the interesting flow characteristics for which Silly Putty is renown.<sup>4,36,39,40</sup> Hydrogen bonding between boric acid and PDMS chains is still possible but this interaction has been relegated to being a minor mechanism of crosslinking in Silly Putty. In this work, solid-state  $^{11}\text{B}$  NMR is used to characterize boron coordination modes in a commercial Silly Putty sample as was done for SiBA elastomers above.

$^{11}\text{B}$  MQMAS was performed at 20 T with 30 kHz MAS on a center-packed Silly Putty sample (Figure 6.11) as was done for **P-49** (Figure 6.7). Four distinct boron coordination environments could be observed (Figure 6.11).

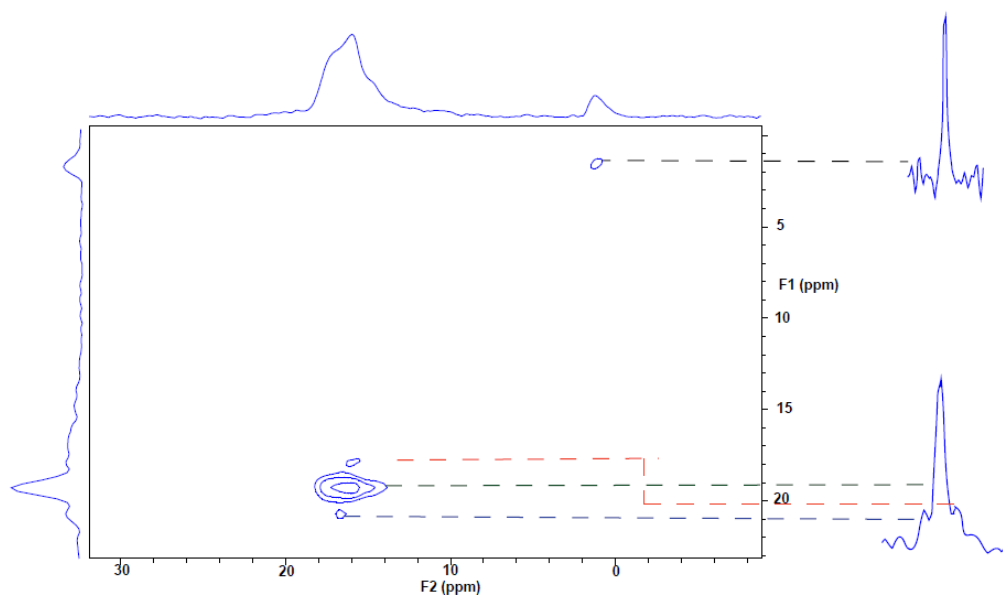


Figure 6. 11. Sheared  $^{11}\text{B}$  MQMAS spectrum of Silly Putty collected at 20.0 T with 30 kHz MAS. The 1D spectra on the right are projections of the F1 dimension.

Deconvolution of the MQMAS spectrum revealed that these sites have isotropic chemical shifts of 1.41, 17.19, 18.04 and 19.24 ppm (Table 6.2). Based on chemical shift alone, it can be determined that the 1.41 ppm site corresponds to a four-coordinate boron environment and that the other sites correspond to three-coordinate boron environments.<sup>15</sup> These assignments are confirmed when  $C_Q$  values for these sites are compared (Table 6.2). The four-coordinate boron environment was assigned to a boric acid center coordinated to four PDMS chains via boronic ester formation (Figure 6.12A). This assignment was made based on the prevalence of crosslinking by esterification in Silly Putty and the high degree of symmetry at this site ( $\eta = 0.1$ ).

Table 6. 2. Lineshape Fitting Parameters for Silly Putty Calculated based on an MQMAS Spectrum

Site	1	2	3	4
$\delta$ (ppm)	$1.4 \pm 0.1$	$17.2 \pm 0.5$	$18.04 \pm 0.2$	$19.2 \pm 0.5$
$C_Q$ (MHz)	$0.82 \pm 0.02$	$1.9 \pm 0.1$	$2.5 \pm 0.2$	$2.5 \pm 0.2$
H	$0.1 \pm 0.1$	$0.2 \pm 0.2$	$0.1 \pm 0.1$	$0.8 \pm 0.2$
LB (Hz)	$620 \pm 20$	$650 \pm 50$	$600 \pm 30$	$550 \pm 50$
Coordination	4	3	3	3

Boron coordination environments for the three-coordinate sites can be assigned based on an analysis of the numerical values of their  $C_Q$  and  $\eta$  parameters. Both of sites B and C have  $\eta$  values below 0.3 (Table 6.2) which suggests that the nearest neighbor coordination spheres of these environments are symmetric.<sup>12</sup> Site D has a higher  $\eta$  value which is indicative of lower symmetry in the coordination sphere. The sites also differ in terms of  $C_Q$ .  $C_Q$  values for the two sites with the

higher isotropic chemical shifts are around 2.5 MHz (Table 6.2).  $C_Q$  tends to decrease upon dimerization or coordination of the boron center which suggests that these environments correspond to free or weakly coordinated boric acids.<sup>31</sup> The site with an isotropic chemical shift of 17.19 ppm had a lower  $C_Q$  value: 1.9 MHz (Table 6.2). This site was therefore assigned to the more strongly coordinated structural motif that is likely to occur at a three-coordinate boron site in a Silly Putty sample: crosslinking via boronate ester formation (Figure 6.12B).

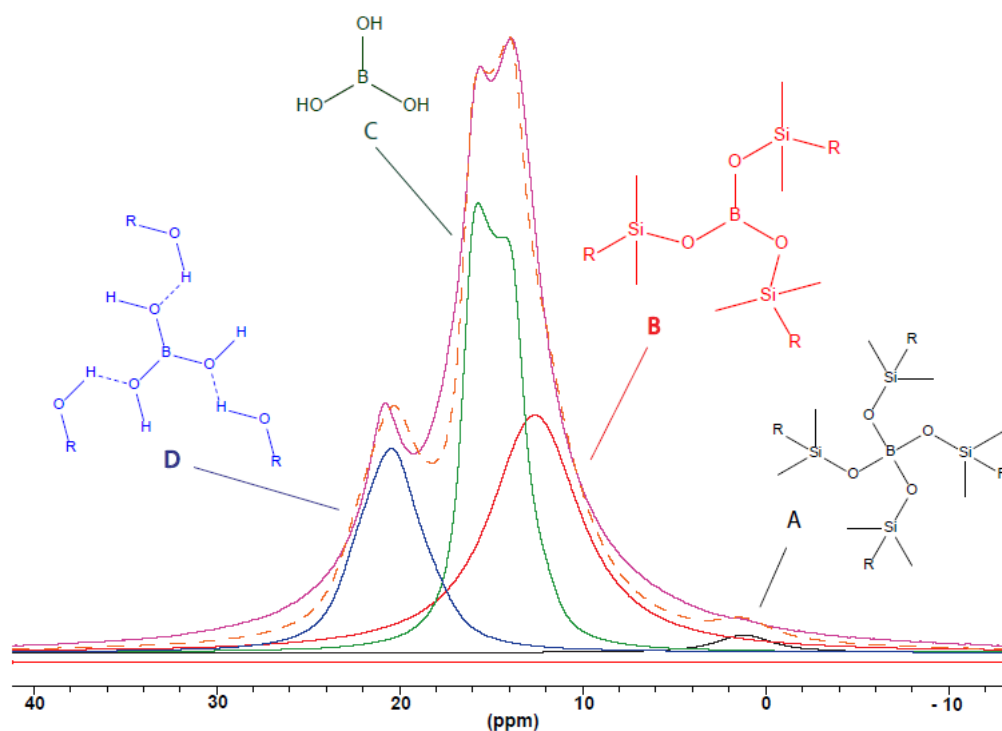


Figure 6. 12. 1D Silly Putty  $^{11}\text{B}$  spectrum acquired at 20 T with 30 kHz MAS. The lineshape was fit with the quadrupole parameters that were obtained from the MQMAS experiments with the dashed line showing the sum of the fits. Each site is labeled with the corresponding coordination environment (A-D). The symbol R denotes the PDMS backbone.

The three-coordinate site with an isotropic chemical shift of 18.04 ppm was assigned to free boric acid (Figure 6.12C) based on similarities in the  $C_Q$  and  $\eta$  values to those of boric acid (Appendix A.8). Free boric acid should exist in Silly Putty samples due to the reversible nature of boron crosslinking in the material. The remaining three-coordinate boron site was assigned to boronic acid crosslinked via hydrogen bonding as a weakly coordinated system is less likely than a more strongly coordinated system to experience a decrease in  $C_Q$  (Figure 6.12D). Additionally, hydrogen bonds are broken and reformed more easily than covalent bonds which could decrease the overall symmetry of the coordination sphere (namely not all the hydroxyl groups are hydrogen-bonded at a given time). The assignment of the higher chemical shift three-coordinate boron sites to free boric acid and hydrogen bonded boric acid is consistent with the assignments that were made for the SiBA elastomers (Figure 6.9).<sup>41</sup> It appears that weakly coordinated sites tend to have higher chemical shift values along with higher  $C_Q$  values. Both characteristics could be a consequence of decreased symmetry in the boron coordination sphere.

All dimerized boron coordination environments were assigned to bonds formed between boronic acid and the PDMS polymer backbone. This assumption was made because the overall boric acid content of Silly Putty is small relative to that of the SiBA elastomers. It is therefore believed that the observation of the appreciable crosslinking via solid-state NMR is a result of these bonds primarily being formed between boronic acids and PDMS. Additionally, the boric acid

content (3 %) and the hydroxyl-terminated PDMS content (4 %) of Silly Putty are similar.<sup>36</sup> These ratios suggest that 1:1 bonding occurs. Since only one Silly Putty sample was available, it was not possible to rank the incidence of boric acid dimerization against boric acid content as was done for the PDMS elastomers (Figure 6.10A).<sup>41</sup> This hypothesis could be tested if a series of Silly Putty samples with known boronic acid content was prepared.

The possibility of directly investigating hydrogen bonding in this system via <sup>1</sup>H NMR was discounted due to the presence substantial amounts of Thixatrol (9 %) present in commercial Silly Putty.<sup>36</sup> Thixatrol, an amide-containing polymer, can be detected in the <sup>1</sup>H spectrum of Silly Putty as it is the next most abundant proton-containing component of the sample following PDMS (Appendix A.7).<sup>36</sup> It is anticipated that signals associated with the amide functional group may be more likely to respond to sample heating for the detection of hydrogen bonding than signals coming from hydroxyl-terminated PDMS or boric acid. This is especially true if we consider that proton signals coming from hydrogen-bonded sites were too broadened to observe in the PDMS samples.<sup>41</sup> However, <sup>1</sup>H NMR was employed to discount the possibility of boroxine formation being a mechanism of boronic acid coordination in Silly Putty. As was observed in the SiBA elastomers, a signal at 8.1 ppm, characteristic of boron aryl protons, was absent from the <sup>1</sup>Hproton NMR spectrum of Silly Putty (Appendix A.7).<sup>3</sup>

#### 6.4 Conclusion

Boron coordination environments were analyzed in SiBA elastomers and Silly Putty using  $^{11}\text{B}$  solid-state NMR which afforded good resolution of distinct boron coordination environments when MQMAS experiments were performed. An analysis of the quadrupolar parameters of each site confirmed that both samples contained three- and four-coordinate boron environments. For the SiBA elastomers, MQMAS experiments were limited to systems containing appreciable amounts of boron due to signal losses in MQMAS experiments relative to conventional  $^{11}\text{B}$  NMR. Experimentally determined quadrupolar parameters were extrapolated to systems with lower boronic acid loading as significant increases in experimental time would be required to adequately characterize these materials directly. Three-coordinate boron sites were identified as being boronic acids dimerized by hydrogen bonding and free boronic acids. Four-coordinate sites were assigned to dative-bonded boronic acids. In the SiBA elastomers, dative bonding was correlated with increased boronic acid loading and increased boronic acid density. This result suggests that dative bonding occurs via the formation of B-O-B bonds in these materials instead of B-O-Si bonds. Boronic acid packing density was deemed to be the more important factor in boronic acid crosslinking with four-coordinate centers being more likely to form in pendant SiBA elastomers. Similar connections between boronic acid loading and the prevalence of four-coordinate boron could not be made in the Silly Putty sample due to the availability of only one Silly Putty sample as a result of difficulties in the in-house synthesis of this material. However, it is assumed that 1:1 boric acid to PDMS linkages are

responsible for crosslinking in Silly Putty based on the ratio of boric acid and hydroxyl-terminated PDMS within the material.

## 6.5 References

1. Bull, S. D. *et al.* Exploiting the reversible covalent bonding of boronic acids: Recognition, sensing, and assembly. *Acc. Chem. Res.* **46**, 312–326 (2013).
2. Brook, M. A., Dodge, L., Chen, Y., Gonzaga, F. & Amarne, H. Sugar complexation to silicone boronic acids. *Chem. Commun.* **49**, 1392 (2013).
3. Zepeda-Velazquez, L., Macphail, B. & Brook, M. A. Spread and set silicone–boronic acid elastomers. *Polym. Chem.* **7**, 4458–4466 (2016).
4. Dodge, L., Chen, Y. & Brook, M. A. Silicone boronates reversibly crosslink using Lewis acid-Lewis base amine complexes. *Chem. - A Eur. J.* **20**, 9349–9356 (2014).
5. Lu, C., Kostanski, L., Ketelson, H., Meadows, D. & Pelton, R. Hydroxypropyl guar-borate interactions with tear film mucin and lysozyme. *Langmuir* **21**, 10032–10037 (2005).
6. Macphail, B. & Brook, M. A. Controlling silicone-saccharide interfaces: greening silicones. *Green Chem.* **19**, 4373–4379 (2017).
7. Peters, G. M. *et al.* G4-quartet- $M^+$  borate hydrogels. *J. Am. Chem. Soc.* **137**, 5819–5827 (2015).
8. Iwasawa, N. & Takahagi, H. Boronic esters as a system for crystallization-induced dynamic self-assembly equipped with an ‘on-off’ switch for equilibration. *J. Am. Chem. Soc.* **129**, 7754–7755 (2007).
9. Nishimura, N., Yoza, K. & Kobayashi, K. Guest-encapsulation properties of a self-assembled capsule by dynamic boronic ester bonds. *J. Am. Chem. Soc.* **132**, 777–790 (2010).
10. Niu, W., Smith, M. D. & Lavigne, J. J. Self-assembling poly(dioxaborole)s as blue-emissive materials. *J. Am. Chem. Soc.* **128**, 16466–16467 (2006).
11. Nishiyabu, R., Kubo, Y., James, T. D. & Fossey, J. S. Boronic acid building blocks: Tools for self assembly. *Chem. Commun.* **47**, 1124–1150 (2011).
12. Kroeker, S. & Stebbins, J. F. Three-coordinated boron-11 chemical shifts in borates. *Inorg. Chem.* **40**, 6239–6246 (2001).
13. Jung, J. K., Song, S. K., Noh, T. H. & Han, O. H.  $^{11}\text{B}$  NMR investigations

- in  $x\text{V}_2\text{O}_5\text{-B}_2\text{O}_3$  and  $x\text{V}_2\text{O}_5\text{-B}_2\text{O}_3\text{-PbO}$  glasses. *J. Non. Cryst. Solids* **270**, 97–102 (2000).
14. Frydman, L., Harwood, J. S. & Street, W. T. Isotropic Spectra of Half-Integer Quadrupolar Spins from Bidimensional Magic-Angle Spinning NMR. 5367–5368 (1995).
  15. MacKenzie, K.J.D., Smith, M. . *Multinuclear Solid-State NMR of Inorganic Materials*. (Elsevier Science Ltd, 2002).
  16. Turner, G. L., Smith, K. A., Kirkpatrick, R. J. & Oldfield, E. Boron-11 nuclear magnetic resonance spectroscopic study of borate and borosilicate minerals and a borosilicate glass. *J. Magn. Reson.* **67**, 544–550 (1986).
  17. Feng, N. *et al.* Understanding the high photocatalytic activity of (B, Ag)-codoped  $\text{TiO}_2$  under solar-light irradiation with XPS, solid-state NMR, and DFT calculations. *J. Am. Chem. Soc.* **135**, 1607–1616 (2013).
  18. Perras, F. A. & Bryce, D. L. Measuring dipolar and J coupling between quadrupolar nuclei using double-rotation NMR. *J. Chem. Phys.* **138**, (2013).
  19. Kobera, L. *et al.* Structure and Distribution of Cross-Links in Boron-Modified Phenol-Formaldehyde Resins Designed for Soft Magnetic Composites: A Multiple-Quantum  $^{11}\text{B}$ - $^{11}\text{B}$  MAS NMR Correlation Spectroscopy Study. *Macromolecules* **48**, 4874–4881 (2015).
  20. Autschbach, J., Zheng, S. & Schurko, Robert, W. Analysis of Electric Field Gradient Tensors at Quadrupolar Nuclei in Common Structural Motifs. *Concepts Magn. Reson. A* **36**, 84–126 (2010).
  21. Kentgens, A. P., A practical guide to solid-state NMR of half-integer quadrupolar nuclei with some applications to disordered systems. *Geoderma* **80**, 271–306 (1997).
  22. Hansen, M. R., Madsen, G. K. H., Jakobsen, H. J. & Skibsted, J. Refinement of borate structures from  $^{11}\text{B}$  MAS NMR spectroscopy and density functional theory calculations of  $^{11}\text{B}$  electric field gradients. *J. Phys. Chem. A* **109**, 1989–97 (2005).
  23. Engelhardt, G., Kentgens, A. P. M., Koller, H. & Samoson, A. Strategies for extracting NMR parameters from  $^{23}\text{Na}$  MAS, DOR and MQMAS spectra. A case study for  $\text{Na}_4\text{P}_2\text{O}_7$ . *Solid State Nucl. Magn. Reson.* **15**, 171–180 (1999).
  24. A. Medek, J.S. Harwood & L. Frydman. Multiple-Quantum Magic- Angle Spinning NMR: A New Method for the Study of Quadrupolar Nuclei in Solids. *J. Am. Chem. Soc.* **117**, 12779–12787 (1995).

25. Hoatson, G. L., Zhou, D. H., Fayon, F., Massiot, D. & Vold, R. L.  $^{93}\text{Nb}$  magic angle spinning NMR study of perovskite relaxor ferroelectrics. *Phys. Rev. B* **66**, 224103 (2002).
26. d'Espinose de Lacaillerie, J. B., Fretigny, C. & Massiot, D. MAS NMR spectra of quadrupolar nuclei in disordered solids: The Czjzek model. *J. Magn. Reson.* **192**, 244–251 (2008).
27. Camino, C., Lomakin, S. M. & Lazzari, M. Polydimethylsiloxane thermal degradation part 1. Kinetic aspects. *Polymer (Guildf)*. **42**, 2395–2402 (2001).
28. Frydman, L., Grant, D. M. & Harris, R. K. Fundamentals of Multiple-Quantum Magic-Angle Spinning NMR on Half-Integer Quadrupolar Nuclei Magic-Angle Spinning NMR on Half-Integer Quadrupolar Nuclei. *Encyclopedia of Nuclear Magnetic Resonance. Volume 9: Advances in NMR* **9**, 262–274 (2002).
29. Mitsuzuka, A., Fujii, A., Ebata, T. & Mikami, N. Infrared Spectroscopy of Intramolecular Hydrogen-Bonded OH Stretching Vibrations in Jet-Cooled Methyl Salicylate and Its Clusters. *J. Phys. Chem. A* **102**, 9779–9784 (1998).
30. Brooks, W. L. A. & Sumerlin, B. S. Synthesis and Applications of Boronic Acid-Containing Polymers: From Materials to Medicine. *Chem. Rev.* **116**, 1375–1397 (2016).
31. Weiss, J. W. E. & Bryce, D. L. A Solid-State B-11 NMR and Computational Study of Boron Electric Field Gradient and Chemical Shift Tensors in Boronic Acids and Boronic Esters. *J. Phys. Chem. A* **114**, 5119–5131 (2010).
32. Hall, D. G. *Boronic Acids*. (Wiley VCH, 2011). doi:10.1002/9783527639328
33. Qin, Y., Cui, C. & Jäkle, F. Silylated initiators for the efficient preparation of borane-end- functionalized polymers via ATRP. *Macromolecules* **40**, 1413–1420 (2007).
34. Smith, M. K. & Northrop, B. H. Vibrational properties of boroxine anhydride and boronate ester materials: Model systems for the diagnostic characterization of covalent organic frameworks. *Chem. Mater.* **26**, 3781–3795 (2014).
35. Hughes, C. E. & Harris, K. D. M. Calculation of solid-state NMR lineshapes using contour analysis. *Solid State Nucl. Magn. Reson.* **80**, 7–13 (2016).

36. Golinelli, N., Spaggiari, A. & Dragoni, E. Mechanical behaviour of magnetic Silly Putty : Viscoelastic and magnetorheological properties. *Intelligent Materials, Systems and Structures*. **28**, 953–960 (2017).
37. Cross, R. Elastic and viscous properties of Silly Putty. *Am. J. Phys.* **80**, 870–875 (2012).
38. Jacoby, M. Errors in C&EN graphic reveal widespread misconceptions about slice chemistry. *Chemical & Chemical Engineering News* (2018).
39. Mansuri, E., Zepeda-Velazquez, L., Schmidt, R., Brook, M. A. & DeWolf, C. E. Surface Behavior of Boronic Acid-Terminated Silicones. *Langmuir* **31**, 9331–9339 (2015).
40. Ren, B. *et al.* Dynamical release nanospheres containing cell growth factor from biopolymer hydrogel via reversible covalent conjugation. *J. Biomater. Sci. Polym. Ed.* **29**, 1344–1359 (2018).
41. Foran, G. Y., Harris, K. J., Brook, M. A., Macphail, B. & Goward, G. R. Solid State NMR Study of Boron Coordination Environments in Silicone Boronate (SiBA) Polymers. *Macromolecules* **52**, 1055–1064 (2019).

## Chapter 7: Summary and Future Work

### 7.1 Summary

The work that was presented in this thesis demonstrated that solid-state NMR is a suitable technique for the characterization of both structure and dynamics in hydrogen-bonded systems. Firstly, solid-state NMR was used in Chapters 3 through 5 to quantify proton dynamics in solid-state proton conductors. It was also used in Chapter 6 to explore the structural role of hydrogen bonding in crosslinked boron-containing elastomers.

In Chapters 3 and 4, homonuclear dipolar recoupling and chemical exchange experiments were used to characterize proton dynamics in phosphate solid acids. Symmetry-based dipolar recoupling pulse sequences have long been used to characterize dipolar coupling in systems with isolated spin pairs.<sup>1,2</sup> However, there are few examples of these experiments being used in complex multi-spin systems like the phosphate solid acids that were discussed in Chapters 3 and 4.<sup>3</sup> Therefore, the validity of this approach was verified by analyzing apparent proton dipolar coupling in calcium hydroxyapatite (a multi-spin system with no proton dynamics) and  $\text{KH}_2\text{PO}_4$  (KDP) (a dynamic multi-spin system with a single proton environment). In both cases, the low-temperature apparent dipolar coupling constant agreed with the zero-motion scenario, which was calculated based on proton-proton distances in the crystal structure. Additionally, homonuclear proton apparent dipolar coupling in KDP decreased with increasing temperature, as was expected based on experimentally observed changes in proton conductivity in this material. These experiments demonstrated that symmetry-based dipolar recoupling

NMR was an effective approach for the determination of proton apparent dipolar coupling constants in dynamic multi-spin systems.

The most extensive dipolar recoupling experiments were performed on  $\text{RbH}_2\text{PO}_4$  (RDP). RDP underwent a phase change from the tetragonal to the monoclinic phase in the experimentally accessible temperature range. The monoclinic phase contains two well-resolved proton sites which provided the opportunity to measure site-specific proton dynamics. The apparent dipolar coupling interaction did not change evenly with increasing temperature at these two sites (labelled A and B in Figure 3.9 from Chapter 3). The apparent proton dipolar coupling constant was more attenuated at site A which exists in a disordered hydrogen-bonded network in monoclinic RDP.<sup>4,5</sup> A preferred proton hopping pathway, site A to site A, was identified in monoclinic RDP for the first time.

In addition to proton hopping between A sites, proton hopping between A and B sites was also predicted to occur based on previous experiments by Vijayakumar et al.<sup>5</sup> These experiments revealed that these sites are proximal to one another and are strongly coupled which would likely allow proton exchange to occur. However, this motion was not quantified in the earlier work. As these proton sites were sufficiently well-resolved,  $^1\text{H}$  hopping between A and B sites was investigated using two exchange-based NMR spectroscopy techniques: exchange spectroscopy (EXSY) and selective inversion. These experiments confirmed that proton exchange occurs between A and B sites in monoclinic RDP. However, this

process occurs more slowly than proton hopping between A sites due to greater structural order in the hydrogen-bonded network along which the B protons lie.<sup>4</sup>

Proton mobility in tin pyrophosphates, another class of phosphate-based proton conductor, was also analyzed using solid-state NMR. Like phosphate solid acids, tin pyrophosphates have been proposed as potential intermediate-temperature proton conductors. Both materials contain phosphate tetrahedra which tend to have 2.5 Å oxygen-oxygen distances which are favourable for proton conduction via the Grotthuss mechanism.<sup>4,6,7</sup> However, unlike phosphate solid acids, tin pyrophosphates do not contain structural protons. Protons must therefore be added via synthesis. This results in proton conductivity in tin pyrophosphates being heavily dependent on the synthetic history of the sample.<sup>8,9</sup>

Tin pyrophosphates with indium loadings between 0 and 20 % were analyzed in Chapter 5 of this thesis. Indium doping is expected to increase proton conductivity because  $\text{In}^{3+}$  has a lower oxidation state than  $\text{Sn}^{4+}$ . Therefore, protons are incorporated into the lattice to balance the resultant charge-deficient metal sites.<sup>8,10,11</sup> Proton conductivity in these materials has been attributed to proton hopping between hydrogen-bonded sites on the metal octahedra (M-O-P) and the phosphate tetrahedra (P-O-P).<sup>7</sup> Proton dynamics in these materials were probed using a combination of proton conductivity and  $^1\text{H}$  NMR experiments. Electrochemical impedance spectroscopy (EIS) showed that proton conductivity increases with indium doping but that the activation energy for proton transport remains the same regardless of indium loading.

The most important result of the  $^1\text{H}$  EXSY experiments is that the separation between peaks corresponding to the M-O-P and P-O-P proton environments tends to decrease as a function of indium loading. This correlates with the proton conductivity data as proton hopping between M-O-P and P-O-P sites is needed for long-range proton conduction in these materials. Crosspeaks were observed in spectra from samples with 5 and 10 % indium loading suggesting that proton exchange occurs in the slow regime in these samples.<sup>12</sup> Kinetic data, including rates of proton exchange and activation energy were obtained. As in the EIS experiments, it was found that activation energy for proton exchange did not increase with indium loading. This supports the idea that changes in proton mobility likely result from increased charge carrier concentration and are not the result of a change in the mechanism of proton conduction. When indium loading is increased to 15 and 20 %, crosspeaks are no longer observed as a result of increasing peak overlap that occurs as the rate of M-O-P to P-O-P proton hopping increases at higher indium loadings. Rates of proton hopping are expected to be higher as indium loading is increased but, as was observed via EIS, activation energies for proton transport are expected to remain similar indicating no change in the proton conduction mechanism.

The tin pyrophosphate samples that were analyzed here were deemed to be relatively pure as  $^{31}\text{P}$  NMR experiments confirmed that they were free from phosphoric acid and low in polyphosphoric acid. Coincidentally, measured proton conductivities were relatively low ( $10^{-8}$  S/cm as opposed to  $10^{-2}$  S/cm)<sup>8</sup> regardless

of indium loading. These results suggest that, as has been proposed by some authors,<sup>9,13</sup> relatively high proton conductivities are a result of proton conduction through impurity phases such as polyphosphoric acid and phosphoric acid. These species are commonly present in tin pyrophosphates as these materials often need to be synthesized in the presence of excess phosphoric acid.<sup>9</sup> As result of low proton conductivity through the tin pyrophosphate phase, pure tin pyrophosphates are not recommended for use as solid-state electrolyte materials in intermediate-temperature fuel cells.

Two types of crosslinked boron-containing elastomers were investigated in Chapter 6: silicone boronate acids (SiBA) and Silly Putty. In both cases, hydrogen bonding was expected to be one of the coordination modes occurring at boron centers in these materials. This is because hydrogen bonding tends to be associated with the viscosity and self-healing properties that are generally found in elastomeric materials.<sup>12,14</sup> Analysis of quadrupolar <sup>11</sup>B lineshapes revealed that both hydrogen bonding and dative bonding are responsible for crosslinking in these materials. As multiple SiBA materials with different boron loadings were analyzed, a relationship between boron loading, the relative amount of four-coordinate boron sites and the Young's modulus of these materials was established. It was found that elastomers with more four-coordinate dative-bonded sites were prepared from starting materials that had higher boronic acid loading. Additionally, more four-coordinate sites were observed in elastomers that were prepared from pendant starting materials (boronic acids hanging off chains) than elastomers prepared from

telechelic starting materials (boronic acids on the ends of chains). The differences in coordination environment between pendent and telechelic samples is believed to be a result of boronic acids being packed closer together in the pendant samples. Increased boronic acid packing density resulted in elastomers with significantly larger Young's moduli than those where boronic acid packing density was lower. Similar comparisons were not made with Silly Putty as only one industrial sample (exact boric acid content unknown) was available for analysis. It is however anticipated, based on observations made in the SiBA materials, that higher boric acid content would promote greater crosslinking in these materials.

## **7.2 Future Work**

### **7.2.1 Phosphate Solid Acids**

The work that was presented in Chapters 3 and 4 of this thesis was mainly focused on proton motion in monoclinic RDP as this phase contains two proton sites and two possible mechanisms for proton hopping. Like  $\text{CsH}_2\text{PO}_4$  (CDP), which has an analogous tetragonal to monoclinic phase transition, RDP is predicted to undergo a superprotonic transition to the cubic phase.<sup>17-19</sup> However, significant increases in proton mobility, signaled by a large decrease in the dipolar coupling constant and caused by a transition to the superprotonic cubic phase, were not observed in our work. The temperature required for the phase transition to cubic RDP, 273 °C,<sup>20</sup> was not accessible under our experimental setup. Additionally, the analysis of the cubic phase via solid-state RDP would be particularly challenging as the material must be kept at high pressure (~10000 atm) to avoid decomposition via dehydration.<sup>17</sup> However, NMR of RDP at higher temperature would be

interesting as changes in proton mobility could definitely be tracked as the material (still in the stable monoclinic phase) approaches the unstable cubic phase. Proton conductivity could also be compared to the previously well-characterized CDP to evaluate the viability of higher-temperature monoclinic RDP as a potential solid-state fuel cell electrolyte material.

### **7.2.2 Tin Pyrophosphates**

One objective of the study of proton dynamics in tin pyrophosphates presented in Chapter 5 is to investigate proton hopping between M-O-P octahedral and P-O-P tetrahedral hydrogen-bonded sites which is necessary for long-range proton transport in these materials.<sup>7</sup> In Chapter 5, this process is monitored indirectly via conductivity measurements (long-range transport is required to observe proton conductivity) and directly via EXSY. However, as a result of differing rates of proton hopping, inter-polyhedral proton exchange could not be directly quantified at all indium loadings. This is because the ability to observe well-resolved crosspeaks in EXSY spectra is strongly dependent on the resolution of individual sites.<sup>12,21</sup> At higher indium loadings, 15 and 20 %, overlap between peaks corresponding to M-O-P and P-O-P proton environments was such that crosspeaks could not be resolved. The lack of well-resolved crosspeaks meant that reliable kinetic data could not be obtained from these spectra. This situation could potentially be remedied by attempting to observe inter-polyhedron proton exchange via selective inversion as opposed to via EXSY.

Like the EXSY experiment, selective inversion (which was used in the analysis of proton exchange in monoclinic RDP in Chapter 4) is also facilitated by having good resolution between exchanging sites.<sup>22</sup> However, as the integration of one dimensional spectra tends to be easier than integrating two dimensional spectra, there is the potential to obtain more reliable kinetic data at higher, and lower, indium loadings. In addition to more facile integration, the analysis of overlapped sites can also be improved by selectively inverting portions of a peak (as opposed to the whole peak) to obtain site-selective kinetic data. The analysis of three different inversion methods in the study of RDP showed that proton exchange rates obtained via different inversion techniques yield similar kinetic information. Overall, it is anticipated that selective inversion could allow rates of interpolyhedron proton exchange and activation energies for this process to be obtained at all indium loadings as a result of the technique being less dependent on the resolution of individual sites.

The tin pyrophosphate study could also be extended to investigate the effects of 2+ versus 3+ cation doping. Magnesium, a 2+ cation, could be used in these studies instead of indium as it has been previously successfully doped into tin pyrophosphates.<sup>11</sup> It is of interest whether proton dynamics in doped tin pyrophosphates are affected by cation charge as more protons would be needed to charge balance the more charge-deficient center. It is therefore assumed, based on the link between proton mobility and the quantity of available protons presented in Chapter 5, that doping with 2+ cations may result in facilitated proton hopping if

the long-range cubic tin pyrophosphate structure remains undisrupted. Doping with magnesium may also resolve another issue that is associated with proton detection in tin pyrophosphate samples: low proton signal, as more protons would be needed to compensate for metal sites with a more significant charge deficiency.

In Chapter 5 of this thesis,  $^1\text{H}$  and  $^{31}\text{P}$  NMR were used to characterize the structure and dynamics of protonated phosphorous environments in indium-doped tin pyrophosphate samples. However, in addition to these nuclei,  $^{119}\text{Sn}$  NMR could also be performed to further characterize these materials. Like  $^1\text{H}$  and  $^{31}\text{P}$ ,  $^{119}\text{Sn}$  is a spin  $\frac{1}{2}$  nucleus and could therefore potentially be used as a means of directly probing indium doping. Pristine cubic phase tin pyrophosphate contains a single tin environment which is expected to translate to a single peak in  $^{119}\text{Sn}$  NMR spectra.<sup>23</sup> It is anticipated that the addition of indium would change the  $^{119}\text{Sn}$  NMR spectrum in some way as there would now be two tin environments: tin sites that are proximal to indium and tin sites that are not. This would likely be manifested by the appearance of a second tin site or by an additional shoulder or other feature on the existing tin lineshape as was observed in Figure 5.5 where protonated and non-protonated pyrophosphate were differentiated by  $^{31}\text{P}$  NMR. Peak deconvolution (if necessary) and integration of these sites could provide a direct measure/confirmation of the indium doping percentage.

Previous  $^{119}\text{Sn}$  NMR studies have been performed on tin pyrophosphate doped with 10 % indium by Mukundan et al.<sup>24</sup> These spectra contained a single broad site that was centered around -860 ppm.<sup>24</sup> Although spectra of undoped tin

pyrophosphate were not provided by Mukundan et al., it is anticipated that changes in features such as lineshape width or chemical shift could be exploited to directly quantify indium doping in tin pyrophosphate samples.

### 7.2.3 Boronic Acid-Containing Elastomers

The  $^{11}\text{B}$  solid-state NMR investigation of boronic acid-containing elastomers: SiBA and Silly Putty used quadrupole lineshape fitting to assign boron coordination environments in these materials. However, these assignments could be further confirmed by performing  $^1\text{H}$ - $^{11}\text{B}$  correlation experiments, such as heteronuclear multiple quantum coherence (HMQC), to verify the proximity of these nuclei through the strength of their through-bond connectivity. HMQC is selective for direct  $^1\text{H}$ - $^{11}\text{B}$  coupling and could therefore be used to distinguish crosslinking via hydrogen bonding ( $\text{B}-\text{O}\cdots\text{H}$ ) and crosslinking via dative bonding ( $\text{B}-\text{O}-\text{B}$ ).<sup>25</sup>  $^1\text{H}$ - $^{11}\text{B}$  through-bond connectivity is expected to be stronger in the hydrogen-bonded case as hydrogen bonds are typically weaker than covalent bonds.<sup>26</sup> The stronger B-O bond that is formed in the dative case is expected to cause a more significant decrease in  $^1\text{H}$ - $^{11}\text{B}$  connectivity than the weaker hydrogen bond is.

One major difference between the studies on SiBA elastomers and Silly Putty presented in Chapter 6 was the fact that several SiBA samples with different and known boronic acid loadings were analyzed as opposed to a single industrially-made Silly Putty sample where the boric acid content was not exactly known. Having a series of materials to analyze allowed conclusions regarding

crosslinking mechanisms (proportion of four-coordinate boron centers) and mechanical properties (Young's Modulus) to be drawn based on boronic acid loading. This offered insight into how the quantity of boronic acid used during synthesis could be tailored to yield elastomers with desired properties. Therefore, a potential expansion of this work would be the synthesis and  $^{11}\text{B}$  NMR characterization of a series of Silly Putty samples with controlled boronic acid content.

### 7.3 References

1. Saalwächter, K. Proton multiple-quantum NMR for the study of chain dynamics and structural constraints in polymeric soft materials. *Prog. Nucl. Magn. Reson. Spectrosc.* **51**, 1–35 (2007).
2. Pileio, G. *et al.* Analytical theory of  $\gamma$ -encoded double-quantum recoupling sequences in solid-state nuclear magnetic resonance. *J. Magn. Reson.* **186**, 65–74 (2007).
3. Yan, Z. B., Brouwer, D. H. & Goward, G. R.  $^{19}\text{F}$  Double Quantum NMR Spectroscopy: A Tool for Probing Dynamics in Proton-Conducting Fluorinated Polymer Materials. *Macromolecules* **49**, 7331–7339 (2016).
4. Kennedy, N. S. J. & Nelmes, R. J. Structural Studies of  $\text{RbH}_2\text{PO}_4$  in its Paraelectric and Ferroelectric Phases. *J. Phys. C Solid State Phys.* **13**, 4841–4853 (1980).
5. Vijayakumar, M., Bain, A. D. & Goward, G. R. Investigations of Proton Conduction in the Monoclinic Phase of  $\text{RbH}_2\text{PO}_4$  Using Multinuclear Solid-State NMR. *J. Phys. Chem. C* **113**, 17950–17957 (2009).
6. Haile, S. M., Chisholm, C. R. I., Sasaki, K., Boysen, D. A. & Uda, T. Solid acid proton conductors: from laboratory curiosities to fuel cell electrolytes. *Faraday Discuss.* **134**, 17–39 (2007).
7. Kreller, C. R. *et al.* Intragranular Phase Proton Conduction in Crystalline  $\text{Sn}_{1-x}\text{In}_x\text{P}_2\text{O}_7$  ( $x = 0$  and  $0.1$ ). *J. Phys. Chem. C* **121**, 23896–23905 (2017).
8. Anfimova, T. *et al.* The effect of preparation method on the proton conductivity of indium doped tin pyrophosphates. *Solid State Ionics* **278**, 209–216 (2015).

9. Paschos, O., Kunze, J., Stimming, U. & Maglia, F. A review on phosphate based , solid state , protonic conductors for intermediate temperature fuel cells. *J. Phys. Condens. Matter* **23**, 234110 (2011).
10. Sato, Y., Shen, Y., Nishida, M., Kanematsu, W. & Hibino, T. Proton conduction in non-doped and acceptor-doped metal pyrophosphate ( $\text{MP}_2\text{O}_7$ ) composite ceramics at intermediate temperatures. *J. Mater. Chem.* **22**, 3973 (2012).
11. Nishida, M. & Tanaka, T. Solid-state NMR study of dopant effects on the chemical properties of Mg-, In-, and Al-doped  $\text{SnP}_2\text{O}_7$ . *Magn. Reson. Chem.* **52**, 163–71 (2014).
12. Bain, A. D. Chemical exchange in NMR. *Prog. Nucl. Magn. Reson. Spectrosc.* **43**, 63–103 (2003).
13. Kreller, C. R., Wilson, M. S., Mukundan, R., Brosha, E. L. & Garzon, F. H. Stability and Conductivity of  $\text{In}^{3+}$ -Doped  $\text{SnP}_2\text{O}_7$  with Varying Phosphorous to Metal Ratios. *ECS Electrochem. Lett.* **2**, F61–F63 (2013).
14. Wu, X., Wang, J., Huang, J. & Yang, S. Robust , Stretchable , and Self-Healable Supramolecular Elastomers Synergistically Cross-Linked by Hydrogen Bonds and Coordination Bonds. *ACS Appl. Mater. Interfaces* **11**, 7387–7396 (2019).
15. Fawcett, A. S., Hughes, T. C., Zepeda-Velazquez, L. & Brook, M. A. Phototunable Cross-Linked Polysiloxanes. *Macromolecules* **48**, 6499–6507 (2015).
16. Brooks, W. L. A. & Sumerlin, B. S. Synthesis and Applications of Boronic Acid-Containing Polymers: From Materials to Medicine. *Chem. Rev.* **116**, 1375–1397 (2016).
17. Martinez, H. High-temperature phase transitions in  $\text{RbH}_2\text{PO}_4$ . (University of Texas at El Paso, 2009).
18. Park, J. & Choi, B. Electrical conductivity and impedance characteristics of  $\text{RbH}_2\text{PO}_4$  crystal above room temperature. *Mater. Lett.* **57**, 2162–2167 (2003).
19. Boysen, D. A., Haile, S. M., Liu, H. & Secco, R. A. Conductivity of Potassium and Rubidium Dihydrogen Phosphates at High Temperature and Pressure. *Chem. Mater.* **16**, 693–697 (2004).
20. Li, Z. & Tang, T. High-temperature thermal behaviors of  $\text{XH}_2\text{PO}_4$  (X = Cs, Rb, K, Na) and  $\text{LiH}_2\text{PO}_3$ . *Thermochim. Acta* **501**, 59–64 (2010).
21. Bain, A. D. Chemical Exchange. in *Annual Reports on NMR Spectroscopy* (ed. Web, G.) 23–48 (Elsevier Ltd, 2008). doi:10.1016/S0066-

4103(07)63002-6

22. Bain, A. D. & Fletcher, D. A. S elective-inversion experiments applied to chemical exchange in coupled spin systems. *Mol. Phys.* **95**, 1091–1098 (1998).
23. Huang, C. H., Knop, O., Othen, D. A., Woodhams, F. W. D. & Howie, R. A. Phosphates of tetravalent elements and a Mossbauer study of  $\text{SnP}_2\text{O}_7$ . *Can. J. Chem. Can. Chim.* **53**, 79–91 (1975).
24. Mukundan, R., Brosha, E., Garzon, F. H. & Einsla, M. L. *Synthesis and conductivity of indium-doped tin pyrophosphates*. **4750**, (2008).
25. Levitt, M. H. *Spin Dynamics: Basics of Nuclear Magnetic Resonance*. (John Wiley & Sons, 2008).
26. Steiner, T. The hydrogen bond in the solid state. *Angew. Chem. Int. Ed.* **41**, 49–76 (2002).



## Appendix

### A.1 Quadrupolar Lineshape Fitting in SiBA Elastomers

Lineshape fitting parameters, calculated based on quadrupolar product values derived from the MQMAS experiment, are provided for **P-49** at 20.0, 11.7 and 7.0 T in Chapter 6 of this thesis (Figure 6.8, Table 6.1). Similar lineshape fitting, based on MQMAS data, was performed for **P-37** (Figure A.1, Table A.1). The same  $C_Q$  and  $\eta$  values were used in all fits.

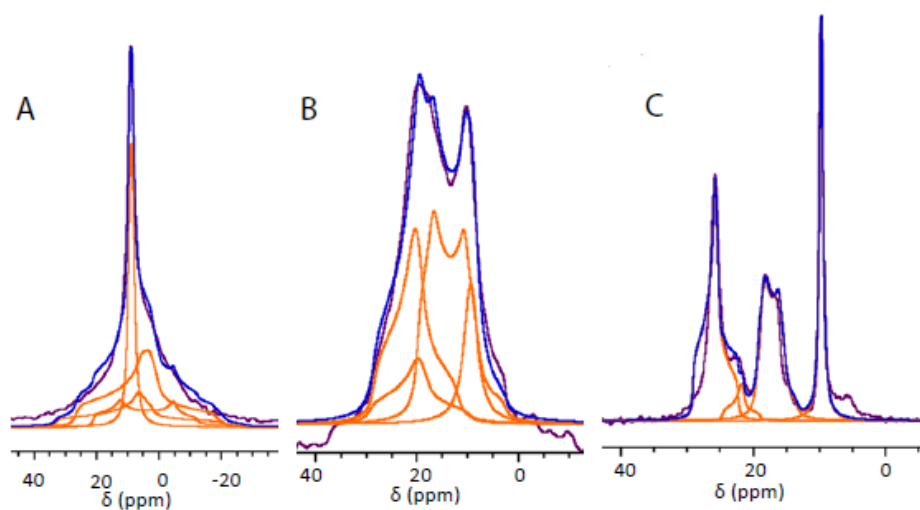


Figure A. 1.  $^{11}\text{B}$  spectra of **P-37** at A) 7.0 T and 15 MAS, B) 11.7 T and 30 MAS and C) 20.0 T and 30 MAS with lineshape fitting.

Table A. 1. Lineshape Fitting Parameters for **P-37** Calculated based on an MQMAS Spectrum

20 T				
Site	1	2	3	4
$\delta$ (ppm)	$9.7 \pm 0.1$	$19.7 \pm 0.1$	$24.5 \pm 0.1$	$29.0 \pm 0.1$
$C_Q$ (MHz)	$0.52 \pm 0.05$	$2.8 \pm 0.2$	$2.5 \pm 0.3$	$2.64 \pm 0.2$
$\eta$	$1.0 \pm 0.1$	$0.3 \pm 0.1$	$0.9 \pm 0.1$	$1.0 \pm 0.1$
LB (Hz)	$180 \pm 30$	$230 \pm 30$	$100 \pm 20$	$100 \pm 20$
Coordination	4	3	3	3
11.7 T				
Site	1	2	3	4
$\delta$ (ppm)	$9.6 \pm 0.3$	$21.1 \pm 0.8$	$28.3 \pm 0.2$	$29.3 \pm 0.2$
$C_Q$ (MHz)	$0.52 \pm 0.05$	$2.8 \pm 0.2$	$2.5 \pm 0.3$	$2.6 \pm 0.2$
$\eta$	$1.0 \pm 0.1$	$0.3 \pm 0.1$	$0.9 \pm 0.1$	$1.0 \pm 0.1$
LB (Hz)	$300 \pm 80$	$250 \pm 40$	$300 \pm 60$	$350 \pm 70$
Coordination	4	3	3	3
7 T				
Site	1	2	3	4
$\delta$ (ppm)	$9.5 \pm 0.3$	$25 \pm 2$	$27 \pm 2$	$33 \pm 3$
$C_Q$ (MHz)	$0.52 \pm 0.05$	$2.8 \pm 0.2$	$2.5 \pm 0.3$	$2.6 \pm 0.2$
$\eta$	$1.0 \pm 0.1$	$0.3 \pm 0.1$	$0.9 \pm 0.1$	$1.0 \pm 0.1$
LB (Hz)	$150 \pm 30$	$100 \pm 20$	$200 \pm 35$	$200 \pm 30$
Coordination	4	3	3	3

SiBA samples with lower boron loading: **P-13**, **T-21** and **T-5**, were not analyzed via MQMAS due to longer experimental times being required. Therefore, boron environments were extracted based on lineshape fitting only. As was done for the samples with higher boron loading,  $C_Q$  and  $\eta$  values were conserved between fits at all magnetic fields.

For **P-13**, two boron environments with chemical shifts above 20 ppm and one boron environment with a chemical shift below 10 ppm were observed (Figure A.2). The two signals at higher chemical shifts were assigned to

three-coordinate boron environments and the signal at 10 ppm was assigned to a four-coordinate boron environment (Table A.2). The observed three-coordinate boron environments were assigned to hydrogen-bonded and free boronic acids based on similarities between the quadrupolar parameters in these and sites that were observed in **P-49**.

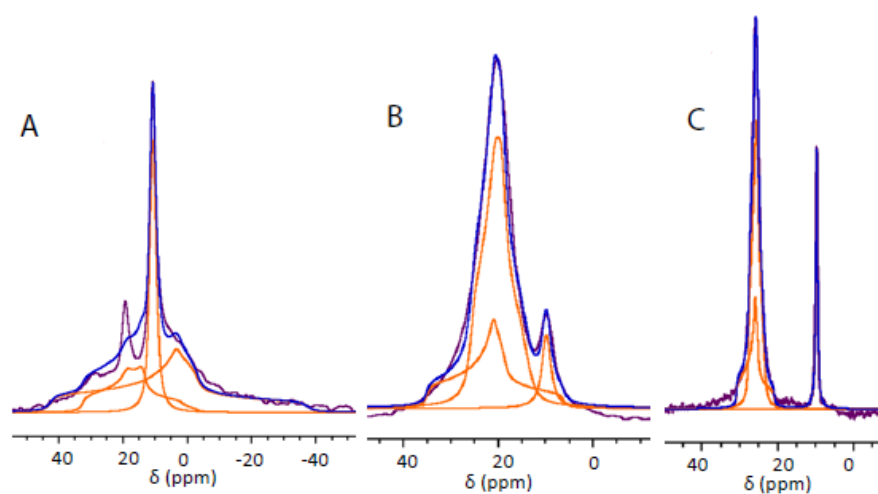


Figure A. 2.  $^{11}\text{B}$  spectra of **P-13** at A) 7.0 T and 15 MAS, B) 11.7 T and 30 MAS and C) 20.0 T and 30 MAS with lineshape fitting.

Table A. 2. Lineshape Fitting Parameters for **P-13** Derived from Lineshape Fitting at Three Magnetic Fields

20 T			
Site	1	2	3
$\delta$ (ppm)	$9.8 \pm 0.1$	$30.8 \pm 0.5$	$27.6 \pm 0.4$
$C_Q$ (MHz)	$0.6 \pm 0.2$	$3.2 \pm 0.4$	$2.2 \pm 0.4$
$\eta$	$1.0 \pm 0.1$	$1.0 \pm 0.2$	$0.8 \pm 0.2$
LB (Hz)	$150 \pm 10$	$200 \pm 40$	$170 \pm 30$
Coordination	4	3	3
11.7 T			
Site	1	2	3
$\delta$ (ppm)	$10.2 \pm 0.1$	$35 \pm 2$	$25.8 \pm 0.9$
$C_Q$ (MHz)	$0.6 \pm 0.2$	$3.2 \pm 0.4$	$2.2 \pm 0.4$
$\eta$	$1.0 \pm 0.1$	$1.0 \pm 0.2$	$0.8 \pm 0.2$
LB (Hz)	$350 \pm 90$	$250 \pm 60$	$300 \pm 90$
Coordination	4	3	3
7 T			
Site	1	2	3
$\delta$ (ppm)	$11.6 \pm 0.1$	$42 \pm 3$	$33 \pm 1$
$C_Q$ (MHz)	$0.6 \pm 0.2$	$3.2 \pm 0.4$	$2.2 \pm 0.4$
$\eta$	$1.0 \pm 0.1$	$1.0 \pm 0.2$	$0.8 \pm 0.2$
LB (Hz)	$150 \pm 30$	$300 \pm 80$	$250 \pm 50$
Coordination	4	3	3

Both telechelic samples also had lower boron loading and were therefore analyzed via lineshape fitting only. **T-21** was similar to **P-13** in the sense that the spectra (Figure A.3) also contained two signals above 20 ppm and one signal around 10 ppm. The signals with higher chemical shifts were assigned to three-coordinate boron centers whereas the signal with the lower chemical shift was assigned to a four-coordinate boron center (Table A.3). Lower relative signal intensity at the four-coordinate site suggests that the telechelic orientation and

therefore lower boronic acid density, results in less crosslinking via four-coordinate dative bonds.

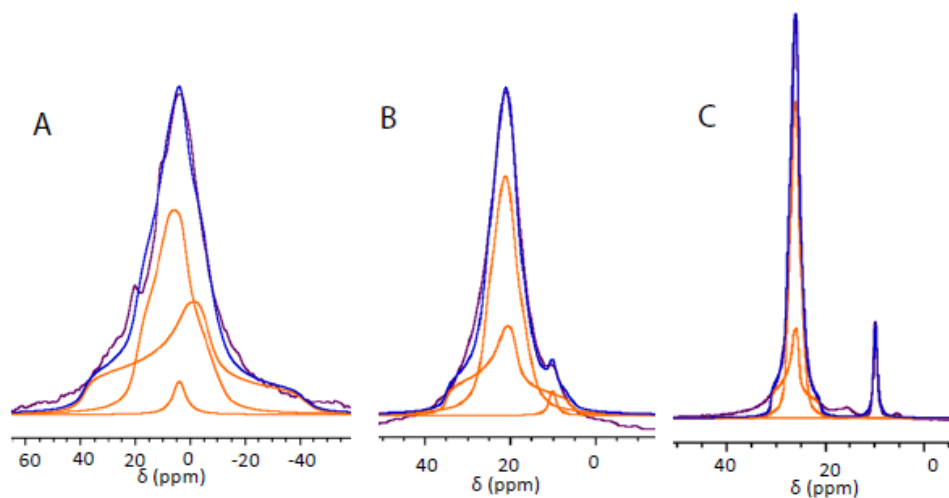


Figure A. 3.  $^{11}\text{B}$  spectra of **T-21** at A) 7.0 T and 15 MAS, B) 11.7 T and 30 MAS and C) 20.0 T and 30 MAS with lineshape fitting.

Table A. 3. Lineshape Fitting Parameters for **T-21** Derived from Lineshape Fitting at Three Magnetic Fields

20 T			
Site	1	2	3
$\delta$ (ppm)	$9.9 \pm 0.1$	$27.7 \pm 0.2$	$31.0 \pm 0.5$
$C_Q$ (MHz)	$0.6 \pm 0.1$	$2.1 \pm 0.5$	$3.3 \pm 0.4$
$\eta$	$1.0 \pm 0.1$	$0.7 \pm 0.2$	$0.9 \pm 0.2$
LB (Hz)	$230 \pm 30$	$200 \pm 30$	$100 \pm 20$
Coordination	4	3	3
11.7 T			
Site	1	2	3
$\delta$ (ppm)	$10.3 \pm 0.1$	$26 \pm 1$	$34 \pm 2$
$C_Q$ (MHz)	$0.6 \pm 0.1$	$2.1 \pm 0.5$	$3.3 \pm 0.4$
$\eta$	$1.0 \pm 0.1$	$0.7 \pm 0.2$	$0.9 \pm 0.2$
LB (Hz)	$400 \pm 50$	$400 \pm 60$	$300 \pm 30$
Coordination	4	3	3
7 T			
Site	1	2	3
$\delta$ (ppm)	$5.0 \pm 0.1$	$19.8 \pm 0.8$	$39 \pm 3$
$C_Q$ (MHz)	$0.6 \pm 0.1$	$2.1 \pm 0.5$	$3.3 \pm 0.4$
$\eta$	$1.0 \pm 0.1$	$0.7 \pm 0.2$	$0.9 \pm 0.2$
LB (Hz)	$500 \pm 90$	$500 \pm 100$	$500 \pm 100$
Coordination	4	3	3

Due to the lower viscosity of the **T-5** sample, MAS spectra were not obtained at 7.0 and 20.0 T. However, spinning was possible at 11.7 T and revealed three boron sites in this material (Figure A.4). As in **P-13** and **T-21**, two of these signals were assigned to three-coordinate boron sites and the other signal was assigned to a four-coordinate site (Table A.4). These assignments were made based on quadrupolar parameters,  $C_Q$  and  $\eta$ . The same quadrupole parameters were used to fit the static lineshapes at 7.0 and 20.0 T (Figure A.4, Table A.4).

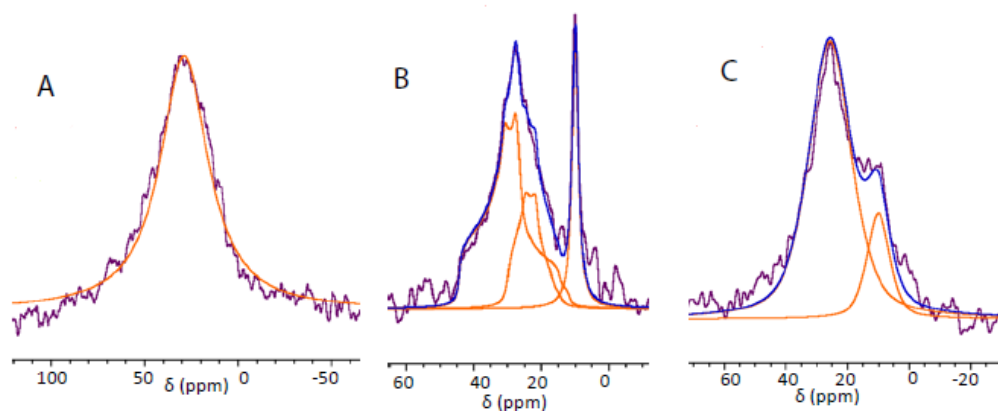


Figure A. 4.  $^{11}\text{B}$  spectra of **T-5** at A) 7.0 T (static), B) 11.7 T and 30 MAS and C) 20.0 T (static) with lineshape fitting.

Table A. 4. Lineshape Fitting Parameters for **T-5** Derived from Lineshape Fitting at Three Magnetic Fields

20 T			
Site	1	2	3
$\delta$ (ppm)	$10.0 \pm 0.1$	$26 \pm 1$	N/A
LB (Hz)	$2400 \pm 400$	$4500 \pm 500$	N/A
Coordination	4	3	N/A
11.7 T (only measurement with MAS)			
Site	1	2	3
$\delta$ (ppm)	$10.1 \pm 0.2$	$3.0 \pm 0.1$	$44 \pm 1$
$C_Q$ (MHz)	$0.5 \pm 0.1$	$2.5 \pm 0.5$	$3.5 \pm 0.5$
$\eta$	$1.0 \pm 0.1$	$0.6 \pm 0.3$	$0.8 \pm 0.3$
LB (Hz)	$340 \pm 30$	$270 \pm 30$	$220 \pm 30$
Coordination	4	3	3
7 T			
Site	1	2	3
$\delta$ (ppm)	$28 \pm 2$	N/A	N/A
LB (Hz)	$3000 \pm 600$	N/A	N/A
Coordination	3	N/A	N/A

## A.2 Direct Analyses of $^1\text{H}$ Coordination in SiBA Elastomers

Hydrogen bonding was not observed via  $^1\text{H}$  NMR in the SiBA elastomers due to significant broadening at these sites. However, hydrogen bonding was observed via infrared spectroscopy. The presence of hydrogen bonding was made apparent by a sharp, intense peak at  $3300\text{ cm}^{-1}$  (Figure A.5). This peak is present in the infrared spectrum corresponding to the hydrolyzed **T-23** elastomer but is not present in the spectrum of the oil precursor. The peak is characteristic of the O-H stretching vibration that is found in hydrogen bonded materials,<sup>1</sup> demonstrating that hydrogen bonding is one of the mechanisms through which elastomeric film formation occurs. The two signals with chemical shifts above 20 ppm that are observed in the **T-23** spectrum (Figure A.3) likely correspond to hydrogen-bonded and free boronic acids. The free boronic acid and the hydrogen-bonded dimer can be further distinguished based on their  $C_Q$  values as dimerized boronic acids tend to have lower  $C_Q$  values.<sup>2</sup>

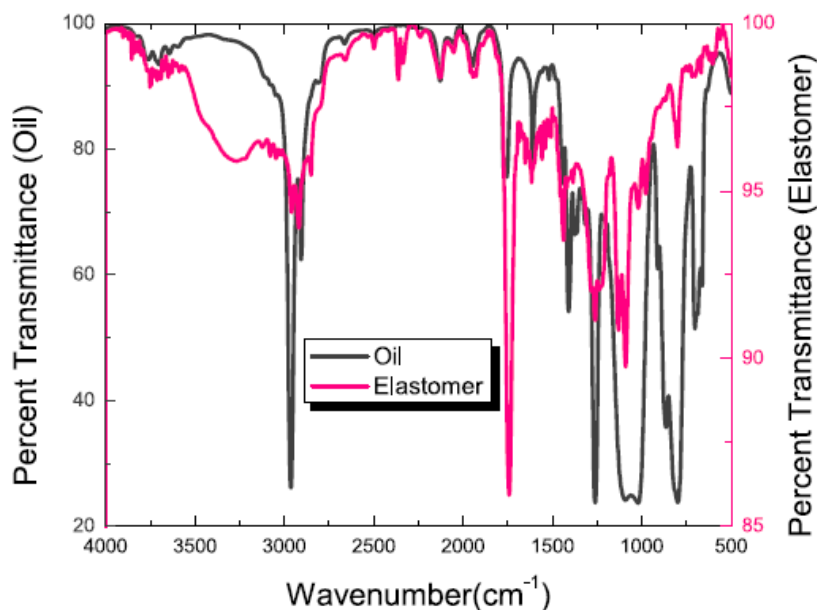


Figure A. 5. Infrared spectrum of **T-23** elastomer (pink) and the tartrate-protected oil precursor (gray). The peak at  $3300\text{ cm}^{-1}$  that is present in the elastomer spectrum but not the oil spectrum is indicative of hydrogen bonding.

The absence of stretching vibrations at  $700$ ,  $1300$  and  $1340\text{ cm}^{-1}$  in the infrared spectrum (Figure A.5) suggests that the SiBA elastomers do not contain boroxines.<sup>3</sup> Boroxines are B-O trimers that are formed by the dehydration of boronic acids.<sup>4</sup> The absence of boronic acids was further confirmed via  $^1\text{H}$  NMR where an absence of peaks above  $8\text{ ppm}$  was observed. Boroxines can typically be identified by a proton signal at  $8.1\text{ ppm}$  which is characteristic of the boron aryl protons (Figure A.6).<sup>5</sup>

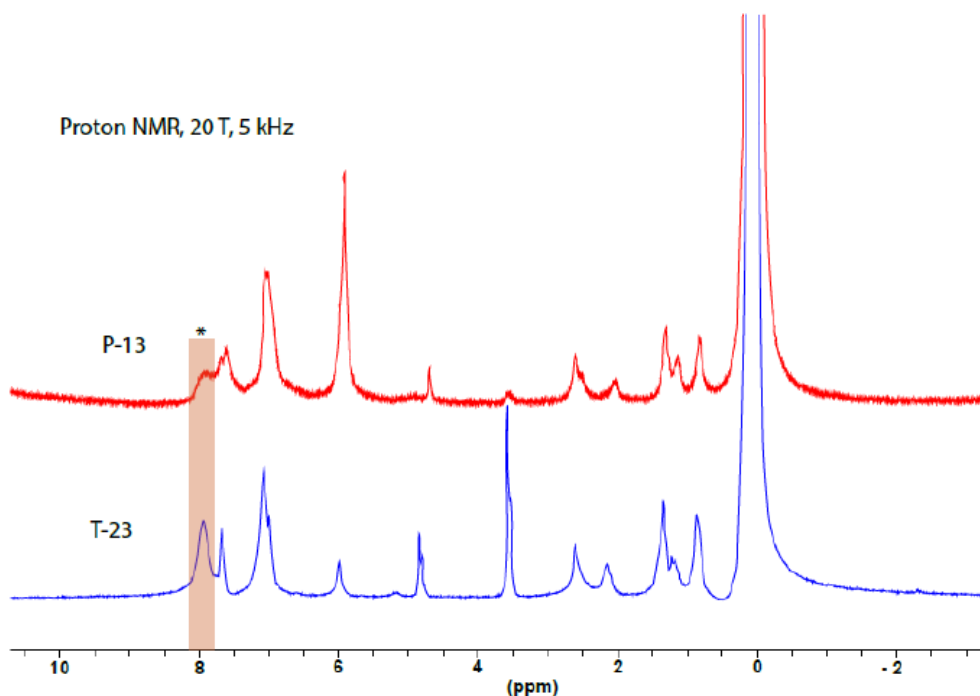


Figure A. 6.  $^1\text{H}$  NMR spectra of **T-23** and **P-13** acquired at 20.0 T with 5 kHz MAS. These spectra do not contain a signal at 8.1 ppm suggesting that boroxines are not present in the SiBA elastomers.

### A.3 Coordination Environments in Silly Putty

Much like  $^1\text{H}$  spectra of SiBA elastomers, the  $^1\text{H}$  spectrum of Silly Putty does not show evidence of hydrogen bonding (Figure A.7). This was attributed to line broadening at these sites. The most intense signal (1), at  $\sim -1$  ppm, was attributed to the methyl groups on the polydimethyl siloxane polymer backbone. All other signals could be attributed to Thixatrol which is a derivative of castor oil.<sup>6,7</sup> The signals at 3.5 ppm (2) could be attributed to alcohols on the fatty acid chains in Thixatrol and the signals at 4 ppm (3) and 5 ppm (4) were attributed to protons on the secondary and tertiary carbons near the carboxyl groups

respectively. All other signals between 1 and 2.5 ppm were similar to those that could be observed in the  $^1\text{H}$  spectrum of castor oil.<sup>7</sup>

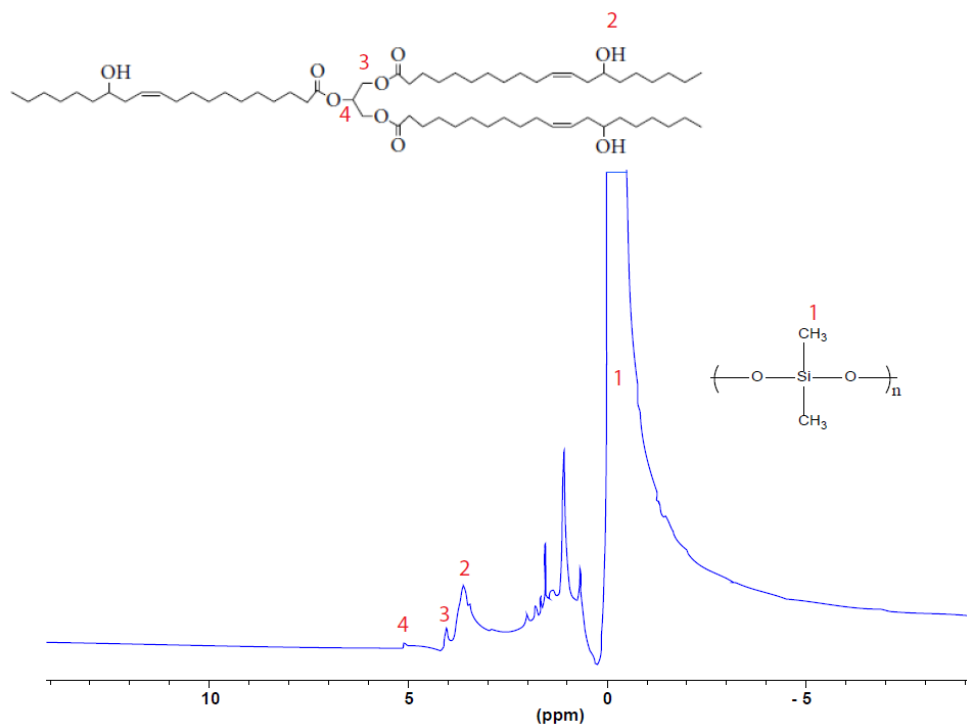


Figure A. 7.  $^1\text{H}$  NMR spectrum of Silly Putty acquired at 20.0 T with 30 kHz MAS. Site labels correspond to the structures in polydimethyl siloxane and castor oil that are responsible for the observed signals.

Free boric acid is believed to be one of the boron coordination modes in Silly Putty. This can be demonstrated based on a  $^{11}\text{B}$  spectrum of boric acid that was acquired at 20.0 T with 30 kHz MAS (Figure A.8). This lineshape was fit yielding a  $C_Q$  value of 2.55 MHz and an  $\eta$  value of 0.05. These agree within error with one of the three-coordinate coordination environments that was identified in Silly Putty. It is likely that Silly Putty contains free boric acid, in addition to crosslinked boron sites, as the characteristic viscosity of elastomers is a result of

the equilibrium between free and crosslinked boronic acids that exist in these materials.<sup>8</sup>

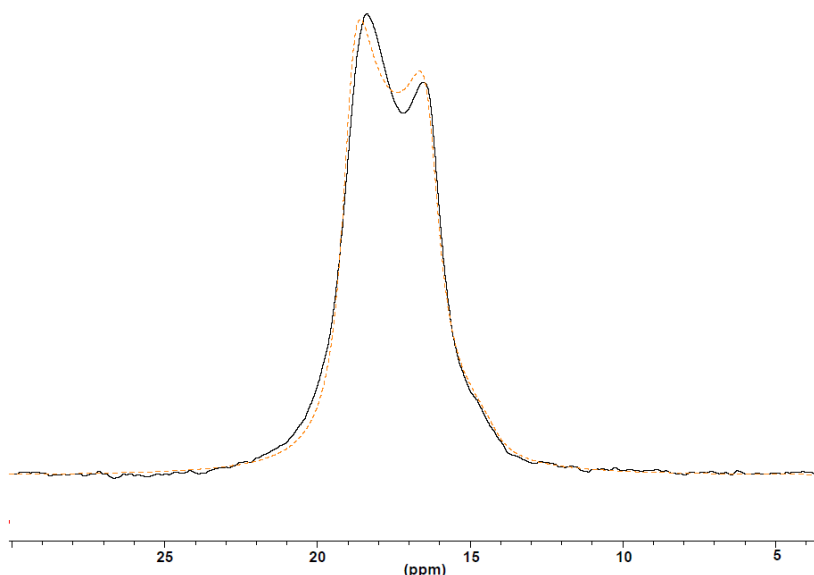


Figure A. 8.  $^{11}\text{B}$  spectrum of boric acid acquired at 20.0 T with 30 kHz MAS. The lineshape was fit with quadrupole parameters yielding a  $C_Q$  of 2.55 MHz and an  $\eta$  of 0.05.

#### A.4 References

1. Mitsuzuka, A., Fujii, A., Ebata, T. & Mikami, N. Infrared Spectroscopy of Intramolecular Hydrogen-Bonded OH Stretching Vibrations in Jet-Cooled Methyl Salicylate and Its Clusters. *J. Phys. Chem. A* **102**, 9779–9784 (1998).
2. Weiss, J. W. E. & Bryce, D. L. A Solid-State B-11 NMR and Computational Study of Boron Electric Field Gradient and Chemical Shift Tensors in Boronic Acids and Boronic Esters. *J. Phys. Chem. A* **114**, 5119–5131 (2010).
3. Smith, M. K. & Northrop, B. H. Vibrational properties of boroxine anhydride and boronate ester materials: Model systems for the diagnostic characterization of covalent organic frameworks. *Chem. Mater.* **26**, 3781–3795 (2014).
4. Hall, D. G. *Boronic Acids*. (Wiley VCH, 2011). doi:10.1002/9783527639328
5. Zepeda-Velazquez, L., Macphail, B. & Brook, M. A. Spread and set

- silicone–boronic acid elastomers. *Polym. Chem.* **7**, 4458–4466 (2016).
6. Golinelli, N., Spaggiari, A. & Dragoni, E. Mechanical behaviour of magnetic Silly Putty : Viscoelastic and magnetorheological properties. *Intelligent Materials, Systems and Structures.* **28**, 953–960 (2017).
  7. Zhang, J., Tang, J. J. & Zhang, J. X. Polyols Prepared from Ring-Opening Epoxidized Soybean Oil by a Castor Oil-Based Fatty Diol. *Int. J. Polym. Sci.* **2015**, 1–8 (2015).
  8. Brooks, W. L. A. & Sumerlin, B. S. Synthesis and Applications of Boronic Acid-Containing Polymers: From Materials to Medicine. *Chem. Rev.* **116**, 1375–1397 (2016).